Magnus Breivik

Fabrication of mid-infrared laser diodes

for gas sensing applications

Thesis for the degree of Philosophiae Doctor

Trondheim, December 2013

Norwegian University of Science and Technology
Faculty of Information Technology,
Mathematics and Electrical Engineering
Department of Electronics and Telecommunications

NTNU – Trondheim
Norwegian University of
Science and Technology

NTNU
Norwegian University of Science and Technology

Thesis for the degree of Philosophiae Doctor

Faculty of Information Technology, Mathematics and Electrical Engineering
Department of Electronics and Telecommunications

ISBN 978-82-471-4899-0 (printed ver.)
ISBN 978-82-471-4900-3 (electronic ver.)
ISSN 1503-8181

Doctoral theses at NTNU, 2013:373

Printed by NTNU-trykk

Abstract

Mid-infrared laser diodes have been fabricated and tested, and semiconductor materials related to mid-infrared lasers have been characterized by X-ray diffraction (XRD).

The temperature dependent lattice constant of $Al_{0.9}Ga_{0.1}As_ySb_{1-y}$, GaSb, AlSb and InSb have been examined using XRD measurements. For $Al_{0.9}Ga_{0.1}As_ySb_{1-y}$, GaSb and AlSb, the lattice constants were measured for temperatures up to 546°C, while for InSb it was examined up to 325°C. For AlSb, also the temperature dependent Poisson ratio was determined. It was found that the thermal expansion of Al-containing layers above room temperature was higher than previously reported. An expression for the lattice matching condition for $Al_{0.9}Ga_{0.1}As_ySb_{1-y}$ epilayers on GaSb substrates as a function of temperature was presented. For GaSb, it was found that the work of Bublik et al. [1] provided accurate data for the temperature dependent lattice constant, and either our data or Bublik et al. [1]'s data should be used. The measurement technique was validated by measuring the lattice constants of Si and GaAs, where our measured values were found to be in agreement with previously published values. For AlSb it was found that the thermal expansion was larger than previously reported in the literature. For InSb it was found that the lattice constant near room temperature was larger than previously reported, and the thermal expansion above 100°C was larger than previously reported.

Laser material was grown using molecular beam epitaxy (MBE). The grown samples were processed into Y-junction laser diodes. The lasers were etched using inductively coupled plasma reactive ion etching (ICP-RIE) and photoresist (PR) ma-N 440 was spun on and baked for use as electrical insulation. The insulation layer was etched using reactive ion etching (RIE) to uncover the top of the etched lasers for contacting. It was found that a O_2/CF_4 etch gave the best uniformity of the insulation layer. The lasers were contacted and tested.

The Y-junction lasers were characterized using power measurements for optical power, multimeters for diode voltage, Fourier transform infrared (FTIR) for spectral measurements, and an infrared camera for near and far field measurements. The measurements suggested that the curved waveguide did not guide the light, most likely due to a low refractive index contrast. This was later supported by scanning electron microscope (SEM) measurements, which showed an etch depth of 1.4 µm, much lower than the etch target of 1.9 µm.

The Y-junction waveguides were simulated using the beam propagation method (BPM). Based on 2D BPM simulations, it was found that an effective refractive index contrast of at least 0.03 is required for guiding light in a curved waveguide for our dimensions, and that waveguide roughness due to processing is less important. The simulations support the findings from the laser measurements, and further suggest that a deeper etch is required for functioning Y-junction laser diodes. Suggestions for improvements to the manufacturing mid-infrared laser diodes are presented.

Preface

This thesis is submitted to the Norwegian University of Science and Technology (NTNU) for partial fulfillment of the requirements of the degree Philosophiae Doctor (PhD). The work has been carried out at the Department of Electronics and Telecommunications (IET) under the supervision of Bjørn-Ove Fimland and co-supervision of Astrid Aksnes.

The main foci of this work were fabrication of Y-junction laser diodes and temperature dependent XRD measurements. The XRD measurements provide useful information for improving the crystalline quality of the grown laser structure. This part of the work is presented by the four papers in chapter 8. The Y-junction laser diode fabrication included growth, clean room processing, testing and simulations. This part of the work is presented in chapters 4 to 7.

I would like to thank my supervisor Bjørn-Ove Fimland for giving me the opportunity to make laser diodes, and become a PhD in the process, and to my co-supervisor Astrid Aksnes for her supportive role in this work. I also want to thank them for all their fruitful discussions and guidance over the years. Hopefully they can find some of the knowledge they have given me over the years in this thesis.

I would also like to thank my group; Tron Arne Nilsen, who I worked closely with on MBE growth and XRD measurements, which have played a key role in both of our works. Saroj Kumar Patra and Thanh Nam Tran for fruitful discussion and involvement in all the projects relating to lasers. I wish all three of them good luck in finishing their own PhD's!

On my PhD journey I have met a lot of people that I would also like to thank: Dr. Guro Kristin Svendsen and soon-to-be-Dr. Erlend Leirset, with whom I have shared countless discussions, coffee breaks and beers over the years. Espen Selvig and Trond Brudevoll at FFI, who have increased my understanding of XRD, MBE, and "the inner workings" of the semiconductors through numerous discussions over the years. Johannes Skaar and Helge Engan for their fruitful discussions related to the optical properties of a laser diode. Erik Poppe for his Y-junction laser masks, and discussions related to the laser structure. Dheeraj Dasa for discussions and help regarding MBE. Professor Luke F. Lester and his group (David, Therese, Mark, Mike, Yan, Nishant, Chang-Yi, Nader, William) at center for high technology materials (CHTM), University of New Mexico, for giving me to opportunity to process laser diodes, which gave me much of the knowledge and experience I needed to fabricate the laser diodes in this work. The staff at Nanolab (Kay, Espen, Ida, Mark, Trine, Ken Roger, Søren and Hanna) for their good spirits, cleanroom facilities necessary to process the lasers, and for (most of the time) keeping their equipment up and running. I would also like to thank them for helping me financially by letting me work there every now and then, (before and) after my PhD funding ran out. Marius Lorvik for his help setting up the laser testing setup during his summer job. Renato, Geir and Eva at Intopto for their experience and discussions relating to fabricating laser diodes and other unrelated topics.

And of course I would like to thank several generations of coffee (or tea) drinkers who I have shared coffee and discussions with over the years, including Erik, Ingrid, Stein Arne, Guro, Erlend, Erlend Magnus, Magnus, Sigbjørn, Kamal, Eivind, Sigrid, Jos, Åsmund, Bendik, .. I could go on.

Finally, I would like to thank my parents for all their support during my PhD.

List of papers

Included papers

[1] T. A. Nilsen, M. Breivik, G. Myrvågnes, and B.-O. Fimland. "Thermal expansion of GaSb measured by temperature dependent x-ray diffraction". *J. Vac. Sci. Technol., B* **28** (2010), pp. C3I17–C3I20. DOI: `10.1116/1.3336341`.
My contributions: *Performed about half of the measurements. Measurement techniques and calculations were developed in co-operation between me and T. A. Nilsen (used for all included papers). Involved in discussions relating to the results and manuscript.*

[2] M. Breivik, T. A. Nilsen, G. Myrvågnes, E. Selvig, and B.-O. Fimland. "Temperature dependent lattice constant of $Al_{0.90}Ga_{0.10}As_ySb_{1-y}$". *J. Vac. Sci. Technol., B* **28** (2010), pp. C3I1–C3I5. DOI: `10.1116/1.3414830`.
My contributions: *Wrote the manuscript. Performed most of the X-ray diffraction measurements and all of the calculations and data analysis, except those relating to the thermal gradient in the sample.*

[3] T. A. Nilsen, S. K. Patra, M. Breivik, and B.-O. Fimland. "Thermal dependence of the lattice constant and the Poisson ratio of AlSb above room temperature". *J. Cryst. Growth* **336** (2011), pp. 29–31. DOI: `10.1016/j.jcrysgro.2011.09.034`.
My contributions: *Suggested using layers of different strain to determine the lattice constant without prior knowledge of the Poisson ratio. Involved in discussions relating to the results and manuscript.*

[4] M. Breivik, T. A. Nilsen, and B.-O. Fimland. "Temperature dependent lattice constant of InSb above room temperature". *J. Cryst. Growth* **381** (2013), pp. 165–168. DOI: `10.1016/j.jcrysgro.2013.06.034`.
My contributions: *Wrote the manuscript. Performed all measurements and calculations, except those relating to the thermal gradient in the sample.*

Other work not included in thesis

[1] T. A. Nilsen, M. Breivik, E. Selvig, and B.-O. Fimland. “Critical thickness of MBE-grown $\mathrm{Ga}_{1-x}\mathrm{In}_x\mathrm{Sb}(x < 0.2)$ on GaSb”. *J. Cryst. Growth* **311** (2009), pp. 1688–1691. DOI: 10.1016/j.jcrysgro.2008.11.083.

[2] A. K. Storebo, T. Brudevoll, O. Olsen, O. C. Norum, and M. Breivik. “Energy relaxation in IR laser excited $\mathrm{Hg}_{1-x}\mathrm{Cd}_x\mathrm{Te}$”. *J. Phys.: Conf. Ser.* **193** (2009), p. 012024. DOI: 10.1088/1742-6596/193/1/012024.

[3] Y. Li, M. Breivik, C.-Y. Feng, C.-Y. Lin, N. Patel, W. Zortman, M. Crowley, and L. F. Lester. “A low repetition rate all-active monolithic passively mode-locked quantum dot laser”. In: *23rd Annual Meeting of the IEEE Photonics Society*. IEEE. 2010, pp. 363–364. DOI: 10.1109/PHOTONICS.2010.5698910.

[4] Y. Li, M. Breivik, C.-Y. Feng, B.-O. Fimland, and L. F. Lester. “A Low Repetition Rate All-Active Monolithic Passively Mode-Locked Quantum-Dot Laser”. *IEEE Photonics Technol. Lett.* **23** (2011), pp. 1019–1021. DOI: 10.1109/LPT.2011.2151281.

[5] T. Brudevoll, A. K. Storebo, O. Skaaring, C. N. Kirkemo, O. C. Norum, O. Olsen, and M. Breivik. “Time-Resolved Laser Spectroscopy of Semiconductors-Physical Processes and Methods of Analysis”. In: *Femtosecond-Scale Optics*. InTech, 2011. Chap. 6, pp. 139–168. ISBN: 978-953-307-769-7. DOI: 10.5772/1932.

[6] M. T. Crowley, D. Murrell, N. Patel, M. Breivik, C.-Y. Lin, Y. Li, B.-O. Fimland, and L. F. Lester. “Analytical modeling of the temperature performance of monolithic passively mode-locked quantum dot lasers”. *IEEE J. Quantum Electron.* **47** (2011), pp. 1059–1068. DOI: 10.1109/JQE.2011.2157953.

[7] M. T. Crowley, D. Murrell, N. Patel, M. Breivik, C.-Y. Lin, Y. Li, B.-O. Fimland, and L. F. Lester. “Modeling the temperature performance of monolithic passively mode-locked quantum dot lasers”. In: *Proceedings of SPIE*. Vol. 7933. 2011, p. 793312. DOI: 10.1117/12.875121.

[8] D. Murrell, M. T. Crowley, M. Breivik, R. Raghunathan, A. Aboketaf, A. Elshaari, S. F. Preble, B. O. Fimland, and L. F. Lester. “Design of uncooled high-bandwidth ultra-low energy per bit quantum dot laser transmitters for chip to chip optical interconnects”. In: *Optical Interconnects Conference, 2012 IEEE*. IEEE. 2012, pp. 72–73. DOI: 10.1109/OIC.2012.6224441.

Contents

1 Introduction and Motivation **1**

2 Laser Theory **9**
- 2.1 Confinement 10
  - 2.1.1 Quantum wells 10
  - 2.1.2 Waveguides 12
- 2.2 Laser 14
  - 2.2.1 Fabry-Perot laser 16
  - 2.2.2 Y-junction laser 21
  - 2.2.3 Other tunable laser structures 23
  - 2.2.4 Gas detection lasers 23

3 Material system **25**
- 3.1 Introduction to material properties 25
  - 3.1.1 Overview of important parameters 25
  - 3.1.2 Recombination mechanisms 26
  - 3.1.3 Effects of strain 29
  - 3.1.4 Band alignment at interfaces 29
  - 3.1.5 Gas properties 31
- 3.2 The 6.1 Å family 31
  - 3.2.1 $Ga_xIn_{1-x}As_ySb_{1-y}$ 34
  - 3.2.2 $Al_xGa_{1-x}As_ySb_{1-y}$ 34
- 3.3 X-ray Diffraction 36
  - 3.3.1 Comparative technique 38
  - 3.3.2 Bond's method 39
  - 3.3.3 Fatemi's method 41
- 3.4 Other characterization techniques 41
  - 3.4.1 Photoluminescence 42
  - 3.4.2 Hall Measurements 42

4 Growth of Laser Diodes 45
4.1 Epitaxial growth 45
4.1.1 Strain and the critical thickness 46
4.2 Molecular Beam Epitaxy 46
4.3 Growth of a laser structure 50
4.3.1 Laser structure 50

5 Processing of Laser Diodes 55
5.1 Photolithography 55
5.2 Etching 56
5.2.1 Selectivity 60
5.3 Insulation 60
5.4 Metallization 61
5.4.1 Lift-off 62
5.4.2 Annealing 64
5.5 Lapping and cleaving 65
5.6 Contacting 65
5.7 Characterization 66
5.7.1 Microscope 66
5.7.2 SEM 66
5.7.3 Profilometer 66
5.8 Processing results 67
5.8.1 Using ma-N 440 as insulation 67
5.8.2 Y-junction laser processing 69

6 Testing of Laser Diodes 75
6.1 Important test parameters 75
6.2 Experimental setup 76
6.3 Test results 77
6.3.1 I-V and L-I measurements 77
6.3.2 Wavelength 82
6.4 Gain measurements 84
6.5 Near field and far field measurements 84
6.6 Other measured parameters 88
6.7 The lack of interferometric tuning 88

7 Light propagation in waveguides 91
7.1 Mode solver 91
7.2 Light propagation in Y-junction waveguides 93
7.2.1 The effects of design parameters on the waveguiding . . . 93

8 Publications 103
- 8.1 Paper I - Thermal expansion of GaSb measured by temperature dependent x-ray diffraction . . . 103
- 8.2 Paper II - Temperature dependent lattice constant of $\mathrm{Al}_{0.90}\mathrm{GaAs}_y\mathrm{Sb}$ 109
- 8.3 Paper III - Thermal dependence of the lattice constant and the Poisson ratio of AlSb above room temperature . . . 115
- 8.4 Paper IV - Temperature dependent lattice constant of InSb above room temperature . . . 119

9 Conclusions and further work 125
- 9.1 XRD measurements . . . 125
- 9.2 Y-junction lasers . . . 126
- 9.3 Further work . . . 127
  - 9.3.1 Computations and simulations . . . 127
  - 9.3.2 Growth and material characterization . . . 129
  - 9.3.3 Laser processing . . . 131
  - 9.3.4 Testing of laser diodes . . . 132

A Important material parameters 133

B Slab waveguide 139

C Laser processing recipe 143

D ma-N 440 insulation etchback 151

E Laser spectrum measurements 157

F Near and far field simulations 177

List of symbols 181

List of acronyms 183

Chapter 1

Introduction and Motivation

The monitoring of gaseous species is of importance in environments where poisonous or otherwise harmful gases are present. Measuring the spectral absorption of gases enables accurate detection of a predefined gas even at low gas concentrations. A good selectivity of a specific gas species can be achieved using this technique, provided no other gas species absorb radiation at the same wavelengths. In fig. 1.1 the gas absorption lines of CO, CH_4 and H_2S are shown together with the atmospheric absorption of water and CO_2.

By measuring the absorption of radiation at wavelengths where water and CO_2 don't absorb, the presence of these gases can be determined from their spectroscopic signature. The gas concentration can be found by measuring the attenuation of a laser diode beam intensity on a detector. The laser wavelength is then continuously tuned across the absorption line, and the attenuation of the beam intensity is used to determine the gas concentration. This is referred to as tunable diode laser (absorption) spectroscopy (TDLS) [2]. Such a laser diode based system has the potential to be very compact, since the laser diodes are usually just a few mm long. A packaged laser diode is shown in fig. 1.2.

In this work, the focus is on fabricating GaSb-based tunable laser diodes in the 2 to 2.5 µm wavelength range utilizing junction structures. GaSb-based laser diodes can cover wavelengths from about 1.6 to at least 3.7 µm [3], by using alloys of Al, Ga, In, As and Sb. This allows for TDLS systems in the atmospheric windows between 2 and 2.5 µm and above 3.5 µm. It is also compatible with standard cleanroom processes, enabling processing of the material into devices with critical dimensions in the µm and sub-µm range.

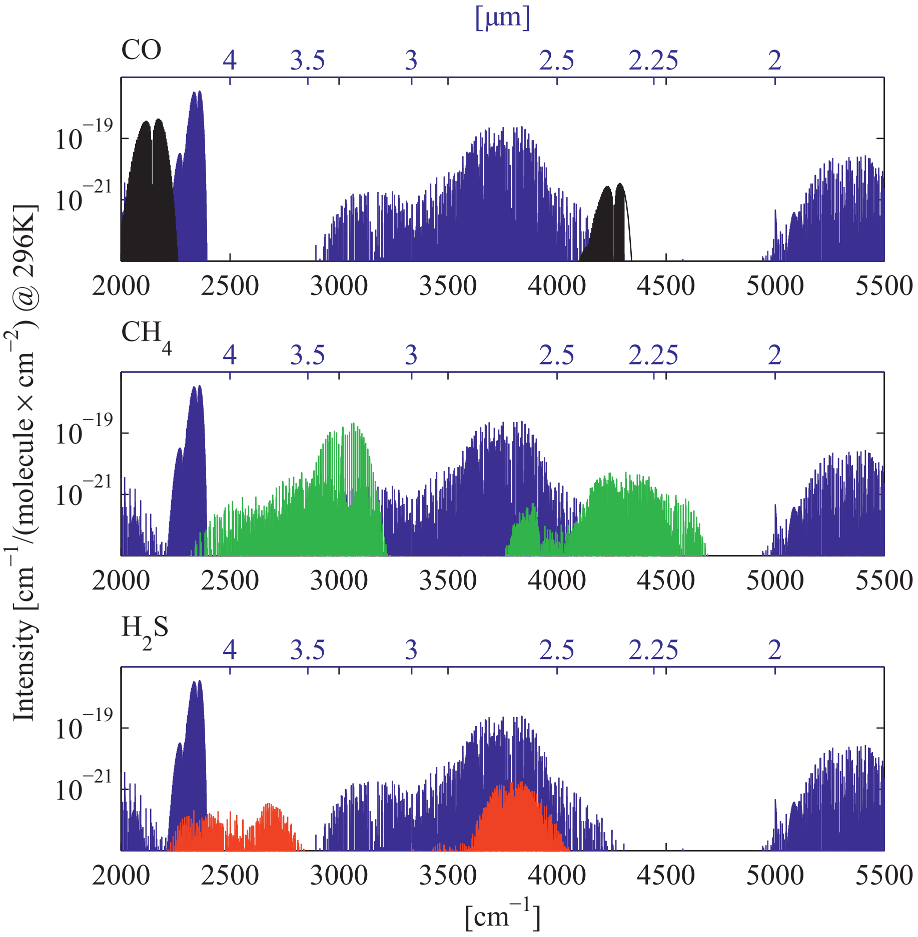

Figure 1.1: The absorption lines of CO (black), CH_4 (green) and H_2S (red) in the mid-infrared compared to atmospheric absorption lines of CO_2 and H_2O (blue). To avoid atmospheric absorption, TDLS in the mid-infrared is usually performed between 2 and 2.35 µm, and between 3.5 and 4 µm. The data is from the high-resolution transmission molecular absorption database (HITRAN) 2004 [4].

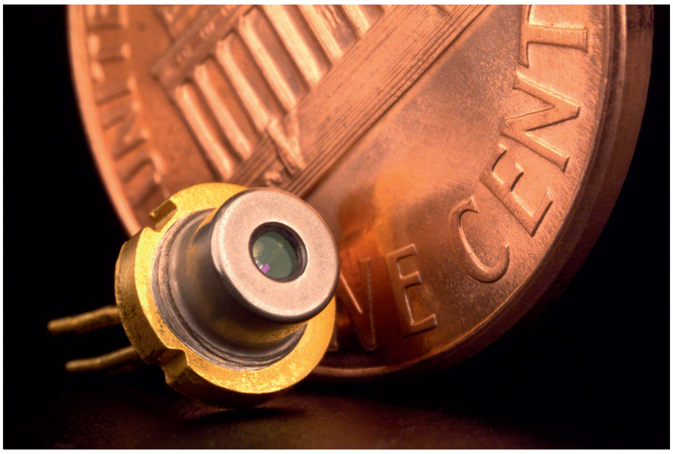

Figure 1.2: A photograph of a packaged laser diode, showing its small size. The actual laser diode is usually only a few mm long, and it is placed behind the window of the laser package. This photograph is downloaded from Wikimedia Commons [5].

History: The fabrication of GaSb-based laser diodes goes back to the 80's, with the first InGaAsSb/AlGaAsSb laser grown by liquid phase epitaxy (LPE) published in January 1980 by Kobayashi et al. [6], lasing at 1.8 µm. This technique has some fundamental problems related to the required thermal equilibrium conditions; it limits the amount of In that can be incorporated in the InGaAsSb core due to the miscibility gap [7]. It also causes problems for AlGaAsSb layers, where a limited incorporation of As limits the maximum Al content in the layers to about 20–40%.

The first InGaAsSb laser grown by molecular beam epitaxy (MBE) was published in 1985 by Tsang et al. [8], where the benefits of this *non*-equilibrium growth technique were demonstrated, by avoiding the miscibility gap problems experienced in thermal equilibrium. It also has other benefits, such as the minimum possible layer thickness, enabling growth of quantum wells (QWs).

There are other material systems that can also be used for mid-infrared lasers, such as IV-VI lead salts and II-VI CdHgTe based lasers. However, current research suggests that the III-Vs are best suited [9]. There has been a lot of research on mid-infrared laser diodes, and a recent update on the field can be found in chapter 5 in Coleman et al. [9], which includes reviews of lasers based on all of these material systems (II-VIs, III-Vs, and IV-VIs).

AlGaAsSb/GaInAsSb soon became an obvious choice for growing the laser structures due to GaInAsSb's low band gap required for mid-infrared lasing, and AlGaAsSb's low refractive index required for light confinement in the waveguide.

The preferred substrate, GaSb, has a very high refractive index[1], which prevents it from being used as a part of the waveguide design in these lasers.

The AlGaAsSb/GaInAsSb type-I laser is the most commonly used structure for lasing at wavelengths close to 2 µm. For wavelengths above ≃2.7 µm, the valence band offset (VBO) of the AlGaAsSb/InGaAsSb material system is too low to confine holes and electrons in the same layer [10]. To reach longer wavelengths, several techniques have been used, such as type-II and interband/quantum cascade lasers (ICL/QCL). Type-II lasers have shown promising results in the wavelength range 2.6–3.5 µm [10], where type-I traditionally have not been usable due to the lack of VBO. However, in recent years the type-I AlGa**In**AsSb/GaInAsSb-based lasers have shown promising results with room temperature (pulsed) lasing up to 3.73 µm [3]. For even longer wavelengths, ICL have shown good performance between 3.4 and 4.2 µm [11].

While growth of the laser diode structures is an essential part of manufacturing laser diodes, it is also important to process the laser material into working devices. Tunable single-mode laser design can be achieved by several techniques, and the most common techniques used are distributed bragg reflector (DBR), distributed feedback (DFB) and vertical (external) cavity surface-emitting lasers (V(E)CSELs). Since the 80's, many groups have been and are still researching these TDLS laser diodes. The following references are a selection of their publications in order to get an overview of the different group's main foci. There are too many groups that have worked on GaSb-based lasers to list all of them, and only the major groups are presented here:

In the early 90's a lot of work on MBE-grown AlGaAsSb/InGaAsSb based laser diodes was performed by Lincoln Laboratory (H. K. Choi, S. J. Eglash, G. W. Turner et al.) at Massachusetts Institute of Technology, on improving the AlGaAsSb/InGaAsSb laser structure. Some of their main topics include laser diodes with high power [7, 12], low-threshold [13], and tapered waveguides [14]. Other lasers in the 2–3 µm range [15, 16] were also fabricated. They also increased the Al-content of the AlGaAsSb cladding from the value of 20–40% obtained in LPE [17] to 50 [16]–75% [17] and ended up at the 90% [18] Al commonly used today, which is important for increased optical and electrical confinement in the laser structure.

Other advances by various groups in the 90's were the introduction of strain in the quantum wells to reduce the Auger recombination and other nonradiative recombination mechanisms [19]. In the 2000's there is still ongoing research on GaSb-based laser diodes:

M. C. Amann et al. at Walter Schottky Institut (Technische Universität München)

---

[1] An overview of material parameters, such as refractive indices, band gaps and band offsets, can be found in appendix A.

have been working on VCSELs [20, 21] and long-wavelength mid-infrared lasers. They have fabricated type-I lasers beyond 3 µm wavelengths using quinternary AlGaInAsSb barriers [3, 22], including the first publication of this laser structure [23].

G. Belenky and L. Shterengas et al. at Stony Brook University have been researching high power 2.3 µm lasers [24, 25] and type-I lasers above 3 µm wavelengths using quinternary barriers [26, 27].

J. R. Meyer, I. Vurgaftman, and W. W. Bewley et al. at Naval Research Laboratory have been researching ”W” type-II lasers [28], especially for use in ICLs [29, 30]. These structures are then used for fabricating DFB lasers [31], including lasers utilizing photonic crystals [32, 33].

J. A. Gupta et al. at Institute for Microstructural Sciences with the National Research Council of Canada have been working on DFB lasers for gas sensing between 2.3 and 3.5 µm [34, 35]. They have also worked on the AlInGaAsSb quinternary barriers, with lasing above 3 µm at room temperature [36].

A. N. Baranov, A. Joullié, and E. Tournié et al. at Centre d’Electronique et de Micro-Optoélectronique de Montpellier (CEM2) have been working on DFB [37] and Fabry-Perot [2, 38] lasers for TDLS, in addition to V(E)CSEL [39–41], type-II [42] and type-III [43] lasers.

A series of review articles on mid-infrared laser diodes have been written, and Coleman et al. [9] (2012), Joullié and Christol [10] (2003) and Choi [44] (1996) provide valuable information with regards to the evolution of the GaSb-based mid-infrared lasers at different stages of development.

While the laser diodes are primarily designed for TDLS, they have also been suggested as lasers for telecommunication purposes. Fluorine-based optical fibres have reduced attenuation for longer wavelengths compared to silica based fibres, and were expected to replace today’s fibres. This change of optical fibers has not yet happened due to problems producing the fibres, and the main focus remains on TDLS. However, recent advances in hollow-core photonic-bandgap fibres offering a 31% reduction in latency and a wide bandwidth (160 nm @ 1550 nm) suggests that sub-0.2 dBm/km fibres utilizing 2 µm tunable laser diodes are realistic [45]. This could again increase the interest in mid-infrared laser diodes for use in telecommunications.

Remaining challenges: The push into the 3 to 4 µm wavelength range is important for gas detection applications, and the material technology still needs more work. AlGaInAsSb has enabled type-I lasers in this wavelength range, due to the increased hole confinement in GaInAsSb wells with AlGaInAsSb barriers, as compared to AlGaAsSb barriers. Wavelengths of 3.73 µm [3] pulsed and 3.44 µm [27] continuous wave (CW) at room temperature have been demonstrated. However, the material has not been fully characterized with regards to its electrical and optical properties, which are important for proper design of laser diodes utilizing this material. The wavelengths reachable by type-I lasers are continuously increasing upwards towards 4 µm, while for ICL they are increasing downwards [11, 30] towards 3 µm. InAs/AlSb QCL lasers can reach the whole range, but only in pulsed mode [9].

Laser processing also needs more work, and research on tunable laser structures is still ongoing. Most of the research in laser structures is towards DFB and VCSEL structures [9]. Furthermore, the high reactivity of AlGaAsSb with oxygen makes it unsuitable for lasers utilizing regrowth [35], which is a common practice for creating widely tunable telecommunication lasers [46]. With the use of regrowth, a wide variety of widely tunable laser structures can be implemented [46].

Adamiec et al. [47] have demonstrated tuning from 1.7 to 2.4 µm in a single laser by varying the pressure in a liquid pressure cell from 0 to 19 kbar. Kruczek et al. [48] have demonstrated 85 nm tuning using an external cavity QCL, and Koslowski et al. [49] have demonstrated 80 nm tuning using binary superimposed gratings. While widely tunable GaSb-based laser diodes have been demonstrated, most of the work has been towards DFB structures. These lasers have a high side-mode suppression ratio (SMSR) ($>$30 dB) [9], but usually at a limited tuning range. While a high SMSR is important for trace gas sensing, manufacturing lasers that can be widely tuned enables the use of a single laser in gas detection systems for several different gases. Fabricating such lasers reduces the number of different lasers required, reducing costs relating both to the fabrication the laser diodes, and to the implementation and servicing the gas sensor systems. More work towards creating widely tunable laser diodes is therefore beneficial.

Virtual substrates and layers composed of GaInSb, AlInSb and InAsSb allows for laser diodes at even longer wavelengths, where InAsSb can reach wavelengths towards 9 µm [50]. Lasers lasing at 3 µm grown on (Al)GaInSb metamorphic layers have already been demonstrated [51]. In addition, growth on GaAs and Si are interesting for future applications, where GaSb-based devices could be integrated into a Si platform [9, 52] to bridge the gap between Si-based electronics and III-V semiconductor photonics [53].

The beam quality of the laser diodes are also poor, with a highly divergent beam [54], requiring relatively sophisticated solutions to collimate the beam. This problem can either be overcome by using VCSEL, or by improving the waveguide design of the lasers [54]. A particular problem is the high refractive index contrast between the AlGaAsSb separate confinement heterostructure (SCH) and the AlGaAsSb cladding layers, which should be solved by waveguide design or change of materials. With regards to the VCSEL, these laser diodes have their own problems, relating to the limited tuning range [54].

Our work: A working TDLS system will need a laser diode, a path for interacting with the gas, a detector and a setup for signal processing. This work focuses on the light source, the mid-infrared laser diodes[2]. For gas sensing one needs a laser with a well defined wavelength, which can be easily tuned over the absorption line of the gas. In a gas detection system, the laser diode should in fact not only be used to measure the total attenuation, but also the wavelength-dependent attenuation. The laser will in this case work as a tunable monochromatic lightsource for a limited-range spectrometer.

Other groups focus mainly on gratings to achieve the wavelength selection (DFB, DBR, VCSEL). We have chosen to focus on junction structures to achieve the wavelength tunability. Junction lasers offer easier processing, but have a complex waveguide junction structure and reduced SMSR, however, they should be sufficient for gas detection. The SMSR can also be improved upon at a later stage if necessary, for example by adding gratings or a third waveguide to the structure [46]. Most other widely tunable monolithic laser structures benefit from passive tunable gratings and phase sections, requiring regrowth of the laser structure [46]. Epitaxial regrowth of GaSb-based laser diodes is currently not feasible due to the reactive nature of AlGaAsSb [35, 57, 58], used for cladding layers, making Y-junction laser diodes an interesting alternative.

Though much characterization of the semiconductor structures used for laser growth has been performed, most of the structural information is based on room-temperature or near-room-temperature measurements. Previous studies in our group suggests that improved crystalline quality can be achieved by lattice matching epilayers at growth temperature [59], which is especially important for thick epilayers. The availability of an X-ray Diffractometer (XRD) with a temperature stage has enabled us to examine the above room temperature thermal expansion of the thick epilayers of the laser structure, the cladding layers. In paper I in chapter 8, the temperature dependent lattice constant of the most common cladding layer alloy for GaSb-based lasers, $\mathrm{Al}_{0.90}\mathrm{Ga}_{0.10}\mathrm{As}_y\mathrm{Sb}_{1-y}$, has been characterized [60]. We have also examined and updated, where necessary, the thermal expansion and temperature dependent lattice constant of binary semiconductors that are important for mid-infrared laser growth, namely GaSb [61], AlSb [62], InAs [63], GaAs [64] and InSb [65]. These studies are presented in the papers II–IV in chapter 8. Good knowledge of the thermal expansion is important for optimizing growth conditions and strain in the laser structure. This research is valuable for all structures using

---

[2] While actual gas detection is beyond the scope of this thesis, Werle [55] and Werle et al. [56] cover the steps involved in realizing a gas detection system based on TDLS, which may be useful for the interested reader.

alloy semiconductors made up of Ga, Al, In, As and Sb where a high crystalline quality is required. This can be pseudomorphic, metamorphic[3], or other structures where the lattice constants and thermal expansions of the different layers are important for strain balancing and determining critical thicknesses at growth and room temperatures. Pseudomorphic and metamorphic structures are used for e.g. lasers [67], detectors [50] and high-electron mobility transistors (HEMT) [68]. Strain control is in general important for thick structures such as high quality cladding layers [60], and highly strained QWs in laser structures [69].

The main goal of this work is the development of widely tunable laser diodes for trace gas sensing. For the implementation of these lasers, the Y-junction waveguide structure was chosen. The potential benefit of these lasers is cheaper processing; while grating based lasers such as DFB and DBR usually require sub-µm precision and resolutions for processing the gratings, the critical dimension of the Y-junction laser is about 1–3 µm, which is attainable with contact photolithography. A reduction in production complexity will in most cases reduce the costs and increase the yield.

To create Y-junction laser structures, many steps are needed; MBE growth of the laser structures, cleanroom processing to create the devices, and additionally a proper setup to test the lasing properties of the devices. A large part of this work has focused on X-ray diffraction (XRD), which is an important characterization technique for controlling the crystalline quality and strain of the MBE-grown laser structures.

In chapter 2 the laser theory is presented, followed by a presentation of the material properties and material system in chapter 3, in addition to the characterization of these materials. In section 3.3 the XRD characterization technique is presented, which is central to all the papers in this work. Chapters 4 to 7 cover the growth, processing, testing and simulations of the junction laser diodes, respectively. The relevant theory and techniques are presented first, followed by the results on a chapter-by-chapter or section-by-section basis. The included papers can be found in chapter 8. Finally the conclusion and suggestions for improvements and further work are presented in chapter 9.

---

[3] A pseudomorphic layer refers to a fully strained layer on top of a substrate of a different lattice constant. For a metamorphic layer the lattice constant also differs from the substrate, but the layer is fully relaxed to its bulk state [66].

Chapter 2

Laser Theory

Light amplification by stimulated emission radiation (Laser) refers to the generation of light by the stimulated emission mechanism. For semiconductor lasers excited electrons in the conduction band can be *stimulated by a photon* to recombine into the valence band, creating a copy of the original photon. This process is called stimulated emission, and it is the central mechanism allowing lasers to work [46]. To achieve lasing, you need three basic "ingredients":

A gain medium A material that amplifies the light transmitted through it, allowing for stimulated emission. A gain medium is defined by its power gain g, so that

$$I(z) = I(0)e^{gz}, g > 0. \tag{2.1}$$

for a beam propagating in the z-direction. $I(z)$ is the light intensity at position z. In an electrically pumped laser diode, the spontaneous emission starts the stimulated emission above the so-called threshold current, where the injected electric current induces an optical gain that equals the losses in the cavity.

A waveguide is a structure that traps and guides the light in certain directions. By placing the gain medium inside a waveguide, a good overlap between the generated light and the gain medium is ensured.

A resonator In order to select the wavelength at which stimulated emission is achieved, a method of selection is needed. By creating a resonator around the gain medium using two mirrors, one on each side of the cavity, the allowed wavelengths can be controlled.

A semiconductor laser diode cavity is sketched in Fig. 2.1.

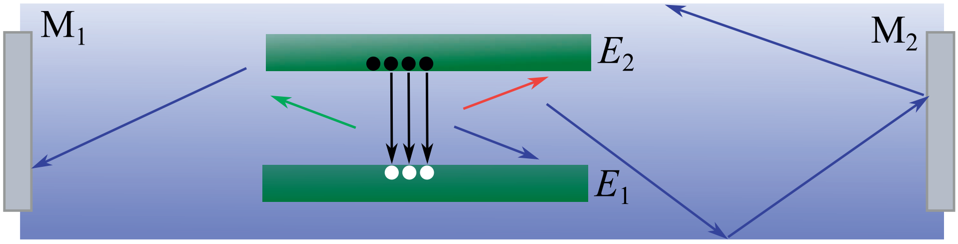

Figure 2.1: Sketch of the principle of a laser cavity which consists of a gain medium (green), resonator (grey) and a waveguide (blue). Spontaneous emission represented by isotropic and colorful arrows, while guided stimulated emission is represented by blue arrows. The resonator is formed by mirrors M_1 and M_2 and the gain is due to recombination of electrons and holes between the excited level E_2 and ground level E_1.

In this chapter these aspects of a laser structure are treated. The electrical and optical confinements required for the gain medium and the waveguide are considered in section 2.1. The resonator and laser properties are then treated in section 2.2, followed by an overview of implementations of the laser diode. The materials and material properties used to make the lasers are the topics of chapter 3. Note that for some figures the laser sample Sb 142 is used for illustrations. This is the sample structure used for the lasers processed and tested in this work.

2.1 Confinement

To achieve lasing, confinement is important; both confinement of the light in the laser cavity, but also of the charge carriers, i.e. the electrons and holes. QWs are often used to confine electrons and holes, while optical confinement is achieved by waveguides, both of which are treated in this section.

2.1.1 Quantum wells

Quantum wells (QWs) refer to a structure where a material with a smaller band gap E_g is placed between two layers of higher band gaps, resulting in a potential well. By making this layer thinner than the de Broglie wavelength of the particles (typically 15 nm [46]), they will be confined and bound by the layer interfaces. The confinement increases the particles energy above E_c and below E_v for conduction and valence bands respectively, as illustrated in fig. 2.2. The bandgap energy is defined by $E_g = E_c - E_v$.

ΔE is the energy difference between the barrier and the well, which relates to

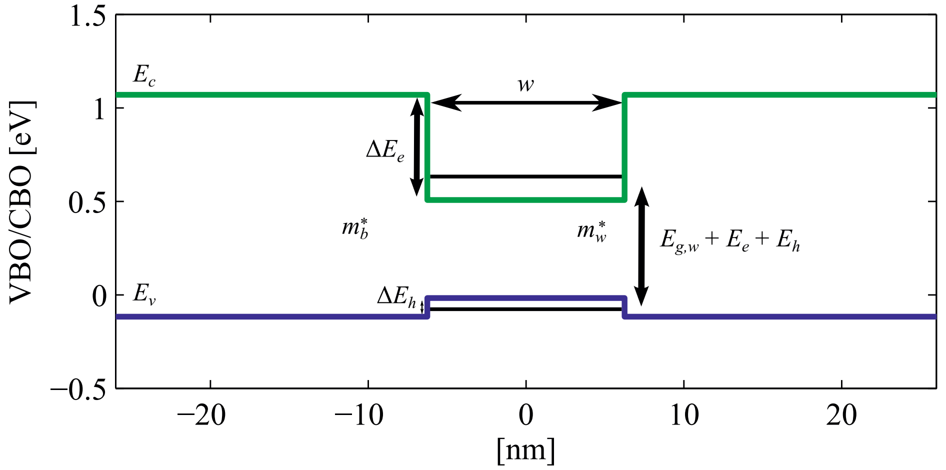

Figure 2.2: QW from the laser structure for sample Sb 142. Well material is $Ga_{0.735}In_{0.265}As_{0.1}Sb_{0.9}$, while the barrier is $Al_{0.25}Ga_{0.75}As_{0.02}Sb_{0.98}$. Here, the well width w is 12.5 nm. Energies related to the conduction band electrons are denoted by E_e, while holes in the valence band are denoted by E_h.

the conduction bands for electrons and the valence bands for holes. The confinement energy E in a QW cannot be expressed analytically, but can be found from the solution of eq. (2.2) [70] using the boundary condition from BenDaniel and Duke [71] including the effective masses required for current conservation:

$$\tan\left(\frac{w\sqrt{2m_w^*E}}{\hbar}\right) = \begin{cases} \sqrt{\frac{m_w^*(\Delta E - E)}{m_b^* E}} & \text{Symmetric wave} \\ -\sqrt{\frac{m_b^* E}{m_w^*(\Delta E - E)}} & \text{Antisymmetric wave} \end{cases} \tag{2.2}$$

Here, w is the width of the QW, m_w^* and m_b^* are the well and barrier effective masses, respectively, and $\hbar$ is the reduced Planck constant.

The width w and height ΔE determines the confinement energy of the well, where reducing w or increasing ΔE increases E. The resulting recombination energy will be $E_{g,w} + E_e + E_h$, where $E_{g,w}$ is the band gap of the well material, and E_e and E_h are the solution for E in eq. (2.2) for electrons and holes, respectively.

As shown in fig. 2.2, ΔE is different for electrons and holes. This is determined by the conduction band and valence band offsets (conduction band offset (CBO) and VBO), and ΔE is not determined by the band gap energy E_g directly. The CBO and VBO will be treated in section 3.1.4.

For laser structures, it is common to utilize more than one QW to provide a better overlap with the optical field. This is referred to as multiple quantum wells

(MQW). The wells are often separated so that the confinement wave functions for each well don't overlap. This separation should be in the (low) tens of nanometers.

2.1.2 Waveguides

When a ray of light is transmitted from one medium to another with a different optical density, it refracts at the interface. The optical densities are usually described by their refractive indices n, and the refraction is described by Snell's law [72]

$$n_1 \sin\theta_1' = n_2 \sin\theta_2', \tag{2.3}$$

as illustrated in fig. 2.3. Since we are interested in the light propagating along the interface instead of across it, it is useful to define $\theta_{1,2} = 90° - \theta_{1,2}'$:

$$n_1 \cos\theta_1 = n_2 \cos\theta_2 \tag{2.4}$$

In the case of a wave propagating from an optically dense medium 2 to a less dense medium 1, $n_2 > n_1$, we get a phenomenon called total internal reflection (TIR). This occurs for angles θ_2 where eq. (2.4) cannot be satisfied, i.e. $\cos\theta_2 < \cos\theta_c = n_1/n_2$. Below this critical angle θ_c, all light is reflected back. Using a three-layer stack, as shown in fig. 2.3, we can trap the light, thereby creating a waveguide. The middle layer is commonly called the core, while the outer layers are referred to as the cladding layers.

A useful entity is the numerical aperture (NA). The NA represents the divergence of the light when it leaves the waveguide and it is defined as

$$\mathrm{NA} = n_0 \sin\theta_{\max} = n_2 \sin\theta_c = \sqrt{n_2^2 - n_1^2}, \tag{2.5}$$

where $\theta_{\max}$ is the exit angle for the rays travelling at the critical angle θ_c, see fig. 2.3.

We can also define an effective refractive index

$$n_{\mathrm{eff}} = n_2 \cos\theta_r \tag{2.6}$$

where $n_1 < n_{\mathrm{eff}} < n_2$. For rays propagating parallell to the interfaces (θ_r) we have $n_{\mathrm{eff}} = n_2$, and it decreases towards n_1 as the angle θ_r approaches θ_c.

Single transversal mode waveguides

When the waveguide thickness is comparable to the wavelength λ/n_{eff} of the light in the medium, light cannot be treated as rays, but must be treated as waves [72].

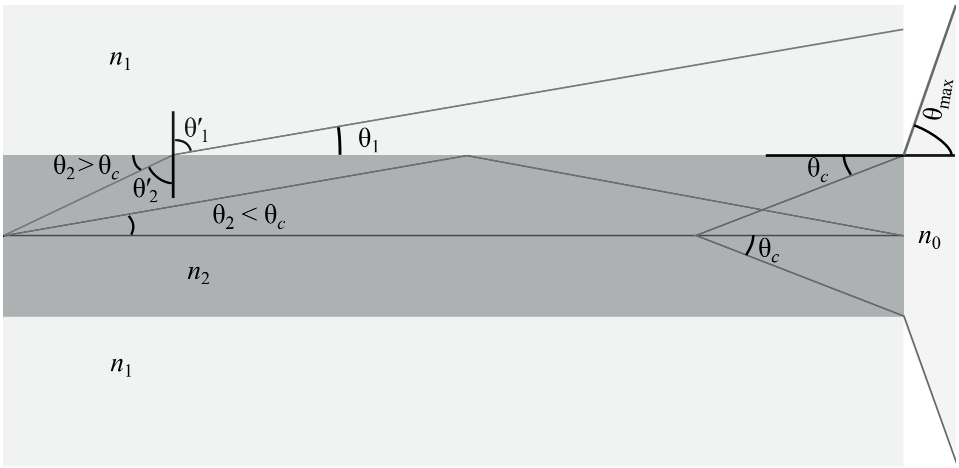

Figure 2.3: A sketch of a three layer slab waveguide. Here $n_2 > n_1$, which leads to total internal reflection for angles $\theta_2 < \theta_c$. n_0 surrounds the waveguide, usually air which has small refractive index. When light rays exits the waveguide, the large difference in refractive indices between n_2 and n_0 leads to significant refraction at the interface.

The waveguiding properties are then solved using Maxwell's equations with appropriate boundary conditions. The effective refractive index n_{eff} of a mode is then related to the amount of light in the core and the cladding of the waveguide.

The light will be bound to the core, but an evanescent field in the cladding can make up a significant part of the optical field. For an optical field with an effective refractive index n_{eff} and a wavenumber

$$\beta = \frac{2\pi}{\lambda} n_{\text{eff}} = k_0 n_{\text{eff}} \tag{2.7}$$

the solutions for the field distribution in each layer of a 1D slab waveguide for a transverse electric (TE) mode in the y-direction $E_y = E(x)\exp(-j\beta z)$ are [46]

$$E_i(x) = A_i \exp\left[q_i(x - x_i)\right] + B_i \exp\left[-q_i(x - x_i)\right]. \tag{2.8}$$

Here A_i and B_i are the coefficients of the field components in layer i travelling in the positive and negative x-directions, respectively, for the layer starting at x_i and where

$$q_i = \sqrt{\beta^2 - n_i^2 k_0^2} = k_0 \sqrt{{n_{\text{eff}}}^2 - n_i^2}. \tag{2.9}$$

For $n_{\text{eff}} < n_i$, q_i becomes imaginary and we get a sine-cosine solution for E_i, while $n_{\text{eff}} > n_i$ gives a real exponential solution. I.e. we get a bound mode in the core, which is analogous to the ray description of angles less than the critical angle in the previous section.

In most cases it is preferable to use simulation software to determine the properties of the waveguide, e.g. Lights [73]. Calculations of the transversal mode of 1D slab waveguides based on simplified slab structures of our laser structure can be found in appendix B.

Leaky modes

If a layer outside the designed waveguide has a refractive index $n_{\text{layer}} > n_{\text{eff}}$, it is possible for the bound mode to radiate into this layer, and the mode is referred to as a leaky mode. If the cladding layer is not sufficiently thick, a portion of the electrical field can radiate into this layer. A simulation of such a laser is shown in fig. 2.4.

If the substrate is sufficiently transparent, this can lead to substrate modes which can be reflected back into the waveguide from the substrate backside and cause interference [74].

The light refracted into the substrate will have an angle θ_{sub} expressed by [75],[1]

$$\tan\theta_{\text{sub}} = \frac{iq_{\text{sub}}}{\beta} = \frac{k_0\sqrt{n_{\text{sub}}^2 - n_{\text{eff}}{}^2}}{k_0 n_{\text{eff}}} = \sqrt{\frac{n_{\text{sub}}^2}{n_{\text{eff}}{}^2} - 1}, \tag{2.10}$$

For a GaSb-based laser with $n_{\text{sub}} = 3.8$ and $n_{\text{eff}} = 3.45$, this angle would be around 25°. It should be noted that this is above the critical angle (θ_c) of approximately 15° for the GaSb-air interface.

2.2 Laser

After achieving electronic confinement of the gain medium and optical confinement of the laser light, it is important to control the light, by forming a resonator across the laser structure. This is usually achieved by inserting mirrors on each side of the cavity, causing a resonance in the structure at certain wavelengths.

For the simplest laser structure, the Fabry-Perot laser, this is achieved by cleaving the semiconductor material to induce a resonator, where only certain wavelengths are allowed to resonate in the cavity [46, 72]. This principle can be extended further, by using two coupled resonators, connected by a Y-junction in the

---

[1] Note that Bogatov et al. [75] has defined $q = \sqrt{k_0^2 n_{\text{sub}}^2 - \beta^2}$, which is iq_i in eq. (2.9), i.e. the sign inside the square root is opposite in the article.

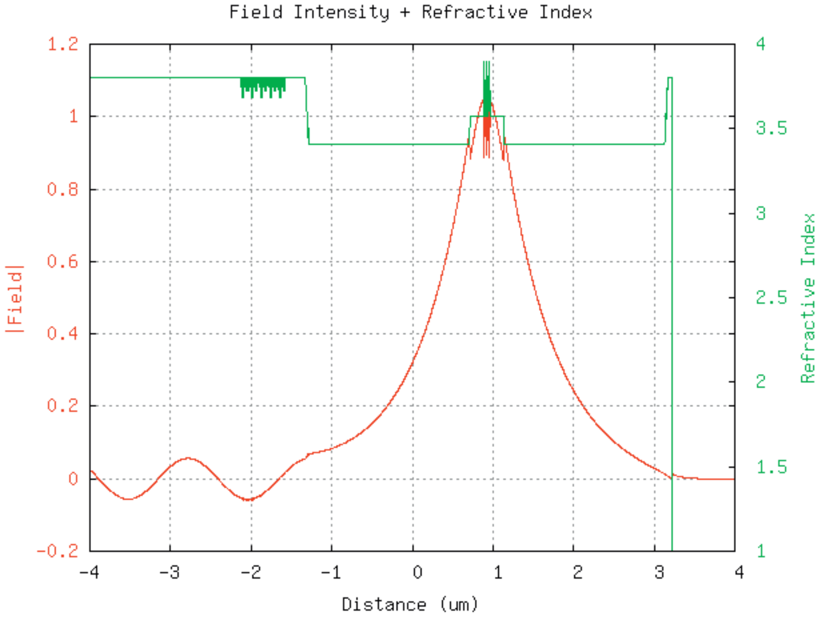

Figure 2.4: Simulation of the optical field in a leaky mode laser. It can be seen that the high refractive index of the substrate (between -4 and -2.2 µm in the figure, where a superlattice is introduced to the laser structure) makes it difficult to completely confine the mode within the waveguide core if the refractive index of the cladding is too high or the cladding thickness is insufficient. Simulated using Lights [73].

waveguide [46]. Other techniques include Bragg gratings, where the mirrors are constructed to only allow reflections for certain wavelengths [46].

In the following section the Fabry-Perot lasers will be introduced, with theoretical aspects relevant for most lasers. This is followed by a short presentation of the Y-junction laser and then some other laser structures are mentioned.

2.2.1 Fabry-Perot laser

The Fabry-Perot laser (FPL) is the easiest structure to understand, and its principles are important for all types of lasers. Some of its main properties will be treated here. This section is based on the theory presented in Buus et al. [46] A more complete treatment of the fundamentals of laser theory can be found in ch. 2 in Buus et al. [46]

The gain inside a FPL can be expressed by $g_{\mathrm{eff}} = \Gamma g_a$, where g_a is the gain in the active medium, the MQW, and Γ is the confinement factor in the wells, i.e. the overlap between the optical field intensity, $|E|^2$, and the MQW. This results in a net gain

$$g_{\mathrm{net}} = g_{\mathrm{eff}} - \alpha_i, \tag{2.11}$$

where α_i is the internal optical losses.

The propagation, or field distribution, along the cavity in the z direction is expressed by $\exp(\pm j\beta^* z)$, where the complex propagation constant is

$$\beta^* = k_0 n_{\mathrm{eff}} + j\frac{g_{\mathrm{net}}}{2}. \tag{2.12}$$

In steady-state conditions, the field must reproduce itself at a reference point $z = z_0$ after a full cavity round-trip, over a distance $2L$, where L is the cavity length. Mathematically, this can be described by

$$r_1 r_2 \exp(-2j\beta^* L) = 1, \tag{2.13}$$

where $r_{1,2}$ are the mirror amplitude reflection coefficients and assumed real. This round-trip oscillation condition can be rewritten as

$$2j\beta^* L + \alpha_m L = 2j\pi N, \tag{2.14}$$

where N is the mode number and α_m are the mirror losses

$$\alpha_m = \frac{1}{2L}\ln\frac{1}{R_1 R_2}, \tag{2.15}$$

where $R_i = r_i^2$ is the reflectance. Solving for the real part of eq. (2.14) we get the equation

$$-g_{\mathrm{net}} L + \alpha_m L = 0 \tag{2.16}$$

which we can rewrite as

$$\Gamma g_a - \alpha_i - \alpha_m = 0 \tag{2.17}$$

where α_m are the mirror losses.

The roundtrip condition, the imaginary part of eq. (2.14), can be rewritten for the allowed wavelengths, or the longitudinal modes;

$$\lambda_N = \frac{2n_{\mathrm{eff}}(\lambda_N)L}{N} \tag{2.18}$$

and the longitudinal mode spacing can be approximated to

$$\Delta\lambda_m = \lambda_N - \lambda_{N+1} \simeq \frac{\lambda_N^2}{2n_{g,\mathrm{eff}}L}. \tag{2.19}$$

Here

$$n_{g,\mathrm{eff}} = n_{\mathrm{eff}}(\lambda_N) - \lambda_N \left.\frac{\mathrm{d}n_{\mathrm{eff}}}{\mathrm{d}\lambda}\right|_{\lambda_N}, \tag{2.20}$$

which accounts for dispersions in the material and waveguide, leading to differences in the (effective) refractive index for different wavelengths λ. The effective refractive index derived from the longitudinal mode spacing is therefore not the same as n_{eff} found from solving the transversal mode.

When the lasing conditions are fulfilled, the longitudinal mode with the highest gain will start to lase, determined by the gain curve. When lasing occurs the gain saturates and eq. (2.17) is fulfilled. This is referred to as "gain-clamping", and the excess pumping of the gain material leads to an increase in the output power of the laser.

The gain curve can in most cases be assumed to be Gaussian in shape. The Fabry-Perot resonator modes can be described by [72, 76]:

$$I = \frac{1}{1+F\sin^2(\pi N)} \tag{2.21}$$

$$I = \frac{1}{1+F\sin^2(\beta L)} \tag{2.22}$$

$$I = \frac{1}{1+F\sin^2(k_0 n_{g,\mathrm{eff}} L)} \tag{2.23}$$

$$F = \frac{4R}{(1-R)^2} \tag{2.24}$$

where R is the reflectance of the mirrors and I is the light intensity in the resonator. $n_{g,\mathrm{eff}}$ is used instead of n_{eff} to account for dispersion. A calculated gain curve with superposed Fabry-Perot modes is shown in fig. 2.5. For a FPL the SMSR, i.e. the difference in peak power for the dominating and the competing mode, is usually limited to about 20 dB [46], depending on the position of the peak of the gain curve relative to the Fabry-Perot modes.

Sub-threshold spectra

For currents just below the threshold current density, j_{th}, required for stimulated emission, one can achieve transparency conditions. This is the case when the spontaneous emission is high enough for light propagating in the waveguide, fulfilling the round-trip requirement, but not high enough to support stimulated emission. Here, the spontaneous emission excited into the waveguide (at an angle $\theta < \theta_c$) can be observed at the facets.

Such sub-threshold spectra gives information about both the gain medium and the FP resonator. It is possible to extract information about the material gain using e.g. the Hakki-Paoli method [78]. An example of a measured sub-threshold spectra is shown in fig. 2.6. In the literature these spectra can also be referred to as the amplified spontaneous emission or superradiance spectra.

Tuning mechanims

Tuning of the lasing wavelength is usually achieved by changing the effective refractive index, leading to a change in the optical path length. This leads to changes in the resonator modes. For FPL the wavelength will then be tunable across a FP mode spacing, at which point the neighbouring FP mode becomes the mode with the highest gain, and the wavelength jumps back to the original lasing wavelength. There are three main tuning mechanisms for tuning the refractive index in laser diodes [46]:

The free-carrier plasma effect (FCPE) is the most used tuning mechanism in telecommunication lasers, where free carriers leads to a change in the refractive index by an increment Δn. FCPE originates from two effects; due to the polarization of the free carriers from the injected electrons and holes on each side of the gain material, and due to a shift in the absorption edge of the gain material. The resulting change Δn is given by [46]

$$\Delta n = -\frac{e^2\lambda^2}{8\pi c^2 n\varepsilon_0}\left(\frac{1}{m_e}+\frac{1}{m_h}\right)\mathbf{N} \tag{2.25}$$

where e is the elemental charge, n is the refractive index of the layer, m_e and m_h are the electron and hole effective masses, respectively. Here $\mathbf{N}$ is the carrier concentration.

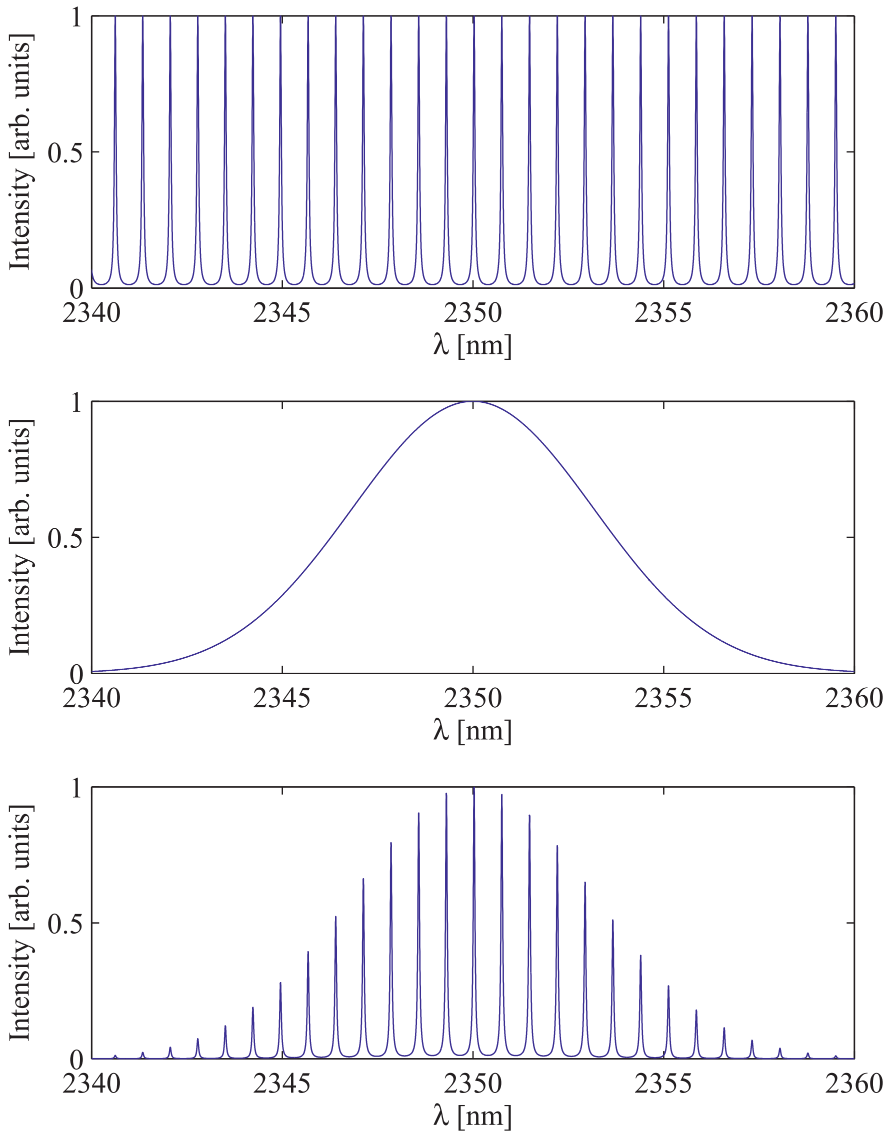

Figure 2.5: Top: Fabry-Perot modes for $R = 0.8$, $n_{g,\mathrm{eff}} = 3.8$, $L = 1$ mm calculated from section 2.2.1. Middle: A Gaussian gain curve. Bottom: Fabry-Perot modes and their relative gains. When the lasing condition is fulfilled, the mode at $\lambda = 2.35$ µm will dominate, and the laser will lase at this wavelength. Note that while the mirror reflectivities for GaSb-based lasers are usually close to $R = 0.3$, the gain in the laser cavity will result in a narrowing of the Fabry-Perot modes [77]. To account for this narrowing, R was chosen to be 0.8 in these figures.

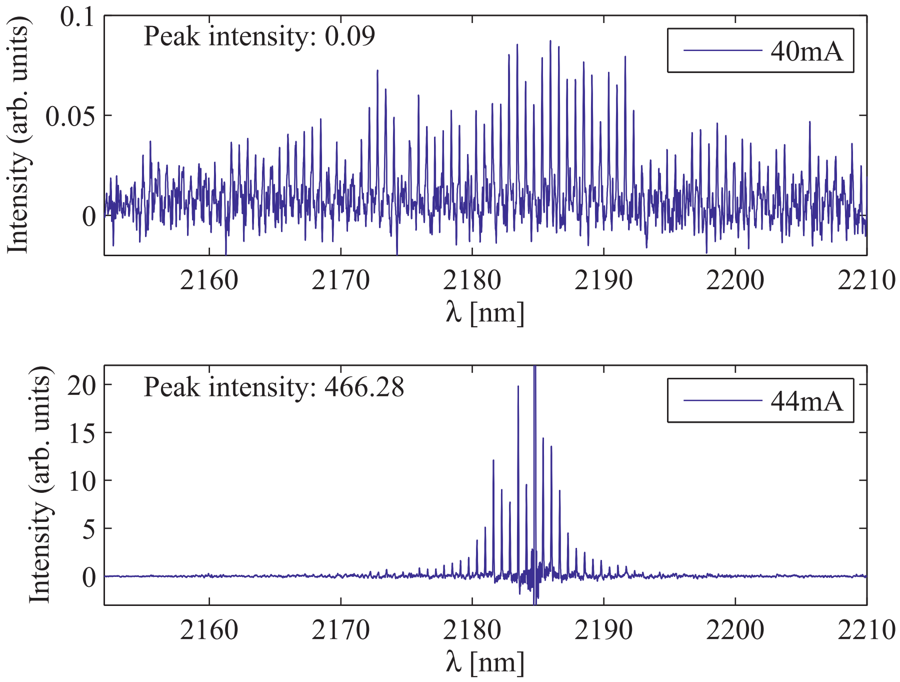

Figure 2.6: Measurement below (40 mA) and above (44 mA) the threshold current density for a 1 mm long 2.5 µm wide FPL. The dominant longitudinal mode has been cropped in the bottom plot to show the intensity distribution for the side-modes. The threshold current density, j_{th}, is close to 1.6-1.8 kA/cm^2, which is quite high.

The change in the wavelength, assuming only that the MQW contribute to the change in refractive index Δn, will be

$$\Delta\lambda = \lambda \frac{\Gamma \cdot \Delta n}{n_{g,\mathrm{eff}}} \propto -\mathbf{N}. \tag{2.26}$$

The carrier concentration $\mathbf{N}$ is related to injected current density j by [46]

$$j = ed\left(\mathbf{N}/\tau_s + B\mathbf{N}^2 + C\mathbf{N}^3\right) \tag{2.27}$$

where τ_s is the recombination lifetime for Shockley-Read Hall (defects and impurities), d is the thickness of the tuning region, B is the band-to-band recombination rate and C is the Auger recombination rate[2]. So the increase in $\mathbf{N}$ decreases with increasing current, meaning that FCPE tuning is most efficient at low currents. For telecommuncations lasers this effect typically can achieve a tuning of up to -8 nm, with a Δn of -0.04 with a tuning speed of up to 100 MHz [46].

The quantum confined stark effect (QCSE) is based on reverse biasing of a QW. By introducing an electric field across the QW, the electrons and holes become displaced in the wells, and it also reduces the confinement recombination energy. This also modifies the refractive index for wavelengths close to the confinement recombination energy, typically by -0.01 to -0.001 [46]. This change is small, but the mechanism is extremely fast, allowing for tuning speeds in excess of 10 GHz [46].

Thermal tuning is a tuning mechanism where, due to heat, the refractive index in the material changes. In addition, the gain curve will shift to longer wavelengths. For telecommunications lasers, the shift of the gain curve is about 0.5 nm/K, while the shift for single-mode lasers (with Bragg gratings) is about 0.1 nm/K, and the change in the refractive index is around 0.01 for typical telecommunication laser structures [46]. It is also the only tuning mechanism where the change in λ and n are positive. For parasitic heating in FCPE or QCSE, thermal tuning will reduce the efficiency of those tuning mechanisms.

2.2.2 Y-junction laser

The Y-junction laser is an interferometric laser structure that uses the combination of two Fabry-Perot cavities, see fig. 2.7, to manipulate the gain for each longitudinal Fabry-Perot mode and thus increases the tuning range.

---

[2] The recombination rates will be presented in section 3.1.2 on page 26.

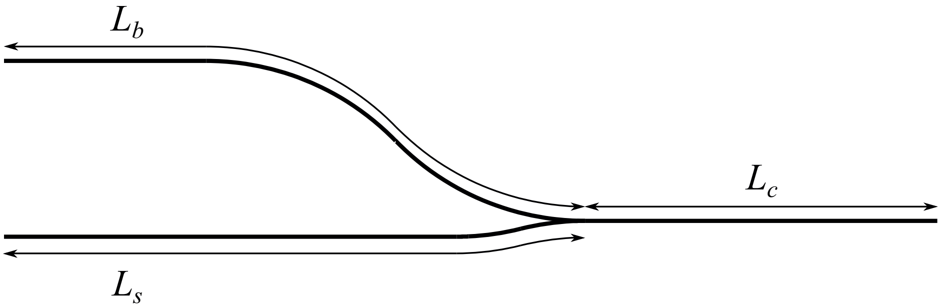

Figure 2.7: The Y-junction laser waveguides. To achieve 50-50 splitting of the light, the Y should be symmetric. Here the two arms have the lengths $L_c + L_s$ for the straight waveguide and $L_c + L_b$ for the bent waveguide, and $\Delta L = L_b - L_s$. L_c, L_s and L_b are the lengths of the common, straight and bent sections, respectively.

The beating between the two Fabry-Perot cavity modes gives a beating wavelength $\Delta\lambda_{\mathrm{Y}}$, or free spectral range, of [46]

$$\Delta\lambda_{\mathrm{Y}} = \frac{\lambda^2}{2n_{g,\mathrm{eff}}\Delta L}, \tag{2.28}$$

which induces a modulation to the cavity gain by a factor $C_{\mathrm{Y}}(\lambda)$

$$C_{\mathrm{Y}}(\lambda) = \cos^2\left[2\pi\frac{n_b(\lambda)L_b - n_s(\lambda)L_s}{\lambda}\right] \tag{2.29}$$

where n_b and n_s are the refractive indices in the bent and straight sections, respectively. L_b and L_s are the lengths of the bent and straight sections, respectively, see fig. 2.7. This increases the maximum tunable range from $\Delta\lambda$ for FPL, to $\Delta\lambda_{\mathrm{Y}}$ in the Y-junction laser, with an increased SMSR, as shown in fig. 2.8.

A Y-junction laser will have an inverse relationship between SMSR and tuning range ($\propto 1/\Delta L$) since the (slowly varying) modulation between two neighbouring longitudinal modes is less, as expressed by eq. (2.29). One solution is to use a three-armed junction laser instead of two [46]. The laser can then be widely tunable by using a short ΔL_1 to increase the tuning range, while using a long ΔL_2 to reduce the SMSR.

The benefits of the Y-junction laser are that there is no need for regrowth and less processing steps than for a grating-based laser. Drawbacks include the slow beating of the FP modes from the cavities.

For bent waveguides the refractive index contrast between the core and cladding required for proper guiding is higher than the requirement for straight waveguides.

Typically the index contrast must be doubled from about $\Delta n \simeq 0.01$–0.02 to 0.03–0.05. See chapter 7 (page 91) for more details regarding waveguiding in bent waveguides.

2.2.3 Other tunable laser structures

Tunable laser diodes are usually tuned by means of changing the effective refractive index n_{eff}, thus changing its optical cavity length. The mechanisms used for changing the effective refractive index are the FCPE, the QCSE and thermal tuning [46]. By themselves, these mechanisms only give a continuous tuning up to about 10 nm.

By combining these mechanisms with structures that enhances the wavelength selectivity and tunability, such as periodic structures (DBR, DFB) or interferometric structures (Mach-Zender or junction structures), the tunability can be greatly enhanced and multimode behaviour reduced. This can lead to a tuning range of more than 100 nm, depending on the structures used, and around 50 nm for Y-lasers [46].

2.2.4 Gas detection lasers

For gas detection purposes, a continuously tunable laser is important, and must be able to tune across the absorption line in question. The linewidths of these spectral lines are pressure dependent.

Werle [55] has written extensively about the requirements for high resolution gas detection using TDLS. It is important that the laser is able to be continuously tuned across the entire linewidth of the gas. This can usually be performed by a combination of temperature and electric tuning. The temperature tuning is slow, but can be used to position the laser wavelength to the absorption line, while electric tuning is used to scan the absorption line rapidly, preferably up to 10 MHz scan speed to reduce the laser noise [56].

The lasers should typically have optical power in the mW range, good SMSR of more than 30 dB [46], and full-width at half maximum (FWHM) less than the gas absorption lines, which are typically in the 0.01 nm-range (0.03 nm for HF [34]), depending on pressure and the different molecules. Thus, for scanning a single absorption line, a continuous scan range of 1 nm is usually sufficient.

While a gas detection laser is only required to be tuned a few nm across an absorption line, a wide tuning range means that the same laser can be utilized for many types of gases, and the requirements for the design can be relaxed if the wavelength can be tuned during use. This includes the growth of the structure, regarding layer thicknesses and compositions of the layers.

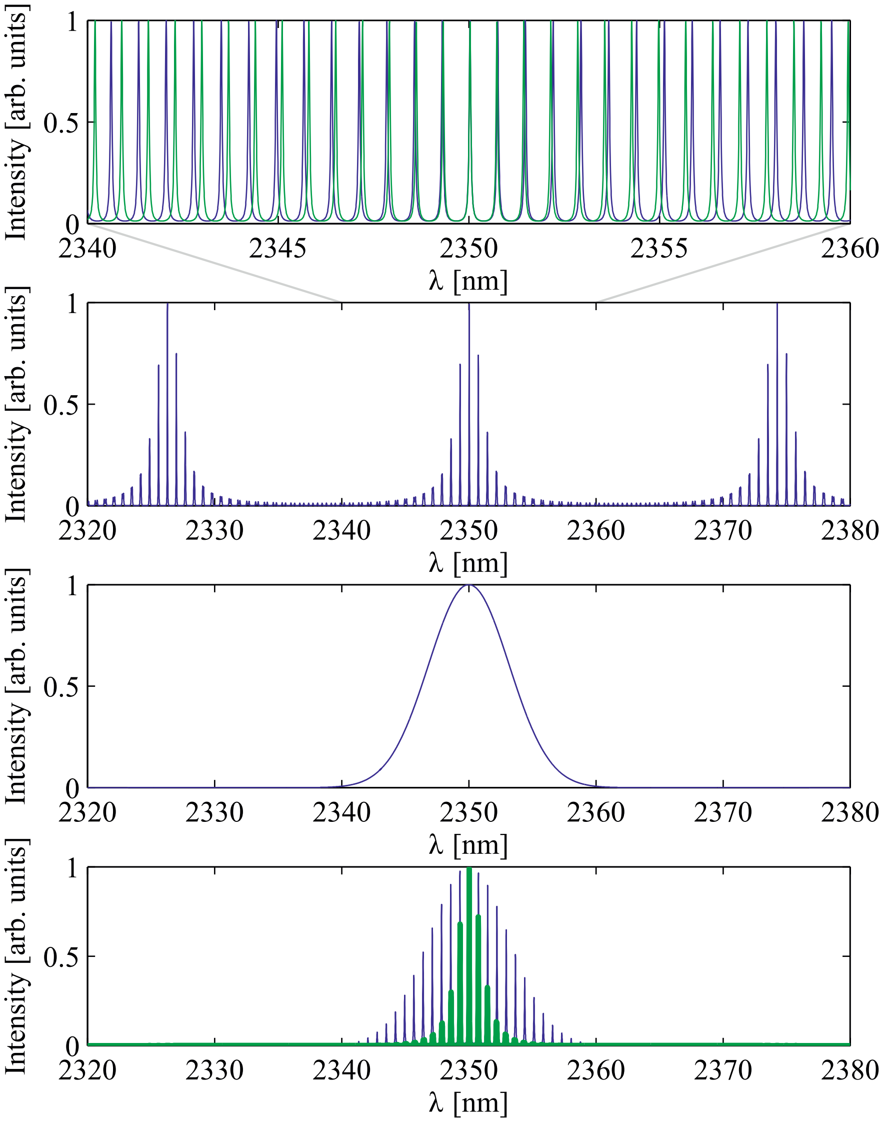

Figure 2.8: From the top, **1:** Fabry-Perot modes for $R = 0.8$, $n_{g,\text{eff}} = 3.8$ (blue) and 3.80112 (green), and $L = 1$ mm and 1.03 mm. The modes were calculated from eq. (2.23). **2:** The overlap of the Fabry-Perot modes, i.e. "Mode 1 × Mode 2". By changing the refractive index in one or both of the resonators, the peak wavelengths can be shifted. The tuning range is then significantly increased compared to the FPL. **3:** Gaussian gain curve. **4:** The gain for the Y-junction structure (green) compared to the Fabry-Perot modes (blue) of a single resonator cavity. The SMSR is improved for the junction structure.

Chapter 3

Material system

For laser fabrication it is important to choose a suitable material system. The most important criterion is the wavelength, which is predefined by the relevant gases to be detected. It is then important to choose a material system that can easily be converted into a laser, and preferably it should be possible to widely tune the laser to enable measurements of several gases. The important features include both the electrical and the optical properties. Other material characteristics, such as how easy the material can be manufactured into a laser, are also important.

This chapter aims to describe the important material parameters with respect to creating a laser diode. Section 3.1 gives an introduction to the key material parameters and topics relevant for laser diodes is given. The choice of an AlGaAsSb / GaInAsSb layered structure on top of a GaSb substrate is then presented and explained, followed by a presentation of relevant characterization techniques used for this work. The characterization of the lattice constant is emphasized in section 3.3, which is the topic for papers I-IV in chapter 8.

3.1 Introduction to material properties

This section is meant as an introduction to the important parameters and topics which should be considered when choosing materials for fabricating laser diodes utilized for gas sensing.

3.1.1 Overview of important parameters

The most important parameters for laser diode materials are:

Crystal structure The different layers must be epitaxially compatible. For thin film growth this means that the lattice constant must be approximately the same in the different layers and that the crystal structure is the same, or very similar.

Band structure E_g, VBO and CBO are important for the confinement of charge carriers. For the gain material the band gap must be direct to allow for a high radiative recombination rate. The band gap energy is crucial to manufacture laser diodes emitting light at a chosen wavelength. Furthermore, the band gaps of the surrounding layers must be larger, to allow for confinement of charge carriers in the quantum wells. A sketch of some of the important aspects of the band structure are given in fig. 3.1.

Optical properties The materials must have refractive indices which support a waveguiding structure. Apart from the gain material, the materials must be transparent, a requirement fulfilled by the band gap requirement. The waveguiding properties of the laser structure were treated in section 2.1.2.

Electrical properties The structures should have high electrical mobility and it should be easy to dope the layers surrounding the active layers by incorporating electrically active impurities. This is important for injecting electrons and holes into the gain material. It must be easy to metallize the top and bottom layers for connecting the device to an external current source.

Chemically and mechanically stable The materials must be chemically stable for processing and operation. It must be possible to handle the sample material and lasers without breaking them, requiring mechanical strength.

Growth conditions The optimal growth temperatures for the different constituents should be about the same; if the growth temperature is too low, the atoms will easily incorporate, leading to a rough surface, is it too high, the atoms will evaporate from the sample surface without incorporating.

3.1.2 Recombination mechanisms

The recombination mechanisms in a semiconductor are usually organized by the number of particles involved in the process. Recombination mechanisms include the impurity-related recombination, which is usually proportional to the number of charge carriers n, the band-to-band recombination proportional to n^2, and the Auger processes proportional to n^3. The mechanisms are illustrated in fig. 3.2.

For the radiative recombination needed for lasing, light can be generated from recombination related to impurities or band-to-band recombination between the

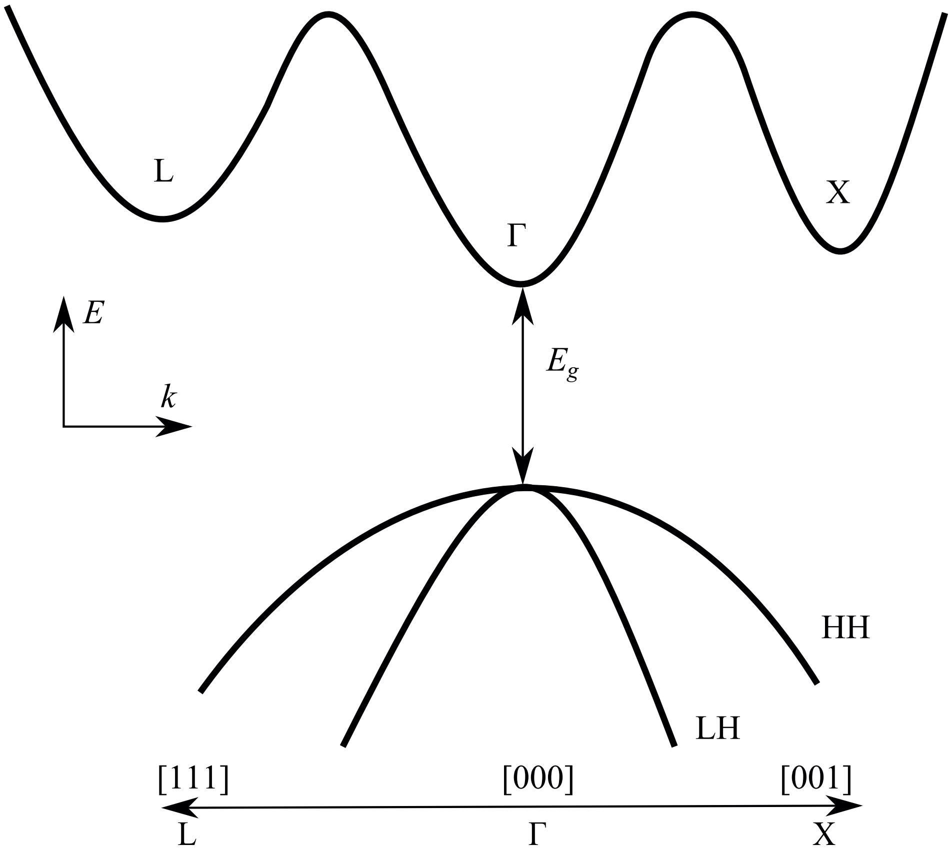

Figure 3.1: A sketch of the band structure (i.e. dispersion relation) annotated with important terms. The bands can have valleys in several crystallographic directions, which represent the propagation directions of the electrons or holes. k is the electron or hole wavenumber, which is related to the momentum of the charge carrier. Examples of L, Γ and X valleys are shown for the conduction band. Γ is here the valley at [000], i.e. the electron is almost at rest, for the X-valley the electrons move in one of the 6 [001] directions, and for the L-valley they move along one of the 8 [111] directions. LH refers to the light hole band and HH to the heavy hole band in the valence band, both centered at the Γ-point. E_g is shown for a direct bandgap semiconductor where the bandgap is between the Γ-point in the conduction band and LH and HH, in some cases referred to as the E_Γ for indirect semiconductors, where $E_g \neq E_\Gamma$.

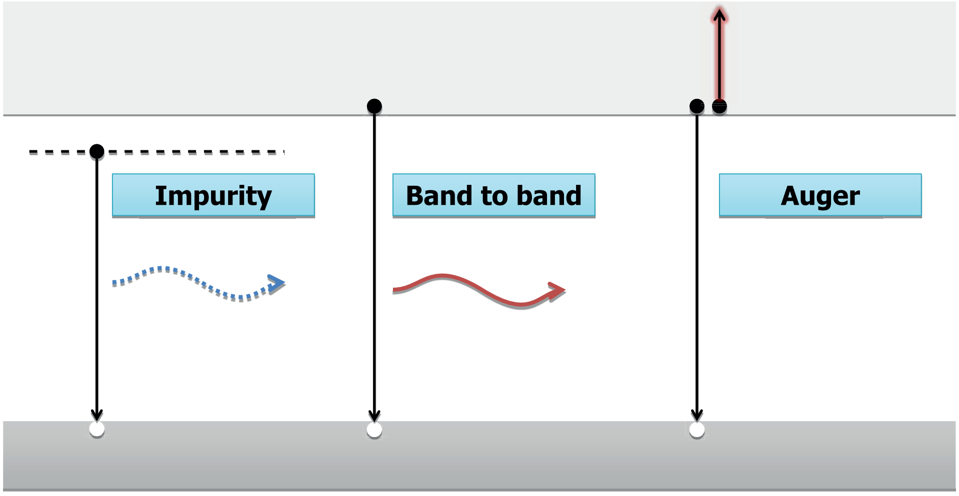

Figure 3.2: Recombination mechanisms. For laser diode applications, the band to band mechanism is preferred. Impurity recombination usually arises from doping, while Auger is a recombination mechanism where the excess energy is transferred to a third particle instead of a photon.

conduction band and valence band. For laser diodes the band-to-band recombination is the desired mechanism, and the impurity and Auger recombination mechanisms should be suppressed. For infrared lasers, the band gap of the gain material is considered small and Auger recombination is a significant mechanism, since the intrinsic carrier concentration n_i increases with decreasing E_g. The current density required for lasing will increase when the Auger recombination becomes more dominant. It has been shown that for lasers lasing at 2.3 µm, Auger strongly affects the threshold current density j_{th} above 60°C, and at lower temperatures for longer wavelengths [79] where the Auger recombination increases exponentially [54].

The recombination rate can be approximated by a polynomial function [46, 80]

$$R(n) = \frac{n}{\tau_{\mathrm{SRH}}} + Bn^2 + Cn^3 \tag{3.1}$$

$$\frac{1}{\tau_{\mathrm{eff}}} = \frac{1}{\tau_{\mathrm{SRH}}} + \frac{1}{\tau_{\mathrm{rad}}} + \frac{1}{\tau_{\mathrm{Aug}}} \tag{3.2}$$

$$\frac{1}{\tau_{\mathrm{eff}}} = \frac{1}{\tau_{\mathrm{SRH}}} + Bn + Cn^2 \tag{3.3}$$

where τ_{SRH} is the nonradiative Shockley-Read-Hall impurity-related recombination lifetime, B is the band to band recombination coefficient, C is the Auger recombination coefficient. τ_{rad} is the radiative band-to-band recombination lifetime, τ_{Aug} is the Auger recombination lifetime, and τ_{eff} is the effective combined recombination lifetime.

3.1.3 Effects of strain

Strain will influence the shape of the band structure, in addition to the quality of the epitaxial growth and mechanical strength. Compressive strain leads to a separation of the LH and HH, see fig. 3.1, pushing the LH down and HH up, resulting in a bandgap E_Γ defined by the Γ-valley in the conduction band and HH in the valence band. Tensile strain will result in a band gap defined by LH instead of HH. Due to the reduced dimensionality from 3D to 2D introduced by the QW structure, the Zinc blende point group symmetry is broken. From the selection rules for optical recombination, HH then only supports TE mode, while LH supports both TE and transverse magnetic (TM) modes [81–83].

In addition to the symmetry considerations, the TE mode has higher optical transverse confinement and facet reflectivity [46, 83], reducing its optical losses in a laser structure. Using a large compressive strain has shown to be beneficial for the gain properties, and a large compressive strain of InGaAsSb QW has shown increased output power and low threshold current density [69].

3.1.4 Band alignment at interfaces

In addition to the band gap, the band offsets are also of importance, shown in fig. 3.3. When semiconductors of different band offsets and band gaps are connected, the electrical and optical properties will be affected by the alignment of the bands and fermi levels. The band alignments for the electrons and holes at heterojunctions are referred to as the CBO and the VBO, which are important parameters for creating QWs.

In fig. 3.3 top plot we can see an illustration of different types of heterojunctions. Between GaSb and AlSb, we see the type-I heterojunction, where electrons in the conduction band and holes in the valence band would both be confined in GaSb. Between AlSb and InAs, we see the type-II behaviour, where the electron and hole confinements are in different layers. The band alignment of InAs and GaSb is called a type-IIb or type-III, where the conduction band edge is lower in energy in one material than the valence band of the other material. Other important parameters such as strain and refractive indices are shown in the middle and bottom plots in fig. 3.3, respectively.

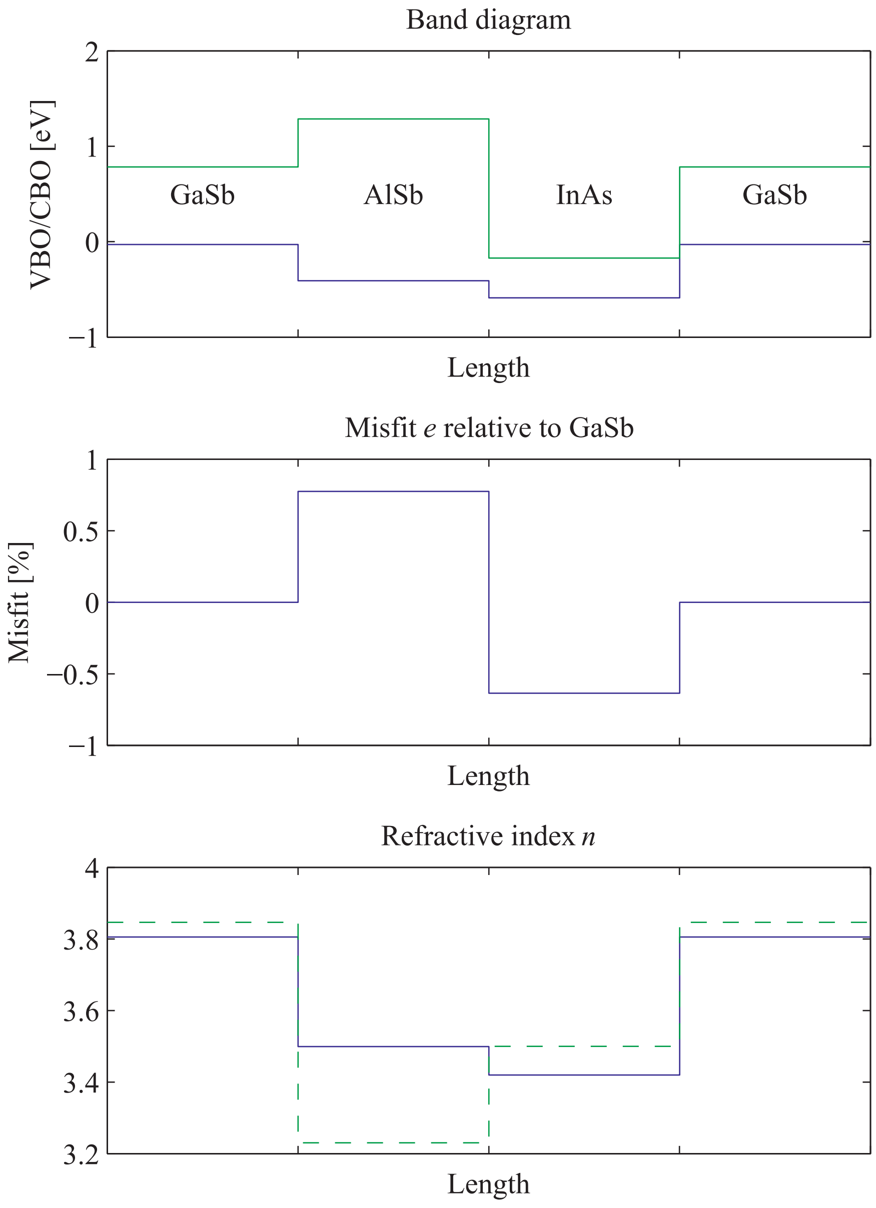

Figure 3.3: Illustration of the structure parameters for the 6.1 Å family of semiconductors – GaSb, AlSb and InAs. The top plot illustrates that the three types of heterojunctions is achievable; GaSb/AlSb is type-I, InAs/AlSb is type-II and InAs/GaSb is type-III. References for the material data can be found in appendix A. The misfit relates to strain and stress for layers, and it is here given by $e = (a_{\mathrm{GaSb}} - a_i)/a_i$, where a_i is the bulk lattice constant for the different binaries. Here, e relates to the misfit relative to GaSb. For the refractive index the solid line is the data from Gonzalez-Cuevas et al. [84] used in appendix A, while the dashed line are the references found in table 3.1.

3.1.5 Gas properties

While gas detection is beyond the scope of this thesis, it is important to be aware of the gas properties, as they influence the important laser characteristics.

In fig. 1.1 some gas absorption lines are shown, and their relation to atmospheric absorption. For lasers to be used in atmospheric conditions such as in factories, open spaces, buildings etc., it is not only important to know the available absorption lines of the gas, but also the wavelengths for which we avoid absorption from water and CO_2.

Some of the important atmospheric windows, i.e. wavelengths transparent in air, are located from 2–2.4 µm and from 3.5–4.2 µm.

For gas detection it is important to measure an isolated absorption line free from absorption by other species. By decreasing the pressure from 1 atm to 0.1 atm a reduction in the FWHM of the absorption line is about a factor 8 [85], which will increase the selectivity without a large reduction in the peak absorption. At lower pressures, however, the peak absorption will decrease due to the reduction of molecules available for absorption [55]. It is also preferable to be able to tune the laser across the whole absorption line for maximum amplitude, so a gas detection system operating at atmospheric pressure will require a wider tuning range. Expected FWHM for gases are around 0.1-0.25 nm [35, 85] for absorption close to a 3 µm wavelength, which can be reduced below 0.05 nm by decreasing the pressure to 0.1 atm [85]. It is important for high sensitivity that the spectral linewidth of the laser is less than the linewidth of the absorption line.

3.2 The 6.1 Å family

The semiconductors made from the alloys of group III and group V elements of the periodic table are very interesting for electro-optical applications. They have mostly direct bandgap, which gives a high rate of spontaneous emission compared to the group IV semiconductors such as Si and Ge with indirect bandgaps.

From the III-V semiconductors comprised of Al, Ga, In, As and Sb, the alloys of AlSb, GaSb and InAs are of particular interest for mid-infrared laser diodes, where you in theory can reach wavelengths up to at least 3.73 µm [3] while keeping the lattice constant more or less constant, which is important for epitaxial growth. They exhibit a zinc blende (ZB) lattice structure, see fig. 3.4. The lattice constant then refers to the distance between nearest corners of the ZB unit cell, and not to the distance between nearest atoms (even of the same element). The group III atoms bond to the group V atoms and vice versa in the ZB structure. The typical size of the unit cell for alloys of AlGaInAsSb is shown in fig. A.1.

For III-V semiconductors, Ga-V and Al-V usually give closely matched lat-

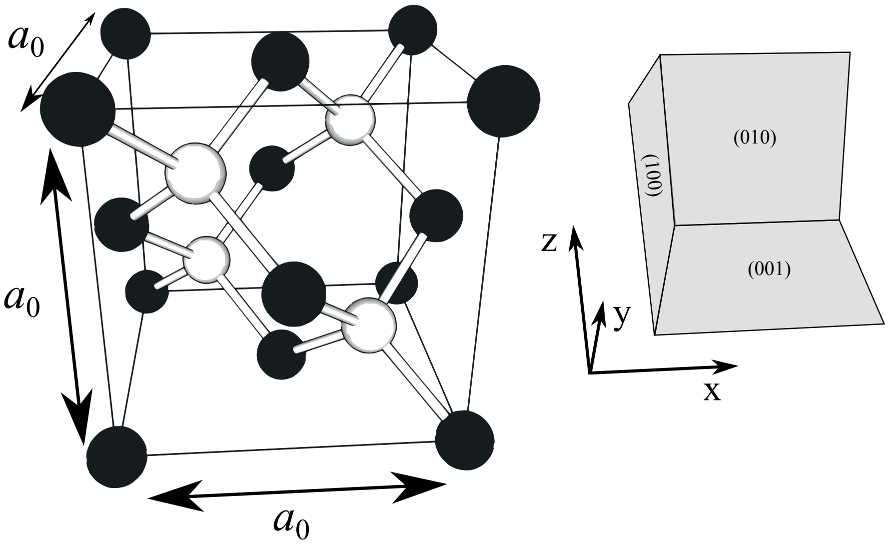

Figure 3.4: Zinc blende (ZB) crystal structure (left). The group III elements (black) bonds to the group V elements (white) to build up the crystal. The lattice parameter a_0 refers to the ZB unit cell, and not to the nearest neighbour distance. On the right, the crystal planes (100), (010) and (001) for the planes referring to the x, y and z-directions, respectively.

Table 3.1: Room temperature parameters for the binaries of the 6.1 Å family of III-V semiconductors. E_g, VBO and CBO are taken from Vurgaftman et al. [86], and are given for 300K. Note that the sources used for the refractive index n here are different from those used in fig. A.3.

Parameter	AlSb	GaSb	InAs
E_g (eV)	2.386 (X)	0.812 (Γ)	0.417 (Γ)
VBO (eV)	-0.41	-0.03	-0.59
CBO (eV)	1.976	0.809	-0.173
n	3.23 [87] (0.7 eV)	3.846 [88] (0.5 eV)	$\approx$ 3.5 [89] (0.5 eV)
a_0 (Å)	6.1358 [62]	6.0968 [61]	6.0583 [90]

tice constants, as shown in figs. A.1 to A.4. The close matching can be seen for GaAs/AlAs and GaSb/AlSb, while the In-V have an increased lattice constant and lower band gap. For laser wavelengths above 2 µm, it can be seen that AlSb/GaSb combined with InAs has a great coverage of wavelength. The lattice constants and thermal expansion coefficients of the binaries are the topics of papers II–IV in chapter 8.

An important feature of most of the III-V semiconductors is that they have a direct band gap, which is important for radiative recombination, while indirect band gap semiconductors such as Si and Ge require a phonon, i.e. a lattice vibration, to allow for optical recombination. Such two-particle processes will have a much lower probability, making indirect band gap semiconductors unsuited for electro-optical devices. Some III-V semiconductors do, however, have indirect band gaps, typically in Al-containing structures. The alloys that have direct and indirect band gaps are shown in fig. A.1 on page 134.

For choosing a suitable substrate, the requirements stated in section 3.1 should be fulfilled. Usually only binary semiconductors are available for substrates. From the requirements of optical and electrical confinement, the substrate should have a low refractive index and large bandgap. From these requirements AlSb is the best choice, as shown in table 3.1.

However, due to its high sensitivity to oxidation [91] in air, it is unsuitable for epitaxial growth. Shibata et al. [92] measured, by Rutherford Backscattering Spectroscopy, that AlSb exposed to air will oxidize a 15 nm thick oxide layer within minutes, and it will continue to oxidize at a mean rate of 1.4 nm/hr for at least 100 nm, at which point the layer was completely oxidized. Most wafer producers sell substrates made of GaSb and InAs, but not AlSb [93–97].

The intermediate refractive index of InAs would make it a better choice than GaSb within the 6.1 Å family. However, due to the VBO and CBO band alignments, it is not suitable for electronic confinement, and GaSb is usually the best suited substrate material despite its high refractive index.

For creating the waveguide and gain medium for the 2–2.4 µm atmospheric window, the alloys $Ga_xIn_{1-x}As_ySb_{1-y}$ and $Al_xGa_{1-x}As_ySb_{1-y}$ are considered the best options. The following sections examine some of the important aspects of these alloys, with respect to laser diode structures.

3.2.1 $\mathbf{Ga}_x\mathbf{In}_{1-x}\mathbf{As}_y\mathbf{Sb}_{1-y}$

GaInAsSb is an important quaternary alloy for the gain material in mid-infrared laser diodes. Grown on GaSb substrates, it can reach wavelengths from about 1.5 µm (GaSb) up to at least 3.73 µm [3]. As seen in figs. 3.3 and A.4, the incorporation of more InAs lowers E_g, VBO and CBO. This can be problematic for proper hole confinement in the QW for wavelengths longer than about 2.7 µm [10].

Recombination mechanisms and rates For p-type InGaAsSb layers with a band gap of 0.55 eV (2.25 µm), the recombination coefficients used in eq. (3.1) have been measured to be $B = (3 \pm 1.5) \times 10^{-11}$ cm^3/s and $C = (1 \pm 0.4) \times 10^{-28}$ cm^6/s [80]. The Auger recombination coefficient C is considered the same for npp and nnp three particle Auger processes in antimonide-based materials [80]. These values suggest lifetimes for radiative and Auger recombination of about 300 and 1000 ns, respectively, for $\mathbf{N} = 1 \times 10^{17}\,\text{cm}^{-3}$ and 30 and 10 ns, respectively, for $1 \times 10^{18}\,\text{cm}^{-3}$.

3.2.2 $\mathbf{Al}_x\mathbf{Ga}_{1-x}\mathbf{As}_y\mathbf{Sb}_{1-y}$

The low refractive index and large bandgap ensures that AlGaAsSb lattice-matched to GaSb provides both optical and electrical confinement, making it the best option in the 6.1 Å family for providing necessary confinement in mid-infrared laser diodes.

Previous work in our group suggests that the best crystalline quality of these fairly thick (typically 1.5–3 µm) epitaxial cladding layers is achieved by lattice matching at growth temperature [59]. The determination of the growth temperature lattice matching composition for $Al_{0.9}Ga_{0.1}As_ySb_{1-y}$ is the topic of paper I in chapter 8.

Band structure and electrical properties The conduction band structure of $Al_xGa_{1-x}As_ySb_{1-y}$ is quite complex. Li et al. [98] have investigated the charge carrier concentration for Te-doped and almost fully relaxed $Al_xGa_{1-x}As_{0.03}Sb_{0.97}$ layers grown on GaAs, to determine its suitability for GaSb-AlSb-based optoelectronic devices. It was concluded from low carrier concentrations, as measured by

Hall measurements (see section 3.4.2), that the conduction band minimum changes from Γ to L around $x = 0.25$, and from L to X around $x = 0.6$–0.7, and that the conduction band minimum is in the X valley for all higher concentrations.

Furthermore, Li et al. [98] show results with high ionization energies for the (n-type) charge carriers around these cross-over points, and the thermal donor ionization energies were 216 meV for $x = 0.24$ and 343–438 meV for $x = 0.69$–0.71, while they were 9.7 and 6.9 meV for $x = 0.14$ and $x = 0.45$, respectively. The thermal ionization energy for $Al_xGa_{1-x}As_{0.03}Sb_{0.97}$ for $x > 0.7$ slowly decreases for increasing x, and the carrier concentration for $x = 0.83$, the highest value of x measured, was just as good as for $x = 0.45$ at room temperature. The measured carrier concentrations at these compositions were about 10^{18} cm^{-3}, compared to less than 10^{16} cm^{-3} for $x = 0.7$ for the same Te incorporation.

Polyakov et al. [99] grew $Al_xGa_{1-x}As_ySb_{1-y}$ on GaAs for compositions close to lattice-matched to GaSb (at room temperature). For Te-doped n-type AlGaAsSb with x equal to 0.5, 0.75, and 1 ($AlAs_{0.08}Sb_{0.92}$), they measured thermal ionization energies of 160, 230 and 120 meV, respectively, which differs from Li et al. [98]. However, both papers suggest high ionization energies for Te-doped n-type AlGaAsSb at the L-X cross-over point for x somewhere between 0.6 and 0.8. Polyakov et al. [99] also point out that Be (p-type) doping up to about 10^{18} cm^{-3} resulted in thermal ionization energies of 8-9 meV for $x = 0.5$ and 1.

In summary, AlGaAsSb lattice matched to GaSb has a conduction band structure not ideal for n-type electrical properties, and compositions with x close to 0.24 and 0.6–0.8 should be avoided in doped layers. For p-type layers these problems do not exist.

Chemical properties Miya et al. [100] have investigated $Al_xGa_{1-x}AsSb$ layers lattice matched to InAs (grown on GaAs substrates) for $x = 1$, 0.8, 0.6 and 0. They found that the oxidation rate decreases with decreasing Al content, where the layer with an Al content of 60% oxidized at about 1/10th the speed of the 80% Al content layer by measuring the volumetric expansion of the oxidized layers due to the oxygen. They found that the oxidation does not stop after more than 200 days. As stated previously, Shibata et al. [92] measured, by Rutherford Backscattering Spectroscopy, that AlSb exposed to air will oxidize a 15 nm thick oxide layer within minutes, and it will continue to oxidize at a mean rate of 1.4 nm/hr for at least 100 nm. This suggests the Al content should be reduced as much as possible with regards to oxidation, and that exposure to air must be minimized. Reducing x from 1 to 0.9 enhances the stability against oxidation [101].

Due to the required low refractive index, a high Al content is necessary. Since AlSb should not be used due to the heavy oxidation, and layers with $x \simeq 0.75$ is not suitable for electrical transport in n-type layers, and $x = 0.9$ is usually chosen as an intermediate solution.

3.3 X-ray Diffraction

X-ray diffraction (XRD) is a technique for characterizing atomic crystal structures by using the interference properties of light.

A crystal can be expressed mathematically by its lattice vectors, which describe the spacing and orientation of atoms relative to their neighbouring atoms. When the crystal structure and extinction rules are known, the available crystal reflections can be determined and measured.

For laser diodes, substrates with a (001) surface is almost exclusively used, and the following treatment is for (001)[1] ZB substrates and thin films (see fig. 3.4).

The in-plane and out-of-plane lattice constants a_x and a_z are related then to the bulk lattice constant a_0 by [102]

$$a_0 = \frac{a_z + \chi \cdot a_x}{\chi} \tag{3.4}$$

where $\chi = 2C_{12}/C_{11}$. C_{11} and C_{12} are the elastic constants for the epilayer material.

For fully strained epilayers, the in-plane lattice constant, a_x, will be the same as the substrate lattice constant, a_{sub}. Using Bragg's equation

$$2d\sin(\theta) = \lambda \tag{3.5}$$

where

$$d = \sqrt[-1]{\frac{h^2+k^2}{{a_x}^2} + \frac{l^2}{{a_z}^2}}, \tag{3.6}$$

we can determine the lattice constants by measuring the Bragg reflection angle θ. Here h and k are the Miller indices in the in-plane directions x and y, and l is the Miller index out of the plane in the z-direction. To determine the ZB crystal lattice parameters a_x and a_z, which are the in-plane and out-of-plane lattice constants, respectively, there are a few techniques commonly used. In our case, a_y is assumed equal to a_x since they are both equivalent in-plane lattice constants. In sections 3.3.1 to 3.3.3, the techniques used to determine the lattice parameters a_x and a_z are explained. These techniques form the foundations for the papers presented in chapter 8. A series of XRD measurements are shown in fig. 3.5, which is a useful reference for the following techniques.

---

[1] (001), (010) and (100) are all equivalent with regards to the crystal symmetry. For XRD, the surface normal is usually defined in the z-direction, i.e. (001).

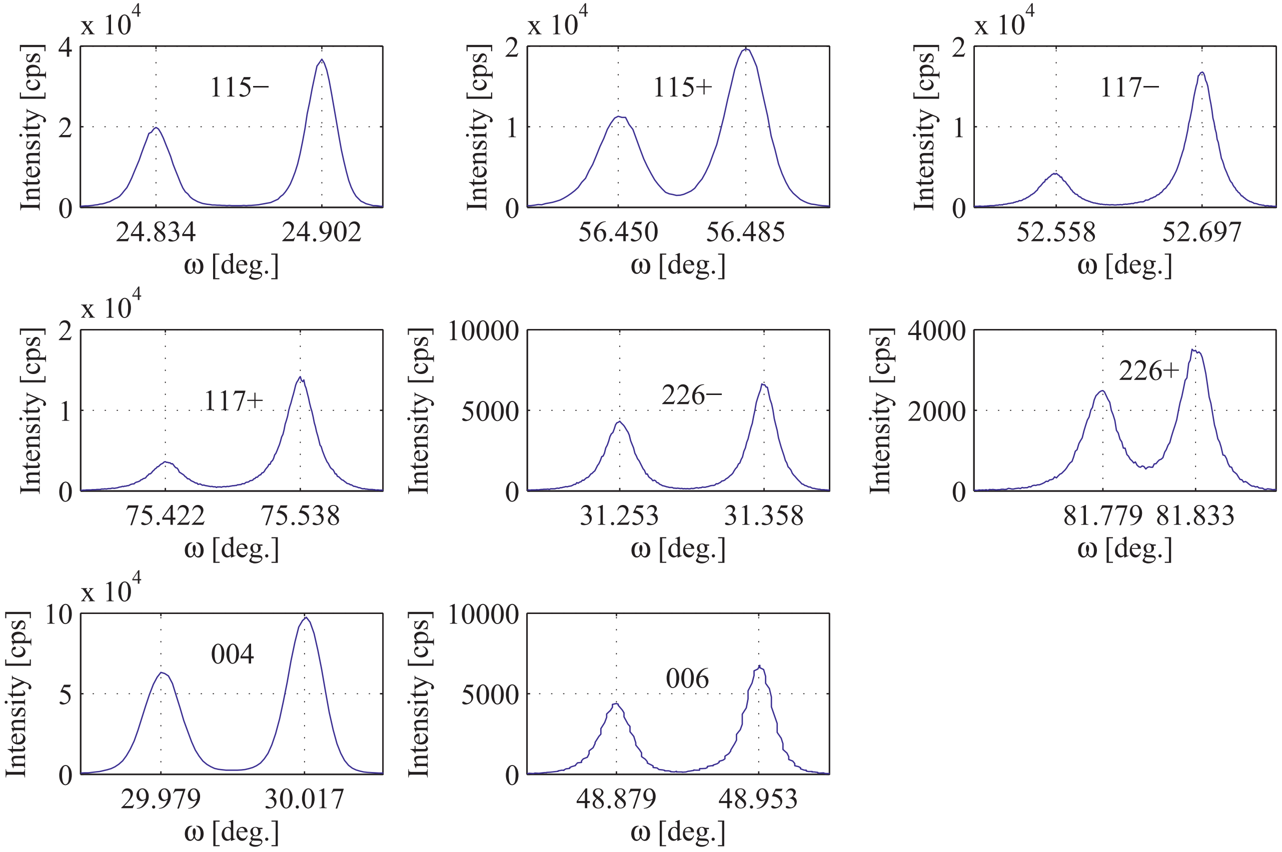

Figure 3.5: Measurements of several reflections from sample Sb 99-1, which is an $Al_{0.9}Ga_{0.1}As_{0.067}Sb_{0.933}$/GaSb sample used in paper I presented in section 8.2. The peak on the left side in each plot is from the cladding layer (AlGaAsSb), while the peak on the right is the substrate (GaSb) peak. Measured at 32°C. In each plot, the reflection (hkl) measured is displayed, and ± indicates which angle is measured (see fig. 3.6 for explanation). Fitting the cladding layer peaks using Fatemi's method (presented in section 3.3.3) yielded $\theta_{\mathrm{off}} = 0.340°$, $a_x = 6.0971$ Å and $a_z = 6.1038$ Å.

For all XRD measurements presented in this work, a Bruker AXS D8 Discover X-ray diffractometer with a Göbel mirror for collimated Cu-K_α radiation and a V-groove to achieve high intensity Cu-$K_{\alpha 1}$ radiation has been utilized. The X-ray wavelength for Cu-$K_{\alpha 1}$ is $\lambda = 1.5406$ Å, and the beam FWHM is specified to be 0.007° for Si(111) [103]. The system allows for a sample rotation angle and detector angle from -10 to 148°. All temperature dependent measurements were performed in a "DHS 900 domed hot stage", which allows for XRD measurements at temperatures from room temperature up to 900°C in a controlled atmosphere [104, 105].

3.3.1 Comparative technique

The lattice parameters of the substrate are often considered to be known. By comparing the angular offset of the thin film layer reflection peak with the substrate peak, the lattice parameter can be determined. Typically the 004 symmetric reflection is used, due to its high intensity and easy alignment (symmetric reflections only require alignment of the rotation of θ and the tilt angle, while asymmetric reflections also require alignment of the azimuthal sample rotation).

It is, however, important to note that this only works for layers above a certain thickness and/or sufficient peak separation. Wie [106] suggests that the product of the layer thickness h and the out-of-plane strain $\varepsilon_\perp$, $h \times \varepsilon_\perp$, should be greater than 5 Å for using this method. Here

$$\varepsilon_\perp = \frac{1+\nu}{1-\nu}\frac{a_0 - a_{\text{sub}}}{a_{\text{sub}}} \approx 2\frac{a_0 - a_{\text{sub}}}{a_{\text{sub}}}, \tag{3.7}$$

where ν is the Poisson ratio (typically close to $^1/_3$ in our materials), a_0 is the thin film layer bulk lattice constant and a_{sub} is the substrate lattice constant. If this criteria is not fulfilled, a simulation tool should be used to determine the lattice parameters/composition of the layer. This requirement also applies to Bond's and Fatemi's methods.

For the comparative method to work, the layer must be fully strained, so that the in-plane lattice constant a_x is identical for the substrate and epilayer. The out-of-plane lattice constant a_z can then be determined from eq. (3.4), by using the fact that the substrate angle θ_{sub} is known. Any offset due to sample mounting or miscut can then be ignored.

This technique is in most cases adequate for determining the composition and strain of epilayers.

3.3.2 Bond's method

For absolute determination of the lattice constants, Bond's method [107] from the 60's can be used. By measuring planes in so-called positive and negative geometries, the lattice constants can be determined.

By exchanging the position of the source and detector, any zero offsets due to sample mounting, errors in the theta drive angle etc. are cancelled. We can then extract 2θ from the measured angles $\omega'_{m,\pm}$:

$$\omega_{m,\pm} = \omega'_{m,\pm} - \Delta\omega_{\pm} \tag{3.8}$$

where

$$\Delta\omega_{\pm} = \delta_n(\tan\theta + \cot\omega_{\pm}) \tag{3.9}$$

is the correction due to refraction of the x-ray beam at the sample surface [108] and θ_{off} is the sample rotation offset. The refractive index is given by $1-\delta_n$ [2]. See fig. 3.6 for an overview of the angles used in the calculations. The relationship between the measured angles $\omega_{m,\pm}$ and the sample surface angle $\omega_{\pm}$ is

$$\omega_{m,\pm} = \omega_{\pm} \pm \theta_{\text{off}} \tag{3.10}$$

for Bond's method.

2θ is then determined from the following equations:

$$\begin{aligned}
\omega_{m,-} &= \theta - \theta_{\text{off}} - \tau && (3.11)\\
\omega_{m,+} &= \theta + \theta_{\text{off}} + \tau && (3.12)\\
\omega_{m,-} + \omega_{m,+} &= 2\theta && (3.13)
\end{aligned}$$

where τ is the angle between the sample surface and the measured plane; for a (001) surface it can be found from [61]

$$\tau = \cos^{-1}\left[\frac{la_x}{\sqrt{(h^2+k^2)\,{a_z}^2 + l^2{a_x}^2}}\right] \tag{3.14}$$

Note that any offset due to miscut of the sample will give an additional contribution to the refraction at the sample surface. The change in angle due to miscut will not be corrected by this method. This is of importance for reflections with low incidence or exit angles (small $\omega_{m,\pm}$). Generally these reflections are avoided for accurate determination of the lattice constant.

---

[2] For AlSb, GaSb and InAs, δ_n is approximately 1.18×10^{-5}, 1.54×10^{-5}, and 1.57×10^{-5} respectively. [109]

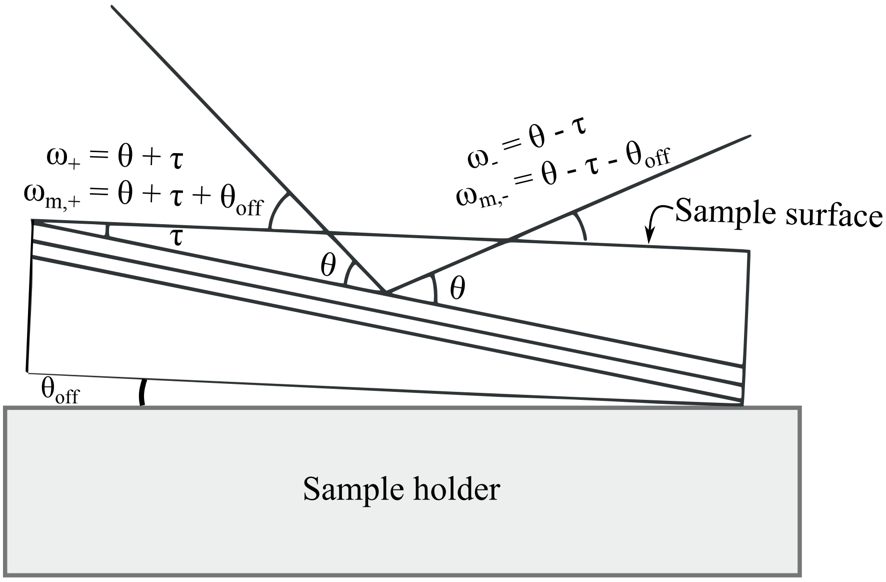

Figure 3.6: Illustration of the angles measured or determined from asymmetric reflection measurements. $\omega_\pm$ are the angles between the sample surface and the measured plane. $\omega_{m,\pm}$ refers to the externally measured angles, and includes the offset, θ_{off}, of the measurement. τ is the angle between the sample surface and the measured plane. The sample surface is here assumed to be parallel to the surface plane (usually (001)). Any deviation between the sample surface and the surface plane is referred to as the "miscut"; its contribution is usually included in the offset angle θ_{off}. The measured angles $\omega_{m,\pm}$ are then used to determine the Bragg angle θ.

3.3.3 Fatemi's method

Another alternative for absolute determination of the lattice constants is Fatemi's method [108, 110]; in Fatemi's method the source and detector positions are not exchanged, so θ_{off} is not cancelled. Instead, θ_{off} is removed mathematically, which requires one extra measurement compared to Bond's method. It's worth noting that to minimize error sources, the lattice parameters h and k are usually kept identical for all measurements, i.e. the sample azimuthal rotation is fixed. This reduces the instrument parameters varied, and usually only leaves a variation in the sample rotation angle ω and detector angle 2θ.

While Bond's method requires an XRD which can preferably move the detector angle, 2θ, close to 360°[3], Fatemi's method can do all measurements for $\theta, 2\theta < 180^{\circ}$.

For tilted planes we then get the equations (after refraction correction):

$$\omega_{\mathrm{m},-} = \theta + \theta_{\mathrm{off}} - \tau \tag{3.15}$$

$$\omega_{\mathrm{m},+} = \theta + \theta_{\mathrm{off}} + \tau \tag{3.16}$$

$$\omega_{\mathrm{m},-} + \omega_{\mathrm{m},+} = 2(\theta + \theta_{\mathrm{off}}) \tag{3.17}$$

$$\omega_{\mathrm{m},-} - \omega_{\mathrm{m},+} = 2\tau \tag{3.18}$$

For Fatemi's method we have $\omega_{\mathrm{m},\pm} = \omega_{\pm} + \theta_{\mathrm{off}}$ (not $\pm\theta_{\mathrm{off}}$), since we do not exchange the position of the X-ray source and detector as in Bond's method, but instead measure the reflections from the equivalent planes (h,k,l) and (-h,-k,l).

Using these measured angles and correcting for refraction and offset θ_{off}, the in-plane and out-of-plane lattice constants a_x and a_z can be determined for (001) substrates using [61]

$$a_x = \frac{\sqrt{h^2 + k^2}\lambda}{2\sin(\theta)\sin(\tau)} \tag{3.19}$$

and

$$a_z = \frac{l\lambda}{2\sin(\theta)\cos(\tau)}. \tag{3.20}$$

The difference between Bond's and Fatemi's methods is illustrated in fig. 3.7.

3.4 Other characterization techniques

In addition to XRD it is also important to characterize the optical and electrical properties. The gain medium is characterized by photoluminesence, while the electrical properties are investigated by Hall measurements.

---

[3] The detector must be able to move at least an angle 2θ in both clockwise and counterclockwise directions, and the sample must be able to move $180^{\circ} - \omega_{+,-}$, as shown in fig. 3.7.

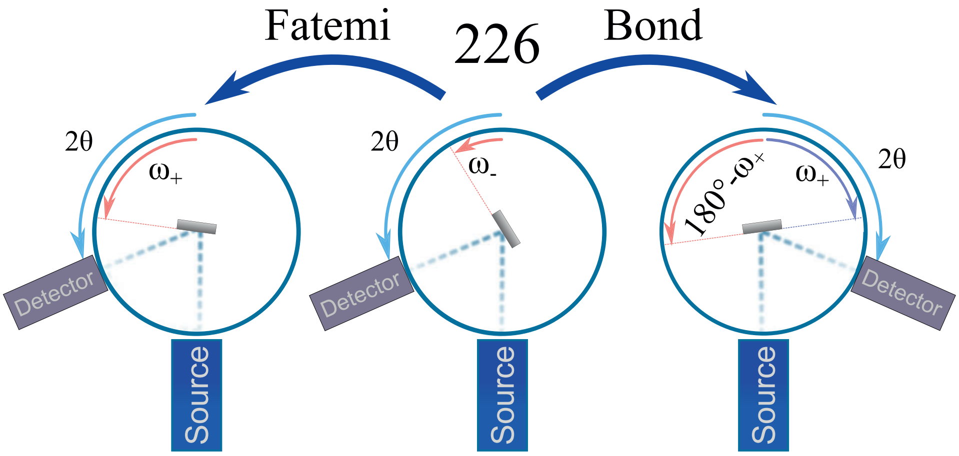

Figure 3.7: Illustration of XRD measurement of 226 reflection on GaSb(001) using Fatemi and Bond's methods. In Bond's method, the source, detector and sample are moved from positive to negative angles to eliminate the sample offset θ_{off} by exchanging the position of the source and detector. This is achieved by moving the detector to an angle -2θ, and the sample to an angle $180^\circ - \omega$. In Fatemi's method the offset must be removed mathematically, and requires an extra measurement from another reflection.

3.4.1 Photoluminescence

photoluminescence (PL) is the process where you produce optical recombination in a material or structure by exciting it with electromagnetic waves. By pumping the material with a light source, typically a laser, with photon energies $h\nu > E_g$, electrons are excited from the valence band to the conduction band. The electrons will after some time, typically tens of ns, recombine through one of the recombination mechanisms described in section 3.1.2. If the recombination is radiative, it can be measured by a spectrometer, producing PL.

For semiconductors the resulting light gives information about the bandgap energy E_g, or for quantum wells the confinement energy. It can also be used to determine doping binding energies by performing low temperature PL.

This information is crucial for designing lasers for gas detection, where the wavelength must match the absorption line of the gas to be measured.

3.4.2 Hall Measurements

The Hall effect is an important effect which can be used to determine the doping concentration in semiconductors. It is a product of the Lorentz force, which states that [111]

$$\mathbf{F} = \pm e(\mathbf{E} + \mathbf{v} \times \mathbf{B}). \tag{3.21}$$

where **F** is the force vector, e is the elemental charge which is $-e$ for electrons and e for holes, **v** is the vectorial speed of the charge and **B** is the magnetic field vector. The force in the y-direction F_y is then

$$F_y = \pm e(E_y - v_x B_z). \tag{3.22}$$

For electrons the charge is $-e$ and the speed v_x is in the opposite direction of E_x, while for holes the charge is e and v_x follows E_x. In a Hall measurement, a electrical field E_x is induced by sending a current through the structure, and a magnet is set up with a magnetic field in the z-direction. The charge carriers will then feel a force F_y, until the induced perpendicular electrical field E_y reaches equilibrium so that

$$E_y = v_x B_z. \tag{3.23}$$

The current is $J_x = v_x ep$ for holes [111], where **P** is the hole carrier concentration, and we get

$$E_y = \frac{J_x B_z}{e\mathbf{P}} = V_y / w \tag{3.24}$$

where V_y is the voltage across the Hall bar, and w is the width. By using a known current J_x and a known magnetic field B_z, the carrier concentration can be determined by the amplitude of V_y, and the doping type is determined by the sign, positive for p-type, and negative for n-type.

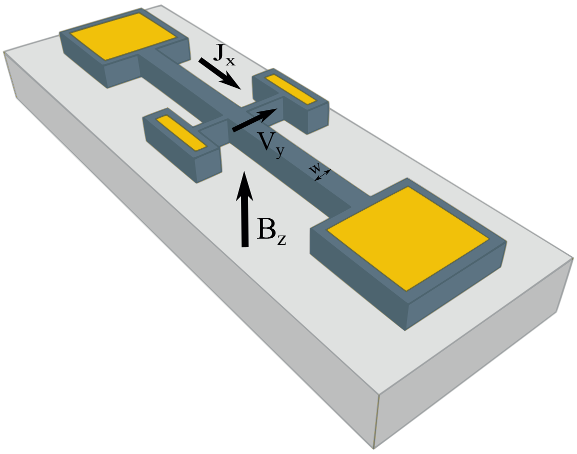

Figure 3.8: Illustration of a Hall bar. The dark structure is the doped semiconductor, placed on top of an insulating substrate.

Chapter 4

Growth of Laser Diodes

Making epitaxial thin films is at the core of laser fabrication. The growth of multilayer structures is necessary to define both the electrical and optical aspects of the laser diode. In this chapter the important aspects of laser growth are presented; first an introduction to epitaxial growth and the importance of managing the strain in the structure, followed by a description of the growth technique. Finally, the layer structure of a laser diode is introduced followed by the laser structure of samples Sb 142 and Sb 145, which is the structure of all lasers tested in this work.

4.1 Epitaxial growth

Deposition or growth is a term used when you apply one material on top of another (or the same) material. This is usually performed by heating or sputtering one or both materials and depositing one of them onto the other, either through a melt or by evaporating one material onto the other.

If the conditions are right, the deposited atoms can bond to the atoms of the material it is deposited on, effectively continuing to build on the existing crystal structure. This is called epitaxial growth, and it is an essential part of semiconductor manufacturing. It is important to maintain a crystalline structure with few defects, as defects will interfere with the operation of the devices. To maintain a single crystalline phase throughout the whole structure it is therefore important that the different epitaxial layers, often called epilayers, have the same crystal structure and interatomic distance. For ZB (001) samples, a mono-layer (ML) of atoms have a height of $a_0/2$, as can be seen from fig. 3.4. This unit is often used for epitaxial growth.

4.1.1 Strain and the critical thickness

The use of strain for improving the properties of the gain material was presented in section 3.1.2. However, for growing thick epilayers on sample surfaces, it is also important to maintain a low average strain throughout the whole structure.

If the relaxed lattice constant of a layer does not match that of the underlying layers and the substrate, it will conform to the in-plane lattice constant $a_x = a_{\text{sub}}$, while the out-of-plane lattice constant a_z will increase or decrease depending on if the strain is compressive ($a_{\text{sub}} < a_{\text{epilayer}}$) or tensile, respectively. While it is the stress energy introduced by the lattice mismatch that is important, the change in the lattice parameters, expressed by the strain, is more easily determined since it can be measured by XRD. The relation between the bulk lattice constant a_0 and the in-plane and out-of-plane lattice constants a_x and a_z is described by eq. (3.4), and the in-plane strain is defined by eq. (3.7).

The lattice mismatch will build up a potential stress energy, which at some point starts to introduce misfit dislocations in the material in order to relax the epilayer towards its bulk state [112]. Dislocations are detrimental to electro-optical devices, and strain balancing is therefore important for laser structures. In addition, it is also important to note that the thermal expansion of the epilayers are different, and our research suggests that the crystalline quality is optimum for lattice matching at growth temperature [59]. The thermal expansion of the cladding layers, the thickest epilayers of the laser structure, is the topic of paper I in chapter 8. Lattice matching of GaSb-based laser structures is often achieved by adding As to the epilayer, to reduce the lattice constant, as shown in fig. A.1.

The critical thickness refers to the thickness at which the stress-induced energy is too high to support a fully strained epilayer. The critical thickness of the main tertiary alloy used for the gain medium, GaInSb, has been investigated by our group [113]. The data suggests that a GaInSb layer with 1% strain on GaSb ($Ga_{0.84}In_{0.16}Sb$) has a critical thickness of about 40-60 nm.

4.2 Molecular Beam Epitaxy

Molecular Beam Epitaxy is a technique for growing epitaxial layers from nm to µm thicknesses with high precision and low impurity and defect concentrations. The rate is typically 1 ML/s, which is about 1.1 µm/hr for our material system (relating to the lattice constant).

By thermal evaporation of the elemental or molecular constituents used in the grown structure, a wide range of compositions can be grown. However, an optimization of the growth parameters for e.g. AlSb may not be the optimal for InAs, and compromises must be made to minimize defects etc. This is usually achieved by finding group V overpressures and a growth temperature compatible with all of the constituents. The optimum growth temperatures are about 550°C for AlSb, 490°C for GaSb and 420-490°C for GaInAsSb.

A sketch of the main components of the growth chamber is shown in fig. 4.1. Alloys, such as GaSb, are created by evaporating more than one source material at a time. The term “molecular beam” relates to a condition where the pressure is low enough for atoms to travel long distances without colliding with another atom, referred to as the mean free path. For lengths of about 0.2 m, this condition is fulfilled for pressures below about 8×10^{-4} millibar [112], which is in a vacuum range referred to as high vacuum. During epitaxial growth on GaSb, the beam flux pressure at the sample surface is usually around 1×10^{-6} millibar, fulfilling the molecular beam pressure requirement.

However, due to the requirements for low impurity concentrations, the base pressure should preferably be less than 2×10^{-11} millibar [112], in the ultra-high vacuum (UHV) range. The base pressure of MBE systems are usually close to 1×10^{-10} millibar.

For all samples grown in this work a Varian Gen II Modular molecular beam epitaxy system has been used. It is capable of growth of III-V semiconductors containing Al, Ga, In, As and Sb. In addition the system has three dopant sources; Si, Te and Be. The materials and their placements are shown in fig. 4.2.

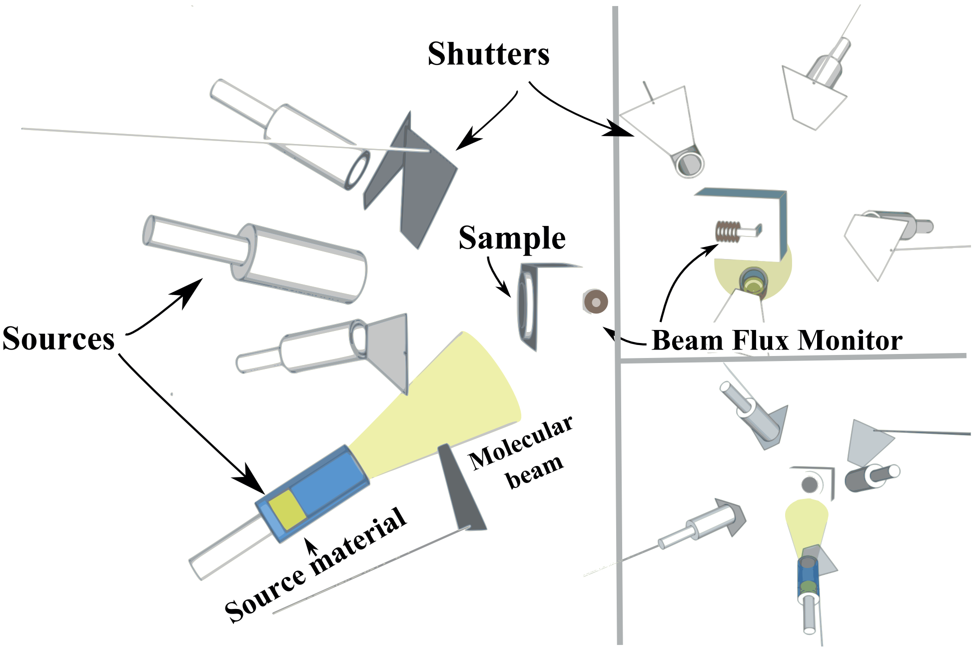

Figure 4.1: Sketch of the MBE chamber, seen from the side (left), behind the sample (top right) and behind the sources (bottom right). By heating the sample to an appropriate growth temperature and evaporating source materials in an UHV environment, thin films can be grown with a precision of about one atomic layer. The beam flux monitor, which is a pressure gauge, can be rotated into the sample position and accurate fluxes of the source materials can be determined. Shutters are used to allow or block the fluxes of the individual sources.

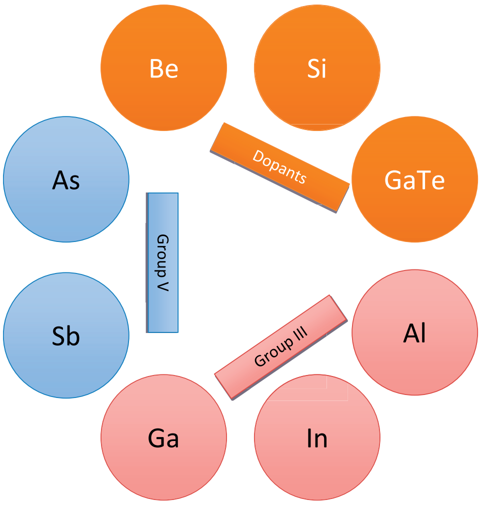

Figure 4.2: The available source materials in the Varian Gen II Modular molecular beam epitaxy system used in this work.

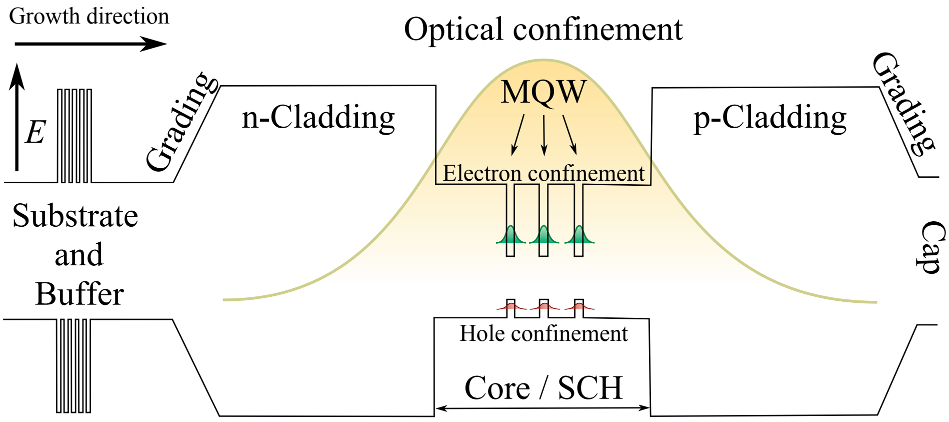

Figure 4.3: A sketch of a laser diode band diagram with focus on its main properties for laser diodes. The top line is the conduction band, and the lower line is the valence band. The layers are described in detail in section 4.3.1. The substrate and buffer improves the crystal quality and uniformity. The grading layers reduce the diode voltage, while the cladding layers provide optical and electrical confinement. Furthermore, the core provides an increased refractive index for waveguiding and further confinement for the charge carriers. The MQW provide the gain for the stimulated emission radiation.

4.3 Growth of a laser structure

In electrical terms, the grown laser structure can be thought of as a p-i-n diode, where the p-layer is on top, and the n-layer (including the substrate) is at the bottom, and the active region (SCH and MQW) are undoped for optimum gain. In optical terms, it is a slab waveguide.

Here, the laser structure is presented, with descriptions of the different epilayers and their functions. The layer structures of samples Sb 142 and Sb 145 are then shown in fig. 4.4 and table 4.1.

4.3.1 Laser structure

The main components of a semiconductor laser structure are shown in fig. 4.3 and described below.

Substrate The substrate is the starting point of the laser. Some of the main properties important for the substrate is that it is sturdy, so that it can be handled without breaking, has a suitable crystal structure with appropriate lattice constant for the epilayers required for the laser structure, and that it is suitable for typical growth temperatures. It should also have good electrical and thermal properties for transport of electrons/holes and heat, respectively. Preferably it should have a refractive index $n_{\mathrm{sub}} < n_{\mathrm{eff}}$ to avoid optical leakage into the substrate.

Buffer A buffer layer is grown prior to the actual laser structure to improve the sample surface quality. A series of thin AlGaSb layers in a superlattice is usually introduced. A superlattice with high Al content is shown to reduce the sample surface roughness [114], which is important to achieve smooth interfaces and well defined QWs.

Grading The cladding layers of the laser have a large bandgap to achieve proper confinement in the core. The purpose of the grading is to improve the electrical properties of the diode by reducing, or smoothing, the barrier for electrons and holes at the heterojunctions. This will usually decrease the series resistance and diode voltage [19].

Cladding The cladding layers are designed to provide optical and electrical confinement of the charge carriers. Important parameters are a low refractive index $n_{\mathrm{clad}} < n_{\mathrm{eff}}$, and sufficient conduction and valence band offsets to the core and MQW. It must also have good electrical conductivity of electrons and holes by n- and p-type doping, respectively.

Core/SCH The core, or separate confinement heterostructure (SCH), acts as a core for the optical waveguide and confinement for the charge carriers. While the MQW usually have a higher refractive index than the cladding, it is too thin to give a proper confinement of the light. By using SCH layers, the light confinement is increased, which increases the overlap of the optical field and the confined electron and hole wavefunctions in the gain material. This layer is usually undoped to reduce optical losses. With the exception of the MQW, these layers should have the highest refractive index $n_{\mathrm{core}} > n_{\mathrm{eff}}$ of the structure, and the CBO and VBO should be intermediate between the cladding and MQW.

MQW The MQW are the gain material of the structure and the important parameters for the well is a bandgap matched to the lasing wavelength. It should have the lowest CBO and highest VBO in the structure, and it should be optimized to reduce the Auger recombination. This is usually achieved by using compressive strain to separate light and heavy holes, and band structure engineering to increase the Auger recombination lifetime, such as reducing the CBO between the barrier and well [115]. If the SCH provides proper electron and hole confinement, the barrier material is usually the same material.

Cap The cap is a protective layer, typically of the same material as the substrate. It might be needed to protect the grown structure from air, and it should be easy to contact by metallization.

Figure 4.4 and table 4.1 shows the nominal material parameters for laser samples Sb 142 and Sb 145, which is the structure used for all lasers in this work. The problem with the GaTe source was most likely due to poor outgassing prior to Hall measurements. This resulted in a too high carrier concentration in the manufactured Hall bars, and a too low GaTe source temperature was used for the laser diodes.

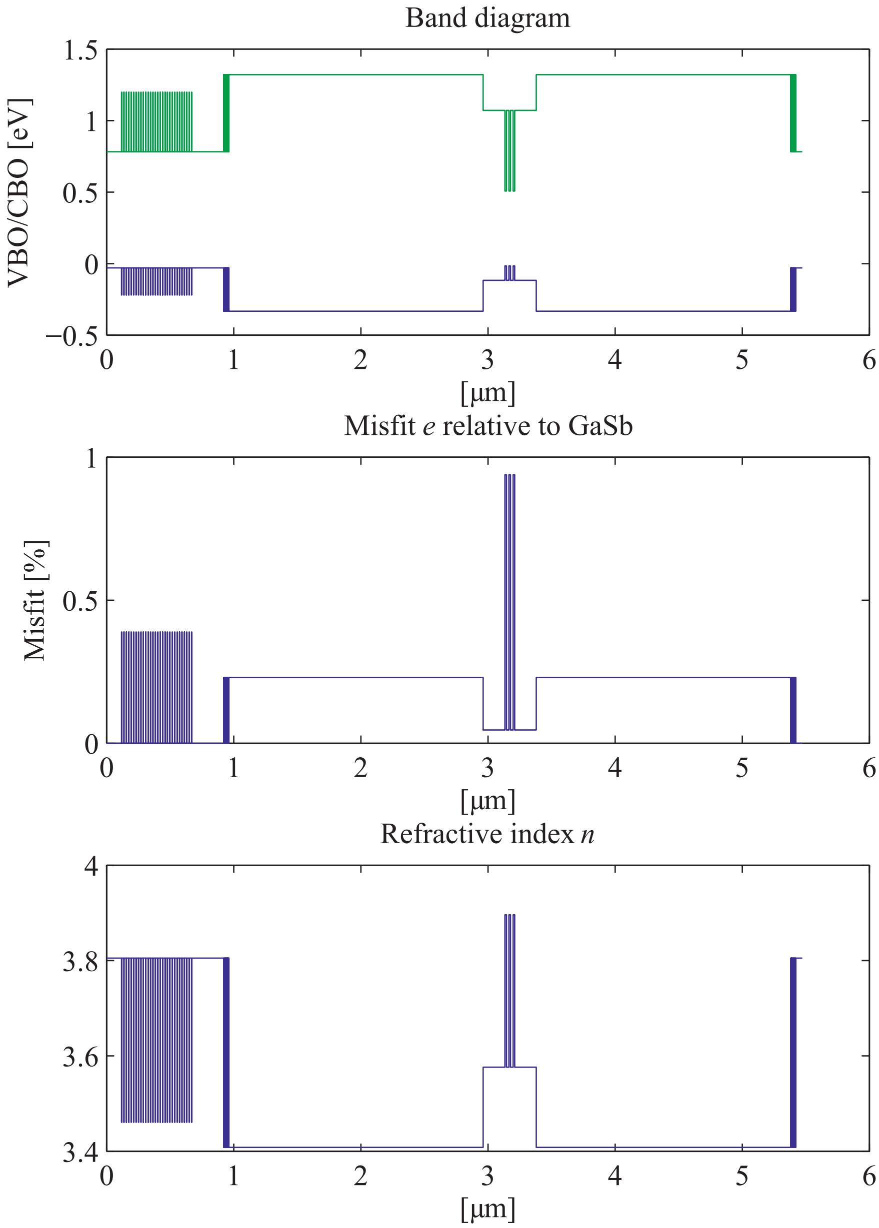

Figure 4.4: Visualization of the grown laser structure for sample Sb 142 and Sb 145. Band diagram, misfit *e* and refractive index *n*. The different layer compositions are shown and explained in table 4.1.

Table 4.1: Layer information for the nominal laser structures of samples Sb 142 and Sb 145. The n-type doping (Te) was nominally $1 \times 10^{18}\,\mathrm{cm}^{-3}$, but due to a problem with the GaTe source, it is most likely closer to $2 \times 10^{17}\,\mathrm{cm}^{-3}$. The substrate doping is about $5 \times 10^{17}\,\mathrm{cm}^{-3}$. For p-type doping, Be was used. For the n-type cladding, the GaTe source temperature was gradually reduced the last 300 nm of the cladding layer, reducing the doping concentration. The grading layers are composed of alternating GaSb/AlGaAsSb layers, where the thickness of the GaSb layers are reduced from 2 nm to 0.1 nm towards the AlGaAsSb layers, while the AlGaAsSb thickness is increased from 0.1 nm to 2 nm. This results in an average linear change in composition from GaSb to AlGaAsSb. The top p-type cladding is usually grown at 490°C. However, for sample Sb 142 an error in the recipe resulted in a top cladding temperature of 550°C, while for sample Sb 145 the temperature was set to 490°C. The resulting lasers lased at 2.0 µm (Sb 142) and 2.2 µm (Sb 145). A blue-shift due to thermal annealing of GaInAsSb is documented in the literature [116].

Layer	Material	Thickness (nm)	Doping	Temp. (°C)	Comment
Substrate	GaSb	5×10^5	n	490	
Buffer	GaSb	100	n	490	
30x superlattice	GaSb/AlGaSb	18/1 x30	n	490	
Buffer	GaSb	250	n	490	
Grading	GaSb/AlGaAsSb	2.1 x20	n	490	See table text
Cap	GaSb	1	n	550	Growth stop
Cladding	$Al_{0.90}GaAsSb$	1700	n	550	
Cladding	$Al_{0.90}GaAsSb$	300	n	550	See table text
Cap	GaSb	1	-	430	Growth stop
SCH	$Al_{0.25}GaAsSb$	150	-	430	
MQW	AlGaAsSb/GaInAsSb	20/12.5x3 + 20	-	430	
SCH	$Al_{0.25}GaAsSb$	150	-	430	Growth stop
Cladding	$Al_{0.90}GaAsSb$	2000	p	550 / 490	
Grading	AlGaAsSb/GaSb	2.1 x20	p	550 / 490	See table text
Cap	GaSb	50	p	550 / 490	

Chapter 5

Processing of Laser Diodes

The laser growth defined the electric properties of the laser diode, together with the gain material and a 1D slab waveguide. The purpose of the processing is to create a 2D waveguide, electrical contacts for external power connections and mirrors for the resonator.

Here, the processing techniques used to create the laser diode are presented, followed by a presentation of the processing results.

Most of the processing presented in this work was performed at the NTNU Nanolab cleanroom facilities. Information regarding the facilities and the available equipment can be found online at `http://www.norfab.no/lab-facilities/ntnu-nanolab/`.

5.1 Photolithography

Lithography is an integral part of most device processing, where the purpose is to transfer a pattern onto the sample surface. This usually involves spinning on a polymer which contains a photosensitive component. By exposing this polymer, referred to as a photoresist (PR), its chemical properties change, making it soluble or insoluble in a developer process. If the exposure makes the PR soluble, it is referred to as a positive resist, since the pattern in the resist will be the same as the pattern on the mask used to block parts of the light used for exposure. For negative resists, the exposure hardens the resist, and the pattern is inverted.

To expose the resist, different techniques can be used. For resolutions from about 2 to 1000 nm, electron beam lithography (EBL) is a popular choice. Here, the PR is exposed by an electron beam. In a scanning electron microscope (SEM), the electron beam can be positioned on the sample surface by deviating the electron beam by electric or magnetic fields. In this way, the electron beam can be used to expose the PR with a resolution (roughly) defined by the spot size of the electron beam, and resolutions below 10 nm are achievable. A critical dimension of 2 nm has been demonstrated [117]. However, one of the limitations of such a system is large area exposure, where exposures can take many hours or many days.

For resolutions from a few nm up to more than 100 µm, nanoimprint lithography (NIL) is a relatively new and interesting alternative [118], where a stamp is used to imprint the pattern into a polymer. By imprinting the resist and hardening it, the pattern can be transferred onto the sample. NIL is very scalable, and research into patterning of full wafers is ongoing [118]. The process usually requires a flat sample, and is best suited for patterning the first process step, prior to structuring the sample surface.

For resolutions from about 0.35 µm and up to wafer size, contact photolithography is usually the most common lithography in a research lab environment. Here, the pattern is transferred using light, usually ultra-violet light at 365 nm (i-line) [119]. A pattern is defined using chrome deposited on a glass plate, and by placing it between an ultra-violet light source and a sample covered by PR. Through advanced techniques such as short wavelengths, focusing and monochromatic light sources (lasers), the resolution can be increased to less than 100 nm. However, this requires more advanced equipment.

In this work a MA56 mask aligner from Karl Suss has been used for the photolithography process. It provides UV light from a mercury bulb, providing exposure of the 365 nm wavelength (i-line). The intensity was continously monitored by the instrument during exposure to ensure a constant intensity.

Edge bead removal (EBR) is the removal of the PR near the edges of the sample. Due to the PR spin-on process, the part of the resist close to the edge is usually significantly thicker than the resist in the middle of the sample. For contact lithography this is problematic, since the mask will be resting on top of the edge bead, creating a gap between the PR and the mask at the center of the sample. This results in a separation between the mask and the PR, resulting in reduced resolution and poor sidewall angles. Figure 5.1 shows the importance of edge bead removal (EBR) for good resist sidewall profiles. A steep sidewall angle is important for both good etch profiles and metallization profiles.

EBR is performed by exposing the edge bead with ultra-violet light, while covering the middle of the sample, a process that only works for positive photoresists.

5.2 Etching

Etching can be divided into two distinct types; wet etching (liquids) and dry etching (gases) [119].

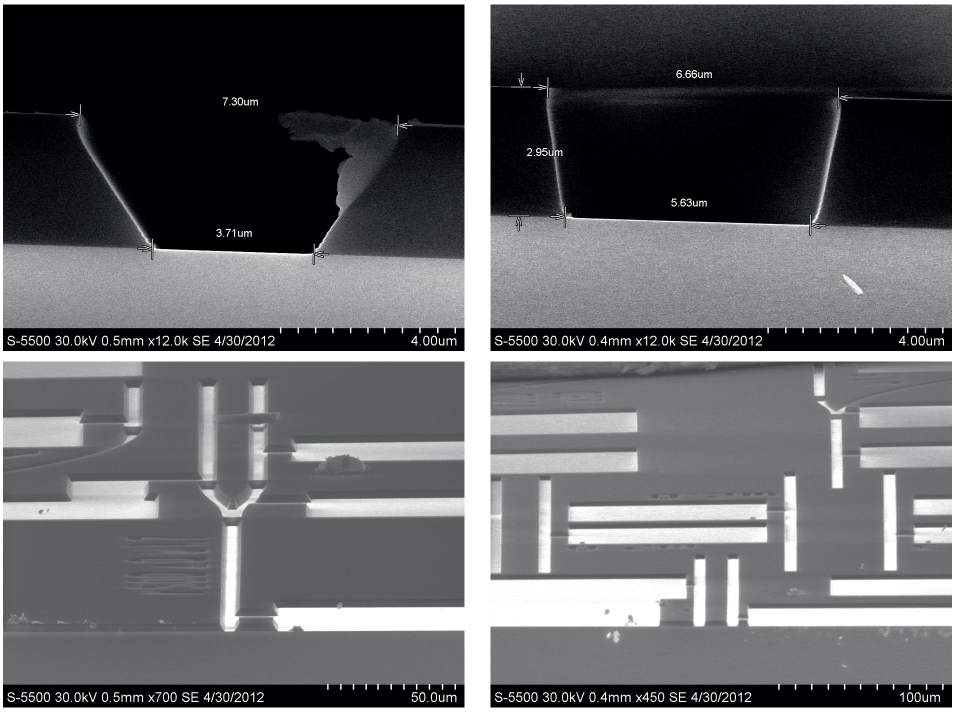

Figure 5.1: SEM photographs of photolithography resist profiles without EBR (left) and with EBR (right). Other parameters are identical. By using EBR, a steeper sidewall angle is achieved, which is important for most processing steps using photolithography for patterning. The resist used is S1818.

In wet etching the sample is immersed into a solution which reacts chemically with the sample surface. Such etches are usually isotropic, or have an etch rate dependent on the crystal lattice, and wet etches are usually not ideal for etching straight sidewalls in a sample. However, they are useful for etching sample surfaces to remove impurities and native oxides prior to further processing.

Dry etching refers to a process where a gas is used instead of a liquid. Typically, it uses a a reactive gas, resulting in chemical etching, or an ionized gas which results in physical etching from bombardment of atoms onto the sample surface. By ionizing reactive gases, the sample can be simulatenously physically and chemically etched, which is referred to as reactive ion etching (RIE). In addition, some gases become reactive due to the ionization.

In RIE, the ionization is created by an oscillating electric field between a top electrode and the sample. The sample is then given a negative potential, attracting the positively charged ions to the surface. Since the etch rate is not only dependent on the chemical reactions, the etch is more anisotropic than the wet etch due to the directional physical etch from the ion bombardment. However, since the electric field amplitude controls both the rate of ionization and the rate of physical etch, the rate of physical and chemical etch cannot be controlled separately. By using, in addition, an oscillating magnetic field to ionize the gas without accelerating it towards the sample, the chemical etching by ionized reactive gas can be controlled separately from the physical etching, controlled by the electric field. This is referred to as an inductively coupled plasma reactive ion etching (ICP-RIE).

Zhang et al. [120] have investigated the etching of GaSb and AlGaAsSb using BCl_3 and Cl_2 and found that BCl_3 provides smooth etch surfaces [120, 121] but low etch rates, while Cl_2 results in high etch rates, but with very rough surfaces for AlGaAsSb. This is due to a very low physical etch rate when using Cl_2. By mixing it with BCl_3, the surface roughness and undercutting is reduced [121]. An example of GaSb etched by a BCl_3/Cl_2 ICP-RIE etch is shown in fig. 5.2.

For polymers such as PR, it is preferred to use an O_2/CF_4 etch chemistry. This is presented in more detail in the laser processing results, see section 5.8.1.

It is also worth noting that the physical etching may damage the electro-optical properties of the sample, and etching too close to the active medium can ruin the gain medium. Germann [122] has shown that RIE etching down to 100 nm above the active medium in an AlGaAs/GaAs laser with ion energies above 500 eV resulted in reduced PL intensity. It is common to only etch the upper cladding to define the waveguide, and the optical confinement in the waveguide is dependent on the etch depth[1]. The etch depth cannot be determined by SEM while processing without sacrificing laser samples, and the etch depth is usually determined by

---

[1] This will be discussed in chapter 7, and the relation between etch depth and transverse mode profile is shown in fig. F.1.

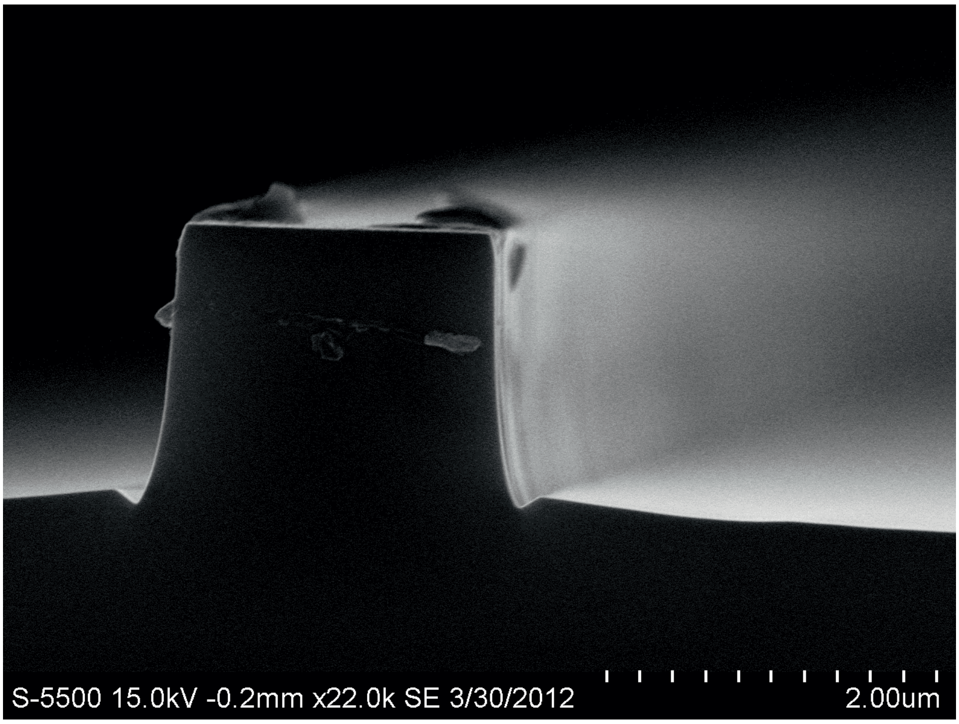

Figure 5.2: SEM photographs of a cross section view of the etch profile from a GaSb dummy wafer etched by ICP-RIE.

a profilometer.

In this work, all dry etching were performed in an Oxford Instruments Plasmalab System 100 ICP-RIE for chlorine based etch chemistries (BCl_3 and Cl_2), and an Oxford Instruments Plasmalab System 100 RIE for fluorine based and related etch chemistries (CF_4, O_2 and Ar).

Etch mask hardening The etch mask will be etched as a part of the etch process. For some etch chemistries, the etch mask can react nonuniformly or the etched material can redeposit on the sidewalls, and result in etch artifacts. An example of this is shown in fig. 5.3.

For proper etching and contacting of ridge laser structures, these artifacts must be removed, typically by using an etch chemistry which only etches the mask material. For III-V semiconductors, an oxygen- or fluor-based etch chemistry can be used.

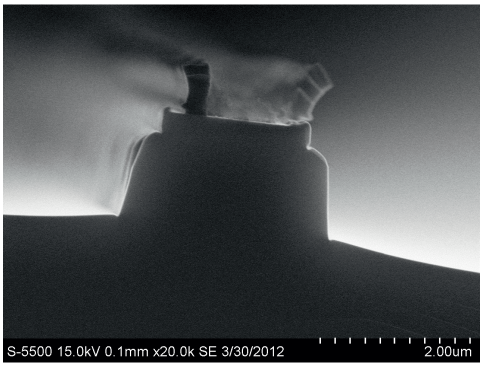

Figure 5.3: SEM photograph of an etch test sample. Here, the resist has hardened, or redeposition of the etched semiconductor has caused the forming of “horns” on the sides. The etch gases used were BCl_3 and Ar.

5.2.1 Selectivity

Selectivity is a term used to define the etch rate of the sample compared to the etch rate of the mask. It is important that the mask, e.g. a PR, is thick enough to support the desired etch depth. The selectivity s can be determined by

$$s = \frac{r_a}{r_b} = \frac{d}{h_1 - H + d} \tag{5.1}$$

where r_a is the sample etch rate, r_b is the mask etch rate, and the heights h_1, H and d are shown in fig. 5.4. If you know the selectivity, it can be used to determine the etch depth without removing the mask, which makes it possible to continue etching if the desired etch depth was not reached. The expression for etch depth is then

$$d = \frac{H - h_1}{1 - \frac{1}{s}}. \tag{5.2}$$

In addition to determining the etch depth, a high selectivity can also be useful for improving the sidewall profile. The sidewall profile of the mask will be transferred on to the sample. However, an increased selectivity will result in straighter sidewalls.

5.3 Insulation

An important part of the processing is to make sure that you only contact the laser ridge, and not the surrounding sample material, which would result in no lasing.

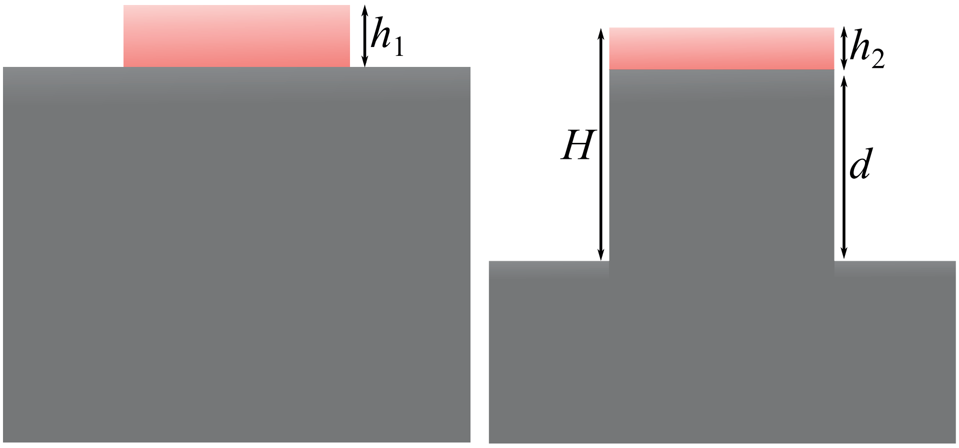

Figure 5.4: Etching of mask and sample. h_1 and h_2 are the mask thicknesses before and after etching, respectively. H is the total height, and d is the etch depth.

Also, the optical field of the laser should be removed from any metal (unless the metal is intentionally placed to change the characteristics of the device), such as bonding pads.

The insulation material is usually a glass/ceramic, a polymer, or both. For thick insulation layers it is preferable that the thickness matches the etch depth, both to planarize the sample, and to create contact pads at the same height as the ridge and protect the ridge structure chemically and mechanically. In addition, it should remove heat from the laser. Since the insulation will be close to the core, it will also be a part of the waveguide through its refractive index. For contacting the laser sample, it is important that the insulation provides sufficient adhesion for the deposited metal.

In section 5.8.1 more details regarding insulation used in this work is presented, including the choice of material and process.

5.4 Metallization

When contacting a laser diode, it is important to create a good ohmic contact.

It is believed that the surface of GaSb has a Fermi level pinning near the valence band edge, which benefits ohmic contacts to p-type GaSb [123]. For p-type contacts, most groups use Ti/Pt/Au [28, 34, 124], where Ti provides adhesion, Pt works as a diffusion barrier for Au, and Au is easily contacted externally and does not oxidize.

For n-type contacts, however, creating a good ohmic contact can be more challenging due to a barrier induced at the semiconductor-metal interface. To reduce this barrier, the most common strategies are either alloying the semiconductor with the metal, or heavily doping the semiconductor near the interface. Both of these techniques require an annealing process, described in section 5.4.2, after the metal deposition.

Robinson and Mohney [125] have shown that by using In in the metallization scheme, an InGaSb alloy at the interface after annealing reduces the contact resistance. Vogt et al. [126] have published another metalization scheme for n-type GaSb, using Pd/Ge/Au/Pt/Au annealed at 300 °C. The diffusion of Ge into the GaSb sample after annealing results in a good ohmic contact. Robinson [127] has pointed out that this recipe may not be well suited for all purposes, since the Pd penetrates 150 nm into the GaSb. However, for mid-infrared laser diodes the n-type contact is usually 100 – 150 μm from the active layers, and this is not an issue. Another alternative is to use Au, which will also diffuse into the sample [128, 129]. However, the diffusion will continue over time causing catastrophic failure of the device [129].

Metallization is usually performed by electron beam evaporation, where the metal is heated by an electron beam and evaporated onto the sample surface. This technique is similar to MBE, however, the deposited thin film is not epitaxial. The sample surface temperature is usually close to room temperature during this deposition, only heated by the evaporated metals. The heating is due to the high temperature of the evaporated metal and the radiative heating from the metal source.

In this work, a Pfeiffer Vacuum Classic 500 e-beam evaporator and a Custom ATC-2200V from AJA International Inc. have been used for electron beam evaporation of metals.

5.4.1 Lift-off

To pattern the deposited metal, a technique called lift-off is commonly used. Lift-off is a technique where the whole sample is covered with a deposited metal layer, and then the unwanted parts of the layer is lifted off. This is a popular technique for depositing layers which are not easily etched without also etching the sample, such as metals.

The technique is usually implemented by photolitography, where openings in the PR are made where the metal is to be deposited. The best results are usually achieved with a negative PR utilizing undercut, where the sidewall angle is greater than 90°. It is important for this technique that the evaporated metal has a normal incidence onto the sample surface, a feature provided by the electron beam evaporation technique. Examples of lift-off are shown in figs. 5.5 and 5.6.

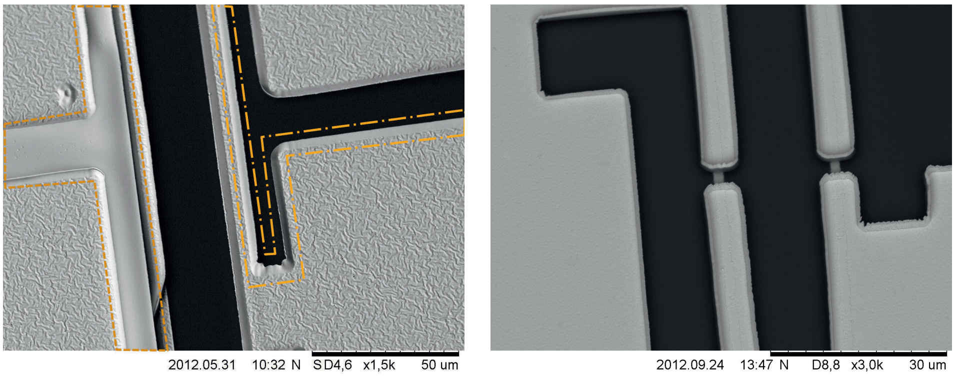

Figure 5.5: SEM photographs of metallized samples after lift-off. **Left:** A bad lift-off process due to a low PR sidewall profile angle (see fig. 5.1), leading to a single continuous metal layer on the sample and PR. During the lift-off process the metal on top of the PR will then tear off or stay on the sample. The dashed line (− −) shows an area of incomplete lift-off, where the metal on top of the PR is still present after lift-off. The dash-dotted line (−·) shows metal deposited on the sidewall of the PR. Here, the metal has been torn off near the top of the resist, leaving an unwanted sloped metal layer (see fig. 5.9 for a cross section view) due to the low PR sidewall angle. The roughness of the metal is due to deposition on top of insulation on a dummy sample. **Right:** A good lift-off process, mainly due to straight PR sidewall profiles. See fig. 5.6 for photographs prior to and after the lift-off.

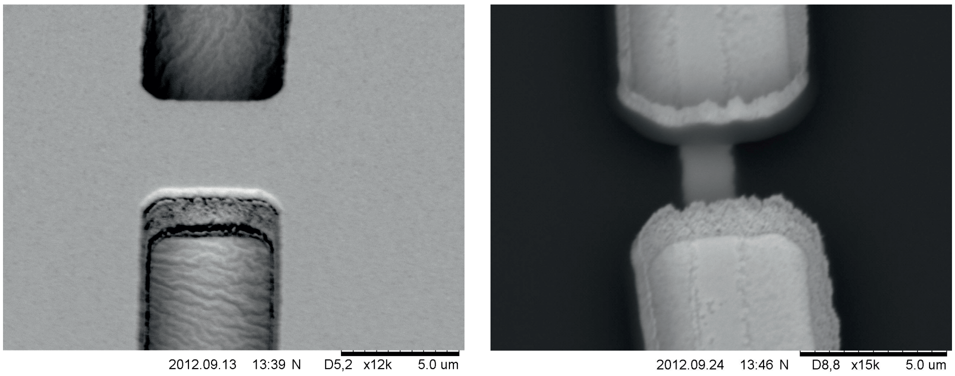

Figure 5.6: SEM photographs of a good lift-off profile. The photoresist thickness should be approximately 3 µm, and the metal layer, Ti/Pt/Au 50nm/25nm/775nm. On the left the sample still has the PR mask, while on the right the lift-off process has been completed.

5.4.2 Annealing

Annealing refers to the process of heat treatment. With regards to laser processing, it relates to the heat treatment of the sample and metal to improve the electrical properties of the contact metal(s). By depositing one or more metals, several issues with contacting can be overcome when combining metallization with an annealing process:

Removal of oxide layer Some metals will react with the native oxide of the semiconductor to provide an improved interface between the metal contact and the semiconductor material. A metal shown to provide good oxidation removal properties is Pd [127, 130–132], and it is therefore used in some metallization schemes.

Adhesion To make sure the contact does not fall off during use, e.g. due to wirebonding, an adhesive metal is often used. A very common example is Ti, but also Al and Cr are used. Adhesive metals are usually very reactive, and exposure to air must be avoided during the deposition process.[2]

Doping and alloying Some metals or semimetals will diffuse into the semiconductor and provide a high-doping region or alloy between the metal contact and the semiconductor device, improving its ohmic characteristics, e.g. Ge or In.

Diffusion barrier To prevent all metal layers from alloying with the semiconductor during the annealing process, a diffusion barrier metal is often used. This ensures that e.g. Au doesn't diffuse into your device [128] and short circuit it. Typically the diffusion barrier metal is Pt, which has a high melting temperature and low reactivity (noble).

Contact metal The top-most metal layer, referred to as the contact metal, should be easy to contact externally and preferably should not oxidise or otherwise break down. In III-V semiconductor devices, the metal used is almost exclusively Au, which doesn't react with the atmosphere. Furthermore, its softness makes it easy to contact by wirebonding using an Au wire.

In this work, a Jipelec Jetfirst 200 mm rapid thermal annealer was used for annealing the samples. It is capable of heating samples up to 1200°C at 50°C/s.

---

[2] A common feature of adhesive metals are that they will improve the vacuum in vacuum chambers, a feature that is sometimes exploited in high vacuum chambers, such as using a Ti sublimation pump in MBE chambers.

5.5 Lapping and cleaving

While thick wafers are important during processing for handling, it negatively affects the performance of the laser diode. By reducing the thickness of the sample, the electrical resistance from the backside metal contact to the diode and the thermal resistance can be reduced. The reduced thickness also makes it easier to cleave the lasers into their proper lengths from about 0.5 to 2 mm, which is in the same length scale as the substrate thickness of 0.5 mm for GaSb.

Lapping is a process where the sample is grinded using sand paper to thin it. The sample is usually mounted (laser structure down) on to a chuck with height adjustment so that the final thickness can be set.

The desired thickness is usually limited by the mechanical strength of the sample; if it is thinned too much, it will break during consequent handling, and a target thickness of 100–150 µm is common for GaSb.

After grinding and backside metallization, the laser devices are cleaved into their correct lengths. The ZB crystal break along the $\{110\}$ planes, making it possible to cleave samples with $\{100\}$ surfaces into squares with straight sidewalls, which is an important feature for defining the mirrors of the laser devices.

5.6 Contacting

In order to connect the device to an external circuit, it is necessary to connect wires to the top and bottom contact. The three most common approaches are probing, soldering and wirebonding.

Probing is achieved by placing thin metal probes onto the metal pads of the device by x-y-z manipulators. The tip radius of the probe usually ranges from 1 to 10 µm, providing a precise contacting of the device. The benefit of probing is that the probes can be quickly attached and detached from the devices, which can be beneficial for testing many devices. It can also deliver high currents due to the relatively large size of the probe, if large tip radiuses are used. The main drawback is that the setup is quite large.

Soldering is achieved by melting a metal, usually tin, onto the contact surface and inserting the wire into the melt. This technique requires a soldering iron, which has poor precision, and the size of the soldered contact is large, usually several hundred µm in diameter. The benefit of soldering is that it is cheap and easy to implement. However, the large size of the contact needed and the high temperatures (typically 200–300°C) used means that it is rarely used for laser fabrication.

Wirebonding is a technique where a wire is fused with the metal on top of the device and with an external circuit. Traditionally the wire and bonding pad are made of Au, but Al and Cu [133] can also be used. In wirebonding, the metal wire is fused to the contact metal using ultrasonic vibrations to achieve the bond [134]. For Au wires, temperatures around 100°C are used in conjunction with the ultrasonic vibrations to soften the material [134]. This technique can produce very small contacts, and is the most used for contacting semiconductor devices. In this work, a TPT HB05 Wedge and Ball Bonder was used for all wirebonding.

5.7 Characterization

For controlling the process, a few characterization techniques are used. The main purpose of these techniques is to control the resulting height and alignment of the different processes.

5.7.1 Microscope

Optical microscopy can be used to magnify the sample surface typically up to about 100 times, and it has a resolving power in the sub-µm range. It is mainly used to control and inspect the alignment of the photolithography process.

In this work, a Carl Zeiss AxoScope A1 was used for microscopy characterization, which has a magnification up to 100 times.

5.7.2 SEM

The scanning electron microscope (SEM) is a microscope where electrons are used instead of light to create an image of the sample surface. By using this technique, feature sizes of a few tens of nm can be investigated.

By cleaving the sample, the cross section profile of processed structures can be investigated, as shown in fig. 5.2. This information can be useful to determine the profile of the ridge waveguide. However, it is very difficult to continue processing cleaved laser structures, and these measurements are unsuitable for laser devices during the processing.

In this work, all SEM measurements were performed in either a Hitachi TM3000 Tabletop microscope, or a Hitachi S-5500 S(T)EM.

5.7.3 Profilometer

In a profilometer, height differences on the sample surface can be measured by using a small needle, which follows the sample surface profile. The profilometer needle tip radius is usually around 10 µm, and precise measurements of small features, such as laser ridges of about 2 µm, can be difficult. Usually, larger structures on the samples are used for determining e.g. etch depths, which must be included in the mask design.

In this work, all profilometer measurements were performed in a Veeco Dektak 150 with a 12.5 µm radius tip.

5.8 Processing results

In this section some of the main results from the laser processing are presented. The y-junction laser process recipe can also be found in appendix C.

5.8.1 Using ma-N 440 as insulation

To insulate the laser samples, both SiO_2 and a polymer, and only a polymer were tested. The options that were considered and tested were

SiO_2 A thin layer of SiO_2 deposited on top of the lasers after ridge etch will electrically isolate the lasers and hinder moisture and oxygen from reaching the laser material. However, due to the fact that no mask was available for the oxide etch, it was not straightforward to implement this solution.

SiO_2 and a polymer An alternative that would allow SiO_2 on the sample is to deposit it, and then spin on a polymer on top. An etch back process could be used to uncover only the top of the laser ridge, since a spin on process would create a flat surface, whereas a SiO_2 deposition would create a layer with the same topography as the lasers.

Polymer The third option would be to skip the SiO_2 layer and only use a polymer.

Due to the lack of masks for insulation lithography, spinning on a thick layer of polymer and performing an etchback in an RIE chamber was considered the best option.

Some of the important features considered were:

Thermal stability The sample will be exposed to temperatures up to 300-400°C (depending on the metallization scheme), and the insulation would have to be stable up to those temperatures, at least for a short period of time (a few minutes).

Chemical stability The sample will be exposed to solvents and acids related to the photolitography and metallization steps, such as acetone and hydrofluoric acid (HF). For lift-off, the samples are usually immersed in acetone for

30 minutes up to several hours. The insulation will have to withstand these processes without dissolving or otherwise deteriorating.

Mechanical stability The insulation will have to endure further processing and operation, including lapping, cleaving, contacting, and in some cases ultrasonic cleaning.

Based on available polymer materials suitable for insulation, mainly photoresists were considered. The photoresists SU-8, SPR-700 and ma-N 440 were tested. SU-8 was quickly rejected due to problems with adhesion and uniformity in the spin-deposition process. The other resists were spun on pieces of silicon and heated up for 5 minutes to about 370°C, as measured by an infrared (IR) thermometer. This was the highest achievable temperature on the hot plates in the lab. After the samples were removed, they were placed in a beaker with acetone for more than one hour to test the chemical stability. Neither ma-N 440 nor SPR-700 dissolved. The mechanical stability was then tested by scraping the resist with a pair of tweezers. It was found that only ma-N 440 did not flake off during this process, and it was chosen as the insulation for the lasers.

It was also found that exposing ma-N 440 in the mask aligner prior to heating it above about 150°C resulted in bubbling, making the resist unusable as an insulation layer. The EBR was therefore not performed using photolithographic exposure and develop process, but by covering the center of the sample with a piece of Si and etching the edge bead in the RIE.

For depositing the insulation layer on top of the laser structure, the resist was spun on to form a thick uniform layer, followed by an etchback process to uncover the top of the ridge. The resist surface was flat, and did not follow the etched ridge profile of the lasers. For the laser samples, the ma-N 440 was heated to about 200°C, which was found to be sufficient to make it insoluble in acetone. The etchback was performed in an RIE chamber, and different gas species were tested for best performance. The etches tested were pure O_2, O_2 and Ar, and O_2 and CF_4. The resulting data can be found in appendix D on page 151. It was found that introducing small amounts of CF_4 to the O_2 etch gave superior results with respect to surface roughness and uniform thickness over 1 mm, as measured by a profilometer [135]. This might be related to a combination of etching and passivation deposition by the CF_4 in the plasma [136], smoothing the surface.

One of the main drawbacks of the ma-N 440 insulation is poor adhesion to the top metal bonding pads. This makes it difficult to perform wirebonding to the devices, as the wire can pull off the whole bonding pad. One solution is to increase the metal thickness. However, this thickness is limited by the lift-off process and the price of Au.

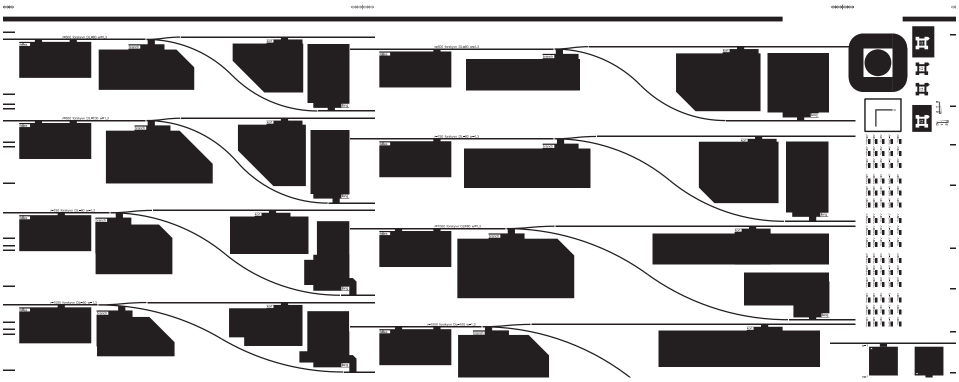

Figure 5.7: A part of the metallization mask for the Y-lasers designed by Erik Poppe and Arne Rønnekleiv for Erik Poppes PhD work [137]. The lasers lengths $L_c + L_s$ are 1.5 mm (left) and 2.0 mm (right) long, respectively. In the designed Y-lasers, the length differences ΔL range from 0 to 200 µm, the ridge widths w from 1.3 to 2.5 µm, the lengths $L_c + L_s$ from 1.0 to 2.0 mm, and the radius of curvature from 300 to 1000 µm, respectively.

5.8.2 Y-junction laser processing

Most of the clean room processes for the Y-junction lasers was developed in 2010 and 2011 on Si and GaSb dummy samples before it was used on laser samples. The process has been continuously evolving, and the last iteration of the recipe can be found in appendix C.

The Y-lasers were designed by Erik Poppe and Arne Rønnekleiv as a part of Erik Poppes PhD work [137], and a part of the metallization mask is shown in fig. 5.7. Here, the main processing results are given. A sketch of the cross section of a processed laser is shown in fig. 5.8.

Samples Sb 142 and Sb 145 were used for laser processing. Due to the limited availability of laser material, each quarter 2 inch sample was cut into three pieces. To account for unforeseen problems during the processing, two or three pieces were processed at a time. A sample consisting of only the upper cladding layer (sample Sb 122) was usually processed together with the laser material, to make sure that each process step was working, and to calibrate the etch time.

The lasers fabricated from sample Sb 142 did not work, most likely due to a curling of the ma-N 440 during Pt deposition (see fig. 5.9). Sb 145 produced functioning lasers. The grown structures of samples Sb 142 and Sb 145 were presented in section 4.3.

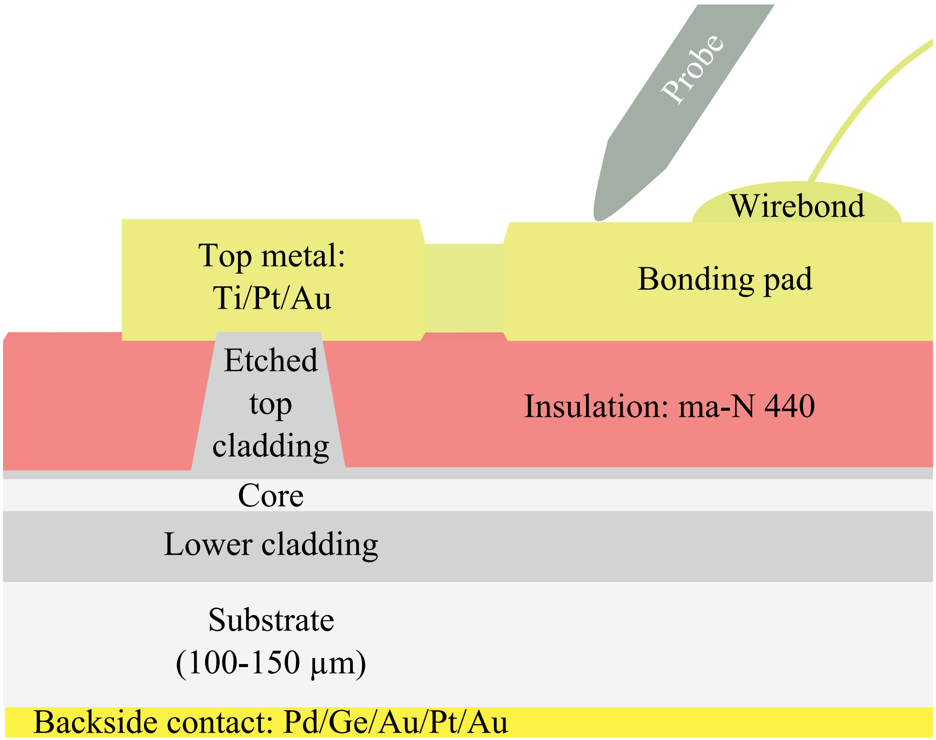

Figure 5.8: A sketch of the cross section of a processed laser. Here, the important parts of the processing can be seen. The process is documented in section 5.8.2, and the process steps can be found in appendix C.

Etching The lasers were etched either by a Cl_2/BCl_3 etch process developed by the company Integrated Optoelectronics for NTNU Nanolab (Sb 142), or a BCl_3/Ar etch process developed by Oxford Instruments [138] (Sb 145). The etch depth was chosen to be about 10% below the upper waveguide thickness; the total thickness of the upper cladding, grading and cap was 2.09 µm. The etch target was then 1.9 µm. This depth was chosen to allow for fluctuations in the etch rate so that etching of the core region could be avoided. The measured etch depths ranged from 1.9 to 2.1 µm.

Insulation For the electrical insulation, the ma-N 440 was used. The process is described in section 5.8.1. The etchback was considered complete when about 100 nm of the laser ridge was exposed.

Metallization For the laser diodes presented in this work, the p-type contacts were Ti/Pt/Au with a thickness of 50nm/25nm/775nm. The Pt thickness was reduced from 50 to 25 nm to avoid excessive heating of the insulation during deposition. The hot Pt during e-beam evaporation caused the insulation to contract for the first batch of lasers, where 50 nm Pt was used, see fig. 5.9.

For the n-type metallization, the recipe published by Vogt et al. [131] was used. The metallization scheme was Pd/Ge/Au/Pt/Au (8.7nm/56nm/23.3nm/47.6nm/250nm) followed by an anneal at 300°C for 45 seconds.

Lapping and cleaving The laser diodes were lapped to a thickness of about 150 µm. The thickness was not reduced further due to problems with cracking of the sample. After n-type metallization and annealing, the samples were then cleaved into laser bars of lengths 1, 1.5 and 2 mm.

Contacting The laser diodes were both wirebonded and probed, as shown in fig. 5.10. Due to the large amount of laser diodes (spectra measured for 20 devices), it was found beneficial to test the devices using probes, since a maximum of three lasers could be wirebonded at a time. Additionally, each laser could only be wirebonded one to two times due to damage to the bonding pad from the wirebonding process.

Investigation of the laser diodes

The laser diode test results are presented in chapter 6, and simulations related to the waveguiding properties of the lasers are presented in chapter 7.

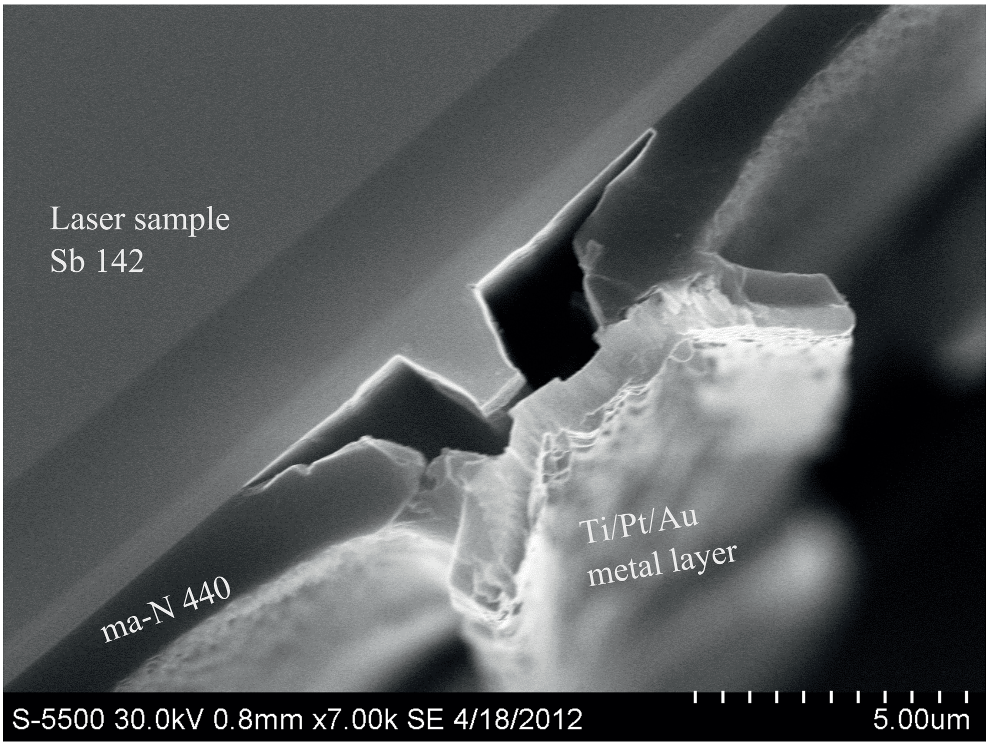

Figure 5.9: A cross section SEM photograph of sample Sb 142 after processing. Text has been added to the photograph to highlight the different materials. Here, the ma-N 440 insulation layer has curled next to the ridge, most likely due to the heat from depositing Pt in an electron beam evaporator. The curling results in poor or no contact between the deposited metal layers and the laser material. None of the lasers from this sample functioned.

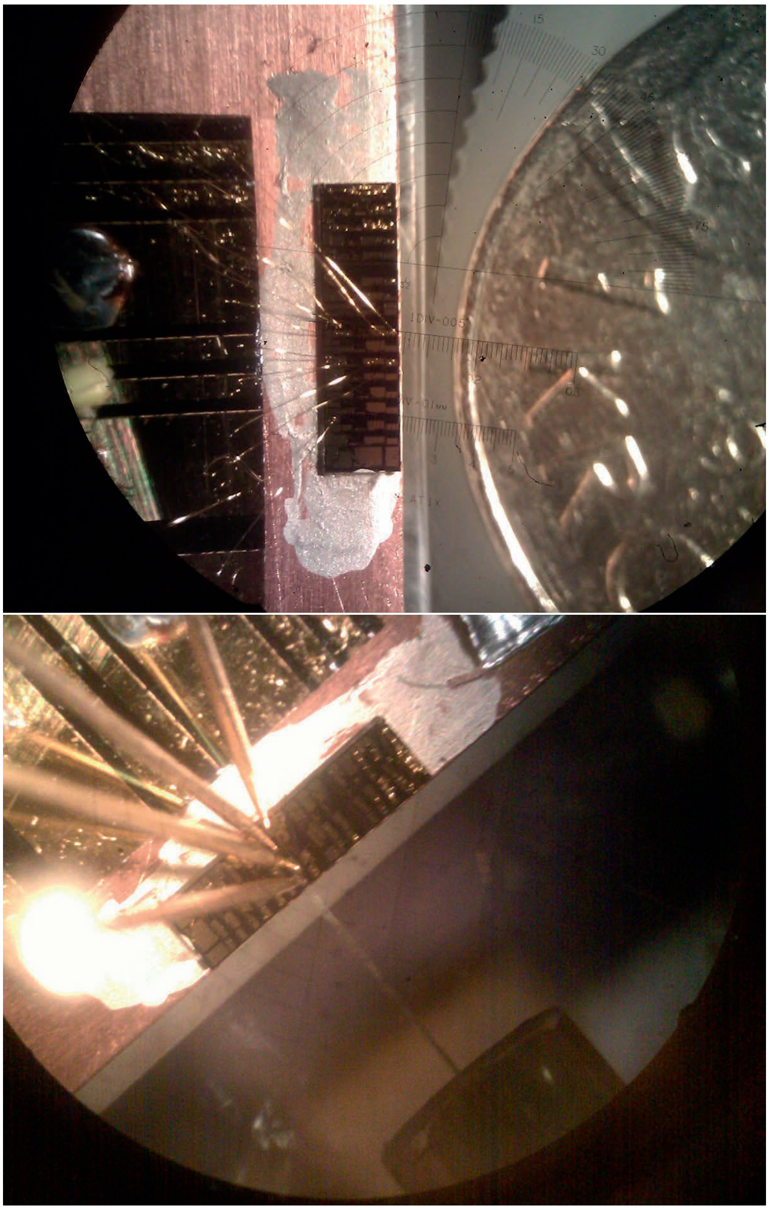

Figure 5.10: Photographs of lasers from sample Sb 145 that are ready for testing. The lasers are mounted onto a copper block, which acts both as a heatsink and connection for the backside contact. The lasers are 2 mm wide. **Top:** Photograph of wirebonded Y-lasers. A norwegian 1 Kroner coin is shown in the background (⌀ = 21 mm). **Bottom:** Photograph of fiber-coupled and probed Y-lasers.

The test results and simulations pointed to a poorly defined waveguide, and when the etch depth was control measured later, the etch depth was found to be only 1.4 µm [139]. This was much lower than the target of 1.9 µm.

This was unfortunately not uncovered during the processing. Due to the reactive nature of the AlGaAsSb cladding layer, the etch depth is quickly measured before the insulation layer is spun on.

Why the thickness measurement failed is uncertain, but contributing factors could be:

Profilometer The etch depth measurements were performed with a profilometer. A problem with the profilometer could result in wrongly determined etch depths, and later investigation in our group has shown that the etch depth measured by profilometer overestimated the etch depth of about 0.2-0.3 µm as compared to an SEM etch depth measurement [140]. Etch depth measurements using an SEM would be an option, but SEM measurements would have required cleaving the laser sample to get a cross section image. This would have been detrimental for further processing of the devices.

Loading effects of the plasma could result in higher etch rates close to the edge of the sample, where large structures (e.g. alignment marks or bonding pads) used to determine the etch depth are located. This could result in an overestimation of the etch depth of the lasers in the center of the sample. Loading effects near the ridge can result in "footing"; here, the etch rate next to the ridge is lower than far from the ridge, causing an over-estimated height of the etched ridge when measured by profilometer.

Leftover etch mask When removing the etch mask photoresist, a part of the resist can be hard to remove, due to a hardening from the etch process. If the resist on top of bonding pads and other large structures was not completely removed, it could lead to erroneous profilometer etch depth measurements.

BCl_3 flow For prolonged use, the BCl_3 flow could go down due to a condensation of the gas in the pipes. This could affect the etch rate of the process, but it would most likely have given an error in the etch software. It would also only affect the etch depth, and not the etch depth measurement.

It is clear that better control of the etch depth is needed to avoid this problem in the future. A suggestion for improved control is presented in "further work" in chapter 9.

Chapter 6

Testing of Laser Diodes

In this chapter the main test parameters are first presented, followed by the main test results from the laser measurements.

6.1 Important test parameters

There are many parameters which can be used to define the laser properties. In this section the parameters are explained together with the commonly used equipment to measure it.

Wavelength The wavelength, λ, of the laser is an important parameter for gas detection and optical communication applications. In gas detection it must match the wavelength of an absorption line of the gas to be measured, while in communication it must match the assigned wavelength of the channel used, to avoid cross-talk with other channels. The wavelength can be measured using a spectrometer such as an Fourier transform infrared (FTIR).

SMSR The side-mode suppression ratio (SMSR) expresses the spectral purity of the laser, and it is represented by the fraction of light in the dominating spectral mode relative to the second most intense mode, and is measured in dB. For gas detection a high SMSR of at least 20 dB should be used to obtain a high signal-to-noise ratio (SNR) in the measurements. The SMSR is measured by a spectrometer.

FWHM The full-width at half maximum (FWHM) is another important parameter for gas detection. The FWHM of the dominating mode should be smaller than the FWHM of the absorption line of gas to be measured. It is measured by a spectrometer such as an FTIR.

Intensity The laser intensity, usually measured in mW, is an important parameter for gas detection. For trace gas sensing, a single mode power intensity of more than 1 mW is desired [55]. The intensity should be constant while changing the wavelength for gas detection measurements, as any change in intensity due to the laser will reduce the gas sensing sensitivity of the system. For intensity measurements, a power meter such as a bolometer is often used. For trace gas detection, more sensitive semiconductor detectors are often used. These detectors should have a good SNR and fast response time [55, 56].

Gain The gain of the laser diode is a useful parameter to determine the internal losses, which affects the quality of the laser. Losses are usually associated with heating, which reduces the laser performance such as the intensity, threshold current density and the maximum operating temperature. Gain is usually determined from sub-threshold measurements using an FTIR.

I-V measurements are used to determine the electrical properties of the diode. These measurements can give information relating to the contacts, the p-n-junction and doping. A low voltage at the threshold current density suggests a good diode with good metal contacts, and is often desired. I-V measurements are usually measured by a multimeter.

L-I measurements are used to determine the light-current properties, such as the threshold current density j_{th}. These measurements can also be used to determine the maximum output power. By introducing the gas to be measured in the beam path between the laser diode and the power meter, L-I measurements can also be used to determine the current where the laser wavelength matches the gas absorption line [34].

Near- and far field measurements are useful for determining the beam profile and divergence of the beam. In most cases a collimated beam with a low NA is desired. Near- and far field measurements can also be used to estimate n_{eff}. It is usually measured by a camera, detector array, or by using a point detector and an aperture, which is moved across the laser beam.

6.2 Experimental setup

For nearly all experiments, the lasers were cleaved into laser bars and mounted using a colloidal silver glue on top of a copper plate[1], see fig. 5.10. The copper

---

[1] For some of the initial testing to see if the laser diodes worked, one of the laser bars was placed on a copper block with a layer of indium instead of colloidal silver glue. These measurements are,

plate was actively cooled using a thermoelectric cooler (TEC), or Peltier element, usually set to 16°C (thermistor resistance of 15 kΩ). The TEC was placed on top of a cooling ribbon designed for computer systems to provide efficient removal of the heat. The lasers were either wirebonded or probed for contacting the p-type contact (anode). The n-type contact (cathode) was contacted externally through the copper plate.

For I-V measurements, multimeters were used to measure the voltage difference between the anode and cathode, while the currents were read out for the laser diode current sources (Newport models 505 and 505B). For L-I measurements, a power meter was placed directly in front of the common facet of the lasers. The power meter was adjusted to 0 mA after the laser diode temperature was reached, as the TEC affected the reading of the power meter due to the change in temperature.

For spectral measurements, most measurements were performed by guiding the light from the laser to the FTIR using a multimode optical fibre. A few of the lasers were wirebonded. However, due to the large amount of lasers and a limitation of only bonding three lasers at a time in the current setup, it was not used extensively.

For large measurements series, such as the measurement data found in appendix E, an automatic measurement setup was implemented. The laser currents were controlled by a National Instruments NI 9263 Voltage source. The voltages were set on a computer using Labview, which was in turn controlled by the FTIR software Omnic for measuring the spectrum and selecting the next set of currents. The measurements were then analyzed using Matlab, where the important test parameters were extracted from each measurement and stored for efficient data processing. The measurement series were up to 1800 measurements, limited by the computer memory available for the analysis. The measurement series could take up to 22 hours.

6.3 Test results

6.3.1 I-V and L-I measurements

The I-V and L-I characteristics of a series of Y-junction laser diodes were tested. These measurements were performed to determine the quality of the diode, through the threshold voltage V_{th}, and the typical output powers of the laser diodes. For the measurements, a Labview program was used to incrementally increase the current in steps of 20 mA from 0 to 200 mA, while the voltages and optical output power were manually recorded from multimeters and a power meter, respectively. The

---

however, not included in the presented results.

same currents were used for all lasers, and no compensation for differences in ridge width w or length difference ΔL were performed. The main results are presented in table 6.1 and the metallization mask for the lasers is shown in fig. 6.1.

Table 6.1: The results of a series of I-V and L-I measurements of Y-junction lasers. The metallization mask for the lasers measured is shown in fig. 6.1, with explanation of the laser parameters. For these measurements, all sections were pumped with the same *current*, i.e. the current densities is not equal for all lasers. The resolution in the set currents were 20 mA to speed up measurements. The given threshold current I_{th} is per section, and must be multiplied by three for the total current. I_{max} is the current that resulted in the highest optical power, P_{max}, for these measurements. All measurements were performed at 16°C and the highest current per section used was 200 mA.

Laser No.	L mm	ΔL µm	r µm	w µm	I_{th} mA	V_{th} V	I_{max} mA	P_{max} mW
1	1.5	50	750	1.7	60	2.38	180	5.12
2	1.5	80	750	1.7	60	2.47	120	7.52
3	2.0	20	500	1.3	60	2.07	200	21.50
4	2.0	80	1000	2.0	100	2.66	200	3.26
5	2.0	80	750	1.5	60	2.94	200	9.65
6	2.0	100	1000	1.7	80	2.66	180	6.03
7	2.0	100	1000	2.0	60	2.37	200	8.55

The results show quite varying output powers and relatively high diode voltages. The high threshold current may be due to a low carrier concentration due to an error in the GaTe doping source in the MBE system. It is believed that the carrier concentration was probably close to $\simeq 2 \times 10^{17}\,\mathrm{cm}^{-3}$ instead of the target of $1 \times 10^{18}\,\mathrm{cm}^{-3}$, due to a poorly outgassed GaTe doping source in the MBE. The diode voltage at threshold was approximately 2.5 V, which is considered high. Voltages of 1–1.5 V have been measured for other (broad area) laser diodes in our lab.

For the output power, P_{max}, the mean power is 8.8 mW. For laser number 3 in table 6.1, the output power is more than twice the mean power. For this laser, the length difference between the two waveguides, ΔL is 20 µm, which is the lowest for all the lasers tested. From fig. 6.1, we can see that the bent part of the bent waveguide is much shorter for this laser than the other lasers, suggesting that the laser diodes have large bending losses in the waveguide. The bending losses will be treated in more detail in chapter 7 “Light propagation in waveguides”.

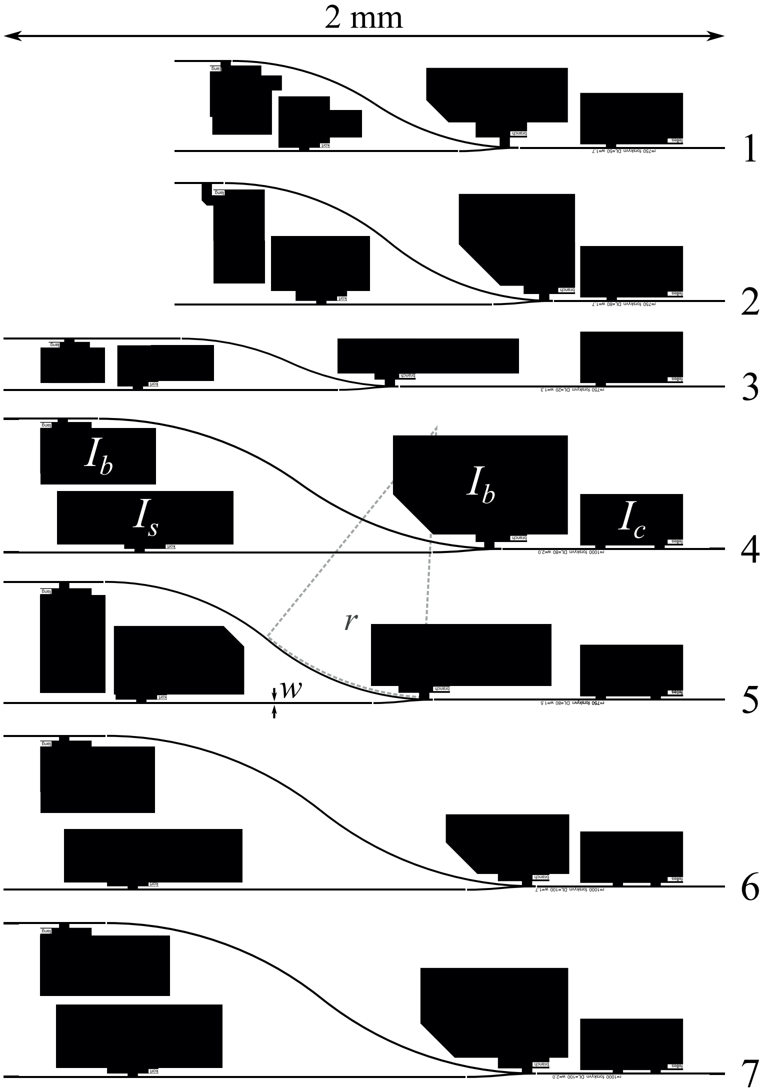

Figure 6.1: The metallization mask for the Y-junction lasers used for the I-V and L-I measurements. The optical measurements were performed on the common facet on the right. The numbers on the right correspond to the numbers in table 6.1. The three currents used, $I_{c,s,b}$, are shown on laser number 4, note that the two contacts marked I_b are connected to the same power source. ΔL is the length difference between the two waveguides, L is the distance between the two facets along the x-axis ($L_c + L_s$), and the radius r and the waveguide width w are illustrated on laser number 5.

Table 6.2: Optical power measurement results from curved FPLs, pumped with a pulsed current of 490 mA at 10 kHz, using a duty cycle of 20%. The laser waveguides are shown in fig. 6.2. The measured optical power suggest that only lasers 7 and 8 achieved lasing. The power of laser 7 deteriorated quickly from 0.4 to 0.1 mW, suggesting damage of the laser cavity as a result of the large current.

Laser No.	ΔL µm	r µm	w µm	Power mW
1	20	1000	1.5	0.01
2	80	750	1.5	0.01
3	50	750	1.5	0.01
4	200	500	1.5	0.01
5	100	500	1.5	0.02
6	80	500	1.5	0
7	100	300	1.5	0.4, 0.1
8	80	300	1.5	1.05

Testing of curved FPL The optical output power of eight curved FPL were measured, see fig. 6.2 for the shape of the waveguides. The width of the laser bar was 1.5 mm. Current densities for which the straight FPL and Y-junction lasers lased, typically 1.6–1.8 kA/cm^2 and 3–4 kA/cm^2, respectively, did not result in lasing for the curved FPL. The lasers were then tested with a pulsed current of 490 mA at 10 kHz, using a duty cycle of 20%. The results are shown in table 6.2.

The results suggest that the bending losses are large, which is consistent with the L-I-measurements of the Y-junction lasers. The FPL with the longest straight sections are the only ones that achieve lasing, suggesting that the gain in the straight sections are large enough to achieve lasing between the cleaved facets of the laser bar.

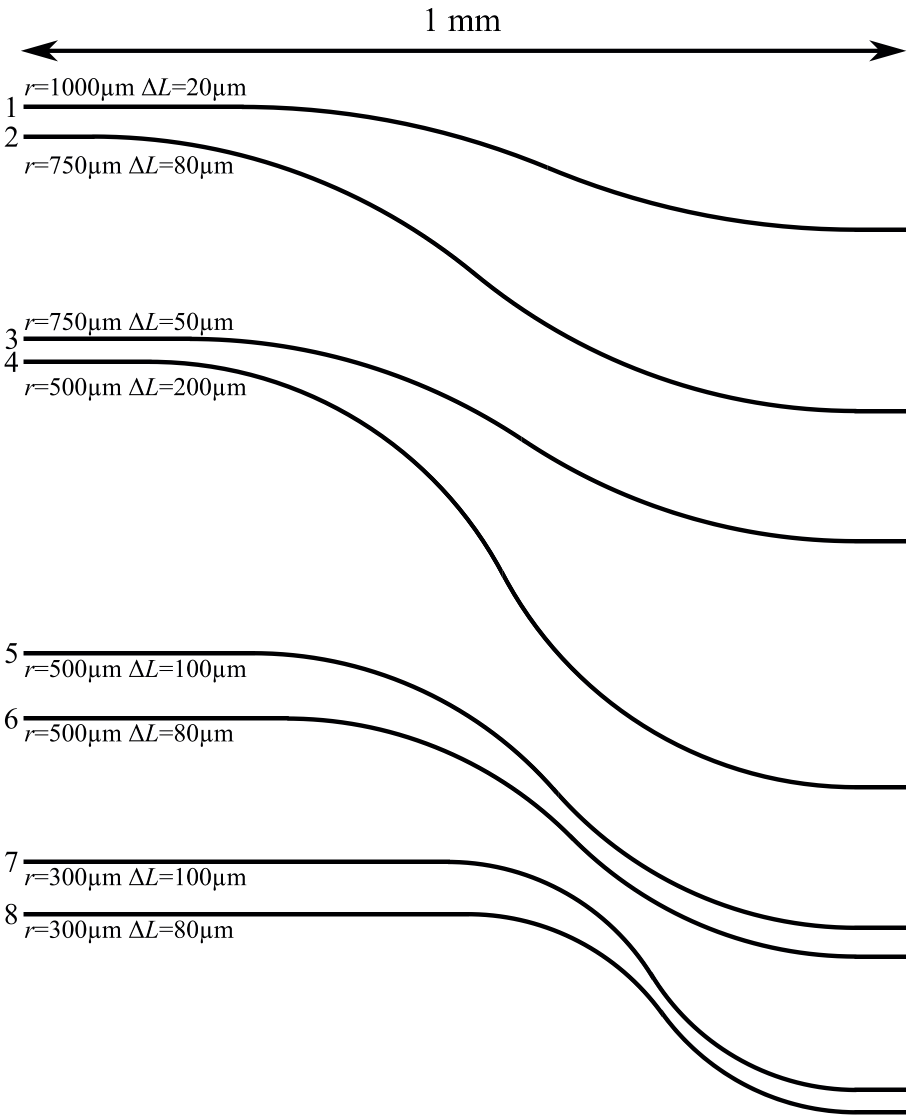

Figure 6.2: Waveguides for the bend FPL extracted from the photolithographic etch mask. The test results for these structures are shown in table 6.2, and the laser number is shown on the left of each waveguide. All intensity measurements were performed at the facet on the right. The total length of each laser is 1 mm plus the given length ΔL for each laser.

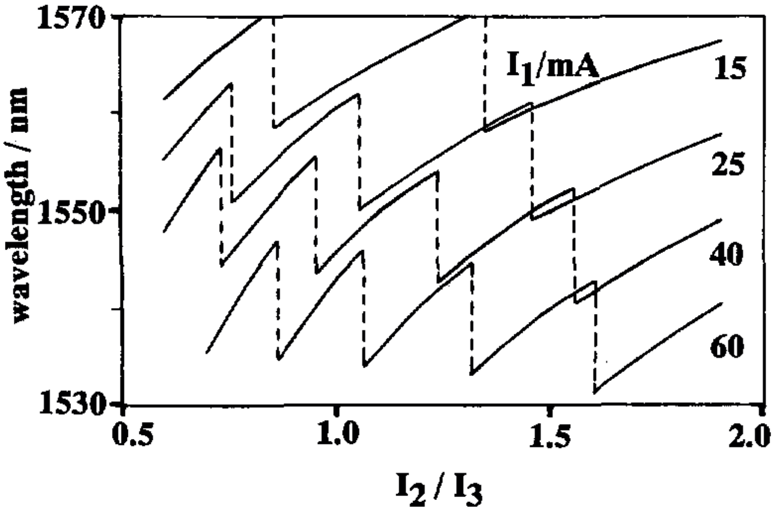

Figure 6.3: The expected tuning spectra of a Y-junction laser according to Fig. 3 b) in Dutting et al. [141] (© 1994 IEEE), where I_1 is for the common section current I_c, I_2 is for the straight section current I_s and I_3 is for the bent waveguide current I_b. The tuning width is then determined by $\Delta\lambda_Y$, see eq. (2.28).

6.3.2 Wavelength

All wavelength characterization was performed with an FTIR. The main focus of the measurements was to determine the tunability of the Y-junction lasers.

According to Dutting et al. [141], a sawtooth pattern should be observed when tuning the Y-junction laser by changing the current of either the straight or bent waveguide, as shown in fig. 6.3. To test the tuning spectra of the manufactured laser diodes, an automated setup was used to test several combinations of the tuning currents successively. A multimode optical fiber was used between the FTIR and the probe setup for the lasers to measure the laser spectra. The peak wavelength λ_{peak} for each measurement was then determined. A representative excerpt of the peak wavelengths as a function of the fraction I_s/I_b are shown in fig. 6.4.

Tuning of the Y-junction lasers using the current schemes published by Dutting et al. [141] were unsuccessful for these lasers. Any change in the wavelength due to tuning of the bent waveguide was minimal, further suggesting a large optical loss in the bent waveguide. From the results presented in appendix E and fig. 6.4, it is likely that the dominant tuning mechanism is heat, since an increase in total current increases the wavelength. It is likely that the FCPE (see section 2.2.1) tuning mechanism was saturated before the lasers reached threshold, due to the

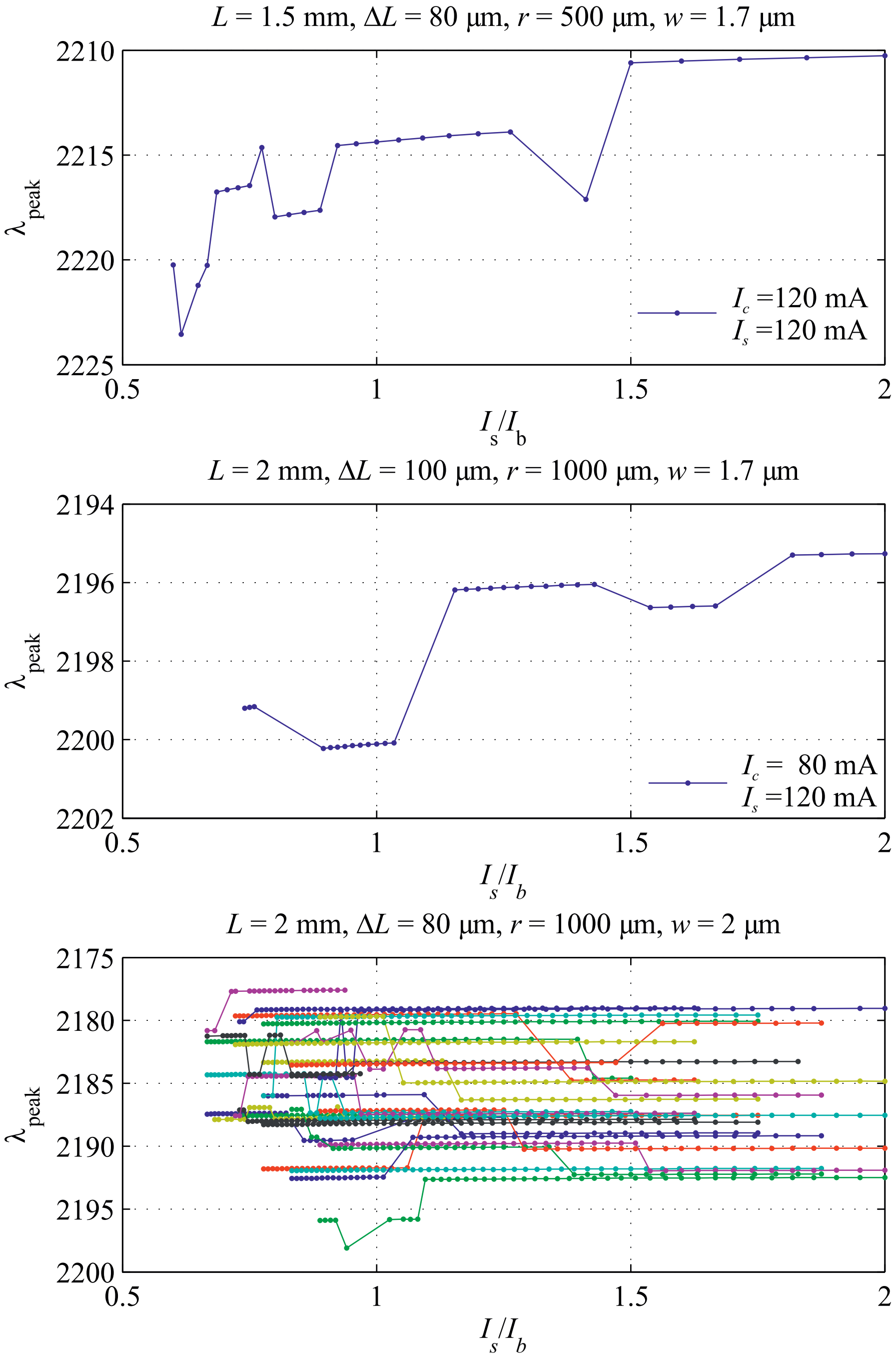

Figure 6.4: Measurements of three Y-junction lasers using the tuning scheme from Dutting et al. [141]. The laser parameters are shown above each plot. The legend shows currents I_c and I_s for the measurements. In the bottom plot, I_c and I_s were varied from 110 to 160 mA and from 120 to 160 mA, respectively.

high threshold current densities (>3kA/cm^2).

6.4 Gain measurements

The sub-threshold spectra were measured for several lasers to determine the gain curve and interferometric oscillations in the spectrum. It was found that the multimode fiber positioning manipulated the spectrum, see fig. 6.5. Due to this extra interference in the spectrum, the gain properties of the laser would have been hard to determine. A subthreshold measurement of a wirebonded Y-laser is shown in fig. 6.6. It can be seen that the gain curve here has a shape close to the expected Gaussian shape. These results indicate that multimode fibers should not be used for testing laser diodes. This may be due to interference in the fiber, and/or reflections between the laser and the fiber.

6.5 Near field and far field measurements

The near-fields and far-fields of the laser diodes were measured for straight FPL. These measurements were performed to determine the NA by measuring the beam divergence.

Near field The near field measurements were performed using a setup sketched in fig. 6.7. A aspherical lens with a focal length f_1 of 4 mm and an NA of 0.56 was placed directly in front of the laser, while a spherical lens with a focal length f_2 of 450 mm was placed between the aspherical lens and the camera. The near fields were only measured for a few straight 1 mm long FPLs, and little variations were found between lasers with different ridge widths w. To avoid damaging the camera, currents close to the treshold current of about 50 mA ($\simeq$ 2.5 kA/cm^2) were used. A measurement of a FPL with a magnification $m = 112.5$ is shown in fig. 6.8. The large in-plane FWHM of the near field suggests poor waveguiding, since the waveguide is designed to be about 2 µm wide. Modelling of the optical field distribution and the resulting far fields due to different etch depths can be found in appendix F. A low expected doping of the n-type cladding or shallow etch depth can both help to increase the width of the pumped area due to electrical spreading from the high resistivity and a poorly defined waveguide, respectively.

Far field Measurements of the far field of 12 straight 1 mm long FPLs were also performed to determine the mode profile of the laser beam. However, the far field measurements resulted in a ring pattern, shown in fig. 6.9 b). It was found that

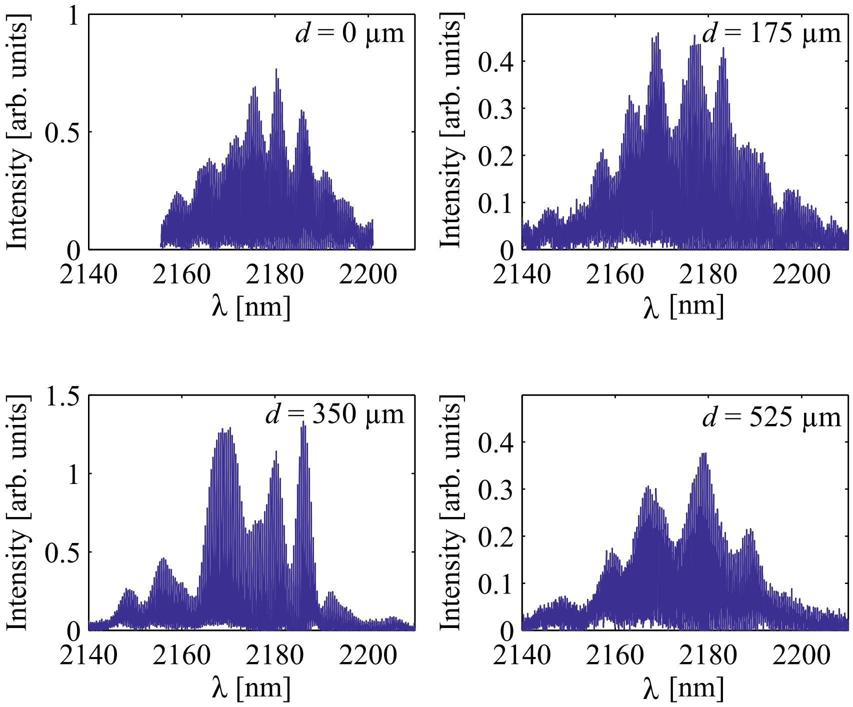

Figure 6.5: Sub-threshold measurements of a laser diode through a multimode fiber (butt coupled) for different spacings, *d*, between the fiber and the laser facet. All other parameters were kept the same. The distances between the fiber and the laser were determined from microscope photographs using a computer and a digital ruler.

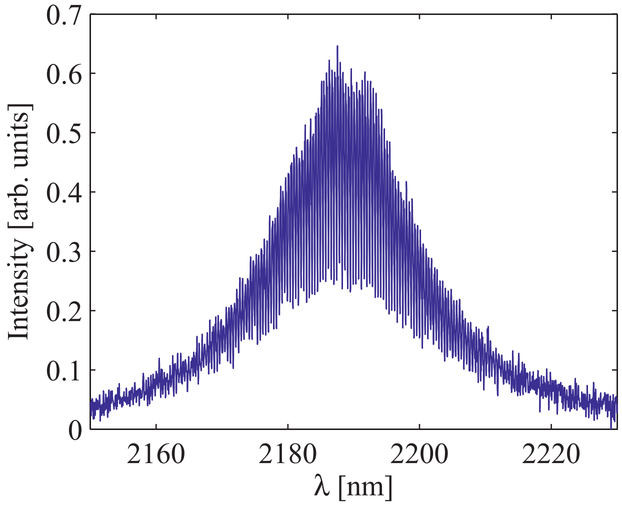

Figure 6.6: Sub-threshold measurements of a Y-junction laser diode measured directly into the FTIR. The sample was wirebonded and placed in the focal point of the FTIR measuring stage.

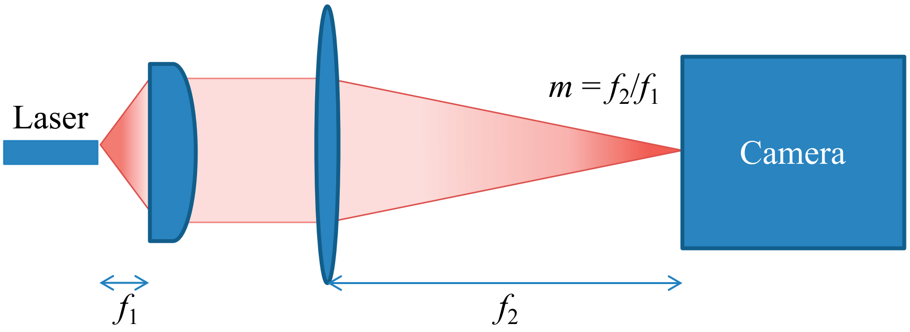

Figure 6.7: Near field measurement setup. The setup was designed according to the setup used by Kinzer et al. [142], referred to as a Gaussian telescope. f_1 and f_2 are the focal lengths of the lenses, and $m = f_2/f_1$ is the magnification of the system.

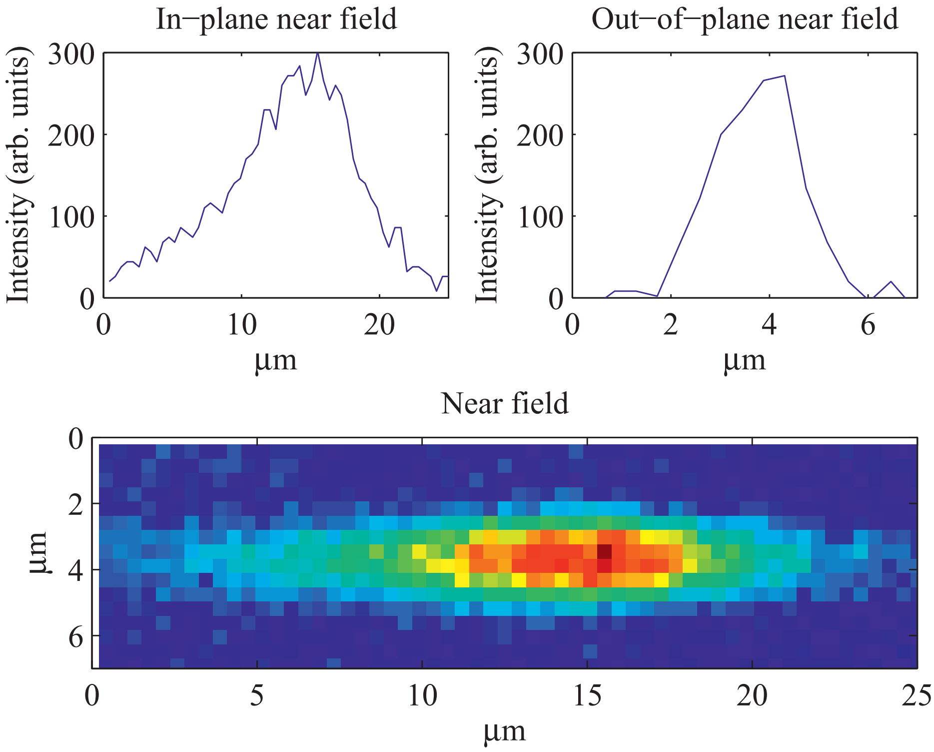

Figure 6.8: Near field measurements of an FPL. The FWHM of the light is about 8 µm in-plane (horisontally) and about 1.8 µm out-of-plane (vertically). The lenses used were an aspherical lens with focal length $f_1 = 4$ mm and a lens with $f_2 = 450$ mm, resulting in a magnification of $m = 112.5$.

this pattern was most likely due to interference inside the camera, caused by an unwanted Fabry-Perot etalon.

The best fits to the far field angular distribution along the narrow axis found an FWHM of about 8–10°, independent of the etched ridge width w. From the simulations shown in appendix F, this suggests a low effective refractive index contrast most likely due to a too shallow etch.

6.6 Other measured parameters

The parameters SMSR, FWHM, $n_{g,\mathrm{eff}}$ and λ were extracted from each spectrum. The measured FWHM of the laser mode during lasing was approximately 0.036–0.040 nm for most of the measurements. This value is most likely limited by the FTIR instrument, which has a specified spectral resolution of about 0.034 nm at 2.2 µm wavelength. The extracted effective group index, $n_{g,\mathrm{eff}}$, from the sub-threshold spectrum mode spacing resulted in a value of about 3.75–3.85 with small variations between different laser diodes and a small increase with increasing current. The measured wavelengths ranged from 2.17 to 2.28 µm, where most of the lasing was observed around 2.20 µm. The SMSR ranged from 0 to 25 dB. For measurements where the SMSR was higher than 10 dB, the most common values were close to 12 dB and 20 dB for reasons unknown to the reader. For FPL, the SMSR is at most of the order 20 dB [46], and it is likely that these values are due to optimum SMSR in the straight waveguide. The effect of a straight waveguide with a 50% loss due to a nonfunctional Y-junction on the SMSR has not been investigated, but could provide insight into these common values.

The measured SMSR and wavelength for several laser diodes can be found in appendix E.

6.7 The lack of interferometric tuning

To explain the tuning behaviour of the lasers, which is inconsistent with the expected tuning performance of an interferometric laser structure, a series of simulations were performed. The main goal of these simulations was to determine the effect of waveguide roughness and etch depth from the laser processing on the waveguiding properties of the laser. These simulations and simulation results are presented in chapter 7.

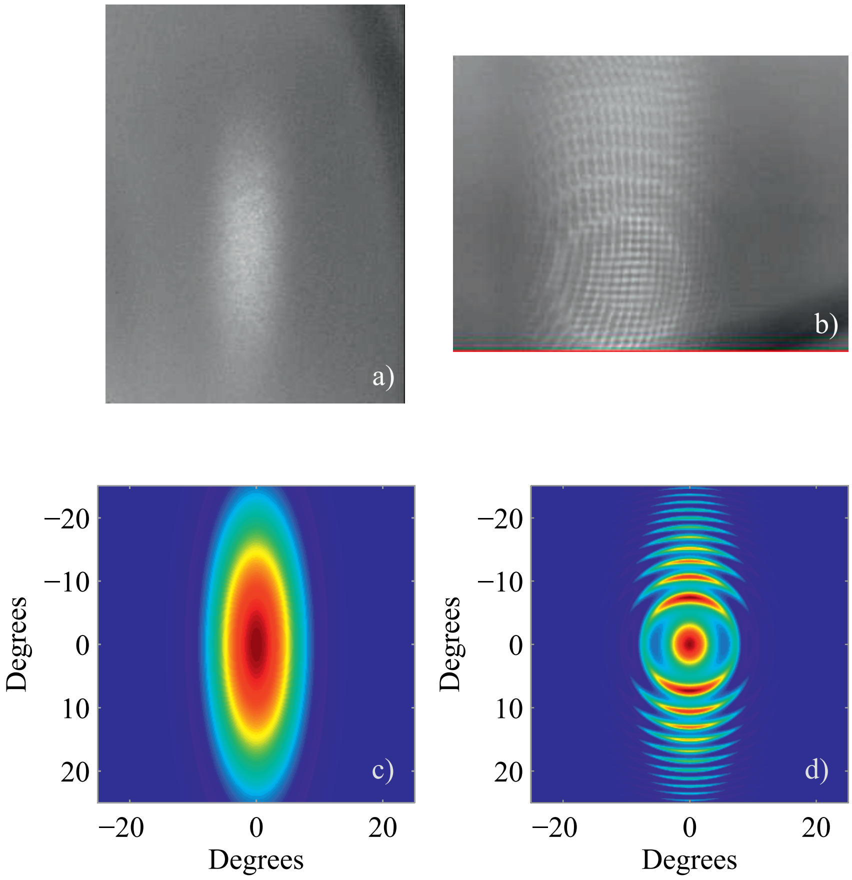

Figure 6.9: Far field measurements. a) Measurements of the far field by scattering the laser light on rough Si surface and imaging the Si surface. b) Measurement of the far field by placing the camera directly in front of the laser without any lenses. c) A 2D gaussian intensity profile as a function of angle. d) The intensity profile depicted in c) after taking the transmission through a Fabry-Perot etalon of optical thickness $nL = 120$ μm in account, using eq. (2.23) with $L \to L/\cos(\theta')$ (θ' is the angle of the light ray, see section 2.1.2).

Chapter 7

Light propagation in waveguides

In this chapter a short introduction to the methods used for laser waveguide simulations and determination are described, followed by the simulation results. Note that all simulations performed have only used the real refractive index, and the effect of gain and absorption have not been accounted for.

In fig. A.3, Gonzalez-Cuevas et al. [84] was used as a reference for the refractive index data. The refractive index for $\mathrm{Al_{0.9}Ga_{0.1}As_{0.06}Sb_{0.94}}$ from this data suggest that it is 3.408. However, other older sources, e.g. Adachi, Alibert et al. [143, 144], suggest that it should be around 3.25. For VCSELs, AlAsSb layers lattice matched to GaSb are commonly used, and refractive indices close to 3.1–3.2 have been used for the AlGaSb layer in several publications [20, 145, 146]. This suggests that a refractive index of 3.408 is a bit high for $\mathrm{Al_{0.9}Ga_{0.1}As_{0.06}Sb_{0.94}}$. This discrepancy in the refractive index data was not initially identified, and some of the older computations in this work have used 3.408, while newer computations have used 3.25. For all other layers, Gonzalez-Cuevas et al. [84] has been used as a reference for the refractive index data.

7.1 Mode solver

To determine the allowed transverse optical modes in the lasers, the field in each layer of the waveguide is calculated. This approach is based on ref. [46, App. B]. For the TE modes, the appropriate boundary conditions are that the electric field propagating in the z-direction, $E_y = E(x)\exp(-j\beta z)$, must be continuous at each interface. $E(x)$ is given by eq. (2.8). A TE mode has magnetic components in the x- and z-directions. See fig. 7.1 for a description of the structure and axes. The appropriate boundary conditions are then

$$E_{i+1}(x_{i+1}) = E_i(x_{i+1}), \tag{7.1}$$

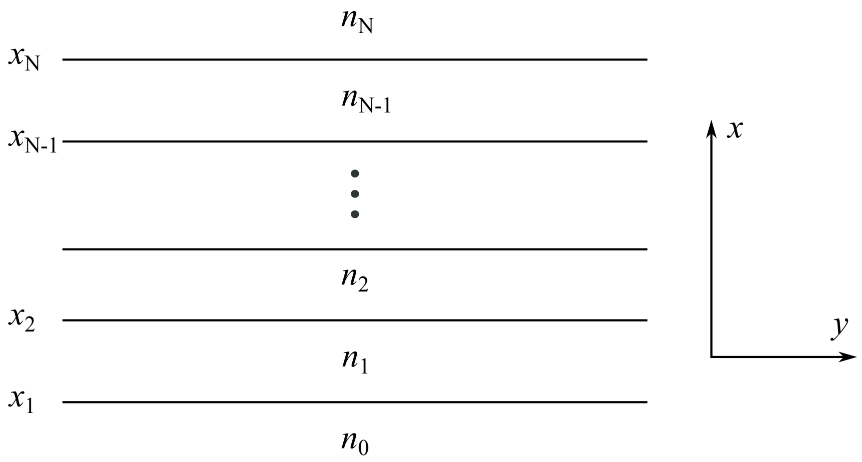

Figure 7.1: Illustration of the slab waveguide interfaces used in eqs. (7.1) and (7.2). The refractive index varies along the x-axis, while the electric field is along the y axis for TE modes. The propagation is along the z-axis.

and that transverse magnetic field H_z must be continuous, leading to [46] [1]

$$\left.\frac{\mathrm{d}E_{i+1}}{\mathrm{d}x}\right|_{x=x_{i+1}} = \left.\frac{\mathrm{d}E_i}{\mathrm{d}x}\right|_{x=x_{i+1}} \tag{7.2}$$

Furthermore, for a bound mode, the field must vanish when $x \rightarrow \pm\infty$, so that $B_0 = 0$ and $A_N = 0$, where N is the last layer. By setting $A_0 = 1$ and $B_0 = 0$ and changing the wavenumber β, the solutions are found from the values of β which result in $A_N = 0$. The full procedure can be found in ref. [46, App. B].

This method results in quick solutions for the distribution of $E(x)$, the effective refractive index n_{eff} and the number of allowed modes when iteration of the input parameters are desired, i.e. parametrization of the layer refractive indices and/or thicknesses. The solution for slab waveguides of varying core thicknesses using these equations can be found in appendix B. These solutions suggest that the core thickness for single TE mode operation can be up to about 0.7 µm thick, and that increasing the core size reduces the necessary required cladding thickness.

For more detailed simulations the website Lights has been used, which contains both a 1D and 2D mode solver[2] and more outputs, such as the far field. Lights can be found at `http://www.nano-fab.com/lights`.

---

[1] The solutions to these equations were also investigated in section 2.1.2 on page 12

[2] Note that Lights also includes a 2D and 3D beam propagation method (BPM) solver. However, it was unavailable at the time BPM simulations were needed.

7.2 Light propagation in Y-junction waveguides

To determine the waveguiding properties of a waveguide, the beam propagation method (BPM) is a very popular technique. In BPM, the propagation of an optical field through a weakly guiding structure can be simulated. It is a requirement for this technique to be used that the refractive index contrast, dn, inside and outside the waveguide is small. A quick introduction to the method can be found from e.g. Loui [147].

For all simulations used in this thesis, the fast Fourier transform (FFT)-BPM Matlab script made by Codina [148] was used. The background refractive index was set to 3.77, and the waveguide refractive index was set to 3.77+dn, where dn $= 0.01, 0.02, 0.03, 0.04, 0.05$. The reason the refractive indices were set so high is based on measurements of the effective group index from sub-threshold measurements, and should in retrospect have been set much lower, in the 3.3-3.5 range. However, the refractive index contrast, dn, is the most important parameter, and the differences in refractive indices are approximately $1-(3.6/3.8) \simeq 5\%$ so the conclusions should still be valid. The resolution was set to 0.12 x 0.12 µm, restricted by available memory. The simulations typically took from a few minutes to more than 30 minutes each, depending on the size of the waveguide.

The main goal of the simulations was to determine why the bent waveguide was not working. The main theories to be tested were; *1)* is the waveguide roughness due to the cleanroom process, such as roughness in the mask, in the PR and/or the ICP-RIE process, responsible for the insufficient waveguiding?, or *2)* is it due to an insufficient refractive index contrast?, or could it be due to something else? To investigate these hypothesis, a series of 2D BPM simulations were performed. The parameters used are shown in table 7.1. The totalt length of the laser was not simulated in all cases, instead the common section was chosen to be 200 µm to stabilize the input gaussian beam, followed by the required length to simulate the bent section. An excerpt of the simulations is shown in fig. 7.2.

When radiation exits the simulation window on the left or on the right, the radiation re-enters on the opposite side, as shown in fig. 7.2. This is due to the periodic nature of the Fourier basis functions [149], and it is usually overcome by using boundary conditions such as perfectly matched layers [149, 150] or absorbing boundaries [147]. In Codina [148]'s Matlab script, this was not implemented, and the problem was overcome by using a wider simulation window, so that the re-entered radiation did not interfere with the waveguides.

7.2.1 The effects of design parameters on the waveguiding

In figs. 7.3 to 7.5, the light guided through the bent waveguide (see fig. 2.7 on page 22) of the Y-junction waveguides is shown. The amount of guided light is

Table 7.1: Simulation parameters for BPM simulations of the waveguiding properties of the Y-laser design. The length L, length difference ΔL, radius of curvature r and width w refers to the ridge waveguide and were defined in fig. 6.1 on page 79. dn refers to the refractive index contrast between the ridge and outside the ridge, $\mathrm{dn} = n_{\mathrm{ridge}} - n_{\mathrm{outside\ ridge}}$. The roughness refers to the width of the area on the sides of the waveguide where the refractive index is somewhere between $n_{\mathrm{outside\ ridge}}$ and n_{ridge}. Note that in fig. 7.4, the roughness 0.2 µm was used, while in fig. 7.5 0.25 µm was used. The roughness in these simulations is randomly distributed, and the roughness width is divided, so that half of the width is on each side of the waveguide.

Parameter	Figure 7.3	Figure 7.4	Figure 7.5
w (µm)	1.3, 1.5, 1.7, 2, 2.5		2
L (mm)	0.8, 1.2, 1.6	1, 1.5, 2	-
Roughness (µm)	0	0, 0.05, 0.1, 0.2/0.25, 0.5, 1	
dn (10^{-2})	4	4	1, 2, 3, 4, 5
	Common parameters		
ΔL (µm)	0, 20, 50, 80, 100		
r (µm)	300, 500, 750, 1000		

presented as a function of two simulation parameters, and all permutations of the parameters have been displayed in a series of sub-plots; each data point in a plot represents the average of the bent waveguide light intensity in the simulations for that condition. For example, the plot ΔL vs r in fig. 7.5; here, each datapoint is averaged over all roughnesses and refractive index contrasts dn (see table 7.1). Based on individual inspection of the simulations, this averaging did not alter any of the observed trends presented in figs. 7.3 to 7.5.

Figure 7.2 shows a few of the simulations. Here, an electric field with a Gaussian profile was placed at the entrance of the common section, where the propagation was simulated. The length of the common section was 200 µm, to stabilize the mode profile before the Y-junction. The electric field was then propagated through the two arms of the waveguide. The numerical value for the maximum intensity at each waveguide exit, i.e. from the straight and bent waveguides, respectively, was extracted from each simulation. For simplicity in the Matlab code, the highest intensity for $x < 0$ µm was chosen as the intensity at the exit of the bent waveguide, see explanation in fig. 7.2. For cases where the bent waveguide did not provide sufficient waveguiding, this value could be determined outside the waveguide exit. Especially for a dn of 0.01, a poor waveguiding results in a discrepancy in the chosen intensity, as shown in fig. 7.6. This is observed in fig. 7.5, that a dn of

0.01 seemingly provides better waveguiding than 0.02. For fig. 7.5, 7 simulations out of 600 are missing. However, analysis of the simulation data suggest that the observed trends for the waveguiding properties are not impacted.

In figs. 7.4 and 7.5 the roughness was simulated for 0, 0.05, 0.1, 0.2, 0.5 and 1 µm, where half the roughness was on each side of the waveguide. However, as stated earlier, the simulation resolution was set to 0.12 x 0.12 µm, suggesting that any roughness below this size would not be noticeable. This may explain the little change in fig. 7.4 for roughnesses below 0.12 µm. For roughnesses below 0.24 µm, the roughness may have only been introduced on one side of the waveguide, due to the resolution constraints.

In fig. 7.4, the plot of w versus r shows best waveguiding for 2 µm instead of 2.5 µm. This may be due to a change from single-mode to multi-mode behavior of the waveguide. For symmetric slab waveguides, the limit for single-mode operation is given by [46]

$$w < \frac{\lambda}{2\sqrt{n_{\text{core}}^2 - n_{\text{clad}}^2}}, \tag{7.3}$$

where w is the core width, in our case the ridge width. Using the simulation parameters used for fig. 7.4 of $\lambda = 2.2$ µm, $n_{\text{core}} = 3.81$ and $n_{\text{clad}} = 3.77$, we get a single mode behavior for $w < 2.0$ µm. Using $n_{\text{core}} = 3.40$ and $n_{\text{clad}} = 3.36$, which are closer to the expected effective refractive indices expected inside and outside the ridge (based on table B.3), respectively, the core width for single mode operation increases to $w = 2.12$ µm. It is therefore likely that the increased loss with increasing w is due to a multi-mode curved waveguide.

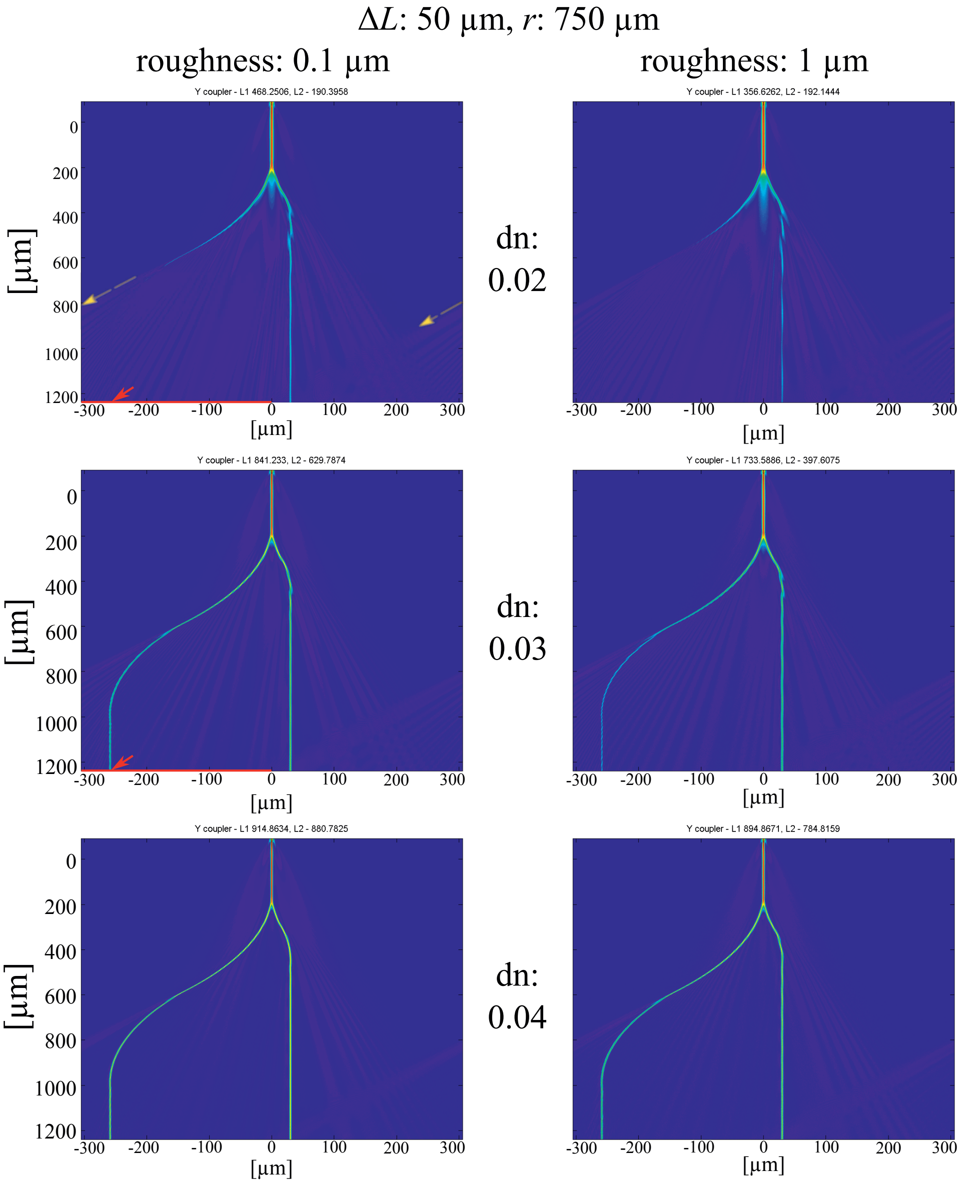

Figure 7.2: 2D BPM simulations of a laser with $\Delta L = 50$ µm, $r = 750$ µm, $w = 2$ µm, etch roughness of 0.1 µm (left) and 1 µm (right). From top to bottom the refractive index contrast dn is 0.02, 0.03 and 0.04, respectively. Note that the aspect ratio in the figures are not correct, they have been compressed along the y-axis. The dashed yellow arrows are a guide to the eye for highlighting the problem with radiation re-entering the simulation on the opposite side. Here, the radiation leaves on the left, and re-enters on the right. The red line illustrates where the intensity of the bent waveguide is extracted from; for simplicity, the highest intensity for $x < 0$ µm was extracted from each simulation, which coincide with the end of the bent waveguide (red arrow) in cases of proper waveguiding.

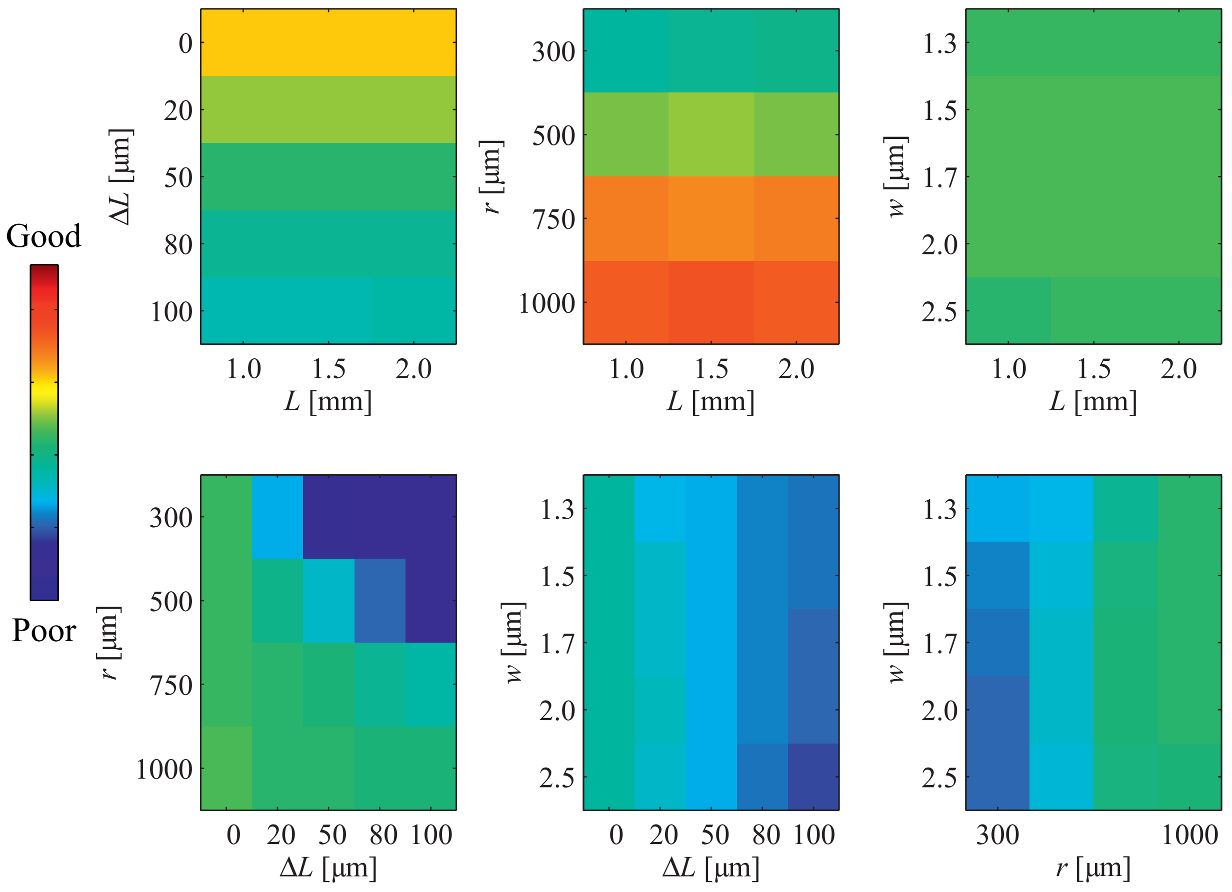

Figure 7.3: The results of 300 BPM simulations of Y-junction lasers with different L, w, ΔL and r (see fig. 6.1 for explanantion of the parameters). In each sub-plot the light guided through the bent waveguide is shown for different combinations of the simulation parameters. Red indicates good waveguiding, where most of the light is guided in the curved waveguide. Blue indicates poor waveguiding, where most of the light has leaked out of the waveguide.

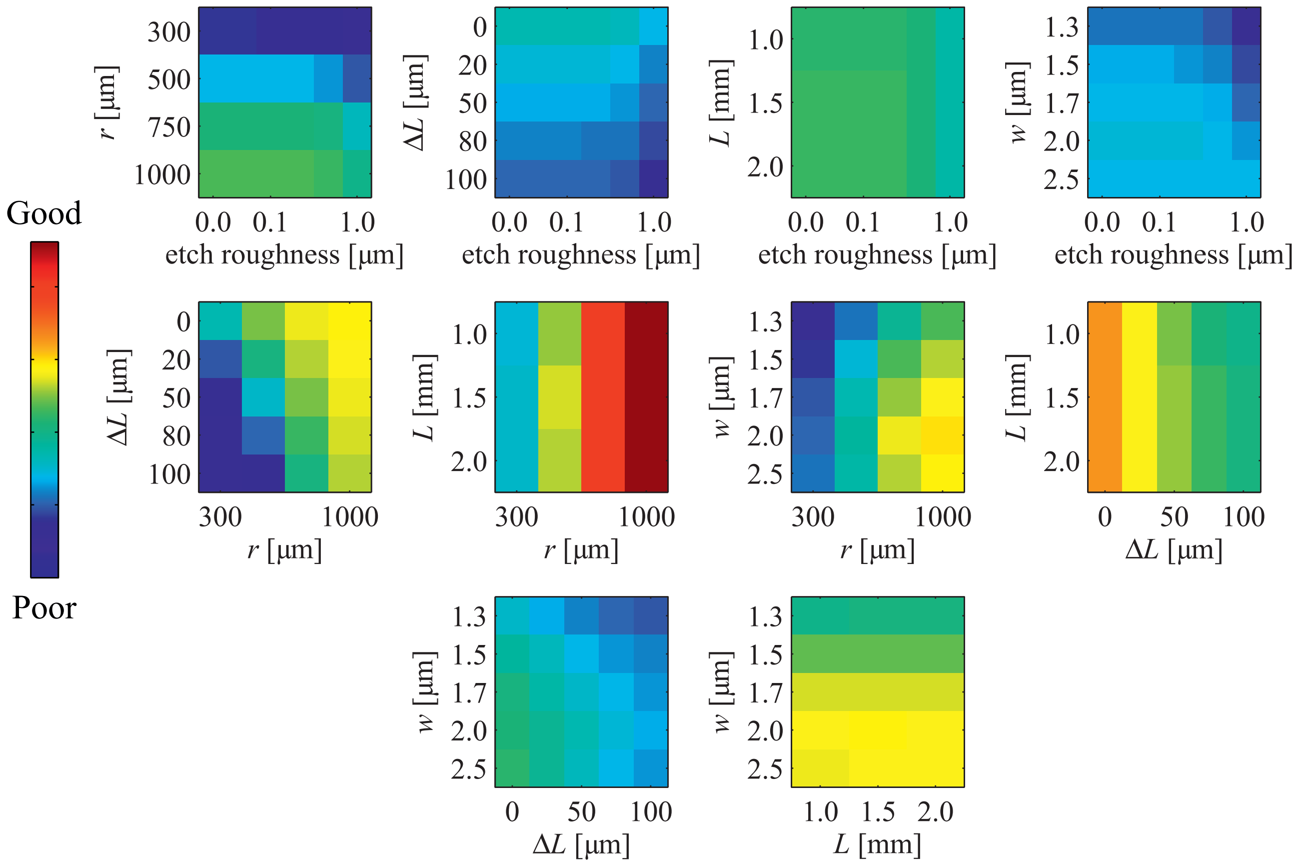

Figure 7.4: The results of 1800 BPM simulations of Y-junction lasers with different L, w, ΔL, r and etch roughness. The etch roughness is the total width which have a random refractive index (between n and n+dn), where half of the roughness width is on each side of the waveguide. In each sub-plot, the light guided through the bent waveguide is shown for different combinations of the simulation parameters. Red indicates good waveguiding, where most of the light is guided in the curved waveguide. Blue indicates poor waveguiding, where most of the light has leaked out of the waveguide.

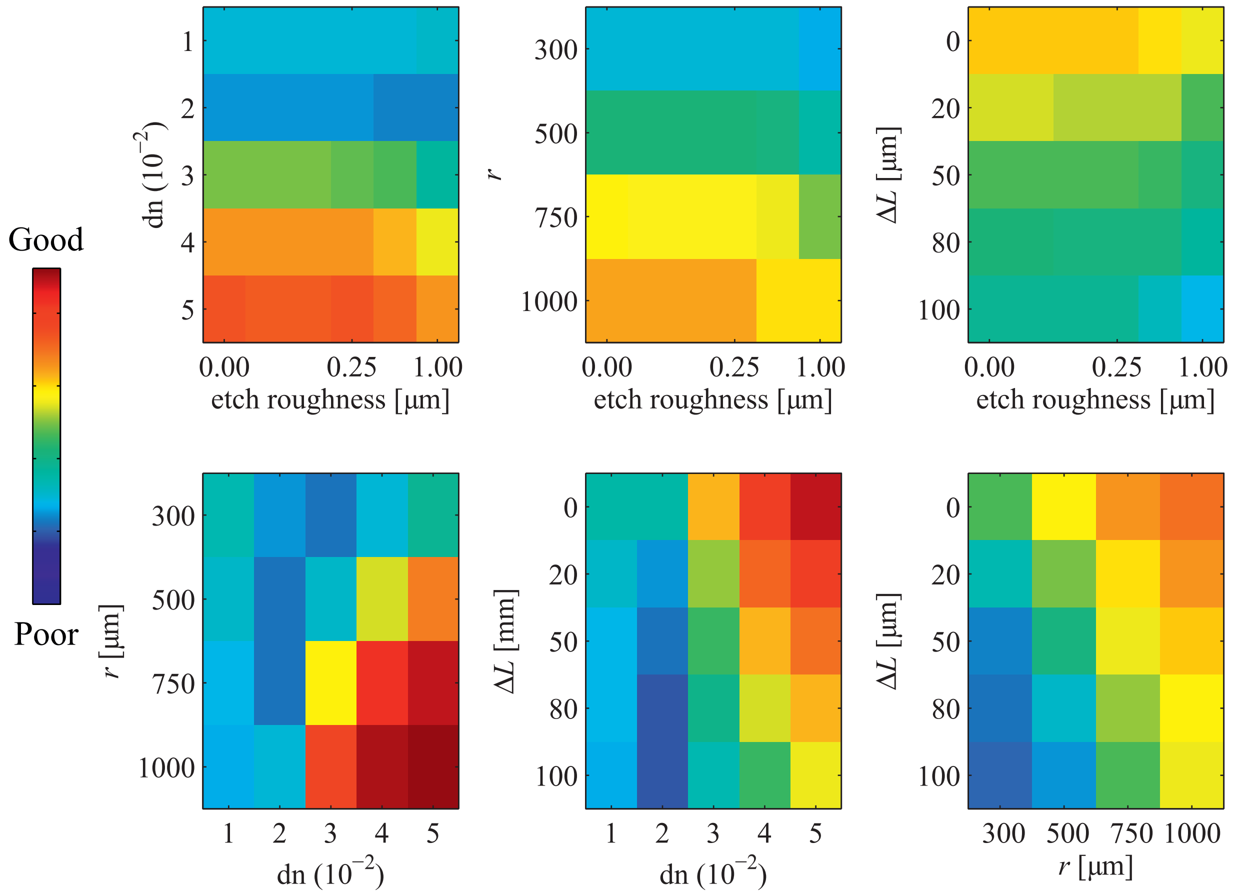

Figure 7.5: The results of 593 BPM simulations of a 2 µm wide ridge for different etch roughness, dn, ΔL and r. 7 simulations are missing from the parametrization, namely for roughness of 1 µm and $r = 1000$ µm (5 simulations), and for $r = 1000$ µm, roughness of 0.5 µm and dn of 0.04 and 0.05 (2 simulations). In each sub-plot, the light guided through the bent waveguide is shown for different combinations of the simulation para meters. Red indicates good waveguiding, where most of the light is guided in the curved waveguide. Blue indicates poor waveguiding, where most of the light has leaked out of the waveguide.

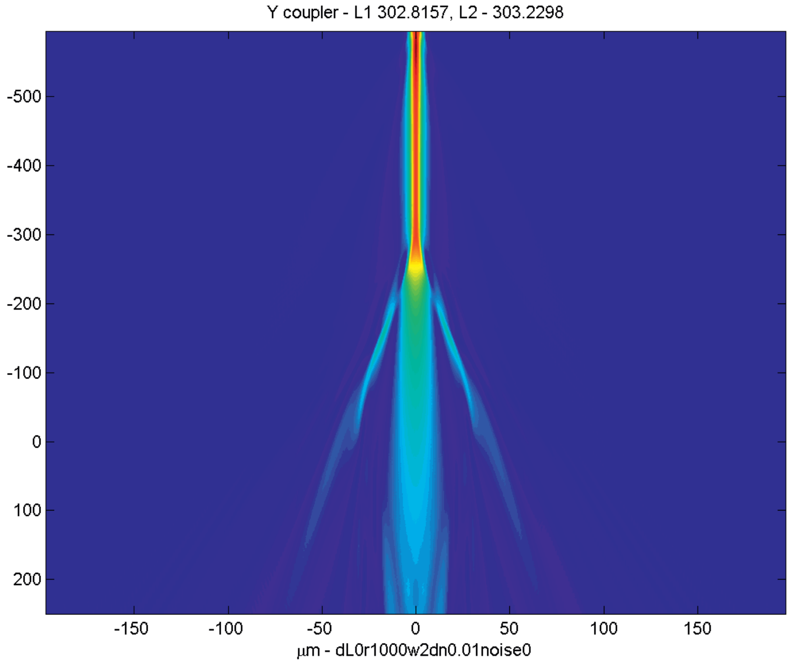

Figure 7.6: 2D BPM simulation of a waveguide with $\Delta L = 0$ µm, $r = 1000$ µm, $w = 2$ µm and no etch roughness. The refractive index contrast dn for this simulation was 0.01, and it can be seen that the light is not guided by the waveguide after the junction. Since the bent waveguide intensity is chosen by using the highest intensity for $x < 0$ µm, it is here over-estimated. This explains why a refractive index contrast dn of 0.01 shows better waveguiding than 0.02 in fig. 7.5.

From analyzing the simulations and mainly the simulation results presented in figs. 7.3 to 7.5, the following observations are made:

- The refractive index contrast, dn, for guiding light in a curved waveguide should be at least 0.04 (for our structures).
- Laser ridge roughness only substantially affects the light guiding if it is more than 25% of the ridge width. However, for increasing ΔL it becomes gradually more important.
- The most important design parameters are; r, which should be large; dn, which should also be large (at least > 0.03); ΔL, which should be small; w, which should be close to the maximum allowed width for single mode operation.
- The guiding properties of the waveguide are more or less independent of L.

The etch depth measurement in SEM found that the etch depth was only 1.4 µm, which is significantly lower than the target depth of 1.9 µm. These simulations confirm that this is the most likely reason for the non-functional Y-junction laser diodes. The simulations further suggest that the etch roughness is less important than the refractive index contrast, and increasing the etch depth should result in functioning bent waveguides even if the etch process could result in a rough waveguide. Furthermore, the bend radius should be increased as much as the total length of the laser diodes allows for to reduce bend losses.

Due to time constraints, new Y-junction laser diodes based on these findings were not fabricated for this work. However, suggestions for further work are presented section 9.3, including a suggestion for improved control of the etch depth.

Chapter 8

Publications

8.1 Paper I - Thermal expansion of GaSb measured by temperature dependent x-ray diffraction

I

Thermal expansion of GaSb measured by temperature dependent x-ray diffraction

Tron Arne Nilsen,[a] Magnus Breivik, Geir Myrvågnes, and Bjørn-Ove Fimland[b]
Department of Electronics and Telecommunications, Norwegian University of Science and Technology, NO-7491 Trondheim, Norway

(Received 23 September 2009; accepted 5 February 2010; published 5 May 2010)

X-ray diffraction measurements were performed using a modified zone technique on Te-doped GaSb wafers, commonly used for molecular beam epitaxial growth, at temperatures between 32 and 546 °C to determine the thermal expansion. The authors found the thermal expansion to be very close to the data published by Bublik *et al.* [Phys. Status Solidi A **73**, K271 (1982)]. Control measurements of the lattice constant of Si were found to agree with the results published by Okada and Tokumaru [J. Appl. Phys. **56**, 314 (1984)] within our measurement error of $\pm 2\times 10^{-4}$ Å. A fourth order polynomial, $a_{(\mathrm{GaSb})}(T)=6.0959+3.37\times 10^{-5}T+5.63\times 10^{-8}T^2-1.29\times 10^{-10}T^3+1.05\times 10^{-13}T^4$ (Å) (T in °C), was found to be a good fit to our data, while a linear fit with a constant thermal expansion coefficient of 7.17×10^{-6} K^{-1} was found to be a poorer fit. © *2010 American Vacuum Society.* [DOI: 10.1116/1.3336341]

I. INTRODUCTION

GaSb is an important material for mid-infrared applications, both as a substrate and part of compound epilayers. In order to obtain high quality, thick lattice-matched epilayers on GaSb substrates, the lattice constant at growth temperatures must be well known. There have been several studies carried out on the linear thermal expansion coefficient (TEC) of GaSb, from Bernstein and Beals,[1] Woolley,[2] and Straumanis and Kim[3] in the 1960s to the work performed by Bublik *et al.*[4] in 1982. Measurements on GaSb of the thermal expansion of the macroscopic length $l(T)$ (Ref. 1) and the microscopic change in the lattice parameter $a(T)$ (Refs. 2–4) have been reported in literature. However, the published results from the previous experiments do not agree well with each other, and review articles published later[5,6] also use differing values. In this work, we have performed temperature dependent x-ray diffraction (XRD) measurements to determine the TEC of Te-doped GaSb wafers. Our data allow temperature dependent XRD measurements of the thermal misfit of epilayers grown on GaSb substrates.[7] Control measurements were also performed on Si and GaAs to verify the accuracy of our measurement method.

II. THEORY

The linear thermal expansion coefficient is defined as

$$\alpha(T)=\frac{1}{a}\frac{da}{dT}, \tag{1}$$

where a is the (temperature dependent) lattice constant of the material and T is the temperature. Equation (1) can be approximated as

$$\alpha(T)=\frac{1}{a(T_0)}\frac{da}{dT} \tag{2}$$

as long as $a/a(T_0)-1$ is small. The lattice constant at any given temperature T is then given by

$$a(T)=a(T_0)\left(1+\int_{T_0}^{T}\alpha(T)dT\right). \tag{3}$$

From Bragg's law and the definitions of reciprocal space and Miller indices,[8] it can be shown that for a crystal sample with tetragonal unit cell (including a tetragonally distorted cubic unit cell) and with a (001) surface, the Bragg angle θ_B for a (hkl) plane can be expressed as

$$\theta_B=\sin^{-1}\left(\frac{\lambda}{2}\sqrt{\left(\frac{h}{a_x}\right)^2+\left(\frac{k}{a_x}\right)^2+\left(\frac{l}{a_z}\right)^2}\right) \tag{4}$$

and the angle τ between the surface and the plane

$$\tau=\cos^{-1}\left(\frac{la_x}{\sqrt{(ha_z)^2+(ka_z)^2+(la_x)^2}}\right). \tag{5}$$

Solving Eqs. (4) and (5) with respect to the in-plane lattice constant a_x and the out-of-plane lattice constant a_z gives only one solution with physical meaning

$$a_z=\frac{l\lambda}{2\sin\theta_B\cos\tau}, \tag{6}$$

$$a_x=\frac{\sqrt{h^2+k^2}\lambda}{2\sin\theta_B\sin\tau}. \tag{7}$$

III. EXPERIMENT

The XRD measurements were performed on a Bruker AXS D8 Discover HRXRD diffractometer with a half circle geometry (i.e., θ, 2θ between 0° and 180°) and equipped with an Anton-Paar DHS900 temperature stage.[9] Incident

---

[a] Electronic mail: tronarne@iet.ntnu.no
[b] Electronic mail: bjorn.fimland@iet.ntnu.no

beam optics include a Göbel mirror and a V-groove beam compressor giving Cu $K\alpha_1$ radiation and a full width at half maximum for Si (111) of less than 0.01°.[10] Symmetric and asymmetric measurements using a modified zone technique[11,12] with an open detector and a 1 mm circular aperture on the source were carried out on (001)-oriented GaSb, GaAs, and Si substrates in a nitrogen atmosphere. The 115, 226, 335, 444, 002, 004, and 006 reflections were measured for GaAs and GaSb. In addition, the 117 reflection was measured for GaSb. For Si, the 115, 224, 335, and 004 reflections were measured. For asymmetrical planes, both positive and negative geometries were used. Due to the large number of peaks (13 in the case of GaSb), the peaks were extracted automatically by taking the average angle between two points with the same intensity on each side of the peak. The intensity used was usually 80% of the peak value. With correctly calibrated azimuthal (φ) and tilt (χ) angles, the measured source to sample angle for a reflection i can be expressed as

$$\omega_{m+,i} = \theta_{B,i} + \tau_i + \omega_{\text{off}} + \Delta\omega_{r+,i}, \tag{8}$$

$$\omega_{m-,i} = \theta_{B,i} - \tau_i + \omega_{\text{off}} + \Delta\omega_{r-,i}, \tag{9}$$

where Eq. (8) is valid for positive geometry and Eq. (9) is for negative geometry. ω_{off} is a constant zero-offset in omega and

$$\Delta\omega_{r+,i} = \delta(\cot(\theta_{B,i} + \tau_i) + \tan\,\theta_{B,i}), \tag{10}$$

$$\Delta\omega_{r-,i} = \delta(\cot(\theta_{B,i} - \tau_i) + \tan\,\theta_{B,i}), \tag{11}$$

with $1-\delta$ being the refractive index of the material for x-rays. The method used for finding the in-plane and out-of-plane lattice constants uses a least-mean-square (LMS) method that varies ω_{off} to find the value that gives the lowest variance of the lattice constants between reflections. For each iteration, the following calculations are performed: First, the refractive index correction is calculated by

$$\Delta\omega_{r+,i} = \delta\left(\cot(\omega_{m+,i} - \omega_{\text{off}}) + \tan\left(\frac{\omega_{m+,i} + \omega_{m-,i}}{2} - \omega_{\text{off}}\right)\right), \tag{12}$$

$$\Delta\omega_{r-,i} = \delta\left(\cot(\omega_{m-,i} - \omega_{\text{off}}) + \tan\left(\frac{\omega_{m+,i} + \omega_{m-,i}}{2} - \omega_{\text{off}}\right)\right), \tag{13}$$

which is not exactly equal to Eqs. (10) and (11), but the error introduced by not including $\Delta\omega_{r+,i}$ or $\Delta\omega_{r-,i}$ in angles inside Eqs. (12) and (13) can safely be neglected.[12] The Bragg angle and the angle between the surface and the plane of the reflection are then calculated

$$\theta_{B,i} = \frac{\omega_{\text{corr}+,i} + \omega_{\text{corr}-,i}}{2} - \omega_{\text{off}}, \tag{14}$$

$$\tau_i = \frac{\omega_{\text{corr}+,i} - \omega_{\text{corr}-,i}}{2}, \tag{15}$$

where $\omega_{\text{corr}+,i} = (\omega_{m+,i} - \Delta\omega_{r+,i})$ and $\omega_{\text{corr}-,i} = (\omega_{m-,i} - \Delta\omega_{r-,i})$. Equations (6) and (7) are then used to calculate a_x and a_z for each asymmetric reflection. For symmetric reflections, $\omega_{m+,i} = \omega_{m-,i}$, $\tau_i = 0$, and only a_z is found. The sum

$$\sum_{i=1}^{N} (a_{x,i} - \overline{a_x})^2 + \sum_{i=1}^{M} (a_{z,i} - \overline{a_z})^2 \tag{16}$$

is then minimized by using the LMS method and varying ω_{off}. Here M is the total number of reflections used, N is the number of asymmetric reflections used

$$\overline{a_x} = \frac{1}{N}\sum_{i=1}^{N} a_{x,i}, \tag{17}$$

$$\overline{a_z} = \frac{1}{M}\sum_{i=1}^{M} a_{z,i}, \tag{18}$$

and $a_{x,i}, a_{z,i}$ are the answers obtained from Eqs. (6) and (7) for the ith reflection. After the optimum value for ω_{off} has been found, additional offsets $\omega_{\text{off}+,i}$ and $\omega_{\text{off}-,i}$ are added to Eqs. (8) and (9) to account for errors in determining the peak position, and the sum in Eq. (16) is minimized again using the LMS method and varying $\omega_{\text{off}+,i}$ and $\omega_{\text{off}-,i}$ for all values of i. After the LMS algorithm has finished, the final a_x and a_z values are given by Eqs. (17) and (18), respectively. For cubic unit cells, the lattice parameter a is calculated as an average of a_x and a_z. Any measurement where the difference between the in-plane and out-of-plane lattice constant exceeded 2×10^{-4} Å was not used, as we have found this to be indicative of bad alignment of φ and χ angles. The GaSb substrates were from Wafer Technology and Galaxy and were Te-doped with a concentration of $(2-7)\times10^{17}$ and 1×10^{18} cm^{-3}, respectively. The GaAs substrates were from Wafer Technology and were undoped or Si-doped with a concentration of $(1-5)\times10^{18}$ cm^{-3}.

XRD measurements were performed at 32, 65, 100, and then every 50 °C up to 550 °C. Azimuthal (φ) and tilt (χ) angles were recalibrated every 100 °C. The temperature was measured by a thermocouple (TC) built into the heater stage.[9] The temperature measured by the TC has an offset with respect to the sample surface that is being probed by the x-rays. This offset is dependent on the sample's temperature, thickness, size, and thermal conductivity, as well as the nature of the thermal contact between the sample and the stage. The thermal offset was estimated by first comparing high temperature (up to 890 °C) XRD measurements on Si to the measurements done by Okada and Tokumaru[13] and assuming the difference in lattice constant to be due to the temperature offset. A simple model for heat transfer from stage to sample and sample to the environment was then fitted to the data to estimate the offsets for lower temperatures and other sample materials (i.e., GaSb and GaAs). For each measurement series on a sample, the lattice constant for each temperature was measured twice, once in the part of the measurement

TABLE I. Measured lattice constant of GaSb vs temperature measured by TC and vs estimated temperature at the XRD-probed GaSb surface.

Temperature TC (°C)	Estimated surface temperature (°C)	a_{GaSb} (Å)	σ (10^{-4} Å)	No. of measurements
32	32	6.0971	1.71	4
65	65	6.0983	2.24	9
100	100	6.0997	1.59	7
150	150	6.1019	2.09	6
200	199	6.1041	1.92	8
250	249	6.1062	1.42	8
300	299	6.1084	1.51	7
350	348	6.1106	1.66	8
400	398	6.1128	0.95	8
450	447	6.1149	0.71	6
500	497	6.1172	0.91	6
550	546	6.1195	0.67	4

series going from low to high temperatures and then again in the part of the measurement series going from high to low temperatures, to check for hysteresis effects. In addition, for temperatures above 350 °C, GaSb was measured again at a lower temperature after each temperature increase to verify if the time at elevated temperature had any effect on the measured lattice constant at the lower temperature. Reproducibility of the measurements was tested by removing the sample completely and remounting it, and then repeating the measurements.

IV. RESULTS AND DISCUSSION

Table I shows the measured lattice constant for GaSb at different temperatures, the standard deviation of the data points, and the number of data points collected for each temperature. The measurements were performed over a period of 3 months and on several samples. From the data in Table I, we estimate the measurement accuracy to be within $\pm 2 \times 10^{-4}$ Å. The temperature stability of the TC temperature was ±1 °C and the uncertainty in the surface temperature estimates was estimated to be ±2 °C at 550 °C.

Figure 1 shows a comparison between some values found in literature and our measurements. As shown in Fig. 1, our results agree well with the results published by Bublik *et al.*,[4] who used a fourth order polynomial to fit their data. A fourth order fit to our measurements yields the following expression:

$$a_{\mathrm{GaSb}}(T) = 6.0959 + 3.37 \times 10^{-5}T + 5.63 \times 10^{-8}T^2 - 1.29 \times 10^{-10}T^3 + 1.05 \times 10^{-13}T^4 \quad (\text{Å}), \tag{19}$$

where T is the temperature in °C. The standard error of the fit in Eq. (19) was 3.6×10^{-5} Å. Using Eq. (2), a T_0 of 25 °C and an $a(T_0)$ of 6.0968 Å gives a linear thermal expansion coefficient of

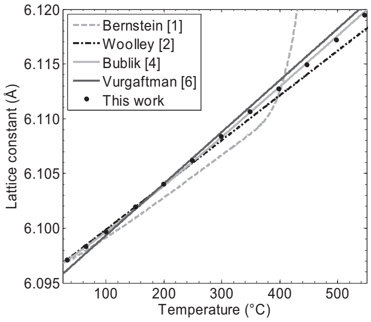

FIG. 1. Comparison between this work and the previous works of Bernstein and Beals (Ref. 1), Woolley (Ref. 2), Bublik *et al.* (Ref. 4), and the values from the review of Vurgaftman *et al.* (Ref. 6). Bernstein and Beals (Ref. 1) measured macroscopic expansion and Woolley (Ref. 2) only reported the linear TEC in his work. In order to calculate the lattice constants from the works of Woolley (Ref. 2) and Bernstein and Beals (Ref. 1), Eq. (3) with a T_0 of 25 °C and an $a(T_0)$ of 6.0968 Å has been used.

$$\alpha_{\mathrm{GaSb}}(T) = 5.53 \times 10^{-6} + 1.85 \times 10^{-8}T - 6.35 \times 10^{-11}T^2 + 6.9 \times 10^{-14}T^3 \quad (\mathrm{K}^{-1}), \tag{20}$$

where T is the temperature in °C.

Table II summarizes the majority of works found in the literature on the thermal expansion of GaSb at temperatures above room temperature. Straumanis and Kim[3] only measured between 0 and 70 °C and Bernstein and Beals[1] reported a rapid increase in the TEC between 300 and 400 °C and stopped at 436 °C due to this increase. All previous works, with the exception of Bublik *et al.*[4] and Bernstein and Beals,[1] reported a constant TEC for GaSb. A linear fit to our data in the temperature range of 32–546 °C gives a constant TEC of 7.17×10^{-6} K^{-1}. The standard error of this fit is 1.2×10^{-4} Å. In addition, the results presented in Fig. 2 suggest that the TEC is not constant with regard to temperature and thus a higher order polynomial fit is in order.

TABLE II. Comparison of TEC values from the literature and from this work. The value from Bublik *et al.* (Ref. 4) is a linear fit to their fourth order polynomial in the temperature range of 0–680 °C. For both Vurgaftman *et al.* (Ref. 6) and Bublik *et al.* (Ref. 4) who reported only the lattice constant as function of temperature and no TEC, Eq. (2) along with a T_0 of 25 °C and $a(T_0)$=6.0968 Å was used to calculate the TEC.

Reference	Linear TEC (K^{-1})
Bernstein and Beals[a]	6.0×10^{-6}
Woolley[b]	6.7×10^{-6}
Straumanis and Kim[c]	7.75×10^{-6}
Bublik *et al.*[d]	7.31×10^{-6}
Vurgaftman *et al.*[e]	7.74×10^{-6}
This work	7.17×10^{-6}

[a] Reference 1.
[b] Reference 2.
[c] Reference 3.
[d] Reference 4.
[e] Reference 6.

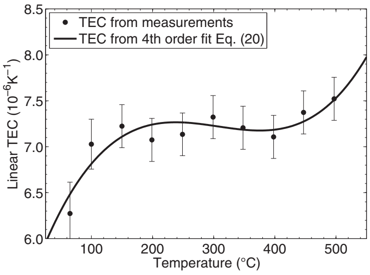

FIG. 2. Linear TEC vs temperature. For each temperature, TEC was calculated by linear regression of three data points in Table I, using the data point of the temperature in question and nearest neighboring data points. $T_0 = 25$ °C.

The results of the control measurements carried out on Si for temperatures up to 550 °C were nearly identical to the values obtained from the empirical equation given by Okada and Tokumaru[13] with the largest deviation being less than 2×10^{-4} Å and the standard error 9.5×10^{-5} Å. This compares well to Okada and Tokumaru's[13] $\pm 1 \times 10^{-4}$ Å difference between their results and empirical equation, indicating no large systematic sources of error in our measurements in addition to the statistical ones estimated in Table I. This also strengthens our assumption that the difference in lattice constant between the measurements of Okada and Tokumaru[13] and our measurements at high temperatures is due to a higher TC reading than the actual surface temperature for our samples. For GaAs, several different values are reported[14–16] for the TEC and the lattice constant of GaAs. For our control measurements at temperatures up to 398 °C, our results agree well with the values presented by Brice[14] and by Bak-Misiuk *et al.*[15] In fact, we obtain a linear TEC from 32 to 398 °C of 6.53×10^{-6} K^{-1}, which is very close to the value 6.50×10^{-6} K^{-1} obtained by Bak-Misiuk *et al.*[15] for temperatures from 23 to 427 °C. At higher temperatures, we currently have only preliminary measurements. Our lattice constant values are between the values reported by Brice[14] and Song *et al.*[16] The differing values in literature for the lattice constant at high temperatures, and the fact that our preliminary data differ from these, indicate the need for further investigation of the thermal expansion of GaAs at high temperatures.

V. CONCLUSION

The lattice constant of Te-doped GaSb wafers has been measured with an accuracy of $\pm 2 \times 10^{-4}$ Å from 32 to 546 °C by temperature dependent XRD. The results obtained agree well with what Bublik *et al.*[4] published in 1982 and a fourth order polynomial has been fitted to the data. Control measurements on Si were found to match earlier published values[13] within our measurement accuracy indicating no significant errors in the measurement method.

ACKNOWLEDGMENTS

The authors would like to thank Christian Resch of Anton-Paar for providing information and help with the DHS 900 heating stage and Espen Selvig of the Norwegian Defense Research Establishment for help and multiple discussions about asymmetrical XRD measurements. This project was partly funded by the Research Council of Norway under Contract No. 177610/V30.

[1] L. Bernstein and R. J. Beals, J. Appl. Phys. **32**, 122 (1961).
[2] J. C. Woolley, J. Electrochem. Soc. **112**, 461 (1965).
[3] M. E. Straumanis and C. D. Kim, J. Appl. Phys. **36**, 3822 (1965).
[4] V. T. Bublik, J. Wilke, and A. T. Pereversev, Phys. Status Solidi A **73**, K271 (1982).
[5] P. S. Dutta, H. L. Bhat, and V. Kumar, J. Appl. Phys. **81**, 5821 (1997).
[6] I. Vurgaftman, J. R. Meyer, and L. R. Ram-Mohan, J. Appl. Phys. **89**, 5815 (2001).
[7] M. Breivik, T. A. Nilsen, G. Myrvågnes, E. Selvig, and B. O. Fimland, J. Vac. Sci. Technol. B **28**, C3I1 (2010).
[8] S. R. Elliott, *The Physics and Chemistry of Solids* (Wiley, Chichester, 1998).
[9] R. Resel, E. Tamas, B. Sonderegger, P. Hofbauer, and J. Keckes, J. Appl. Crystallogr. **36**, 80 (2003).
[10] *D8 Discover Series 2 X-ray Diffractometer User's Manual* (Bruker AXS, Karlsruhe, 2004), Vol. III.
[11] M. Fatemi, Appl. Phys. Lett. **80**, 935 (2002).
[12] M. Fatemi, Acta Crystallogr., Sect. A: Found. Crystallogr. **61**, 301 (2005).
[13] Y. Okada and Y. Tokumaru, J. Appl. Phys. **56**, 314 (1984).
[14] J. C. Brice, *Properties of Gallium Arsenide*, 2nd ed. (INSPEC, London, 1990).
[15] J. Bak-Misiuk, H. G. Brühl, W. Paszkowicz and U. Pietsch, Phys. Status Solidi A **106**, 451 (1988).
[16] S. K. Song, Y. H. Park, and B. W. Lau, J. Korean Phys. Soc. **5**, 35 (1972).

8.2 Paper II - Temperature dependent lattice constant of $Al_{0.90}Ga_{0.10}As_ySb_{1-y}$

Temperature dependent lattice constant of $Al_{0.90}Ga_{0.10}As_ySb_{1-y}$

Magnus Breivik,[a] Tron Arne Nilsen, and Geir Myrvågnes
Department of Electronics and Telecommunications, Norwegian University of Science and Technology, NO-7491 Trondheim, Norway

Espen Selvig
Norwegian Defence Research Establishment, P.O. Box 25, NO-2027 Kjeller, Norway

Bjørn-Ove Fimland[b]
Department of Electronics and Telecommunications, Norwegian University of Science and Technology, NO-7491 Trondheim, Norway

(Received 24 September 2009; accepted 5 April 2010; published 5 May 2010)

Using x-ray diffraction, the in-plane and out-of-plane lattice constants of $Al_{0.90}Ga_{0.10}As_ySb_{1-y}$ epilayers grown on GaSb and GaAs substrates were determined between 30 and 398 °C for $y = 0.003-0.059$. The bulk lattice constant was then calculated from the in-plane and out-of-plane lattice constants. A polynomial function for the bulk lattice constant as a function of y and temperature was derived from a fit to the resulting data. Comparison to measured out-of-plane lattice constants of platinum-coated $Al_{0.90}Ga_{0.10}As_ySb_{1-y}$ indicates that the polynomial function is valid up to around 550 °C. The polynomial function can be used to determine the lattice matching of $Al_{0.90}Ga_{0.10}As_ySb_{1-y}$ to, e.g., GaSb at typical growth temperatures used for growth of cladding layers in laser structures. A formula is given for calculating the As mole fraction for lattice matching to GaSb at a given temperature. *© 2010 American Vacuum Society.* [DOI: 10.1116/1.3414830]

I. INTRODUCTION

$Al_xGa_{1-x}As_ySb_{1-y}$ is a popular cladding material for GaSb-based laser structures due to its large band gap and low refractive index for high x and lattice matching to GaSb for low y. Using a high Al mole fraction also enables doping to a high electron carrier concentration.[1] From literature, e.g., Refs. 2–5, the chosen values for the As mole fraction y are typically 0.05–0.07. The As mole fraction is usually chosen to be close to the lattice matching value at room temperature, which depends on the Al mole fraction.

We have experimental results showing that lattice matching at the growth temperature is important in order to achieve dislocation-free layers. When comparing to $Al_{0.90}Ga_{0.10}As_ySb_{1-y}$ lattice-matched to GaSb at room temperature, x-ray diffraction (XRD) measurements show that a slight decrease in the As mole fraction results in a lower full width at half maximum (FWHM).[6] We believe this to be due to a difference in the thermal expansion coefficients of $Al_{0.90}Ga_{0.10}As_ySb_{1-y}$ and GaSb.[6] The difference in strain at room temperature and at growth temperature, respectively, is called the "thermal misfit." If large, the thermal misfit can significantly affect the critical thickness and the density of misfit dislocations. It is therefore important to take this into consideration when designing structures. To the authors' knowledge, no systematic measurements have been performed on the temperature dependence of the lattice constant of $Al_{0.90}Ga_{0.10}As_ySb_{1-y}$. Additionally, no data for the thermal expansion coefficient (TEC) of AlSb above 340 K (Ref. 7) is reported in literature, making any interpolation of TEC data for the binary constituents uncertain above 340 K.

Using XRD measurements from several crystal lattice plane orientations, it is possible to measure the lattice constants accurately. The preferred method has been Bond's method from the 1960s.[8] For our measurements, we chose the Zone technique developed by Fatemi,[9,10] as this method can be utilized in diffractometers with half circle geometry, i.e., $\theta, 2\theta \in [0°, 180°]$, while giving the same level of accuracy as Bond's method.

In this work, we will present a polynomial fit for the temperature dependent lattice constant of $Al_{0.90}Ga_{0.10}As_ySb_{1-y}$ valid from room temperature to around 550 °C, as determined from XRD measurements. The data are then used to determine the As mole fraction for lattice matching of $Al_{0.90}Ga_{0.10}As_ySb_{1-y}$ to GaSb as a function of temperature.

II. THEORY

In order to calculate the bulk lattice constant of a zinc blende crystal from a strained epilayer, both the in-plane and out-of-plane lattice constants must be known, hereafter referred to as a_x and a_z, respectively. The relationship between the lattice constants of the strained layer and the bulk lattice constant can be calculated from the following equation:[11]

$$a = \frac{a_z + (2C_{12}/C_{11})a_x}{1 + (2C_{12}/C_{11})}, \tag{1}$$

where a is the (unstrained) bulk lattice constant and C_{11} and C_{12} are the stiffness tensor elements. In this study, C_{11} and C_{12} were determined using interpolation of data for the binary constituents of (Al,Ga)(As,Sb).[12,13] According to Ref. 14, C_{11} and C_{12} are temperature dependent for GaAs. However, the error induced in a by assuming that C_{11} and C_{12} are

---

[a] Electronic mail: magnus.breivik@iet.ntnu.no
[b] Electronic mail: bjorn.fimland@iet.ntnu.no

temperature *independent* is less than 1×10^{-4} Å from 0 to 550 °C. Since the error contribution is so small and since we have no corresponding data for the other binary constituents, the stiffness tensors were assumed to be temperature independent in our calculations.

The linear thermal expansion coefficient, $\alpha(T)$, is given by[15]

$$\alpha(T) = \frac{1}{a(T)}\frac{da(T)}{dT} \simeq \frac{1}{a(T_0)}\frac{da(T)}{dT}, \tag{2}$$

where T is the temperature at which α is evaluated and T_0 is a reference temperature for which a is known, typically the room temperature. The above approximation, setting $a(T) \simeq a(T_0)$, is a good approximation for all temperatures in this study since $[a(T)/a(T_0)]-1$ is small.

The lattice constant at a given temperature can then be calculated as

$$a(T) = a(T_0)\left(1 + \int_{T_0}^{T} \alpha(T)dT\right). \tag{3}$$

III. EXPERIMENT

All samples were grown in a Varian Gen II Modular molecular beam epitaxy system on (001)-oriented GaSb substrates, except sample As 510-2 that was grown on a (001)-oriented GaAs substrate. The group III composition was calibrated using reflection high-energy electron diffraction on dedicated GaAs samples.

High resolution XRD measurements were performed on a Bruker AXS D8 Discover XRD diffractometer with a half circle geometry. Incident beam optics include a Göbel mirror and a V-groove beam compressor giving Cu $K\alpha_1$ radiation and a FWHM for Si (111) of less than 0.01°.[16] The diffractometer was equipped with an Anton-Paar DHS 900 temperature stage used to do measurements from 30 to 550 °C, as measured by a thermocouple (TC) inside the hot plate.[17] A 5 min pause was used to allow the temperature to stabilize after each step in temperature. For temperatures above 150 °C, the temperature of the XRD-probed sample surface has been shifted by up to −4 °C (at 550 °C) relative to the TC reading to compensate for the temperature gradient through the sample, based on lattice constant measurements of a Si substrate on the DHS 900 temperature stage.[18]

Lattice constants were determined from symmetric and asymmetric reflections using a modified Zone technique.[9,10] All XRD measurements were performed with an open detector and a 1 mm circular aperture on the source. Measurements were carried out on samples in a nitrogen atmosphere using at least four of the 115, 117, 226, 335, 444, 002, 004, and 006 reflections at each temperature. Asymmetric reflections were measured both in positive ("steep incidence") and negative ("shallow incidence") geometries. The 444 reflection was only used for sample As 510-2 due to an overlap of the substrate peak and the epilayer peak in positive geometry for all other samples at most temperatures. Reflections where the overlap of the substrate and epilayer peaks became too large for an accurate determination of the peak positions were not included in the calculations. The azimuthal (φ) and tilt (χ) angles of the samples were aligned to get a correct incidence angle on to the sample. This was done one to three times during a measurement series, at different temperatures.

TABLE I. Samples used for XRD study of $\mathrm{Al_{0.90}Ga_{0.10}As_{y}Sb_{1-y}}$. All samples were capped with 5–50 nm GaSb.

Sample ID	Thickness (μm)	y	Growth temperature (°C)
As 510-2	6	0.0027	530
Sb 54-3	2	0.0524	490
Sb 99-1	2	0.0670	490
Sb 122	2	0.0569	550
Sb 130-4	2	0.0589	550
Sb 141-2	0.5	0.0579	465

Due to the large number of peaks (6–13 peaks each for epilayer and substrate for each calculated pair of lattice constants a_x and a_z), the peak positions were extracted automatically by taking the average angle between two points on opposite sides of the peak. The points were usually taken at 70% of the peak intensity but higher values were chosen when overlap of epilayer and substrate peaks became an issue.

The lattice constant was then determined by correcting for incident angle offsets and refractive index, in that order. Using a least-mean-square (LMS) approach, the extracted peak positions were shifted to account for an incident angle offset, followed by refractive index correction, minimizing for the residual error in a_x and a_z from different reflections. The refractive indices were taken to be $n=1-\delta$, with δ calculated using values from Ref. 19. The resulting LMS fit gave a good agreement between the lattice constants calculated from each reflection, as the standard deviation for a_x and a_z was between 5×10^{-5} and 3×10^{-4} Å. The bulk lattice constant a was then calculated using Eq. (1).

For each sample, the As mole fraction, y, was determined from the interpolation of lattice constants of the binaries at 30–32 °C to fit the found bulk lattice constant, assuming $x=0.90$ and that Vegard's law is valid. The lattice constant of GaSb (6.0970 Å) was taken from our own measurements.[18] The lattice constant of GaAs (5.6538 Å) was taken from Ref. 14, while for AlAs (5.6610 Å) and AlSb (6.1359 Å), the lattice constants were taken from Refs. 7 and 20. The values given in parenthesis are at 32 °C.

XRD measurements were performed at TC temperatures from 100 to 400 °C in steps of 50 °C, as well as at 30–32 °C and at 65 °C. More than 50 values for a were calculated from the measurements of the samples. The important sample parameters are given in Table I. While the uncertainty in y is closer to $\pm4\times10^{-4}$ ($\pm2\times10^{-4}$ Å), it was determined down to 1×10^{-4} as this gave a smaller residual error between the measurements and the polynomial fit found in Sec. IV.

The As mole fraction was found to vary slightly (up to ±0.001) across a 2 in. wafer. Smaller pieces (typically 8

$\times 8$ mm^2) from the same sample in Table I would therefore often have slightly different As content. Typical values for y are listed in Table I.

Due to a degradation of the epilayer at temperatures above 350–400 °C, believed to be due to outdiffusion of the group V constituents, the measurements have mainly been performed up to 400 °C. The samples measured above 400 °C were prepared by evaporating Pt layers of varying thicknesses on to the sample in an e-beam evaporator. A minimum thickness of 100 nm was found to be necessary to stop the degradation of the epilayer.

IV. RESULTS AND DISCUSSION

The calculated lattice constants from all samples except Sb 99-1 and Sb 122 resulted in 52 values for a in the temperature range of 30–398 °C. These values were used to make the polynomial fit

$$a(y,T) = b_0 + b_1 \times y + b_2 \times T + b_3 \times T^2 \ (\text{Å}). \qquad (4)$$

Sb 99-1 was not included due to an overlap of the peaks in the measured temperature range (lattice matching). For Sb 122, temperature dependent XRD measurements were only performed on Pt-coated pieces due to time constraints. To avoid any potential Pt influence on Eq. (4), these results were not used in the polynomial fit.

The best fit was with b_0=6.1310 Å, b_1=−0.4702 Å, b_2 =2.856×10^{-5} Å/°C, and b_3=5.03×10^{-9} Å/°C^2, when T is given in °C. yT and y^2 were not included, as the contributions were found to be less than the measurement uncertainty in the measured ranges for y and T. The standard error of the fit was 1.5×10^{-4} Å.

Equations (2) and (4) then give the following linear TEC:

$$\alpha(T) \simeq \frac{b_2 + 2b_3T}{b_0 + b_1y}$$
$$\simeq 4.68 \times 10^{-6} + 1.65 \times 10^{-9} \times T \ (°\mathrm{C}^{-1}) \qquad (5)$$

for $y \simeq 0.06$, where T is given in °C and $a(T_0)$ is evaluated at 0 °C.

The As mole fraction y required for lattice matching to GaSb as a function of T has been calculated from Eq. (4) and our measurements for GaSb (Ref. 18) and is presented in Fig. 1.

A linear fit to the curve in Fig. 1 gives the following criterion for lattice matching to GaSb:

$$y = 0.0751 - 2.59 \times 10^{-5} \times T, \qquad (6)$$

where T is given in °C. For a fully strained $Al_{0.90}Ga_{0.10}As_ySb_{1-y}$ epilayer on GaSb, y can quickly be determined from a 004 XRD scan at room temperature (25 °C) using y=0.0744−0.1971×$\Delta\theta$, where $\Delta\theta$ is the angular separation (in degrees) between the $Al_{0.90}Ga_{0.10}As_ySb_{1-y}$ peak and the GaSb peak.

A topographical representation of the temperature shift of the $Al_{0.90}Ga_{0.10}As_{0.0671}Sb_{0.9329}$ and GaSb 004 XRD peaks for a piece of sample Sb 99-1 is shown in Fig. 2. The substrate and epilayer peak positions merge close to 305 °C. This is close to the value of 309 °C found from Eq. (6) and the As mole fraction calculated from asymmetric XRD measurements at 32 °C. Note that for all topographical plots (Figs. 2–4), each constituent scan has been shifted so that the GaSb peak is at its theoretical position, given by the polynomial in Ref. 18. The shift is necessary due to an inhomogeneous expansion of the DHS 900 hot plate, leading to a temperature dependent angular offset of the sample.[17]

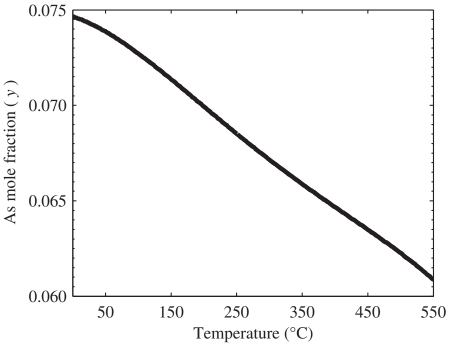

FIG. 1. Lattice matching criteria for $Al_{0.90}Ga_{0.10}As_ySb_{1-y}$ on GaSb.

In order to measure the lattice misfit at higher temperatures and examine the validity of Eq. (4) above 400 °C, 8 ×8 mm^2 pieces of sample Sb 122 were capped with either a 100 nm thick or a 200 nm thick Pt layer on the episide. A topographical representation of the temperature shift of 004 peaks up to 546 °C for the piece coated with 100 nm is shown in Fig. 3.

The resulting bulk lattice constants a of (unstrained) $Al_{0.90}Ga_{0.10}As_{0.0566}Sb_{0.9434}$ at different temperatures are listed in Table II. The bulk lattice constant was calculated from Eq. (1), where a_x was assumed to be equal to the GaSb lattice constant[18] (i.e., fully strained epilayers) and a_z was derived

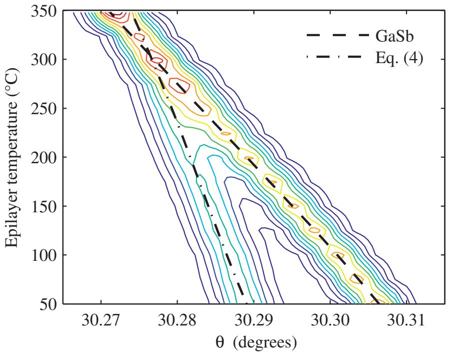

FIG. 2. (Color online) Topographical representation of the temperature shift of $Al_{0.90}Ga_{0.10}As_{0.0671}Sb_{0.9329}$ and GaSb 004 XRD peaks for a piece of Sb 99-1, with measurements performed at about 25 °C intervals from 50 to 348 °C. The dashed curves show theoretical peak positions calculated from lattice constants found in Ref. 18 (GaSb) and from Eq. (4) ($Al_{0.90}Ga_{0.10}As_ySb_{1-y}$).

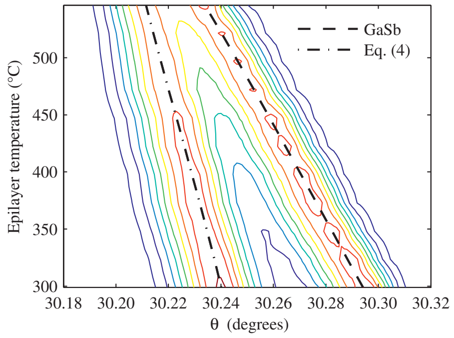

FIG. 3. (Color online) Topographical representation of the temperature shift of 004 peaks for a piece of Sb 122 coated with 100 nm Pt. Measurements were performed at about 25 °C intervals from 299 to 546 °C. The dashed curves show theoretical peak positions calculated from lattice constants found in Ref. 18 (GaSb) and from Eq. (4) ($Al_{0.90}Ga_{0.10}As_ySb_{1-y}$), with $y=0.0566$.

TABLE II. Sb 122 (100 nm Pt): Comparison of a from Eq. (4) and a calculated from Eq. (1) using literature values of GaSb (Ref. 18) for a_x and values derived from 004 reflection measurements (Fig. 3) for a_z. $\Delta\theta$ is the observed angular separation between the two peaks shown in Fig. 3 and θ is the angular position of the $Al_{0.90}Ga_{0.10}As_{0.0566}Sb_{0.9434}$ peak.

Temperature (°C)	$\Delta\theta$ (deg)	θ (deg)	a from Eq. (1) (Å)	Equation (4) (Å)
299	0.054	30.239	6.1134	6.1134
324	0.051	30.236	6.1142	6.1142
348	0.048	30.234	6.1149	6.1149
373	0.044	30.231	6.1157	6.1157
398	0.041	30.228	6.1165	6.1166
423	0.038	30.225	6.1173	6.1174
447	0.035	30.222	6.1181	6.1182
472	0.032	30.220	6.1189	6.1190
497	0.028	30.217	6.1197	6.1198
522	0.025	30.214	6.1206	6.1207
546	0.022	30.211	6.1214	6.1215

from the 004 scans presented in Fig. 3. Due to a high degree of overlap of the epilayer and substrate peaks at most of these temperatures, the usual 70% of peak value method could not be used for extracting the peak position. Instead, a weighted mean over a range of higher intensities was used, with the peak intensity being weighted the most. The As mole fraction ($y=0.0566$) was derived from the best fit to Eq. (4) at 299 °C, which was then used to determine $C_{11,12}$ and δ.

In Table II, the bulk lattice constants derived from measurements are also compared to the bulk lattice constants calculated from Eq. (4) at different temperatures up to 546 °C. It can be seen that the deviation between a derived from measurements and a calculated from Eq. (4) is within $\pm 1\times 10^{-4}$ Å from 300 to 546 °C. An analysis of the uncertainties involved in the determination of the peak positions and a_{GaSb} suggests that the uncertainty in a derived from the 004 reflection measurements is $\pm 2.4\times 10^{-4}$ Å, close to the standard error of Eq. (4). We take the above results as a strong indication that Eq. (4) is valid up to around 550 °C. Note that since we have not measured the in-plane lattice constant, these measurements cannot be considered to be absolute proof of validity for Eq. (4) up to 550 °C.

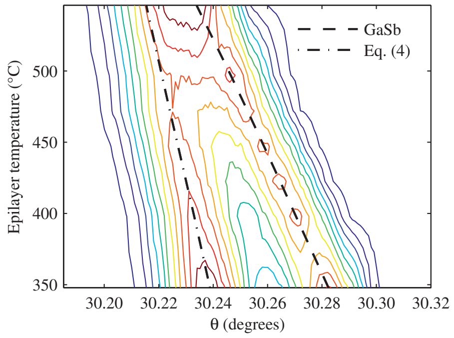

FIG. 4. (Color online) Topographical representation of the temperature shift of 004 peaks for a piece of Sb 122 coated with 200 nm Pt. Measurements were performed at 348 °C, at about 25 °C intervals from 398 to 497 °C, and at 546 °C. The dashed curves show theoretical peak positions calculated from lattice constants found in Ref. 18 (GaSb) and from Eq. (4) ($Al_{0.90}Ga_{0.10}As_ySb_{1-y}$), with $y=0.0574$. Equation (4) was found to fit the measurements to within $\pm 1\times 10^{-4}$ Å up to 450 °C (i.e., as far as both peaks are well resolved).

A topographical representation of the temperature shift of 004 peaks up to 546 °C for the piece coated with 200 nm Pt is shown in Fig. 4. Also in this case, Eq. (4) was found to fit the measurements up to 450 °C (i.e., as far as both peaks are well resolved).

The TEC of AlSb has only been reported up to 340 K (Ref. 7) (where it flattens out) and is thus currently the best estimate for the TEC of AlSb at higher temperatures. Using this TEC, we can calculate the lattice constant at higher temperatures from Eq. (3). A comparison of the interpolation of the binary constituents, Eq. (4) ($y=0.0589$) and the derived bulk lattice constants for Sb 130-4 is shown in Fig. 5. It can be seen that the binary interpolation deviates significantly

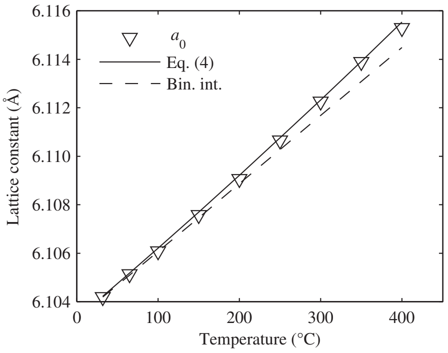

FIG. 5. Derived bulk lattice constants of $Al_{0.90}Ga_{0.10}As_{0.0589}Sb_{0.9411}$ from experimental data for sample Sb 130-4 compared to Eq. (4) and interpolation of the binary constituents from 32 to 400 °C.

from the measured lattice constants at elevated temperatures, and thus further investigation of AlSb above 340 K is needed.

A. Error sources

Uncertainties include errors in x, y, and T. For sample Sb 141-2, x was measured by using a 200 nm $Al_xGa_{1-x}Sb$ calibration layer. A simulation of the 004 XRD peaks for sample Sb 141-2 using the LEPTOS software package from Bruker AXS resulted in $x=0.911$. Assuming an uncertainty of $\Delta x = \pm 0.02$ around $x=0.90$, at 30 °C, y would be determined within $\pm 1.5\times 10^{-3}$ from the actual As mole fraction in the sample (according to binary interpolation). This shift in y would, however, not be detrimental to Eq. (4). The error would mainly impact Eq. (4) through the thermal coefficients b_2 and b_3 since the thermal expansion for, e.g., $x=0.88$ would slightly differ from $x=0.90$. An estimation of the uncertainty in $a(T)$ for a deviation in x, Δx, of 0.02 can be evaluated by comparing the deviation in $a(T)$, $\Delta a(T)$, at the lowest (30 °C) and highest (400 °C) temperature measured using

$$\Delta a(T) = \frac{da(T)}{dx} \times \Delta x \simeq \frac{a_{Al_{0.90}Ga_{0.10}Sb}(T) - a_{GaSb}(T)}{0.9} \times 0.02, \quad (7)$$

where Eq. (4) is used for $a_{Al_{0.90}Ga_{0.10}Sb}$ ($y=0$) and data in Ref. 18 are used for a_{GaSb}. The difference between Δa at 30 and 400 °C was found to be $\mp 1.0\times 10^{-4}$ Å for $x=0.90\pm 0.02$, which is the best estimate for the contribution of this error.

The uneven thermal expansion of the hot plate, causing thermally induced tilt, also contributes to the temperature-related errors. Investigation suggests that the contribution to the incident angular offset is approximately 0.01° in θ when going from 50 to 350 °C. This contribution is, however, included in the incident angle offset calculations mentioned in Sec. III. It is assumed that the angular offset is constant for the measurement series (6–13 measured epilayer and substrate peaks) at each temperature, which lasts about 1.5–2 h. The angular offsets for the peak positions seem random for the different measured peaks, suggesting that there is no steady drift in the angular offset at constant temperature.

The temperature dependence of C_{11} and C_{12} can also contribute to thermally induced errors. However, as mentioned in Sec. II, this temperature dependence is weak and is ignored. For strained GaAs, this error would be approximately 1×10^{-4} Å in the lattice constant a under similar conditions. If the other binary constituents have temperature dependences in C_{11} and C_{12} of the same order, the total error would be approximately the same.

Many of these errors are hard to quantify. For the majority of the measurements (90%), the calculated values for a were within $\pm 2\times 10^{-4}$ Å of the values predicted by Eq. (4) (and 96% within 2.7×10^{-4} Å). The discussed error sources may both increase and decrease the value for a, and they are all within $\pm 2\times 10^{-4}$ Å. Since we have performed over 50 measurements on four samples with potentially slightly differing Al mole fractions (x), $\pm 2\times 10^{-4}$ Å is probably the best estimate for the deviation in the fit for the bulk lattice constant of $Al_{0.90}Ga_{0.10}As_ySb_{1-y}$. In addition, measurements on sample Sb 99-1 show that Eq. (4) can be used for y up to at least 0.067 and measurements on Sb 122 show that Eq. (4) can be used up to around 550 °C.

V. CONCLUSIONS

Measurements of the lattice constant of $Al_{0.90}Ga_{0.10}As_ySb_{1-y}$ from 30 to 398 °C for $y=0.003-0.059$ were performed. A polynomial function for the bulk lattice constant was derived from a fit to the resulting data. Measurements on Pt-coated samples at higher temperatures indicate that the polynomial function is valid up to around 550 °C. We have shown the lattice matching condition for growth of $Al_{0.90}Ga_{0.10}As_ySb_{1-y}$ lattice matched to GaSb. At 450 °C–550 °C, an As mole fraction of 0.063–0.061 should be used. An interpolation of the binary constituents (Al,Ga)(As,Sb) was shown to give a poor fit to the bulk lattice constant at elevated temperatures, probably due to the lack of data in literature for the thermal expansion coefficients, especially for AlSb.

ACKNOWLEDGMENTS

Thanks are due to Mike Pochet for assistance in improving the language of this article. This project was partly funded by the Research Council of Norway under Contract No. 177610/V30.

[1] A. Z. Li, J. X. Wang, Y. L. Zheng, G. P. Ru, W. G. Bi, Z. X. Chen, and N. C. Zhu, J. Cryst. Growth **127**, 566 (1993).

[2] A. Gassenq, L. Cerutti, A. Baranov, and E. Tournié, J. Cryst. Growth **311**, 1905 (2009).

[3] D. Donetsky, J. Chen, L. Shterengas, G. Kipshidze, and D. Westerfeld, J. Electron. Mater. **37**, 1770 (2008).

[4] J. B. Rodriguez, L. Cerutti, and E. Tournié, Appl. Phys. Lett. **94**, 023506 (2009).

[5] S. Suchalkin, S. Jung, G. Kipshidze, L. Shterengas, T. Hosoda, D. Westerfeld, D. Snyder, and G. Be-lenky, Appl. Phys. Lett. **93**, 081107 (2008).

[6] E. Selvig, G. Myrvågnes, R. Bugge, and B. O. Fimland, J. Cryst. Growth (submitted).

[7] O. Madelung, *Semiconductors—Basic Data*, 2nd ed. (Springer, Berlin, 1996).

[8] W. L. Bond, Acta Crystallogr. **13**, 814 (1960).

[9] M. Fatemi, Appl. Phys. Lett. **80**, 935 (2002).

[10] M. Fatemi, Acta Crystallogr., Sect. A: Found. Crystallogr. **61**, 301 (2005).

[11] M. Fatemi and R. E. Stahlbush, Appl. Phys. Lett. **58**, 825 (1991).

[12] I. Vurgaftman, J. R. Meyer, and L. R. Ram-Mohan, J. Appl. Phys. **89**, 5815 (2001).

[13] I. Vurgaftman and J. R. Meyer, J. Appl. Phys. **94**, 3675 (2003); see Ref. 10.

[14] J. C. Brice, *Properties of Gallium Arsenide*, 2nd ed. (Inspec, London/New York, 1990).

[15] G. A. Slack and S. F. Bartram, J. Appl. Phys. **46**, 89 (1975).

[16] D8 DISCOVER User Manual, Bruker AXS GmbH, 2006, Vol. 3.

[17] R. Resel, E. Tamas, B. Sonderegger, P. Hofbauer, and J. Keckes, J. Appl. Crystallogr. **36**, 80 (2003).

[18] T. A. Nilsen, M. Breivik, G. Myrvågnes, and B. O. Fimland, J. Vac. Sci. Technol. B **28**, C3I17 (2010).

[19] E. N. Maslen, *International Tables for Crystallography* (Kluwer Academic, Dordrecht, 1995), Vol. C.

[20] G. Giesecke and H. Pfister, Acta Crystallogr. **11**, 369 (1958).

8.3 Paper III - Thermal dependence of the lattice constant and the Poisson ratio of AlSb above room temperature

Journal of Crystal Growth 336 (2011) 29–31

III

Contents lists available at SciVerse ScienceDirect

Journal of Crystal Growth

journal homepage: www.elsevier.com/locate/jcrysgro

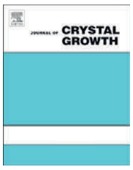

Thermal dependence of the lattice constant and the Poisson ratio of AlSb above room temperature

Tron Arne Nilsen*, Saroj Kumar Patra, Magnus Breivik, Bjørn-Ove Fimland

Department of Electronics and Telecommunications, Norwegian University of Science and Technology, NO-7491 Trondheim, Norway

ARTICLE INFO

Article history:
Received 27 June 2011
Accepted 16 September 2011
Communicated by M.S. Goorsky
Available online 24 September 2011

Keywords:
A1. High resolution X-ray diffraction
A3. Molecular beam epitaxy
B1. Antimonides
B2. Semiconducting aluminum compounds

ABSTRACT

Temperature dependent X-ray diffraction measurements were performed on two samples with AlSb epilayers of differing thickness grown on GaSb by molecular beam epitaxy to determine the temperature dependence of the lattice constant (a_{AlSb}) and the Poisson ratio of AlSb between 32 and 546 °C. At 32 °C, a_{AlSb} was found to be 6.1361 Å, which is in good agreement with previous work. At higher temperatures, it differed significantly from the linear extrapolation of previously published values (below 67 °C). A polynomial was fitted to the results: $a_{AlSb} = 6.1353 + 2.85 \times 10^{-5}T + 6.11 \times 10^{-9}T^2$ (Å). The Poisson ratio was found to be approximately constant up to 300 °C while decreasing above.

1. Introduction

AlSb is a binary often used as a part of III–V compounds grown on GaSb substrates. Compound antimonides containing Al are often used as cladding materials and quantum well barriers in antimonide based emitters. Previous work [1] suggests that in order to obtain thick epilayers of Al containing compound antimonides of high quality, lattice matching needs to be done at growth temperature. This requires the bulk lattice constants of the epilayer and the substrate to be known at typical growth temperatures. The bulk lattice constant can be obtained through direct measurement of the in-plane (a_x) and out-of-plane (a_z) lattice constants at growth temperature and using an estimated Poisson ratio from the binary constituents, or using Vegard's law and the lattice constant of the binaries at growth temperature. Previous work [2] has shown that using Vegard's law with currently known or estimated lattice constants of binaries at growth temperature is not accurate for $Al_{0.9}Ga_{0.1}As_ySb_{1-y}$.

There has been limited work reported on the thermal expansion and lattice constant of AlSb. Some theoretical work [3] has been performed for low temperatures and measurements have been made from 20 to 340 K [4]. No measurements of the thermal expansion from 67 °C up to typical growth temperatures for AlSb have been reported. To the authors' best knowledge, no previous work has been reported on the Poisson ratio of AlSb above room temperature (RT). The lattice constant of AlSb at RT used in literature was determined by Giesecke and Pfister [5] in 1957 and was reproduced by Bocchi et al. [6] in 1996. However, the original work by Giesecke and Pfister included measurements of several III–V materials and their findings on the lattice constant of GaSb is not in agreement with later published results [7,8]. In addition, the reproduction by Bocchi et al. [6] used the GaSb lattice constant value published by Straumanis and Kim [9], which is not in agreement with later works [7,8], to calculate the AlSb lattice constant from the separation between the AlSb peak and GaSb substrate peak in their X-ray diffraction (XRD) measurements.

In this work, we present the results of temperature dependent XRD measurements on two samples with AlSb epilayers of different thickness grown on GaSb by molecular beam epitaxy (MBE). We have determined the thermal expansion of AlSb and the temperature dependence of the Poisson ratio from 32 to 546 °C.

2. Theory

The relation between the bulk lattice constant (a) of a cubic lattice and the in-plane (a_x) and out-of-plane (a_z) lattice constants of the tetragonally distorted cubic lattice is given by [10]:

$$a = \frac{a_z + \frac{2C_{12}}{C_{11}} \cdot a_x}{1 + \frac{2C_{12}}{C_{11}}} \qquad (1)$$

where C_{11} and C_{12} are stiffness tensor elements of the strained material. Eq. (1) can also be expressed using the Poisson ratio

---

* Corresponding author.
E-mail addresses: tronarne@iet.ntnu.no (T.A. Nilsen), bjorn.fimland@iet.ntnu.no (B.-O. Fimland).

0022-0248/$ - see front matter © 2011 Elsevier B.V. All rights reserved.
doi:10.1016/j.jcrysgro.2011.09.034

$\nu = C_{12}/(C_{12}+C_{11})$:

$$a = a_z\left(\frac{1-\nu}{1+\nu}\right)+a_x\left(\frac{2\nu}{1+\nu}\right) \tag{2}$$

By using Eq. (2) and knowing the in-plane (a_{x1}, a_{x2}) and out-of-plane (a_{z1}, a_{z2}) lattice constants of two tetragonally distorted lattices of the same material with different degrees of distortion, both the bulk lattice constant and the Poisson ratio can be found. Solving Eq. (2) for both lattices gives:

$$\nu = \frac{1}{2\cdot\dfrac{a_{x2}-a_{x1}}{a_{z1}-a_{z2}}+1} \tag{3}$$

$$a = \frac{a_{x1}\cdot a_{z2}-a_{x2}\cdot a_{z1}}{(a_{x1}-a_{x2})-(a_{z1}-a_{z2})} \tag{4}$$

The linear thermal expansion coefficient (TEC) is defined as:

$$\alpha(T) = \frac{1}{a}\frac{da}{dT} \tag{5}$$

where a is the (temperature dependent) lattice constant of the material and T is the temperature. Eq. (5) can be approximated as:

$$\alpha(T) = \frac{1}{a(T_0)}\frac{da}{dT} \tag{6}$$

as long as $a/a(T_0)-1$ is small. The lattice constant at any given temperature T is then given by

$$a(T) = a(T_0)\left(1+\int_{T_0}^{T}\alpha(T)\,dT\right) \tag{7}$$

3. Experiment

Samples with a 500 nm GaSb buffer, an AlSb layer of differing thickness and a 50 nm GaSb cap layer were grown in a Varian Gen II Modular MBE system. The layers were grown on Te-doped (001)-oriented GaSb substrates with a doping concentration of $(2\text{–}7)\times10^{17}\,\mathrm{cm}^{-3}$. The epilayers were grown at 550 °C as measured by a Minolta Land Cyclops 241 pyrometer. Sample Sb 144-2 had an AlSb thickness of 74 nm, which is below the critical thickness of around 100 nm when a 50 nm GaSb cap is used [11,6]. The AlSb thickness of sample Sb 144-1 was 2.8 μm. A Bruker AXS D8 Discover X-ray diffractometer with a half circle geometry and equipped with an Anton-Paar DHS 900 temperature stage [12] was used to examine the AlSb layers at temperatures ranging from 32 to 546 °C in a nitrogen atmosphere. A modified version [8] of the zone technique [13,14] was used to determine a_x and a_z of the AlSb layer of each sample.

Table 1 shows the reflections measured for the different materials on the two samples. For the AlSb layer, reflections were not measured if the intensity was too low. For GaSb on Sb 144-1, the reflections were chosen to minimize the contribution of the strained 50 nm GaSb cap layer. In all cases both positive and negative geometries were measured for asymmetric reflections. Values of a_x and a_z used in the determination of the thermal expansion and the Poisson ratio are the average of four measurements in a row at a temperature without recalibration of tilt angle (χ) and azimuth angle (φ) between the measurements. In the following, a measurement series is defined as a series of measurements with varying temperature. For each measurement used in the determination of the lattice constant at 32 °C, the DHS 900 heating stage was taken off the X-ray diffractometer, the sample remounted and χ, φ calibrated after remounting the DHS 900. For sample Sb 144-2, the AlSb layer is thin enough that the AlSb peak will undergo a shift in peak position due to interference with the substrate peak [15]. In order to correct for this effect, the uncorrected values for the bulk lattice constant and the Poisson ratio were used with the simulation program Leptos-2 by Bruker AXS to simulate the peak positions of all reflections used for a sample identical to Sb 144-2 and a sample with a 3 μm unrelaxed AlSb layer. The lattice constants (a_x and a_z) were then calculated for both simulated cases and the differences in calculated lattice constants between the thick and thin sample were then used as corrections for the measurements on Sb 144-2.

4. Results and discussion

Table 2 shows values for the bulk lattice constant of AlSb (a_{AlSb}) at 32 °C deduced from our measurements using Eq. (1), C_{11}=87.69 GPa and C_{12}=43.41 GPa [4]. No temperature is given in the work of Bocchi et al. [6], but since Straumanis and Kim's [9] value of the GaSb lattice constant (a_{GaSb}) at 25 °C is used to calculate the AlSb lattice constant, it is assumed here that their measurements were at 25 °C. They reported a_{AlSb}=6.1353 Å which gives a lattice constant of 6.1355 Å at 32 °C, using a TEC of $5.2\times10^{-6}\,\mathrm{K}^{-1}$, which is 6×10^{-4} Å lower than our results. However, if their measurements are used with a_{GaSb}=6.0968 Å [7,8], a lattice constant for AlSb of 6.1362 Å is obtained at 25 °C and 6.1364 Å at 32 °C. Giesecke and Pfister [5] measured the lattice constant of AlSb to be 6.1356 Å at 18 °C after refractive index correction. This value has been misquoted in later works; Madelung [4] gives it as 6.1355 Å at 18 °C, which is the value before refractive index correction, while Vurgaftman et al. [16] gives it as 6.1355 Å at 25 °C. Using a TEC of $5.2\times10^{-6}\,\mathrm{K}^{-1}$ with Giesecke and Pfister's data [5], one finds a_{AlSb} = 6.1360 Å at 32 °C which agrees well with our results at 32 °C. From Table 2, the agreement with literature values, and the accuracy obtained with the same instrument and measurement method in our earlier work [8], we estimate the measurement accuracy to be within $\pm2\times10^{-4}$ Å.

Fig. 1 shows the bulk lattice constant of AlSb calculated by using Eq. (4) and our measurements of a_x and a_z for Sb 144-1 and Sb 144-2. Fig. 2 shows the Poisson ratio calculated from the same data and Eq. (3). In both cases the calculations are based on two measurement series of Sb 144-1 and one for Sb 144-2 in the temperature range from 348 °C to 546 °C. For the lower temperatures, three measurement series were used for Sb 144-1 and one for Sb 144-2. The accuracies of the calculated bulk lattice constant and the Poisson ratio of AlSb were estimated to $\pm3.5\times10^{-4}$ Å

Table 1
Reflections measured for GaSb and AlSb on samples Sb 144-1 and Sb 144-2.

Sample, material	Reflections measured
Sb 144-1, AlSb	115, 117, 226, 444, 002, 004, 006
Sb 144-1, GaSb	115, 117, 226, 004, 006
Sb 144-2, AlSb	115, 335, 444, 002, 004
Sb 144-2, GaSb	115, 117, 226, 335, 444, 002, 004, 006

Table 2
Lattice constant of AlSb at 32 °C.

Sample	Calc. a (Å)	σ (10^{-4} Å)	No. of measurements
Sb 144-1	6.1362	1.8	10
Sb 144-2	6.1360	1.2	3
All	6.1361	1.7	13

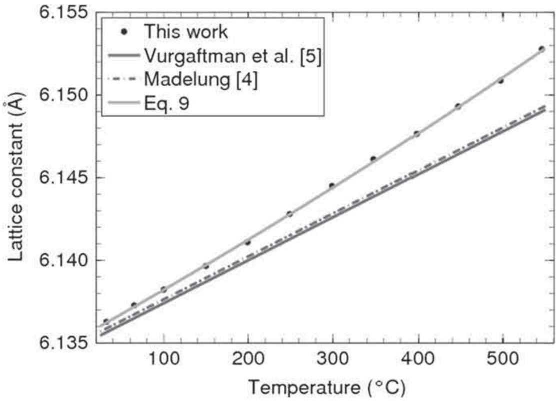

Fig. 1. Bulk lattice constant of AlSb vs. temperature; this work and linear extrapolation of the values given by Vurgaftman et al. [16] and Madelung [4].

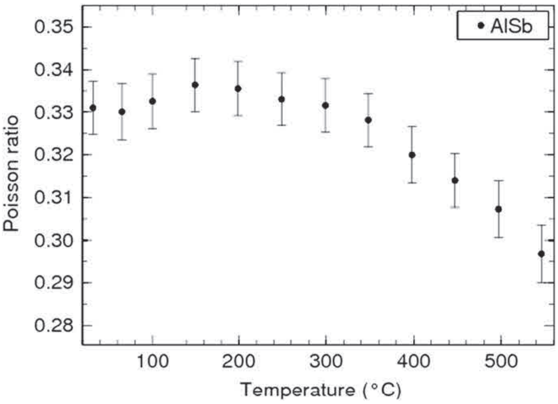

Fig. 2. Poisson ratio for AlSb vs. temperature.

and ± 0.008, respectively. As can be seen from Fig. 1, our results differ significantly from the linear extrapolation above 67 °C of earlier published values. A linear fit to our data gives the following expression for the bulk lattice constant of AlSb:

$$a_{AlSb} = 6.1350 + 3.20 \times 10^{-5} T \text{ (Å)} \tag{8}$$

where T is the temperature in °C. The standard error of the fit is 1.7×10^{-4} Å. Using Eq. (6) and $a(T_0) = 6.1358$ Å where $T_0 = 25$ °C gives a constant TEC of 5.2×10^{-6} K^{-1}, which is significantly higher than the TEC of 4.2×10^{-6} K^{-1} published earlier [4,16]. In an earlier work, we found a second order expression to be a good fit to our $Al_{0.9}Ga_{0.1}As_ySb_{1-y}$ data [2]. Due to the similarity between this material and AlSb, a second order expression was fitted to our data:

$$a_{AlSb} = 6.1353 + 2.85 \times 10^{-5} T + 6.11 \times 10^{-9} T^2 \text{ (Å)} \tag{9}$$

which has a standard error of 7.5×10^{-5} Å. Using Eq. (6) gives a temperature dependent linear TEC of

$$\alpha(T) = 4.65 \times 10^{-6} + 1.99 \times 10^{-9} T \text{ (K}^{-1}\text{)} \tag{10}$$

where T is in °C and $a(25\ °C) = 6.1360$ Å. The AlSb lattice constant obtained from Eq. (9) at 32 °C was found to be 1×10^{-4} Å higher than the average value for the AlSb lattice constant given in Table 2, whereas the lattice constant obtained from Eq. (8) is 1×10^{-4} Å lower than the average value from Table 2.

Fig. 2 shows the temperature dependence of the Poisson ratio for AlSb. It can be seen that the Poisson ratio is approximately constant up to 300 °C and then starts decreasing above. The value obtained at 32 °C is 0.331, which agrees well with the Poisson ratio of 0.331 calculated from room temperature values of C_{11} and C_{12}.

5. Conclusion

The lattice constant of AlSb at 32 °C was found to be 6.1361 Å with an accuracy of $\pm 2 \times 10^{-4}$ Å, which is in agreement with earlier published results [5]. The bulk lattice constant and the Poisson ratio of AlSb were deduced from XRD measurements in the temperature range 32–546 °C. The temperature dependent lattice constant was found to be different from linear extrapolation of earlier results [4,16]. The Poisson ratio was found to be approximately constant up to 300 °C and decreasing above this temperature.

Acknowledgments

We acknowledge funding from the Research Council of Norway under Contract No. 177610/V30.

References

[1] B.O. Fimland, R. Bugge, G. Myrvågnes, E. Selvig, in preparation.
[2] M. Breivik, T.A. Nilsen, G. Myrvågnes, E. Selvig, B.O. Fimland, Temperature dependent lattice constant of $Al_{0.90}Ga_{0.10}As_ySb_{1-y}$, Journal of Vacuum Science & Technology B: Microelectronics Processing and Phenomena 28 (3) (2010) 1–5.
[3] H.M. Kagaya, T. Soma, Specific heat and thermal expansion coefficient of AlP, AlAs and AlSb, Solid State Communications 62 (10) (1987) 707–709.
[4] O. Madelung, Semiconductors – Basic Data, second ed., Springer, Berlin, 1996.
[5] G. Giesecke, H. Pfister, Präzisionsbestimmung der Gitterkonstanten von $A^{I}IIIB^{V}$-Verbindungen, Acta Crystallographica 11 (5) (1958) 369–371.
[6] C. Bocchi, A. Bosacchi, C. Ferrari, S. Franchi, P. Franzosi, R. Magnanini, L. Nasi, Determination of lattice parameters in the epitaxial AlSb/GaSb system by high resolution x-ray diffraction, Journal of Crystal Growth 165 (1-2) (1996) 8–14.
[7] V.T. Bublik, J. Wilke, A.T. Pereversev, Die natur der festen lösungen der überschüssigen komponenten in unlegiertem galliumantimonid, Physica Status Solidi A Applied Research 73 (2) (1982) K271–K273.
[8] T.A. Nilsen, M. Breivik, G. Myrvågnes, B.O. Fimland, Thermal expansion of GaSb measured by temperature dependent X-ray diffraction, Journal of Vacuum Science & Technology B: Microelectronics and Processing and Phenomena 28 (3) (2010) 17–20.
[9] M.E. Straumanis, C.D. Kim, Lattice parameters, thermal expansion coefficients, phase width, and perfection of the structure of GaSb and InSb, Journal of Applied Physics 36 (12) (1965) 3822–3825.
[10] M. Fatemi, R.E. Stahlbush, X-ray rocking curve measurement of composition and strain in Si-Ge buffer layers grown on Si substrates, Applied Physics Letters 58 (8) (1991) 825–827.
[11] W.L. Sarney, L. Salamanca-Riba, J.D. Bruno, R.L. Tober, Strain relaxation in AlSb/GaSb heterostructures, Solid State Electronics 46 (10) (2002) 1643–1649.
[12] R. Resel, E. Tamas, B. Sonderegger, P. Hofbauer, J. Keckes, A heating stage up to 1173 K for X-ray diffraction studies in the whole orientation space, Journal of Applied Crystallography 36 (1) (2003) 80–85.
[13] M. Fatemi, An X-ray rocking curve technique for the absolute characterization of epitaxial layers and single-crystal solids, Applied Physics Letters 80 (6) (2002) 935–937.
[14] M. Fatemi, Absolute measurement of lattice parameter in single crystals and epitaxic layers on a double-crystal X-ray diffractometer, Acta Crystallographica A 61 (3) (2005) 301–313.
[15] C.R. Wie, Rocking curve peak shift in thin semiconductor layers, Journal of Applied Physics 66 (2) (1989) 985–988.
[16] I. Vurgaftman, J.R. Meyer, L.R. Ram-Mohan, Band parameters for III–V compound semiconductors and their alloys, Journal of Applied Physics 89 (11) (2001) 5815–5875.

8.4 Paper IV - Temperature dependent lattice constant of InSb above room temperature

Journal of Crystal Growth 381 (2013) 165–168

Contents lists available at ScienceDirect

Journal of Crystal Growth

journal homepage: www.elsevier.com/locate/jcrysgro

Temperature dependent lattice constant of InSb above room temperature

Magnus Breivik, Tron Arne Nilsen, Bjørn-Ove Fimland*

Department of Electronics and Telecommunications, Norwegian University of Science and Technology, NO-7491 Trondheim, Norway

A R T I C L E I N F O

Article history:
Received 19 April 2013
Received in revised form
28 June 2013
Accepted 29 June 2013
Communicated by P. Rudolph
Available online 5 July 2013

Keywords:
A1. Crystal structure
A1. High-resolution X-ray diffraction
A1. Substrates
B1. Antimonides
B2. Semiconducting indium compounds
B2. Semiconducting III–V materials

A B S T R A C T

Using temperature dependent X-ray diffraction on two InSb single crystalline substrates, the bulk lattice constant of InSb was determined between 32 and 325 °C. A polynomial function was fitted to the data: $a(T)=6.4791+3.28\times10^{-5}\times T+1.02\times10^{-8}\times T^2$ Å (T in °C), which gives slightly higher values than previously published (which go up to 62 °C). From the fit, the thermal expansion of InSb was calculated to be $\alpha(T)=5.062\times10^{-6}+3.15\times10^{-9}\times T\ \mathrm{K}^{-1}$ (T in °C). We found that the thermal expansion coefficient is higher than previously published values above 100 °C (more than 10% higher at 325 °C).

1. Introduction

InSb is an important binary for electrooptical components, and it is an important constituent in many semiconductor alloys such as InAsSb, GaInSb and GaInAsSb in the mid- and long wavelength infrared range (2–12 μm). The small bandgap of the InAsSb alloy allows wavelengths up to at least 10 μm [1] to be reached. However, for most of the range of the InAsSb lattice constant (6.06–6.48 Å), there are no substrates suitable for lattice matching. AlInSb or GaInSb metamorphic buffers have been utilized as virtual substrates for InAsSb alloys in laser structures [2–6], high electron mobility structures [7,8] and light emitting diodes [9]. GaInAsSb and GaInSb are also popular constituent alloys in semiconductor laser structures on GaSb in the mid-infrared wavelength range due to their small bandgaps.

Optimizing growth parameters, such as lattice matching at elevated temperatures, and modeling structures require accurate material parameters both at room temperature and at higher temperatures. We have previously examined the temperature dependent lattice constants of GaSb [10] and AlSb [11]. Preliminary studies of the thermal expansion of GaAs and InAs up to 400 °C and 300 °C, respectively, are in agreement with previous work [12,13]. For InSb, however, no measurements of the temperature dependent lattice constant above 62 °C [14] were found. The thermal expansion coefficient, α, was measured by Gibbons [15] from 4 to 300 K and by Bernstein and Beals [16] from room temperature up to 500 °C, both using the technique developed by Nix and MacNair [17], measuring the thermal expansion $\Delta l/l$ of a crystal of height l using interferometric measurements of monochromatic visible light.

In this work, temperature dependent X-ray diffraction (XRD) measurements of InSb(001) from 32 to 325 °C were performed. From these measurements the temperature dependent lattice constant and the thermal expansion of the crystal were calculated and the results compared to earlier work.

2. Theory

The linear thermal expansion coefficient, $\alpha(T)$, is expressed by the equation [18]

$$\alpha(T)=\frac{1}{a(T)}\frac{\mathrm{d}a(T)}{\mathrm{d}T}\simeq\frac{1}{a(T_0)}\frac{\mathrm{d}a(T)}{\mathrm{d}T}, \qquad (1)$$

where T is the temperature at which α is evaluated and T_0 is a reference temperature for which a is known, typically taken at room temperature. Using $a(T_0)$ in Eq. (1) is a good approximation for all temperatures in this study, since $(a(T)/a(T_0))-1$ is small.

3. Experiment

All measurements were performed on a Bruker AXS D8 Discover XRD diffractometer equipped with an Anton-Paar DHS 900 temperature dome [19]. Incident beam optics include a Göbel

---

* Corresponding author. Tel.: +47 73594424; fax: +47 73591441.
E-mail addresses: magnus.breivik@gmail.com, magnus.breivik@ntnu.no (M. Breivik), bjorn.fimland@ntnu.no (B.-O. Fimland).

0022-0248/$ - see front matter © 2013 Elsevier B.V. All rights reserved.
http://dx.doi.org/10.1016/j.jcrysgro.2013.06.034

mirror and V-groove resulting in $K_{\alpha 1}$ radiation, with a specified full-width at half maximum (FWHM) ($\Delta\theta$) of 0.007° (25″) for the Si 111 reflection. The X-ray beam spot size was approximately 1 mm by 0.3 mm and the temperature dome was continuously purged with 10–20 sccm N_2. No aperture was used on the detector, and the FWHM for the InSb(001) 004 reflection (θ) was typically between 0.007° and 0.008°. The scan resolution was 0.001°, and the scan time was set to give a peak intensity of about 10^4 counts or higher. The reflections measured were 115, 117, 226, 002, 004 and 008. A modified version [10] of the Zone Technique [20,21] was used to determine the lattice constant.

In this study, $1\times 1\ \text{cm}^2$ square samples of undoped epi-ready and test-grade InSb(001) substrates from Wafer Technologies were examined. The nominally undoped epi-ready substrate was specified n-type with a carrier concentration of $1\text{–}3\times 10^{14}\ \text{cm}^{-3}$, a Hall mobility of $5.1\text{–}5.7\times 10^5\ \text{cm}^2/\text{V s}$ and an average etch pit density (EPD) of $11\text{–}22\ \text{cm}^{-2}$, whereas the carrier concentration, Hall mobility and EPD were not specified for the test-grade substrate. The measurements were performed at 32, 65, 100, 150, 200, 250, 300 and 325 °C, as shown in Table 1, with a temperature change between each individual measurement. XRD measurements at higher temperatures were not performed due to a thermal decomposition of the sample surface above 325 °C.

The temperature offset between the sample surface and the thermocouple was determined from measurements of the temperature dependent lattice constant of Si, where the deviation between the published values and our measurements up to 890 °C was attributed to a thermal offset between the hot plate surface and the sample surface [10]. The thermal conductivities of Si and InSb [22] were then used to determine the thermal gradient through the samples and the surface temperature of the InSb samples. For temperatures above 226 °C, the thermal conductivity was extrapolated from the published data [22], and the highest estimated temperature offset, at 325 °C, was −1.3 °C.

The peak position was determined by the mid-point between the peak slopes at 75% of the peak intensity. Measurements where the in-plane (a_x) and out-of-plane (a_z) lattice constants differed by more than 3×10^{-4} Å were not used, as $a=a_x=a_z$ for cubic crystals such as InSb. A difference between a_x and a_z was attributed to the misalignment of sample rotation and tilt, which were realigned when $|a_x - a_z| > 3\times 10^{-4}$ Å. Changes in the rotation and tilt are most likely due to the non-uniform expansion of the hot plate [19]. $a=(a_x+a_z)/2$ was used in further calculations.

4. Results and discussion

The measurements resulted in a total of 82 values for a, with a minimum of 6 for each temperature. The average value for each measured temperature is listed in Table 1. The polynomial equation

$$a(T) = b_0 + b_1 \times T + b_2 \times T^2 (\text{Å}) \tag{2}$$

was fitted to the calculated values for the lattice constant at different temperatures by the least squares method. The best fit was for $b_0 = 6.4791$ Å, $b_1 = 3.28\times 10^{-5}$ Å/°C, $b_2 = 1.02\times 10^{-8}$ Å/°C^2 (T in °C), which had a standard error of 1.29×10^{-4} Å, and $\sigma_{\text{fit}} = \sqrt{(1/N)\sum_{i=1}^{N}(a_i(T) - a(T)_{\text{fit}})^2}$ for each temperature was less than 2.2×10^{-4} Å as shown in Table 1.

Using Eq. (1) and the polynomial fit with $a(T_0 = 25\ °\text{C}) = 6.4799$ Å gives $\alpha(T) = 5.062\times 10^{-6} + 3.15\times 10^{-9} \times\ T\ \text{K}^{-1}$ (T in °C). Comparisons to the previous work are shown in Fig. 1 and Tables 2 and 3. From the figure and tables it is reasonable to assume that the data source for Vurgaftman et al. [23] is Straumanis and Kim [14], which implies that the equation for the InSb lattice constant in Vurgaftman et al. [23] is only valid up to 62 °C.

For temperatures near room temperature, the thermal expansion coefficient α is similar to the published values, while the lattice constant a is 3–8 × 10^{-4} Å higher than values from the literature.

Table 1
Calculated lattice constants for each temperature T measured, and the standard deviation σ. a_{InSb} is the average lattice constant from the XRD measurements at the given temperature, while a_{fit} is the fitted value from Eq. (2).

T (°C)	a_{InSb} (Å)	σ (10^{-4} Å)	a_{fit} (Å)	σ_{fit} (10^{-4} Å)	No. of measurements (N)
32	6.4802	1.17	6.4802	1.18	7
65	6.4813	1.29	6.4813	1.33	8
100	6.4825	0.95	6.4825	0.95	9
150	6.4842	1.01	6.4843	1.01	7
200	6.4861	1.94	6.4861	2.10	7
201	6.4861	0.66	6.4861	0.72	6
249	6.4880	0.82	6.4879	0.86	9
250	6.4879	0.95	6.4880	1.45	6
299	6.4900	0.95	6.4898	1.63	6
300	6.4898	1.19	6.4899	1.35	10
325	6.4908	1.25	6.4908	1.25	7

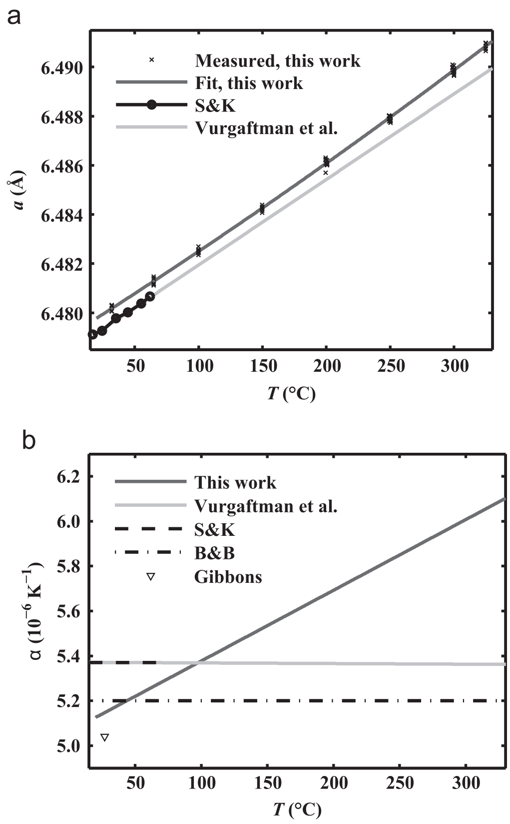

Fig. 1. Comparisons of our work with the previously published values. (a) Bulk lattice constant of InSb vs. temperature: this work, the XRD measurements by Straumanis and Kim [14] (S&K), and the review article by Vurgaftman et al. [23]. See also Table 2. (b) Thermal expansion coefficient vs. temperature for InSb: this work, the review article by Vurgaftman et al. [23], measurements by S&K, and interferometric measurements by Bernstein and Beals [16] (B&B) and by Gibbons [15]. See also Table 3. Our work suggests that the lattice constant, a, near room temperature is $3\text{–}8\times 10^{-4}$ Å higher than previously published values, and it shows a thermal expansion, α, higher than previously published above 100 °C.

Table 2
Comparison of the derived temperature dependent lattice constant, $a(T)$, with values from the literature. While Vurgaftman et al. [23] is a review article, it was included as it is one of the most used references for material parameters. Italics indicates an extrapolation of the data or data from a review article.

Source	17 (°C) (Å)	18 (°C) (Å)	25 (°C) (Å)	62 (°C) (Å)	300 (°C) (Å)
This work	*6.4797*	*6.4797*	*6.4799*	6.4812	6.4899
Straumanis and Kim [14]	6.47912		6.47937	6.48067	
Giesecke and Pfister [25]		6.4789			
Ozolin'sh et al. [24]			6.47962[a]		
Vurgaftman et al. [23]	*6.4791*	*6.4791*	*6.4793*	*6.4806*	*6.4889*

[a] Ozolin'sh et al. [24] is not corrected for refraction.

Table 3
Comparison of values for the thermal expansion coefficient α from this work and from the literature. The value from Bernstein and Beals [16] was extracted from the linear range in Fig. 1 of their article, excluding the non-linear thermal expansion above 475 °C.

Source	α (10^{-6} K^{-1})
This work	5.16–6.09 (32–325 °C)
Straumanis and Kim [14]	5.37 ± 0.5 (10–70 °C)
Gibbons [15]	5.04 (300 K)
Bernstein and Beals [16]	≃5.2 (25–475 °C)
Vurgaftman et al. [23]	5.37[a]

[a] Value from Vurgaftman et al. [23] was deduced by us from their equation for $a(T)$.

Table 4
XRD control measurements (of lattice constants) for GaSb and InSb. The control measurements were taken separately from the measurements used to fit Eq. (2).

Sample	Temperature (°C)	Nilsen et al. [10] (Å)	Control (Å)
GaSb	32	6.0971	6.0971
	150	6.1019	6.1018
Sample	Temperature (°C)	Eq. (2) (Å)	Control (Å)
InSb	32	6.4802	6.4801
	150	6.4843	6.4842

It is known that large concentrations of impurities, via the size effect and free carriers [26], or defects may cause measurable variations in the lattice constant. The free carrier contribution can be calculated from Eq. (1) in Leszczynski et al. [26]; using a deformation potential of −7.3 eV [23], a bulk modulus of 47 GPa [27] and a free electron concentration of 3×10^{14} cm^{-3} result in a positive contribution to the lattice constant of 1.6×10^{-8} Å at 25 °C. A measurable contribution of 1×10^{-4} Å would require a free electron concentration of 1.9×10^{18} cm^{-3}. For our samples we can thus rule out any measurable contributions to the lattice constant due to this effect.

Straumanis and Kim [14] reviewed several papers regarding the lattice constant of InSb at room temperature, and a steady increase in the value from 6.465 Å in 1926 [28] to 6.47932 Å in 1963 [24] is observed. One could speculate that this might, at least partly, be due to an improving crystal quality over the years, with a lower concentration of contracting defects and impurities. The low specified carrier concentration of $1–3\times10^{14}$ cm^{-3}, high Hall mobility of $5.1–5.7\times10^{5}$ cm^2/V s and low EPD of 11–22 cm^{-2} suggest that the defect and impurity concentrations for our epi-ready sample are low.

Measurements of the Si lattice constant by powder XRD have shown a reduced lattice constant of about 1.5×10^{-4} Å as compared to the single crystalline XRD measurements [29]. Hubbard and Mauer [30] point out that an absorption correction of the measured reflection must be performed for powder diffraction measurements due to an uneven absorption of the diffracted X-rays in spherical crystals. For powder samples of small spherical Si crystals with a diameter of 0.25 mm, the suggested correction was $+0.79\times10^{-4}$ Å when using the 444 reflection [30]. This effect could explain part of the difference between the data of Straumanis and Kim [14], Giesecke and Pfister [25] and Ozolin'sh et al. [24], all measured by powder XRD, and our data, as we have used nominally undoped and high purity single crystalline InSb samples.

Additionally, for Ozolin'sh et al. [24] the result is not corrected for refraction. Based on the refraction correction method for powder diffraction measurements used by Giesecke and Pfister [25], with experimental parameters for Ozolin'sh et al. [24], an increase of a in the range $1.2–2.0\times10^{-4}$ Å can be expected for the results. Correcting the values given in Ozolin'sh et al. [24] for both refraction and absorption in powder would result in a lattice constant close to our extrapolated value at 25 °C (i.e. to within the experimental error of our measurements).

In order to verify the accuracy of our InSb measurements, the GaSb lattice constant at 32 and 150 °C was measured and compared to published values. In addition, the InSb lattice constant was measured in the same session and compared to Eq. (2). The results are shown in Table 4 and show good agreement with published data for GaSb and our fit for InSb.

5. Conclusions

The temperature dependent lattice constant and thermal expansion of bulk InSb from 32 to 325 °C were determined using high-resolution X-ray diffraction. The results were compared to earlier work for the temperature range of 17–62 °C where the lattice constant was found to be slightly higher than previously reported [14,24,25], which could be due to a difference in measurement techniques and structural quality of samples. The thermal expansion was found to be close to measured values in the previous works [14-16] for temperatures below 100 °C, while it was found to be higher for temperatures above 100 °C.

Acknowledgments

This project was partly funded by the Research Council of Norway under Contract no. 177610/V30.

References

[1] S.P. Svensson, W.L. Sarney, H. Hier, Y. Lin, D. Wang, D. Donetsky, L. Shterengas, G. Kipshidze, G. Belenky, Band gap of InAs$_{1-x}$Sb$_x$ with native lattice constant, Physical Review B 86 (2012) 245205, http://dx.doi.org/10.1103/PhysRevB.86.245205, URL: http://link.aps.org/doi/10.1103/PhysRevB.86.245205.

[2] E.A. Pease, L.R. Dawson, L.G. Vaughn, P. Rotella, L.F. Lester, 2.5–3.5 μm optically pumped GaInSb/AlGaInSb multiple quantum well lasers grown on AlInSb metamorphic buffer layers, Journal of Applied Physics 93 (6) (2003) 3177–-3181, http://dx.doi.org/10.1063/1.1544425, URL 〈http://link.aip.org/link/?JAP/93/3177/1〉.

[3] G. Kipshidze, T. Hosoda, W. Sarney, L. Shterengas, G. Belenky, High-power 2.2−μm diode lasers With metamorphic arsenic-free heterostructures, IEEE Photonics Technology Letters 23 (5) (2011) 317–319, http://dx.doi.org/10.1109/LPT.2010.2103053, ISSN: 1041-1135.

[4] G.R. Nash, S.J. Smith, S.D. Coomber, S. Przeslak, A. Andreev, P. Carrington, M. Yin, A. Krier, L. Buckle, M.T. Emeny, T. Ashley, Midinfrared GaInSb/AlGaInSb quantum well laser diodes grown on GaAs, Applied Physics Letters 91 (13) (2007) 131118, http://dx.doi.org/10.1063/1.2793821, URL 〈http://link.aip.org/link/?APL/91/131118/1〉.

[5] M. Yin, G.R. Nash, S.D. Coomber, L. Buckle, P.J. Carrington, A. Krier, A. Andreev, S.J.B. Przeslak, G. de Valicourt, S.J. Smith, M.T. Emeny, T. Ashley, GaInSb/AlInSb multi-quantum-wells for mid-infrared lasers, Applied Physics Letters 93 (12) (2008) 121106, http://dx.doi.org/10.1063/1.2990224, URL 〈http://link.aip.org/link/?APL/93/121106/1〉.

[6] N.E. Fox, A.D. Andreev, G.R. Nash, T. Ashley, T.J.C. Hosea, Room temperature spectroscopic characterization of mid-infrared GaInSb quantum-well laser structures, Semiconductor Science and Technology 25 (3) (2010) 035005, URL 〈http://stacks.iop.org/0268-1242/25/i=3/a=035005〉.

[7] G. Delhaye, L. Desplanque, X. Wallart, Metamorphic high electron mobility Te-doped AlInSb/GaInSb heterostructures on InP(001), Journal of Applied Physics 104 (6) (2008) 066105, http://dx.doi.org/10.1063/1.2978365, URL 〈http://link.aip.org/link/?JAP/104/066105/1〉.

[8] L. Desplanque, D. Vignaud, S. Godey, E. Cadio, S. Plissard, X. Wallart, P. Liu, H. Sellier, Electronic properties of the high electron mobility Al$_{0.56}$In$_{0.44}$Sb/Ga$_{0.5}$In$_{0.5}$Sb heterostructure, Journal of Applied Physics 108 (4) (2010) 043704, http://dx.doi.org/10.1063/1.3475709, URL 〈http://link.aip.org/link/?JAP/108/043704/1〉.

[9] T.G. Tenev, A. Palyi, B.I. Mirza, G.R. Nash, M. Fearn, S.J. Smith, L. Buckle, M. T. Emeny, T. Ashley, J.H. Jefferson, C.J. Lambert, Energy level spectroscopy of InSb quantum wells using quantum-well LED emission, Physical Review B 79 (2009) 085301, http://dx.doi.org/10.1103/PhysRevB.79.085301.

[10] T.A. Nilsen, M. Breivik, G. Myrvågnes, B.O. Fimland, Thermal expansion of GaSb measured by temperature dependent x-ray diffraction, Journal of Vacuum Science and Technology B 28 (3) (2010), http://dx.doi.org/10.1116/1.3336341, C3I17–C3I20.

[11] T.A. Nilsen, S.K. Patra, M. Breivik, B.O. Fimland, Thermal dependence of the lattice constant and the Poisson ratio of AlSb above room temperature, Journal of Crystal Growth 336 (1) (2011) 29–31, http://dx.doi.org/10.1016/j.jcrysgro.2011.09.034, ISSN: 0022-0248, URL 〈http://www.sciencedirect.com/science/article/pii/S0022024811007913〉.

[12] J.C. Brice, Properties of Gallium Arsenide, 2nd ed., Inspec, 1990.

[13] N.N. Sirota, Y.I. Pashintsev, Dynamic displacements of atoms as related to linear expansion coefficients in aluminum, gallium and indium arsenides, Doklady Akademii Nauk SSSR 127 (3) (1959) 609–611.

[14] M.E. Straumanis, C.D. Kim, Lattice parameters, thermal expansion coefficients, phase width, and perfection of the structure of GaSb and InSb, Journal of Applied Physics 36 (12) (1965) 3822–3825, http://dx.doi.org/10.1063/1.1713955, ISSN: 00218979.

[15] D.F. Gibbons, Thermal expansion of some crystals with the diamond structure, Physical Review 112 (1) (1958) 136–140, http://dx.doi.org/10.1103/PhysRev.112.136.

[16] L. Bernstein, R.J. Beals, Thermal expansion and related bonding problems of some III–V compound semiconductors, Journal of Applied Physics 32 (1) (1961) 122–123, http://dx.doi.org/10.1063/1.1735941, ISSN: 00218979.

[17] F.C. Nix, D. MacNair, An interferometric-dilatometer with photographic recording, Review of Scientific Instruments 12 (2) (1941) 66–70, http://dx.doi.org/10.1063/1.1769828, URL 〈http://link.aip.org/link/?RSI/12/66/1〉.

[18] G.A. Slack, S.F. Bartram, Thermal expansion of some diamondlike crystals, Journal of Applied Physics 46 (1) (1975) 89–98, http://dx.doi.org/10.1063/1.321373, URL 〈http://link.aip.org/link/?JAP/46/89/1〉.

[19] R. Resel, E. Tamas, B. Sonderegger, P. Hofbauer, J. Keckes, A heating stage up to 1173 K for X-ray diffraction studies in the whole orientation space, Journal of Applied Crystallography 36 (1) (2003) 80–85, http://dx.doi.org/10.1107/S0021889802019568.

[20] M. Fatemi, An X-ray rocking curve technique for the absolute characterization of epitaxial layers and single-crystal solids, Applied Physics Letters 80 (6) (2002) 935–937, http://dx.doi.org/10.1063/1.1447012, URL 〈http://link.aip.org/link/?APL/80/935/1〉.

[21] M. Fatemi, Absolute measurement of lattice parameter in single crystals and epitaxic layers on a double-crystal X-ray diffractometer, Acta Crystallographica Section A 61 (3) (2005) 301–313, http://dx.doi.org/10.1107/S0108767305004496.

[22] W. Nakwaski, Thermal conductivity of binary, ternary, and quaternary III–V compounds, Journal of Applied Physics 64 (1) (1988) 159–166, http://dx.doi.org/10.1063/1.341449, URL 〈http://link.aip.org/link/?JAP/64/159/1〉.

[23] I. Vurgaftman, J.R. Meyer, L.R. Ram-Mohan, Band parameters for III–V compound semiconductors and their alloys, Journal of Applied Physics 89 (11) (2001) 5815–5875, http://dx.doi.org/10.1063/1.1368156, URL 〈http://link.aip.org/link/?JAP/89/5815/1〉.

[24] G.V. Ozolin'sh, G.K. Averkieva, N.A. Goryunova, A.F. Ievin'sh, An X-ray diffraction investigation of gallium and indium antimonides, Kristallografiya 8 (2) (1963) 272. (English Transl.: Soviet Physics, Crystallography 8 (1963) 207).

[25] G. Giesecke, H. Pfister, Präzisionsbestimmung der Gitterkonstanten von $A^{\mathrm{III}}B^{\mathrm{V}}$-Verbindungen, Acta Crystallographica 11 (5) (1958) 369–371, http://dx.doi.org/10.1107/S0365110X58000979.

[26] M. Leszczynski, J. Bak-Misiuk, J. Domagala, J. Muszalski, M. Kaniewska, J. Marczewski, Lattice dilation by free electrons in heavily doped GaAs:Si, Applied Physics Letters 67 (4) (1995) 539–541.

[27] M.L. Cohen, Calculation of bulk moduli of diamond and zinc-blende solids, Physical Review B 32 (12) (1985) 7988.

[28] V.M. Goldschmidt, Skrifter utgitt av Det Norske Videnskaps-Akademi i. Oslo, I. Matematisk-naturvitenskapelig Klasse 8 (1926) 110.

[29] Y. Okada, Y. Tokumaru, Precise determination of lattice parameter and thermal expansion coefficient of silicon between 300 and 1500 K, Journal of Applied Physics 56 (2) (1984) 314–320.

[30] C.R. Hubbard, F.A. Mauer, Precision and accuracy of the Bond method as applied to small spherical crystals, Journal of Applied Crystallography 9 (1) (1976) 1–8.

Chapter 9

Conclusions and further work

To summarize, this work has examined the crystal parameters at elevated temperatures for the thickest layers used in GaSb-based laser diodes, the cladding layers. Furthermore, an investigation of the binaries which form the constituents for laser epilayers have been examined. Laser structures have been grown by molecular beam epitaxy (MBE), Y-junction and Fabry-Perot lasers (FPLs) have been processed and tested, and Y-junction waveguides have been simulated. The conclusions have been divided into two parts. First, the conclusions relating to the X-ray diffraction (XRD) measurements in the included papers (chapter 8) are presented in section 9.1. Second, the conclusions relating to Y-junction lasers presented in chapters 4 to 7 are presented in section 9.2. Finally, suggestions for further work are given in section 9.3.

9.1 XRD measurements

The temperature dependent lattice constants of the binaries GaSb, AlSb and InSb, and the quaternary $Al_{0.9}Ga_{0.1}As_ySb_{1-y}$ have been measured.

We have measured the temperature dependent lattice constant of GaSb up to 546°C using XRD. Our measurements fit well with the previously published values from Bublik et al. [1], and it can therefore be concluded that both sets of data are valid and should be used for the temperature dependent GaSb lattice constant. We also confirmed our measurement technique by measuring the temperature dependent lattice constant of Si and comparing it to literature values presented by Yasumasa and Yozo [151], where we have a good fit. At 550°C, a deviation of 2×10^{-4} Å in the measured lattice constant of Si between our and Yasumasa and Yozo [151]'s measurements was found, which was accounted to a thermal gradient through the wafer. Measurements of the lattice constant of Si up to 890°C were then used to determine the thermal gradient through the sample. The determined thermal gradient of Si was then used to estimate the thermal gradient for all samples presented in our publications.

We have also measured $Al_{0.9}Ga_{0.1}As_ySb_{1-y}$ epilayers on either GaSb or GaAs for y ranging from 0.003 to 0.059 up to 398°C using XRD, and determined the temperature dependent lattice constant, $a(T)$, and the thermal expansion $\alpha(T)$. Measurements on Pt-coated samples at higher temperatures indicate that the presented polynomial for $a(T)$ is valid up to 550°C. The required y for lattice matching at temperatures up to 550°C was derived. An interpolation of the binary constituents (Al,Ga)(As,Sb) was shown to give a poor fit with the bulk lattice constant of $Al_{0.9}Ga_{0.1}As_ySb_{1-y}$ at elevated temperatures, most likely due to lack of data for the thermal expansion coefficients in the literature, especially for AlSb. This information is directly relevant to grown laser structures, since this alloy is used as the cladding material. Lattice matching at growth temperature increases the critical thickness during growth, which reduces the risk of dislocations, not just in the cladding layers, but also in the following core and multiple quantum wells (MQW) layers.

The temperature dependent lattice constant of AlSb was investigated. Measurements of AlSb epilayers on GaSb up to 546°C by XRD were performed. We found that the lattice constant and thermal expansion above room temperature were larger than previously reported (up to 67°C [90]). By using AlSb epilayers of different strain, we were also able to determine the Poisson ratio of AlSb.

We have measured the temperature dependent lattice constant of InSb from 32°C to 325°C by XRD. Our measurements indicate that the lattice constant for InSb was larger than previously reported, most likely due to better crystalline quality and in part due to the measurement techniques used, where previous measurements have been mainly powder diffraction measurements. We also found that the thermal expansion above 100°C was higher than previously reported.

These data will help to improve the growth of epilayers sensitive to strain, where lattice matching is important for increasing the critical thickness and crystal quality.

9.2 Y-junction lasers

Two laser material samples (Sb 142 and Sb 145) were grown and processed into Y-junction laser diodes using standard cleanroom processes. The Y-junction laser diodes were tested and single-mode behavior was observed from sample Sb 145. Optical power, wavelength, near and far field of different Y-junction lasers and FPL were measured. It was concluded that large optical losses in the bent waveguide of the lasers resulted in no contribution to the tuning from the bent waveguide. The Y-junction waveguides were simulated using 2D beam propagation method

(BPM), and the simulation results suggested that the optical losses were caused by a low refractive index contrast and that waveguide roughness is of less importance for the waveguiding properties of Y-junction lasers. It was suggested that the (2D) refractive index contrast should be at least 0.03. Cross section scanning electron microscope (SEM) characterization confirmed a poor etch depth. This is the most likely reason for the lack of interferometric tuning from the processed Y-junction lasers.

The reasons for the poor etch depth were discussed, such as problems with the profilometer measurement, loading effects from the dry etch, leftover etch mask on the sample, poor selectivity determination and/or problems with the etchant gas.

The results suggest that an increased refractive index contrast, by e.g. increasing the ridge etch depth, should result in functioning Y-junction laser diodes. Suggestions for further work for fabricating functioning laser diodes, including suggestions related directly to Y-junction laser diodes, are presented in section 9.3.

9.3 Further work

To improve the Y-junction laser performance, and mid-infrared laser structures in general, many modifications can be explored. Ideas and suggestions are presented here.

9.3.1 Computations and simulations

Improved simulations of laser diodes An increased focus on modeling and simulating laser structures would be beneficial for fabrication process of Y-junction lasers. This would help to improve the grown structures, and give insight to which parameters give significant changes in the laser diodes.

Different aspects of the laser diodes could be simulated. Examples include modeling and simulating the electrical characteristics of the p-i-n diode, to optimize the doping concentration and the doping profile, and to determine the impact of different epilayer thicknesses and ridge etch profile. 3D optical modelling and simulations of the Y-junction waveguides would give further insight into the proper etch depths and the impact of process related issues, e.g. roughness. Such simulations would provide more information than the 2D BPM simulations presented in chapter 7.

When the electrical and optical properties have been analyzed, laser simulations, including both electrical and optical properties, would result in further understanding of the design aspects of the laser diodes. This includes both the compositions and thicknesses of the laser material, and the processed laser structure, where an improved understanding of the gain and lasing properties of the

Y-junction laser would be useful. E.g. the large optical intensity inside the common section compared to the straight and bent part of the laser after the Y-splitter may have an appreciable impact on the lasing properties of the diodes, such as maximum power, side-mode suppression ratio (SMSR) etc.

Modelling and simulation of the band structure for AlGaAsSb An ab-initio modelling and simulation of the band structure for AlGaAsSb could be helpful for determining its electrical properties [152]. This is especially interesting for n-doped AlGaAsSb with more than 50% Al, due to the band gap minima in the X direction in *k*-space [98] (see section 3.2.2 and fig. 3.1). Devi et al. [153] have performed an ab-initio study of structural, electronic and optical properties of $Al_{1-x}Ga_xSb$. However, their results are in poor agreement with experimental values; for $Al_{0.5}Ga_{0.5}Sb$ their calculations resulted in $E_g = 0.1269$ eV, while the data from Donati et al. [154] suggests it is about 1.4185 eV. This suggests that further work is needed.

Previous studies in our group suggest that the crystalline quality of $Al_{0.9}GaAs_ySb$ grown on GaSb is optimum if the lattice matching is made at or close to growth temperature [59]. However, the electrical properties have not been characterized. When the AlGaAsSb epilayer is strained, the degenerate conduction band minima in the X-valley could be lifted. It would be helpful to know if the conduction band minimum is in the in-plane crystal directions, in the out-of-plane direction, or if something else happens. This can significantly affect the electrical properties of the laser diode, and further investigations should be made. An experimental study of the electrical properties of the cladding layer as a function of strain could also be beneficial for improving the laser diode performance.

Studies of AlGaAs/GaAs suggest that the introduction of a conduction band minimum in the L or X valley, depending on the Al content, are related to the microscopic strain induced by the Al atoms [155]. The same effect may also be present in AlGaAsSb/GaSb, and a literature study of the electrical properties of AlGaAs may give more insight into the matter.

Alternative interferometric structures An investigation into other interferometric waveguide structures could be of interest to improve the SMSR and tunability of the lasers. An interesting alternative is V-coupled cavities [156, 157], where the SMSR can be improved by coupling two waveguides optically over a well defined distance instead of intersecting the waveguides like in the Y-junction structure.

Improvements to the Y-junction laser structure could also be made, such as a third waveguide [46], a multi-mode interferometer coupler, and/or Bragg reflectors [158]. However, a working Y-junction laser should be fabricated before increasing the complexity of the structure.

Leaky modes Another interesting possibility is to introduce an extra modulation on the cavity gain by intentionally using leaky modes (see section 2.1.2). This can be achieved by growing a thin lower cladding layer to allow for the bound mode to leak into the substrate, due to the substrates large refractive index n. The modulation period would be determined by the substrate thickness, while the amplitude is determined by the lower cladding thickness. This effect has been demonstrated for InGaAs/GaAs laser diodes with AlGaAs cladding layers [74]. The benefit would be an increased SMSR. However, the modulation curve is adjusted by changing the substrate thickness, which would be a major drawback. Small adjustments may be achievable by changing the temperature of the laser device.

9.3.2 Growth and material characterization

Reduction of the threshold current density Simple modeling suggests that the optical confinement in the core is poor for the lasers using a core width of about 442 nm (see appendix B), which was used for our lasers. Increasing the core width results in an increase of n_{eff}. The implications of this are a larger overlap of the gain medium and the optical field, and a possible reduction of the required cladding thickness. Using a thicker core has been documented in the literature to decrease the threshold current density [159]. Garbuzov et al. [159]'s results suggest that an increase in the core size from 0.4 to 0.8 µm should reduce the internal losses almost ten-fold, mainly due to losses in the cladding layer.

The DX centers present in n-type cladding layers result in a reduced doping efficiency, with ionization energies which could be more than 100 meV, see section 3.2.2. A reduction in the n-type cladding layer thickness could help decrease the series resistance of the device, which would also reduce heating close to the gain medium.

Electrical properties of AlGaAsSb According to Li et al. [98] the band gap of $\text{Al}_x\text{Ga}_{1-x}\text{As}_{0.03}\text{Sb}_{0.97}$ changes from direct to indirect for $x = 0.25$. It is reasonable to believe that strain will affect the band structure of AlGaAsSb as it does for InGaAsSb, see section 3.1.3. It is beneficial that the band gap is, if possible, direct in the MQW barriers so that the charge carriers can easily enter the wells, since their momentum k is small.

By using the tilted sample method, described by Nilsen et al. [113], a single sample can be grown with varying As and Al incorporation across the sample. By mapping the sample along the x and y-directions using XRD and photoluminescence (PL), the composition, strain and band gap properties could be determined;

when the band gap changes from direct to indirect, a drop in the PL from the layer is expected. This information could be beneficial when choosing appropriate composition of the MQW and separate confinement heterostructure (SCH).

It has also been suggested that the deep ionization levels help to increase the SMSR, due to the Te-doped cladding layer acting as a saturable absorber [160]. This increases the optical losses of modes whose longitudinal mode maxima are spatially located between the maxima of the dominating mode.

Alternatively, measurements could be designed to experimentally determine the electrical properties of n-doped AlGaAsSb layers. It would be beneficial to differentiate between in-plane and out-of-plane electrical properties.

Longer wavelengths Developing gain material for longer wavelengths is important for increasing the number of gas species that can be detected. Especially wavelengths around 2.35 µm and 3.5 µm provide atmospheric windows with available gas species, as shown in fig. 1.1. This may require growth of AlGaInAsSb, and an effort should be made to develop laser material and laser diodes for these longer wavelengths.

Refractive indices of AlGaAsSb alloys Gonzalez-Cuevas et al. [84] suggest AlSb has a refractive index of about 3.5 at 0.5 eV, while newer work by Jung et al. [87] suggests 3.23 at 0.7 eV. There seems to be a lack of data for the refractive index of $\mathrm{Al}_x\mathrm{Ga}_{1-x}\mathrm{As}_y\mathrm{Sb}_{1-y}$ lattice matched to GaSb for $x > 0.5$, which are important alloys for optical confinement for GaSb-based lasers and waveguides. An investigation of the refractive indices of $\mathrm{Al}_x\mathrm{Ga}_{1-x}\mathrm{As}_y\mathrm{Sb}_{1-y}$ lattice matched to GaSb for $x > 0.5$ could be beneficial for optimizing the design of the waveguide for our laser structures.

Bowing parameters While the lattice constant of alloys can be approximated by a linear interpolation of the lattice constants for the binary constituents, there is often a small deviation between the linear interpolation and the actual lattice constant. This deviation is usually expressed by the bowing parameter B in the following equation:

$$a = xa_1 + x(1-x)B + (1-x)a_2 \tag{9.1}$$

Here $a_{1,2}$ are the lattice constants of the binary constituents of the alloy and a is the lattice constant for the alloy, e.g. the lattice constants GaSb and InSb for GaInSb. A binary interpolation for $\mathrm{Al}_{0.9}\mathrm{Ga}_{0.1}\mathrm{Sb}$ using our measured values for AlSb and GaSb extrapolated to 25°C yields a result of 6.1321 Å, while extrapolating the lattice constant from our results for $\mathrm{Al}_{0.9}\mathrm{Ga}_{0.1}\mathrm{As}_y\mathrm{Sb}_{1-y}$ with $y = 0$

yields a value of 6.1317 Å, a deviation of 4×10^{-4} Å[1]. To account for such discrepancies, the temperature dependent bowing parameter B should be determined (by XRD) for the AlGaAsSb and GaInAsSb material systems. Determination of B would further increase the accuracy of the lattice constant used for calculations regarding strain at both room temperature and higher temperatures, such as growth temperatures.

9.3.3 Laser processing

Improvement of the etch process To produce working interferometric lasers, better control of the etch process is needed. In-situ etch depth measurements would result in better control. One option would be to use interferometric measurements during the etch process, which could be used to determine the etched depth of the laser diodes. Another option would be to use an end-point detection system, where a thin layer containing e.g. In could be inserted into the laser structure during growth. By using an optical emission detector in the etch chamber, the etch could then be stopped when this layer is reached. These detectors measure the emitted light from the plasma, which relates to the material being etched [161]. This would, however, require a modification of the laser structure, and any side-effects of introducing an In-containing layer would have to be investigated.

Since an interferometric laser measurement system is available for the inductively coupled plasma reactive ion etching (ICP-RIE) at NTNU Nanolab (`http://www.norfab.no/lab-facilities/ntnu-nanolab/`), in-situ etch depth measurements using this system should be utilized.

Improvement of bonding pad metal adhesion to insulation Increased adhesion of the bonding pad metal to the insulation would be beneficial for a good wirebonding process. One alternative would be to replace the ma-N 440 with e.g. SiO2 or SiN. Improved adhesion can also be achieved by increasing the metal thickness, which may require changes to the lift-off process parameters.

Surface passivation Capasso and Williams [162] have suggested that a hydrogen or hydrogen-nitrogen, such as ammonia (NH_3), plasma can be used to passivate the surface of GaAs and GaSb and related materials. It could be beneficial to investigate if an H_2 plasma step at the end of the ICP-RIE etch could improve the performance of the laser diodes, due to e.g. a reduced surface recombination on the sidewalls of the laser ridge.

---

[1] Using $B = -4 \times 10^{-3}$ Å would account for the deviation (within our measurement uncertainty).

9.3.4 Testing of laser diodes

Top-down measurements of the optical power leakage By connecting a sensitive IR camera to a microscope, it may be possible to directly measure the optical leakage from the bent waveguide. In conjunction with beam propagation simulations, this could give further insight into the waveguiding nature of the Y-junction laser diodes.

Replacement of the multimode fiber setup It is clear from the sub-threshold measurements presented in section 6.4 and fig. 6.5 that our fiber setup should not be used for these measurements. A free space setup or single-mode fiber may remove the observed oscillations, and such setups should be investigated.

Appendix A

Important material parameters

In this chapter an overview of important material parameters are shown. This data gives an overview of the properties of the alloys of AlGaInAsSb. Figure A.1 shows the band gaps as a function of material and lattice constant. This data is taken from Donati et al. [154], and the values for E_g are given for 0 K, and will be slightly higher than room temperature values. The band gap for e.g. GaSb will change from about 0.81 eV at 0 K to about 0.78 eV at 300 K [163]. Besides the temperature, other parameters such as strain and doping will also affect the band gap. In fig. A.2, the same data is presented, but instead of E_g, it is presented by the expected recombination wavelength $\lambda \simeq 1.24/E_g$.

In fig. A.3, the refractive indices n are shown. Note that the values for layers with high Al content, such as AlSb and AlGaAsSb, are probably over-estimated by the semi-empirical paper from Gonzalez-Cuevas et al. [84] The refractive indices were extracted from fig. 2 in Gonzalez-Cuevas et al. [84], at 0.5 eV ($\lambda \simeq 2.5$ µm).

In fig. A.4 the conduction band offset (CBO) and valence band offset (VBO) are shown as a function of material and lattice constant. This information is useful when designing quantum wells (QWs) and defining proper electron and hole confinement in laser structures.

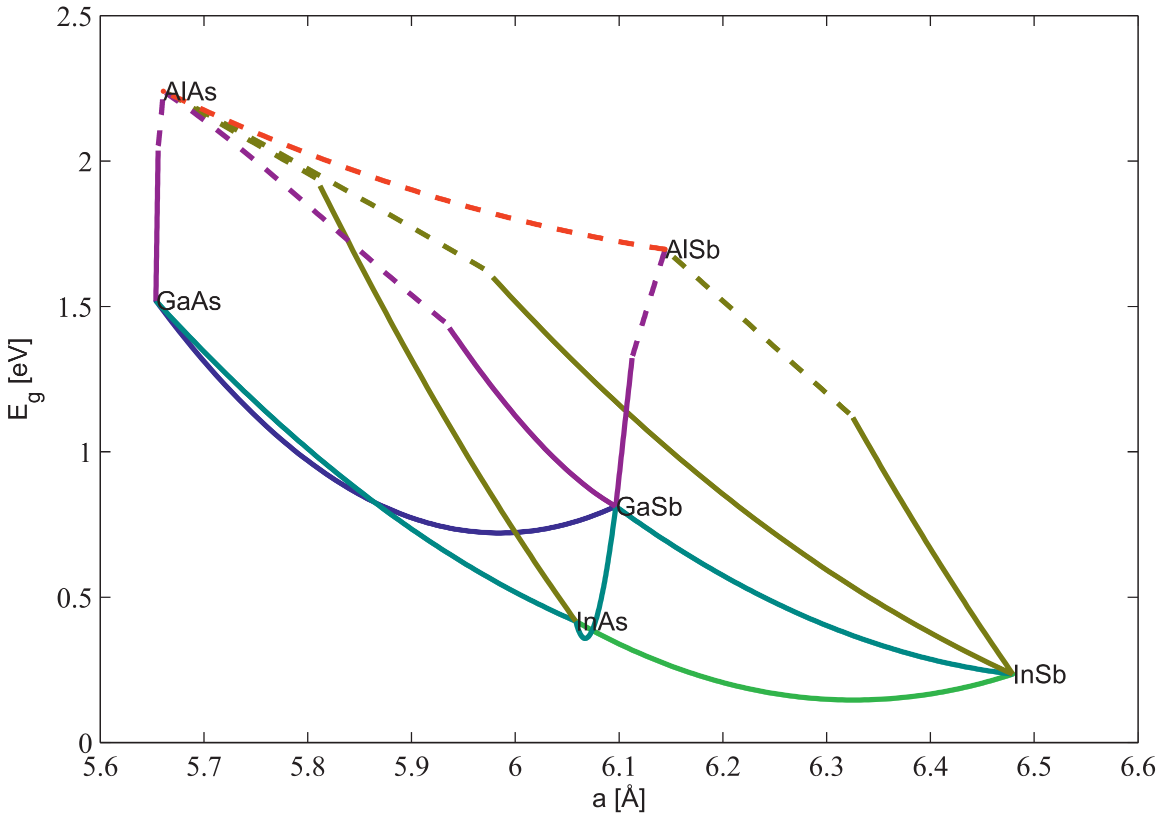

Figure A.1: Band gap energy [154] as a function of the lattice constant [61, 62, 64, 86, 90, 151]. Note that the band gap energy is calculated for 0 K, and it will be smaller for temperatures near room temperature.

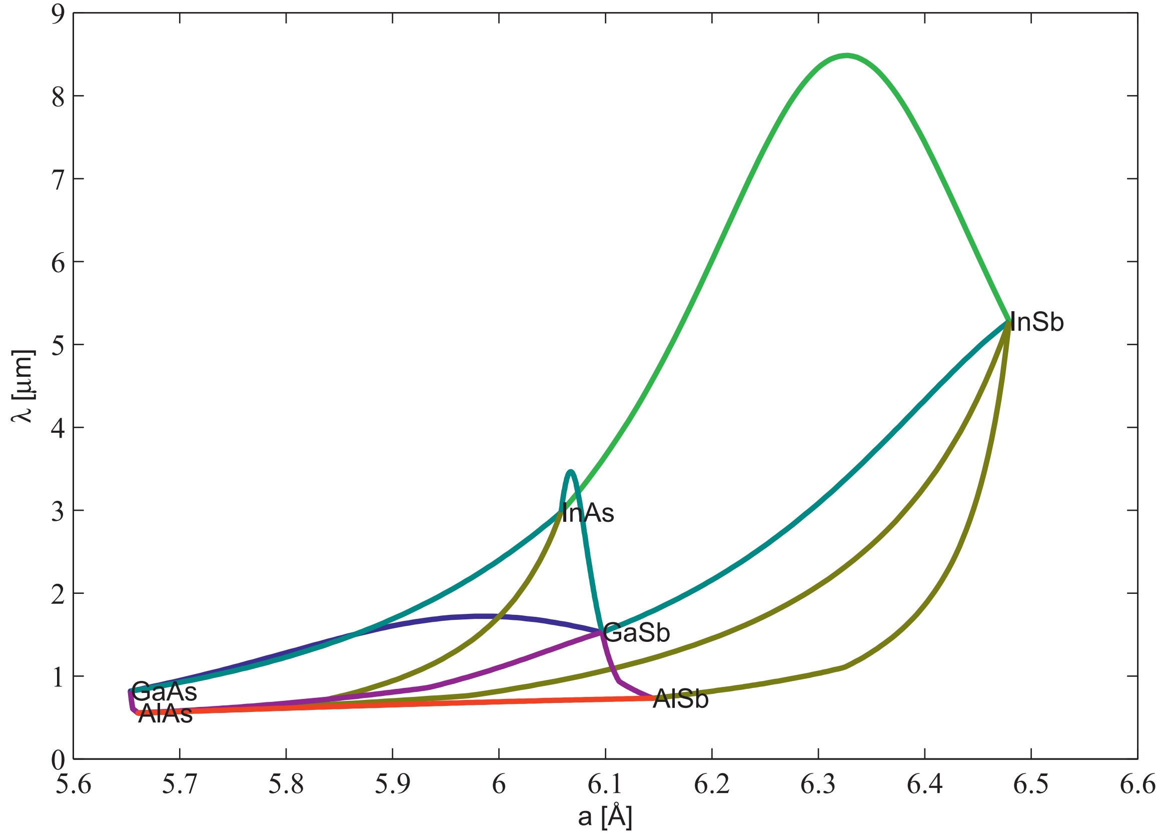

Figure A.2: Band gap energy [154] as a function of the lattice constant [61, 62, 64, 86, 90, 151] expressed by the optical recombination wavelength at the band gap.

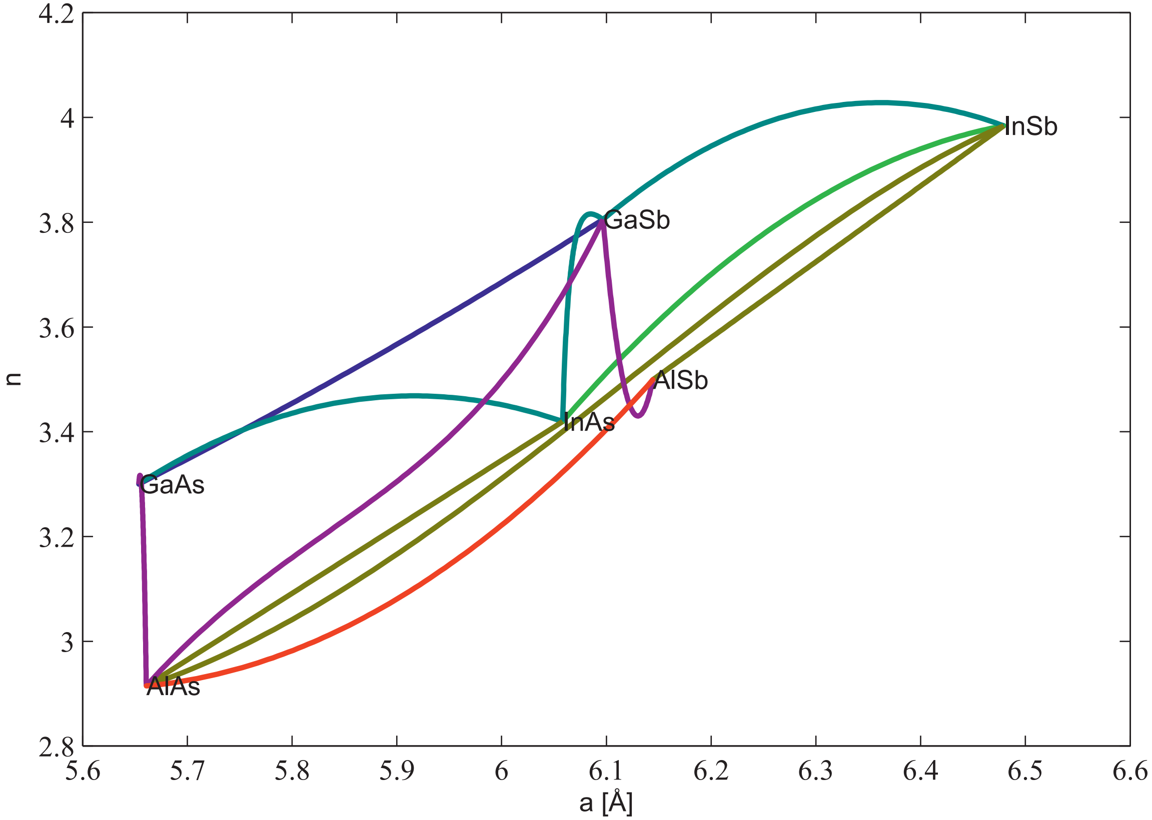

Figure A.3: Refractive index *n* [84] as a function of the lattice constant [61, 62, 64, 86, 90, 151].

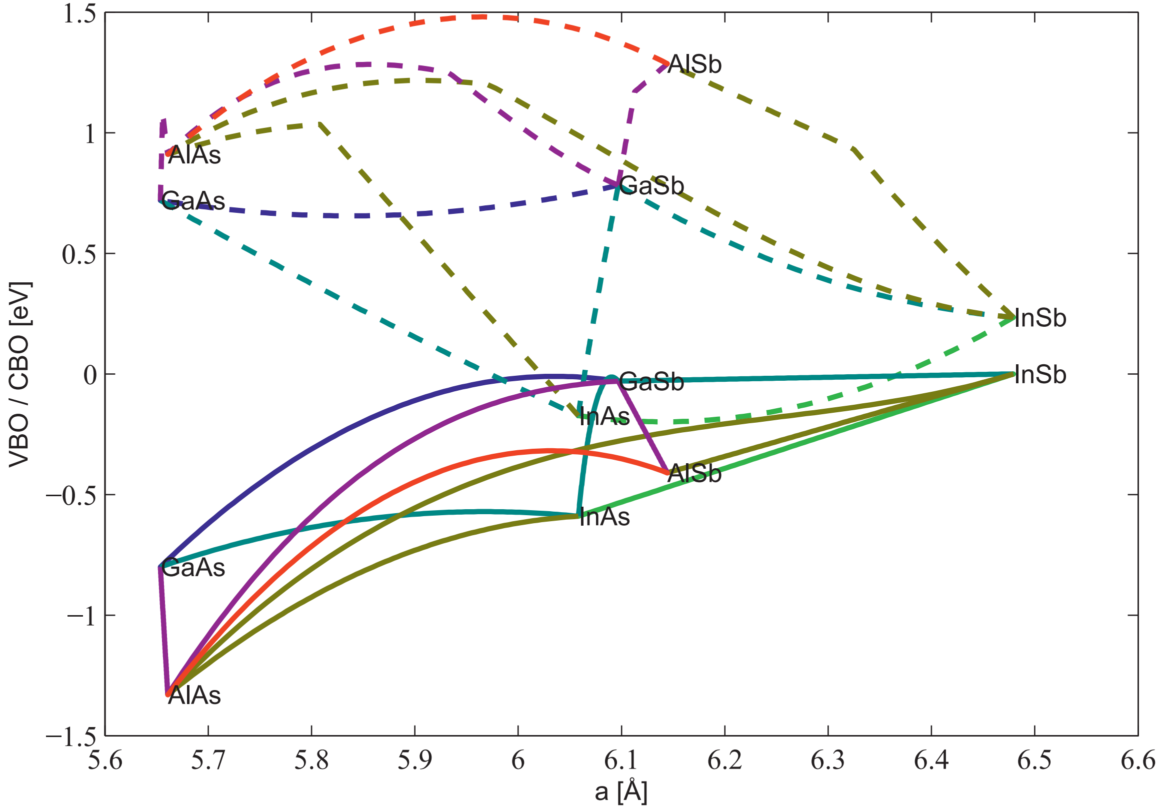

Figure A.4: Conduction band offsets (CBO) (dashed lines) and valence band offsets (VBO) (whole lines) [86] as a function of the lattice constant [61, 62, 64, 86, 90, 151]. CBO calculated using CBO $= \mathrm{VBO} + E_g$.

Appendix B

Slab waveguide

This chapter contains results from calculations of an infinite slab waveguide with a core thickness w. The parameters are explained in fig. B.1 and the results are shown in table B.1. The calculations are performed using the theory described in ref. [46, App. B]. While Γ refers to the optical power, a parameter $\Gamma_{\mathrm{E,wg}}$ has been included in the tables. This parameter refers to the optical field $E(x)$. If the waveguide is leaky (see section 2.1.2), the field can radiate into e.g. the substrate and be reflected back into the waveguide and cause interference, and the resulting optical power in the waveguide, in the case of destructive interference, will be given by $|E_{\mathrm{inside}} - E_{\mathrm{reflected\ back}}|^2$, and not $|E_{\mathrm{inside}}|^2 - |E_{\mathrm{reflected\ back}}|^2$.

For reference, the laser samples Sb 142 and Sb 145 have nominal core thicknesses of 442 nm.

The calculations contain the effective refractive indices (n_{eff}), the width of the confined optical power (Γ) and the number of allowed modes for different core thicknesses. These calculations may be helpful for determining growth parameters, with relation to the optical leakage and confinement in the core. Good confinement provides good overlap of the gain material and the optical field.

In table B.1 solutions for the slab waveguide modes using the refractive index data from Gonzalez-Cuevas et al. [84] is presented, while in table B.2 the cladding refractive index has been changed to 3.25, under the assumption that Gonzalez-Cuevas et al. [84]'s values are too high.

In table B.3 the change in the effective refractive index n_{eff} as a function of etch depth is illustrated for the slab waveguides investigated in tables B.1 and B.2. While these computations are based on 1D slab waveguides, they give some insight into how important the etch depth is on the waveguiding properties of the laser diode, expressed by n_{eff}.

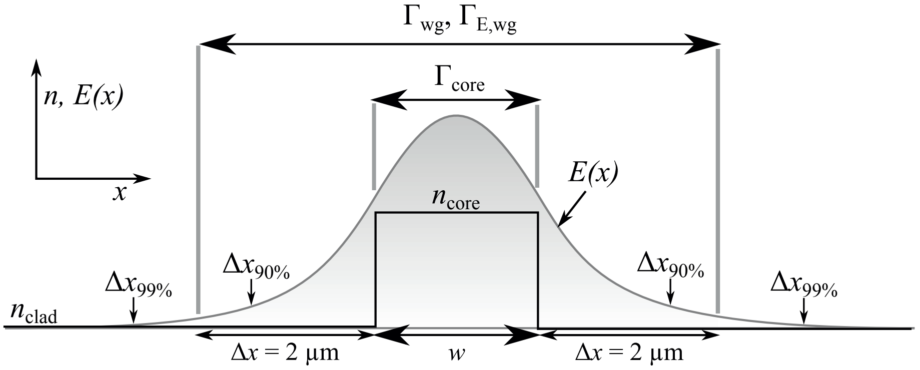

Figure B.1: Slab waveguide along x direction. Illustration of parameters shown in tables B.1 and B.2. n_{clad} and n_{core} are the cladding and core refractive indices, respectively. Γ refers to the confinement, i.e. how much of the optical power ($|E(x)|^2$) is within the specified region. $\Gamma_{\text{E,wg}}$ refers to the confined E-field ($E(x)$) inside the waveguide. Δx is the width of the cladding on each side, and $\Delta x_{90\%,99\%}$ refers to the cladding thickness required to confine 90% and 99% percent of the optical power, respectively.

Table B.1: Results from 1D mode solver based on theory described in Buus et al. [46], App. B. w is the width of the core, n_{clad} and n_{core} are based on values from sample Sb 142, and are 3.408 and 3.576, respectively. λ was chosen to be 2.3 µm. See fig. B.1 for an illustration of parameters.

w (µm)	n_{eff}	No. of modes	Γ_{core}	$\Delta x_{90\%}$ (µm)	$\Delta x_{99\%}$ (µm)	Γ_{wg}	$\Gamma_{\text{E,wg}}$
0.1	3.41	1	0.05	2.67	5.33	0.64	0.16
0.2	3.42	1	0.09	1.39	2.78	0.93	0.62
0.3	3.43	1	0.14	0.98	1.96	0.98	0.81
0.4	3.45	1	0.19	0.79	1.58	0.99	0.89
0.5	3.46	1	0.26	0.68	1.36	1	0.93
0.6	3.48	1	0.36	0.61	1.23	1	0.95
0.7	3.49	1	0.50	0.57	1.14	1	0.97
0.8	3.50	1	0.65	0.54	1.07	1	0.97
0.9	3.51	1	0.79	0.51	1.02	1	0.98
1.0	3.51	1	0.88	0.49	0.99	1	0.98
1.1	3.52	1	0.94	0.48	0.96	1	0.98
1.2	3.53	2	0.97	0.47	0.93	1	0.99

Table B.2: Results from 1D mode solver based on theory described in ref. [46, App. B]. w is the width of the core, n_{clad} and n_{core} are based on values from sample Sb 142, with the assumption that the cladding refractive index is closer to 3.25, and are 3.25 and 3.6, respectively. λ was chosen to be 2.3 µm. See fig. B.1 for an illustration of parameters.

w (µm)	n_{eff}	No. of modes	Γ_{core}	$\Delta x_{90\%}$ (µm)	$\Delta x_{99\%}$ (µm)	Γ_{wg}	$\Gamma_{\text{E,wg}}$
0.1	3.27	1	0.05	1.32	2.65	0.94	0.65
0.2	3.30	1	0.09	0.71	1.43	1	0.92
0.3	3.35	1	0.15	0.53	1.05	1	0.97
0.4	3.39	1	0.26	0.44	0.88	1	0.99
0.5	3.42	1	0.44	0.39	0.79	1	0.99
0.6	3.45	1	0.66	0.36	0.73	1	1
0.7	3.47	1	0.84	0.34	0.69	1	1
0.8	3.49	2	0.93	0.33	0.66	1	1
0.9	3.50	2	0.97	0.32	0.64	1	1
1.0	3.52	2	0.99	0.31	0.63	1	1
1.1	3.53	2	1	0.31	0.62	1	1
1.2	3.54	2	1	0.30	0.61	1	1

Table B.3: Results from 1D mode solver based on theory described in ref. [46, App. B]. The values below illustrate the change in the effective refractive index, n_{eff}, for different etch depths in to the top cladding, for core thicknesses w of 0.442 µm and 0.6 µm. The wavelength λ was chosen to be 2.3 µm. The refractive index above the cladding was set to 1.5, which is an approximate refractive index value expected for the ma-N 440 insulation layer. The value dn illustrates the change in refractive index of etched cladding with insulation, compared to an unetched cladding layer. These numbers illustrate the change in the refractive index as a function of etch depth. Note that these values are extracted from 1D slab simulations, and not full 2D ridge calculations, which should be used for more accurate etch depth calculations. The parameters for the slab waveguide are described in the descriptions of tables B.1 and B.2, respectively.

Remaining cladding	Table B.1		Table B.2	
thickness (µm)	n_{eff}	dn	n_{eff}	dn
$w = 0.442$ µm				
1.50	3.455	0.000	3.403	0.000
1.00	3.454	0.002	3.403	0.000
0.70	3.451	0.004	3.402	0.001
0.60	3.449	0.006	3.401	0.002
0.50	3.447	0.009	3.399	0.004
0.40	3.443	0.013	3.397	0.006
0.30	3.437	0.018	3.391	0.011
0.25	3.434	0.022	3.388	0.015
0.20	3.429	0.026	3.382	0.021
0.15	3.424	0.031	3.375	0.028
0.10	3.419	0.037	3.365	0.038
0.05	3.413	0.042	3.351	0.052
0.00	3.409	0.047	3.333	0.069
$w = 0.6$ µm				
1.50	3.476	0.000	3.450	0.000
1.00	3.476	0.001	3.450	0.000
0.70	3.474	0.003	3.449	0.000
0.60	3.473	0.004	3.449	0.001
0.50	3.471	0.006	3.448	0.002
0.40	3.468	0.009	3.446	0.003
0.30	3.464	0.013	3.443	0.006
0.25	3.461	0.016	3.441	0.009
0.20	3.457	0.020	3.438	0.012
0.15	3.452	0.024	3.433	0.017
0.10	3.447	0.030	3.426	0.024
0.05	3.440	0.036	3.417	0.033
0.00	3.432	0.044	3.404	0.045

Appendix C

Laser processing recipe

The following pages contain the recipe used for laser processing of sample Sb 145. It should be noted that the recipe is constantly evolving to compensate for problems and improvements made during processing. The process typically takes several months from start to finish; this is both due to the actual time each step takes, but also to accomodate to a multi-user environment, changes to instruments requiring adjustments of the recipe, downtime etc.

Processing Run card, y-junction laser nanolab

Notebook: Documents for thesis
Created: 23.05.2011 11:24 **Updated:** 04.10.2013 10:19
Tags: lab
URL: about:blank

Sample:

Sample nr: ________________________
Sketch of sample:

Ridge Etch

Sample Clean
1. 5 min in Acetone
2. 5 min in Ethanol
3. 5 min in IPA
4. IPA rinse
5. DIW rinse + immediate N2 dry
6. ~~Light etch - 1:30 NH4OH:H2O 30s + N2 dry~~
    1. ~~Should be made fresh daily~~
    2. ~~Do NOT rinse with water after etch~~
7. Dehydration bake 150 C / 10 min
	Comments:

Photolitography 1. Spin SPR-700-1.0 @ 3500 rpm / 30 s (0.975 µm) 2. Clean backside of sample carefully with a swab moisted with acetone if resist is present 3. Soft bake 95 C / 60 s 4. Edge bead removal exposure 60-70 mJ/cm2 5. Develop until edge bead is gone 6. Soft bake 95 C / 60 s 7. Exposure - 35-40 mJ/cm2 8. PEB 115 C / 60 s 9. Develop in mf26a 15-25 s (Varies from run to run, keep an eye on it, always use a test) 10. Spin dry @ 1000 rpm / 45 s	Comments:

ICP-RIE etch
1. ~~Do a 30 sec plasma clean in plasma cleaner. 30 O2 / 50 W (~= 15 nm, 33 nm / min)~~
2. Check that it has been used for Cl-gases
    1. If not, run the necessary cleaning steps
3. Do condition run w/o sample
    1. Use recipe developed by renato and tron, or Oxford recipe
4. Do test run with test sample (preferably cladding sample, or alternatively GaSb)
5. Check etch rate from test sample
6. Etch to desired etch depth (typically 100 nm above core)
7. PR removal
    1. Do a 5 min plasma clean
    2. Remove PR by putting sample in acetone (5-15 min)
        1. If not removed you can ignore the photoresist and it will be etched away in the passivation etchback
        2. If not removed - use acetone gun or swabs
	Comments:
	(etch depth, rates, selectivity, etc)

3. Rinse immediately in IPA + N2 dry 8. Rinse sample in running DIW for 5 min (Cl-removal)	

Passivation, Nitride

Not sure if needed, only do for half of the lasers

Sample clean 1. Acetone + IPA rinse + N2 dry 2. 5 min dehydration bake @ 150 C on hot plate	Comments:
PECVD 1. Deposit 100 nm SiN in PECVD 1. Or less. 1 min deposition is ok	Comments: (Deposited thickness, dep. rate)

Passivation, Resist

Do for all samples

Sample Clean 1. Acetone + IPA rinse + N2 dry 2. 5 min plasma clean (?) 3. 10 min dehydration bake 150 C	Comments:
Resist 1. Spin ma-N 440 @ 3000 rpm / 30 s 2. Soft bake: 60 s @ 95C 3. Do not expose the sample!! 4. Place sample on 3" Si wafer on black ceramic hot plate @ 100 C (TC, temperature on the display) 5. Ramp to 160 C, bake at 160 C for 5 minutes 6. Start timer for 2 minutes, ramp to 220 C (TC) 7. Take off sample after 2 minutes (including ramp time, so approx 1 min at 220C)	Comments:
Etch Back, RIE 1. Do condition run, recipe: ~~"O2 mask clean 100W"~~ "O2 resist etch 100W" for 10-30 minutes (plasma should be yellow not blue) 2. Etch sample(s), recipe: 1. 15 sccm O2 2. 3 sccm CF4 3. 100 W 4. 10 mTorr (Strike at 50 mTorr/20 V/5 ramp) 5. Etch time TBD 3. Etchback of edge bead first 1. Use piece of silicon to cover lasers (like for flood exposure) when you insert sample into RIE 2. Etchback of edge bead until completely removed 4. Do many etches, e.g. 3-4-5 minutes, and check result every time (microscope / profilometer) 5. Inspect in microscope/profilometer to make sure ridge is uncovered 6. Do SiN/SiO2 etch if sample has oxide/nitride passivation 1. Recipe: CHF3 ... (33 sccm Ar, 17 sccm CHF3 or other way around) 2. NOTE: O2/CF4 recipe probably attacks SiN/SiO2 as well	Comments:

Top contact layer

Sample Clean	Comments:

1. Acetone + IPA rinse + N2 dry 2. 10 min dehydration bake 150 C	
Photolitograhy 1. Spin S1818 @ 1500 rpm / 30 s (1500 rpm ~= 3 µm) 2. Soft bake: 115 C / 60 s 3. Edge bead removal: ca 3x normal exposure - 400-500 mJ/cm2 4. Develop until clear edge 5. Soft bake 115 C / 60 s 6. Align and (over-)expose: ca. 165 mJ/cm2 (150 mJ/cm2 is probably ok) 7. Develop: 1-2 minutes. Remove immediately when pattern is developed	Comments:

Metallization
1. Do a 30 sec 50 W, 30 % O2 plasma clean
2. Just before loading sample
    1. 1:1:800 NH4OH:H2O2:DI-Water for 5 sec
    2. 1:30 NH4OH:DI-Water for 30 sec
    3. Blow dry with N2
    4. Load sample immediately
3. Metallization: Ti/Pt/Au 50nm/25nm/775nm (for bonding)
	Comments:

Lift-off. Recipe will need revising if not working!
1. Put sample in closed container for 10-20 minutes
2. If lift-off is not successfull, try following (stop when lift-off is done)
    1. Spray sample with acetone gun
    2. Use brush, then spray with acetone
    3. Ultrasonic in plastic beaker (max 20 minutes)
    4. Acetone + swab
    5. If nothing works, change recipe!!!
3. Clean sample in ethanol + IPA + N2 rinse
4. Inspect sample
	Comments:

Bottom contact, Lapping

Done at the supporting lab

	Comments:

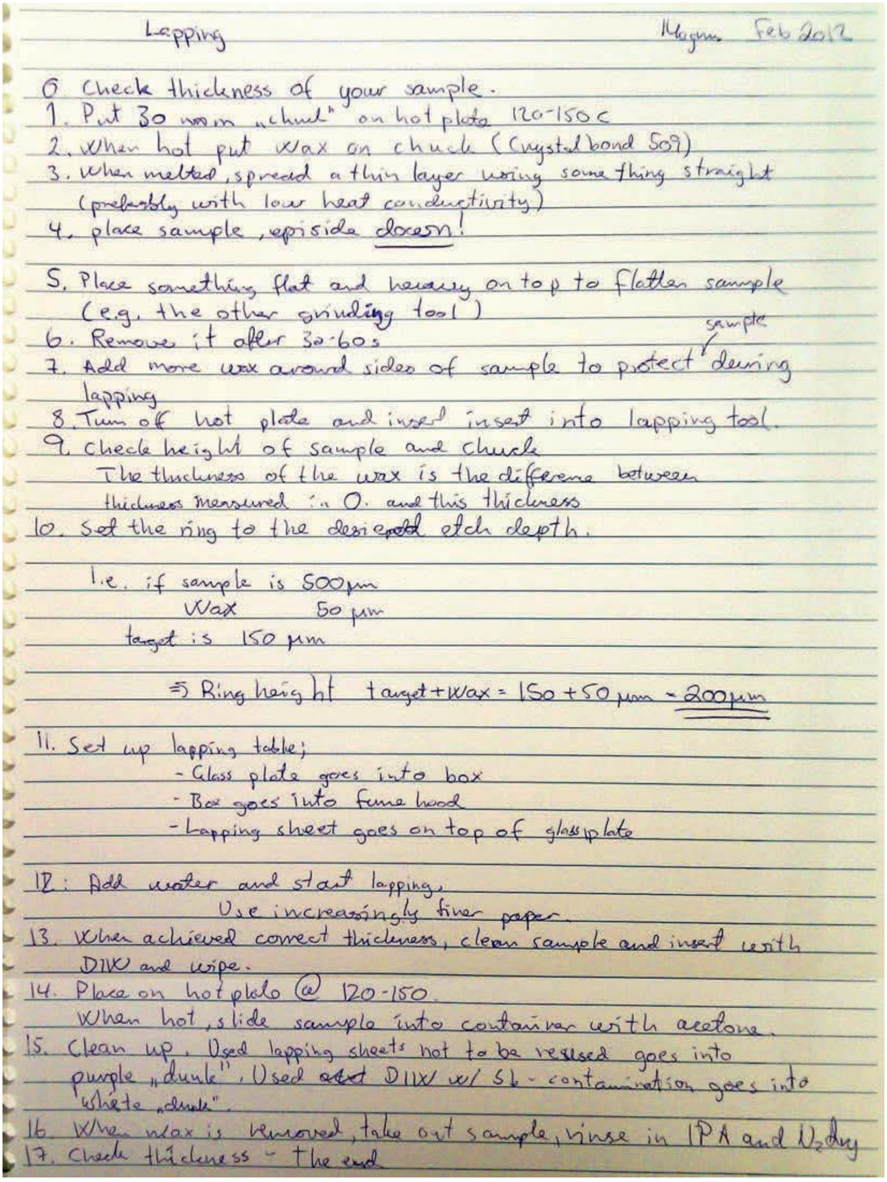

Lapping

Magnus Feb 2012

0 Check thickness of your sample.
1. Put 30 mm „chuck" on hot plate 120-150C
2. When hot put wax on chuck (Crystalbond 509)
3. When melted, spread a thin layer using something straight (preferably with low heat conductivity)
4. place sample, episide down!
5. Place something flat and heavy on top to flatten sample (e.g. the other grinding tool)
6. Remove it after 30-60s
7. Add more wax around sides of sample to protect sample during lapping
8. Turn off hot plate and insert inset into lapping tool.
9. Check height of sample and chuck
   The thickness of the wax is the difference between thickness measured in 0. and this thickness
10. Set the ring to the desired etch depth.

i.e. if sample is 500µm
Wax 50 µm
target is 150 µm

⇒ Ring height target + Wax = 150 + 50 µm = 200µm

11. Set up lapping table;
   - Glass plate goes into box
   - Box goes into fume hood
   - Lapping sheet goes on top of glass plate
12: Add water and start lapping.
   Use increasingly finer paper.
13. When achieved correct thickness, clean sample and insert with DIW and wipe.
14. Place on hot plate @ 120-150.
   When hot, slide sample into container with acetone.
15. Clean up. Used lapping sheets not to be reused goes into purple „dunk", Used ~~and~~ DIW w/ Sb-contamination goes into white „dunk".
16. When wax is removed, take out sample, rinse in IPA and N_2 dry
17. Check thickness - the end

Bottom contact, Metallization

Done at nanolab.

Mounting

Comments:

1. Clean and dehydrate a piece of silicon large enough to fit all samples
2. Spin ma-N 440 @ 1000 rpm / 30 s
3. Place all samples, backside up, on the photoresist *BEFORE* baking
4. Soft bake 110 C / 10 minutes

Metallization

1. Immediately before loading samples, do a
    1. 1:1:200 NH4OH:H2O2:DI-Water 5 sec
    2. 1:30 NH4OH:DI-Water for 30 sec
    3. Blow dry with N2
    4. Load immediately
2. Do n-type contact deposition
    1. Vogt et al.; Pd/Ge/Au/Pt/Au 87Å/560Å/233Å/476Å/1056Å (make thicker Au layer at end, at least 300 nm)

De-mount

1. Place samples in acetone for 1 hour in closed beaker (as always)
2. Remove and clean acetone + ipa + n2 dry
3. Inspect

Bottom contact, Annealing

Done at nanolab.

Rapid thermal annealer

Comments:

1. Make or use annealing recipe in the RTP
    1. Make new recipe for Vogt et al. metal; 45 s @ 300 C

Scribing

Supporting lab, nanolab.

Comments:

1. Mount sample on blue tape
2. Make a recipe based on the length of the laser
3. Make sure you hit the laser at the end - will be difficult!! Machine not calibrated
    1. DO NOT scribe across the ridge - the laser will not work (just cleave)
    2. Use edge scribes for scribing perpendicular to the ridge

Mounting and bonding

Either nanolab or basement at IET

Comments:

1. Glue laser to a laser copper plate using silver epoxy or silver glue
2. Tape the bonding pads to the copper with kapton tape (double sided)
    1. Bonding pads must have soldered on wires BEFORE taping them to the copper
3. Wirebond the laser contacts to the laser bonding pads.

1. Bonding settings, nanolab:

Ball bond (Spring 2011)
T = 118 C

Ultrasonic:	180	280
Time:	100	55
Force:	85	65

Tail: 300

Feed +/- 12

Wedge bond (March 2012)
T = 118

Ultrasonic: 200 200
Time: 220 220
Force: 40 40

Tail: 300
Feed +/- 12

1. Should be ready for testing! (If test setup in FTIR lab is operational)

Appendix D

ma-N 440 insulation etchback

To improve the uniformity of the passivation etchback, the established recipe in our lab for reactive ion etching (RIE) of photoresists, using only O_2, was compared to other etch recipes using scanning electron microscope (SEM) and profilometer characterization. The passivation procedure was applied to a silicon wafer, which was then cleaved into four pieces, where each piece was etched for 3 minutes using one of the recipes 1 to 4 in table D.1. The samples were then cleaved for cross section SEM photographs, shown on the following pages. The recipe numbers in table D.1 correspond to the numbers on the photographs.

The process development for using ma-N 440 as an insulation layer can be found in section 5.8.1 and the process steps used can be found in appendix C.

Table D.1: The parameters used for etching the ma-N 440 insulation layer.

Recipe	Pressure (mTorr)	Power (W)	O_2 (sccm)	Ar (sccm)	CF_4 (sccm)
1	10	100	15	0	0
2	8	100	12	7	0
3	20	50	15	0	0
4	10	100	15	0	3

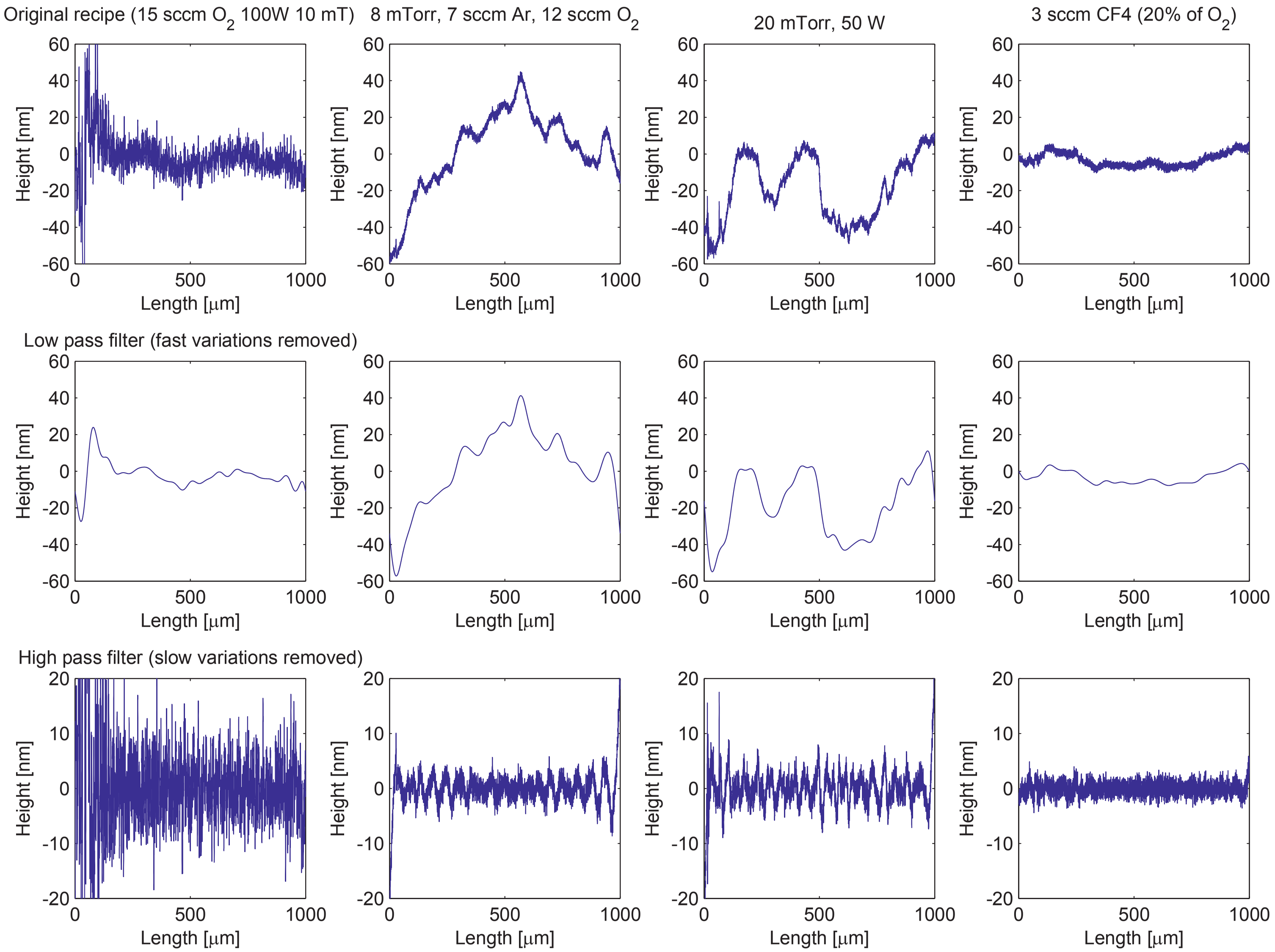
Original recipe (15 sccm O_2 100W 10 mT)
8 mTorr, 7 sccm Ar, 12 sccm O_2
20 mTorr, 50 W
3 sccm CF4 (20% of O_2)
Low pass filter (fast variations removed)
High pass filter (slow variations removed)
Height [nm]
Length [μm]
60
40
20
0
-20
-40
-60
10
-10
500
1000

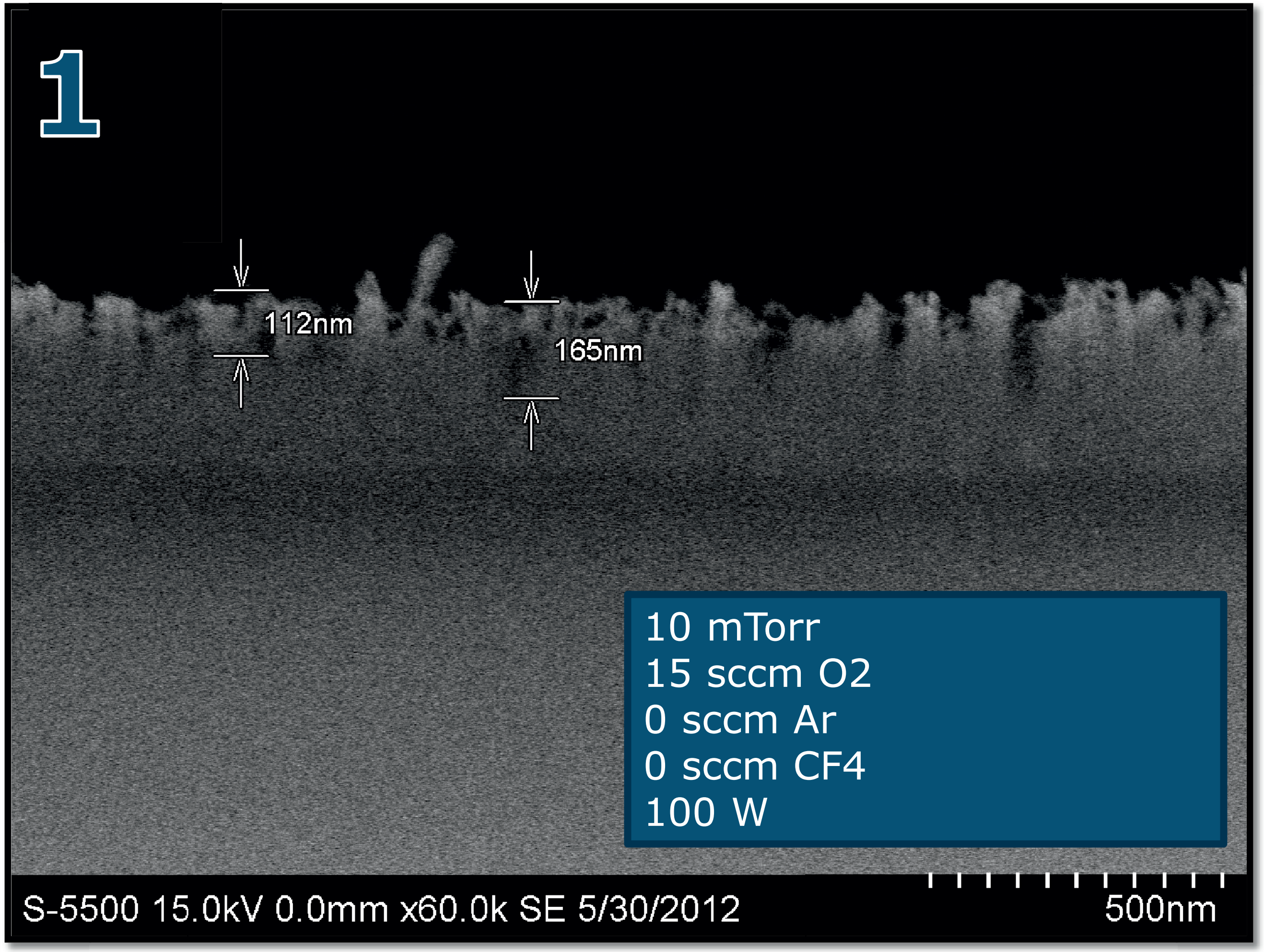

10 mTorr
15 sccm O2
0 sccm Ar
0 sccm CF4
100 W

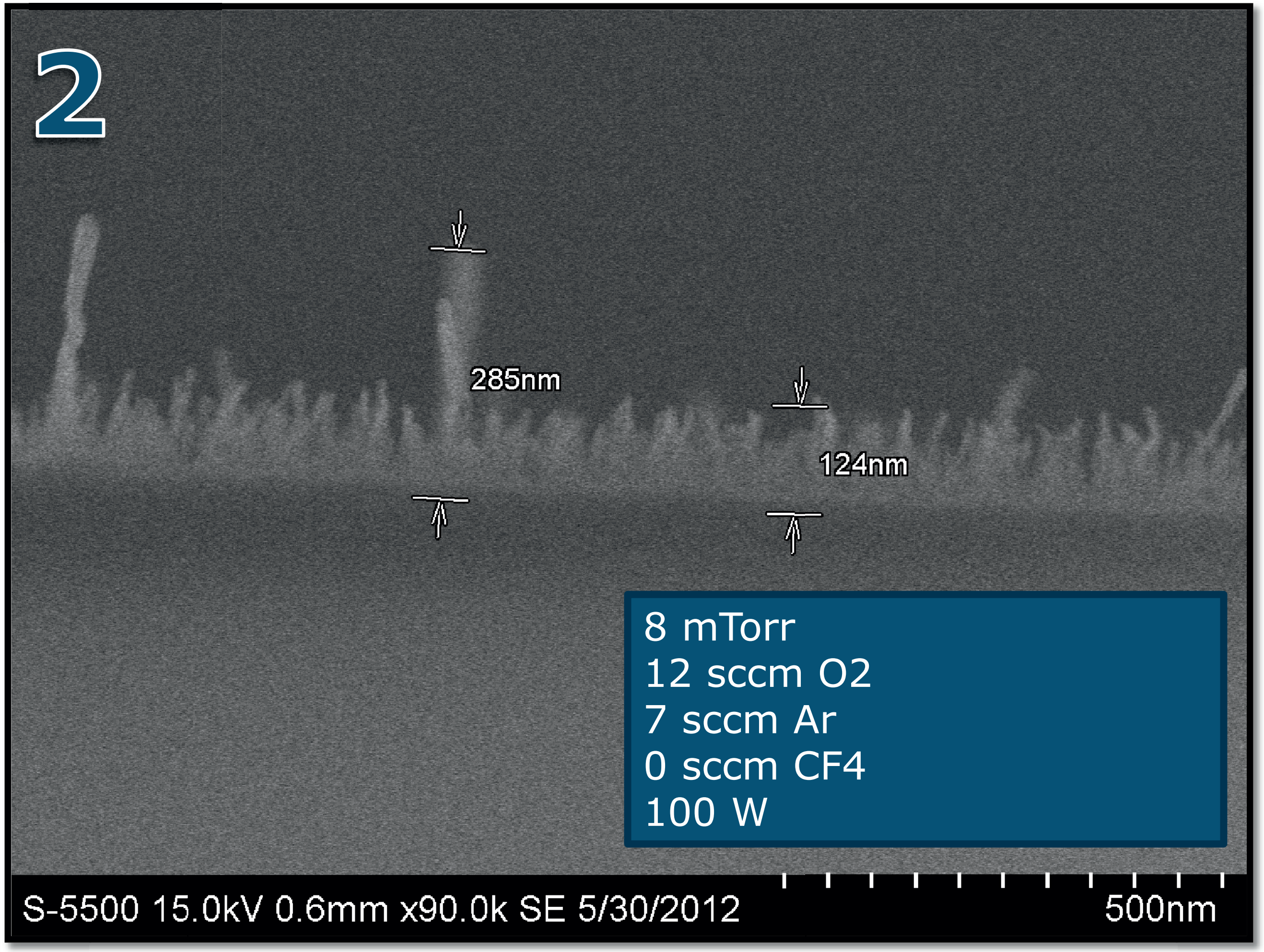
2
285nm
124nm
8 mTorr
12 sccm O2
7 sccm Ar
0 sccm CF4
100 W
S-5500 15.0kV 0.6mm x90.0k SE 5/30/2012
500nm

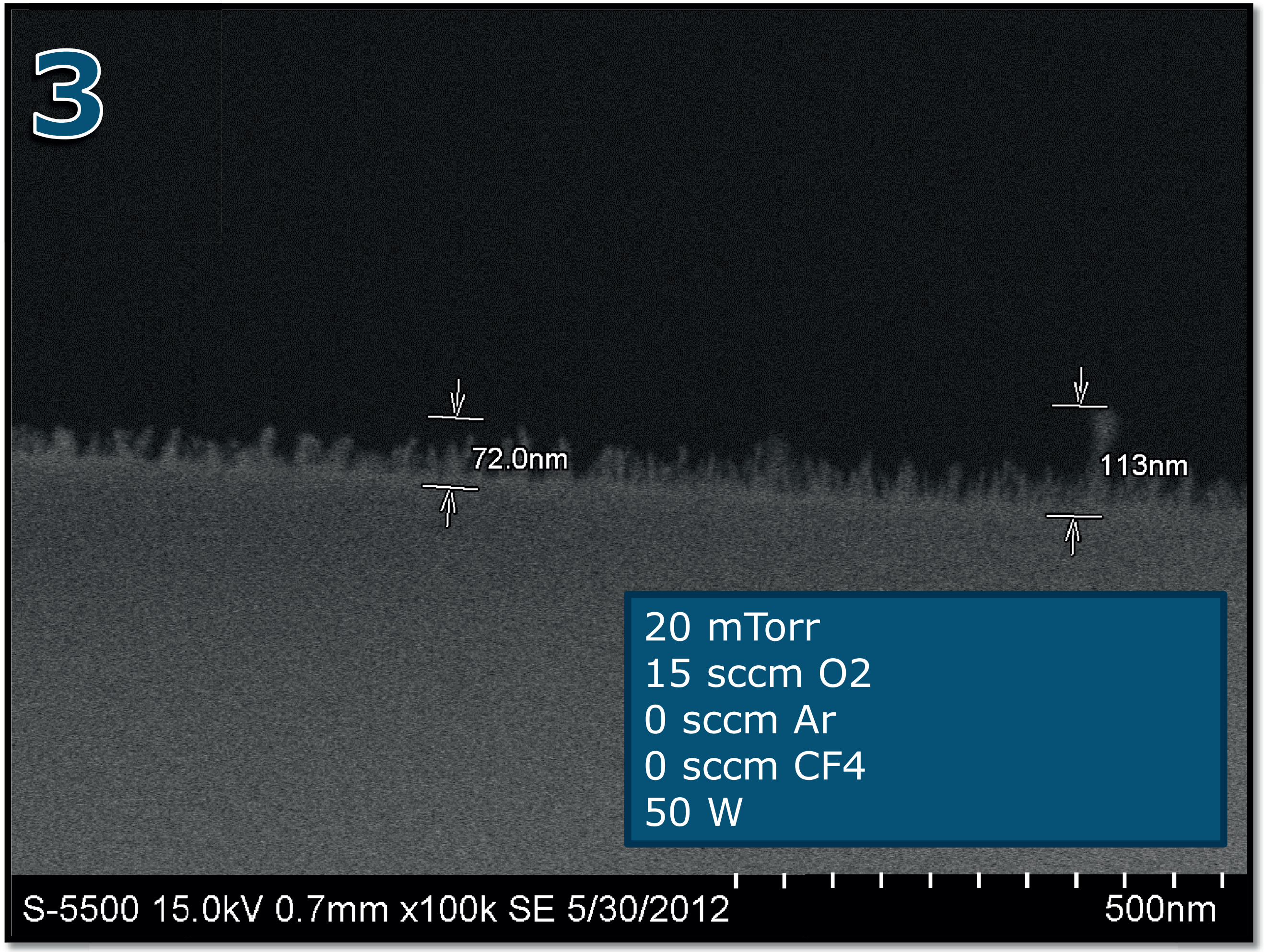
3
72.0nm
113nm
20 mTorr
15 sccm O2
0 sccm Ar
0 sccm CF4
50 W
S-5500 15.0kV 0.7mm x100k SE 5/30/2012
500nm

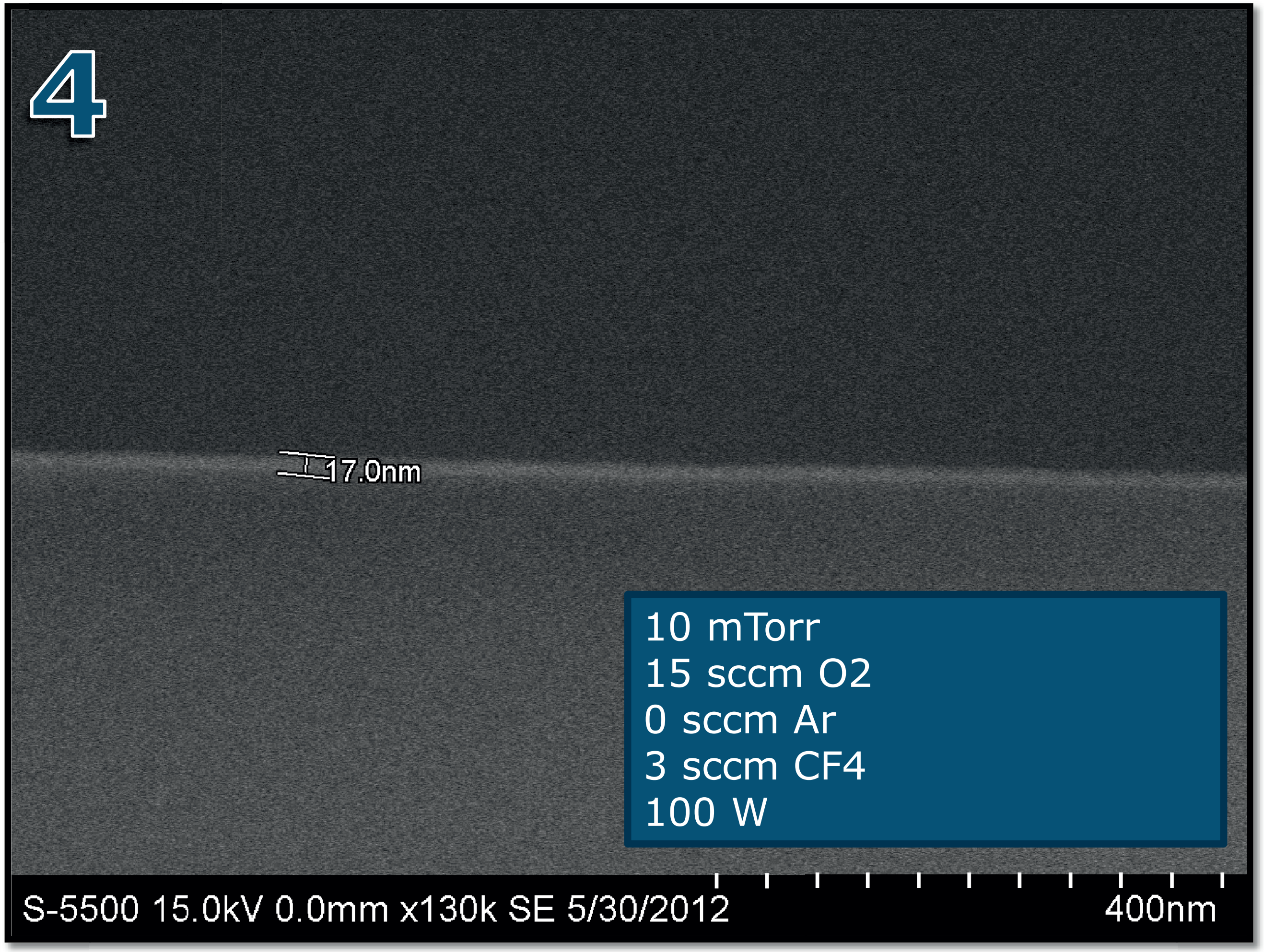
4
17.0nm
10 mTorr
15 sccm O2
0 sccm Ar
3 sccm CF4
100 W
S-5500 15.0kV 0.0mm x130k SE 5/30/2012
400nm

Appendix E

Laser spectrum measurements

The following figures are laser measurements of Y-junction lasers where at least 1000 combinations of the three currents $I_{c,s,b}$ (see fig. E.1) were measured. The different sub-plots in the measurement results are explained in fig. E.2. These measurements were performed in an attempt to determine the relationship between the wavelength and the current. In many cases the relationship was purely a function of total current, see e.g. the measurements presented on top of page 159. Here, the wavelength is more or less independent of any one of the currents $I_{c,s,b}$, but it is highly dependent on the total current $I_c + I_s + I_b$. This suggests that the tuning mechanism was mainly due to increased temperature from the total injected current.

SMSR, full-width at half maximum (FWHM), $n_{g,\mathrm{eff}}$ and wavelength were extracted from each spectrum. The data for the wavelength are presented from page 167, see fig. E.3 for explanation of the figures. The measurements with an SMSR above 10 dB are highlighted in the figures. The measured FWHM of the laser mode during lasing was usually between 0.036 and 0.040 nm for most of the measurements. This value is most likely limited by the Fourier transform infrared (FTIR) instrument, which has a specified spectral resolution of about 0.034 nm at 2.2 µm wavelength. The extracted effective group index, $n_{g,\mathrm{eff}}$, from the subthreshold spectrum mode spacing resulted in a value of about 3.75–3.85 with small variations between different laser diodes and a small increase with increasing current.

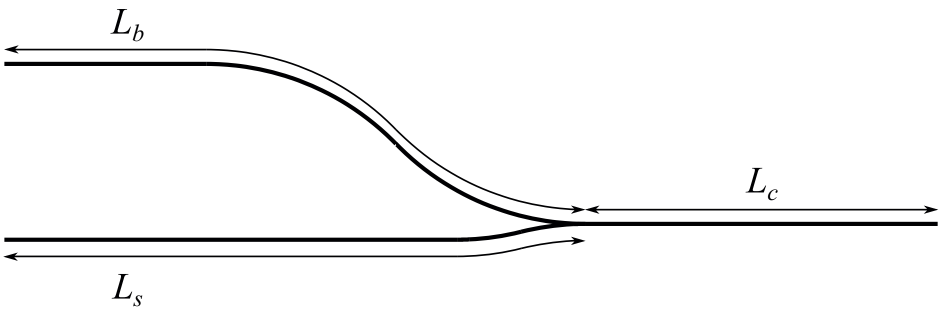

Figure E.1: The Y-junction laser waveguides. To achieve 50-50 splitting of the light, the Y should be symmetric. Here the two arms have the lengths $L_c + L_s$ for the straight waveguide and $L_c + L_b$ for the bent waveguide, and $\Delta L = L_b - L_s$. L_c, L_s and L_b are the lengths of the common, straight and bent sections, respectively.

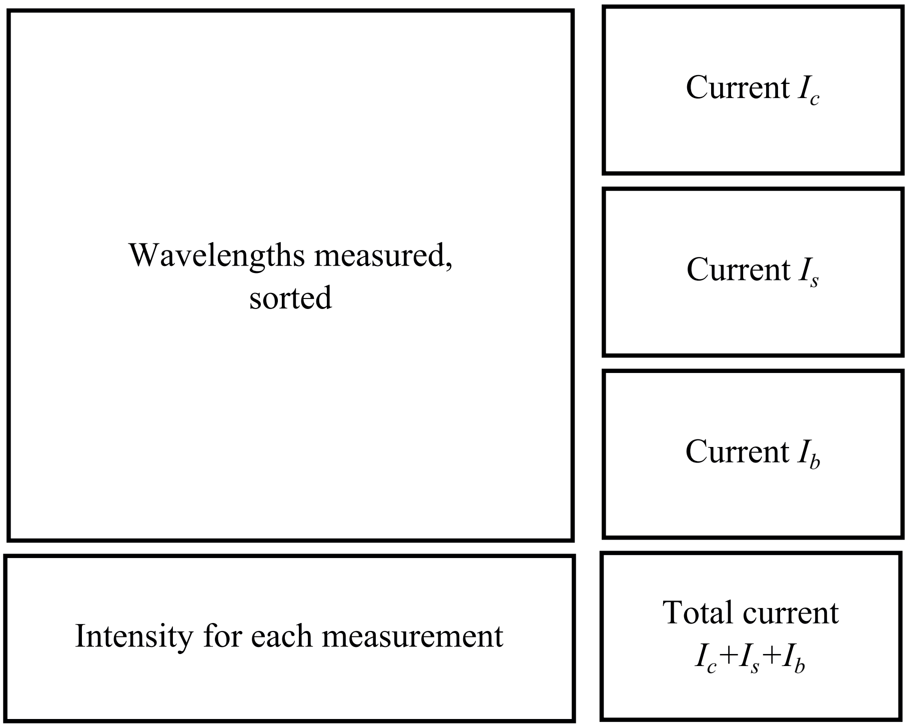

Figure E.2: Description of the plots of the laser measurements. The x-axis in all plots is measurement number, sorted by wavelength. The colors of the plotted measurement points give extra information regarding the measurement; Green indicates an SMSR of at least 18 dB, gray indicates low intensity, and **black** indicates that the measurement is missing. Blue is used for all other measurements.

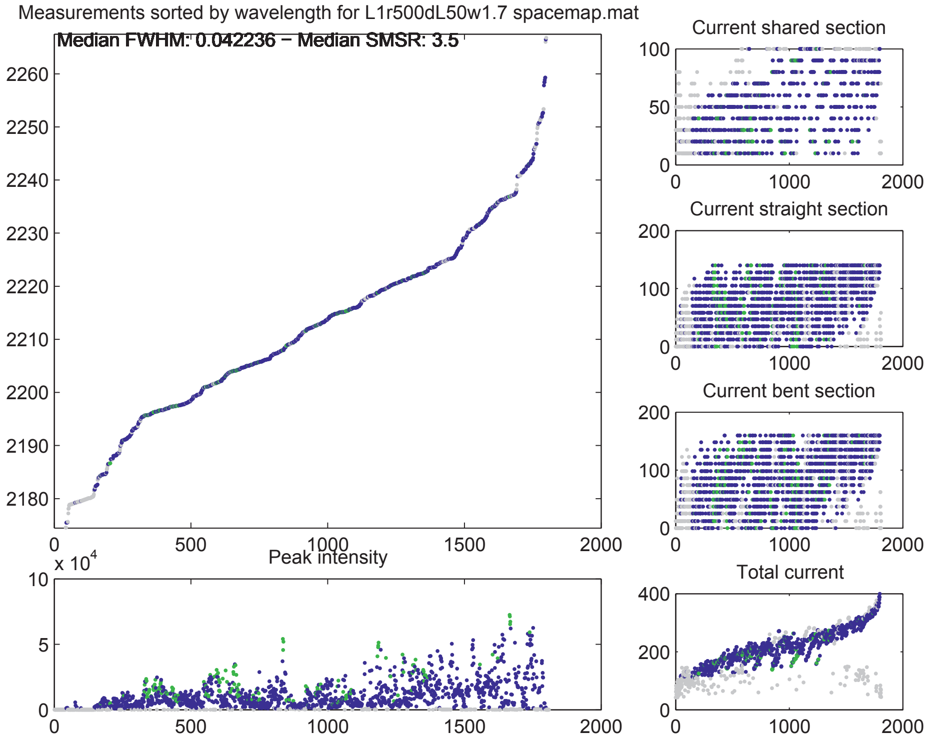

Measurements sorted by wavelength for L1r500dL50w1.7 spacemap.mat

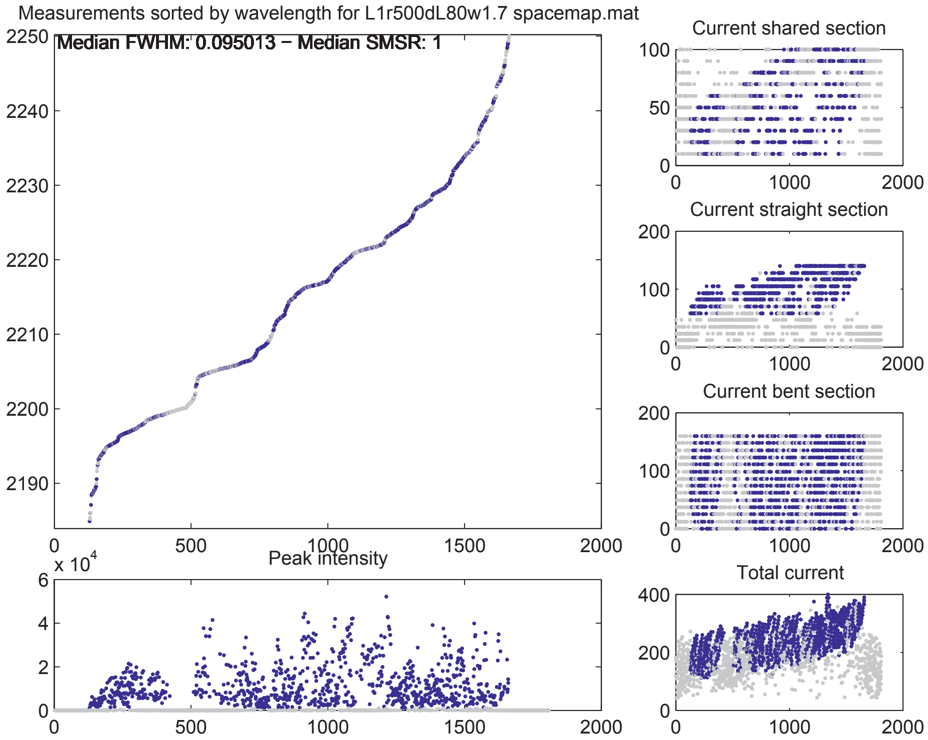

Measurements sorted by wavelength for L1r500dL80w1.7 spacemap.mat

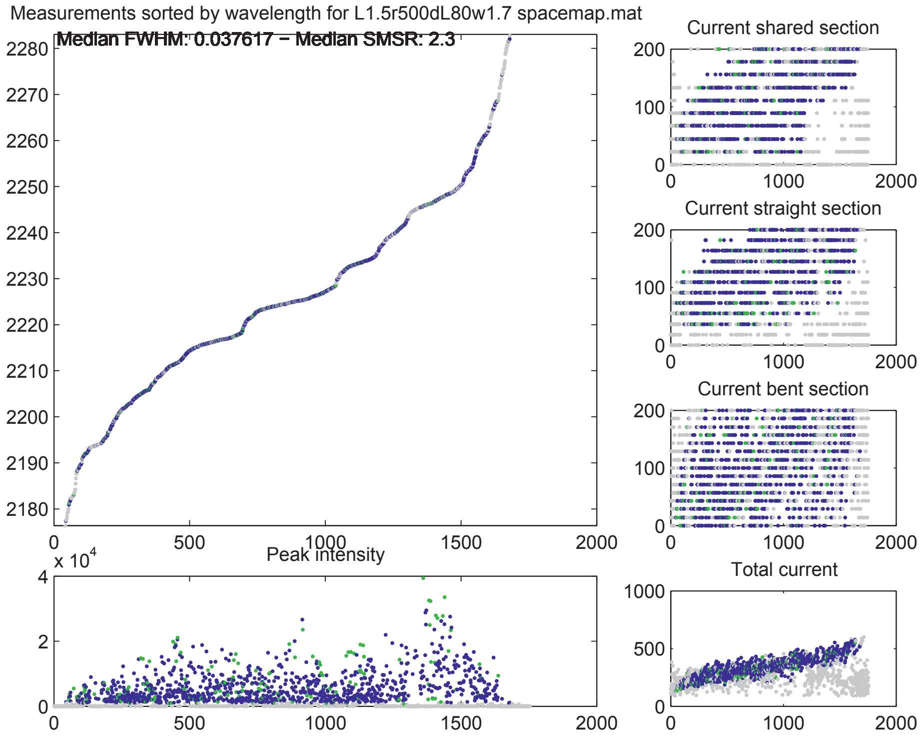
Measurements sorted by wavelength for L1.5r500dL80w1.7 spacemap.mat
Median FWHM: 0.037617 − Median SMSR: 2.3
2280
2270
2260
2250
2240
2230
2220
2210
2200
2190
2180
0
500
1000
1500
2000
Current shared section
Current straight section
Current bent section
200
100
0
0
1000
2000
Peak intensity
x 10^4
4
2
0
Total current
1000
500
0

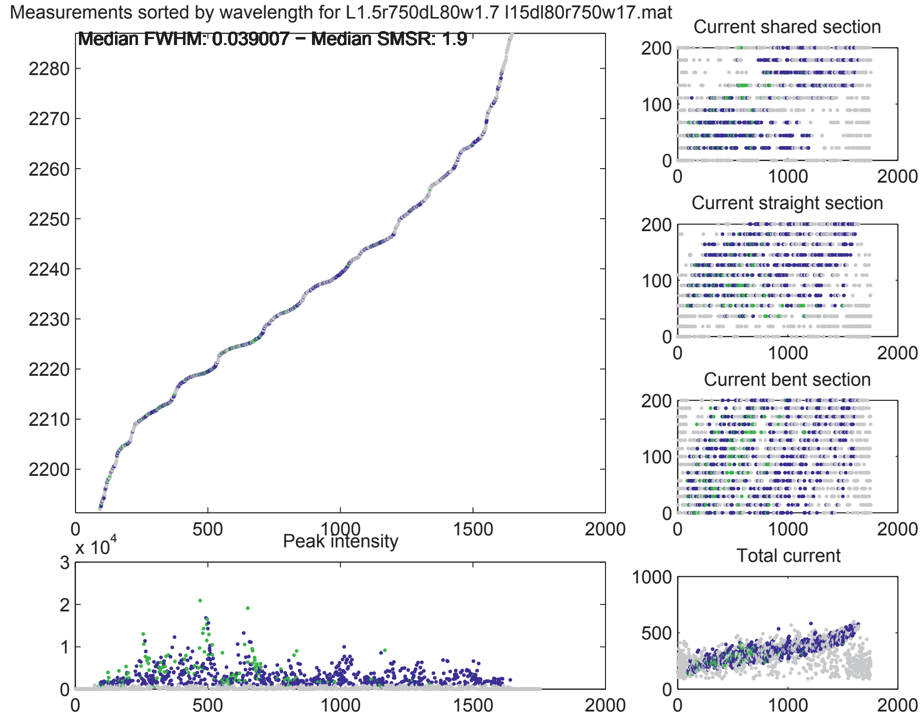
Measurements sorted by wavelength for L1.5r750dL80w1.7 l15dl80r750w17.mat
Median FWHM: 0.039007 − Median SMSR: 1.9
2280
2270
2260
2250
2240
2230
2220
2210
2200
0
500
1000
1500
2000
Current shared section
Current straight section
Current bent section
200
100
0
0
1000
2000
Peak intensity
x 10^4
3
2
1
0
Total current
1000
500
0

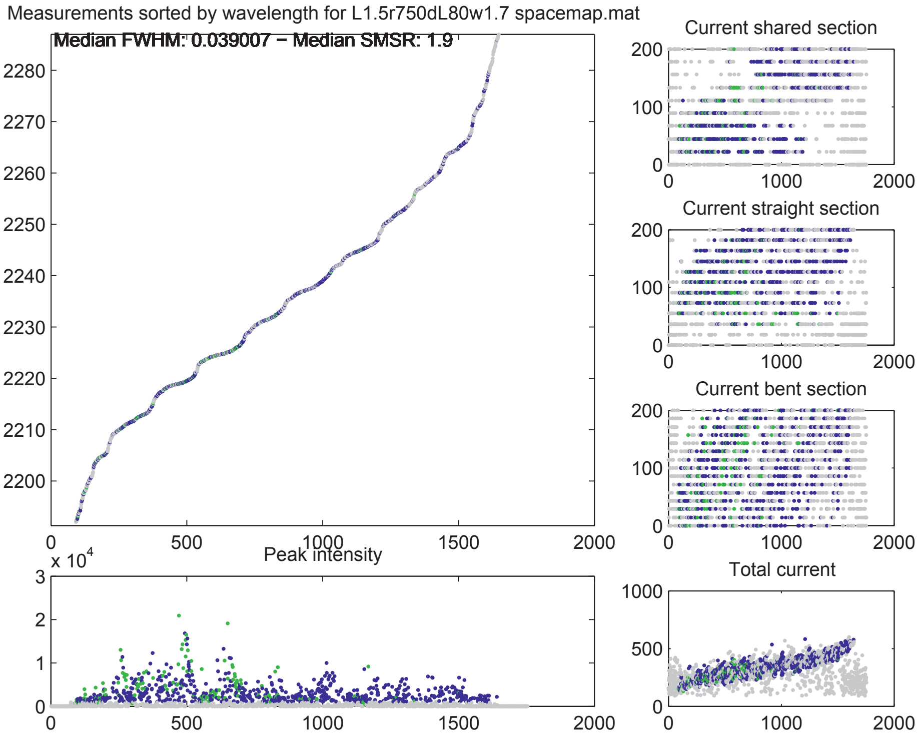
Measurements sorted by wavelength for L1.5r750dL80w1.7 spacemap.mat
Median FWHM: 0.039007 – Median SMSR: 1.9
2280
2270
2260
2250
2240
2230
2220
2210
2200
0
500
1000
1500
2000
Current shared section
Current straight section
Current bent section
200
100
0
0
1000
2000
x 10^4
Peak intensity
3
2
1
0
Total current
1000
500
0

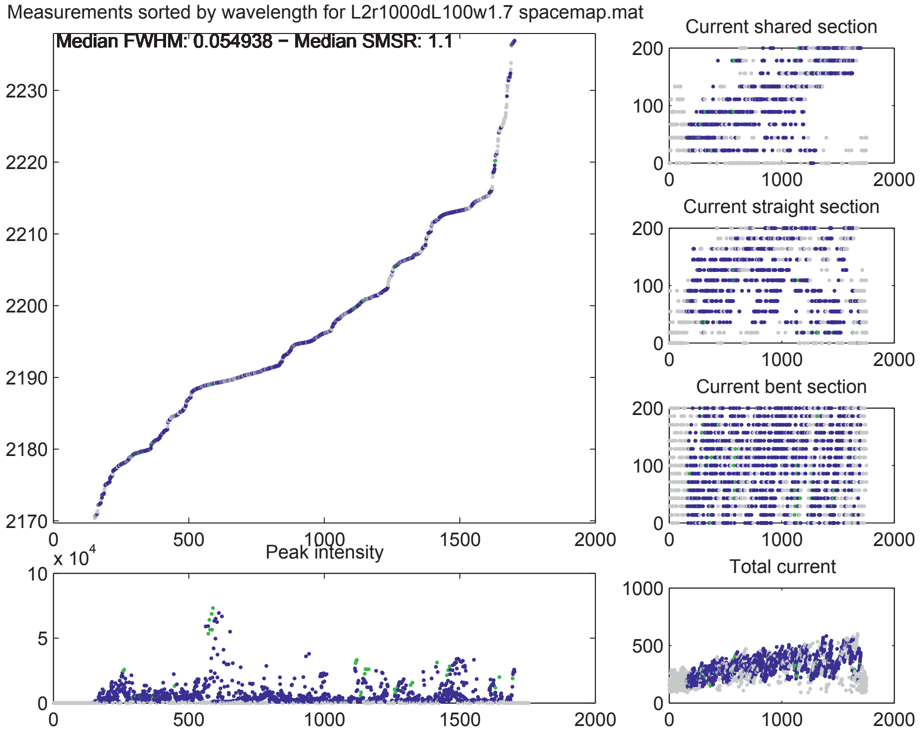
Measurements sorted by wavelength for L2r1000dL100w1.7 spacemap.mat
Median FWHM: 0.054938 – Median SMSR: 1.1
2230
2220
2210
2200
2190
2180
2170
0
500
1000
1500
2000
Current shared section
Current straight section
Current bent section
200
100
0
0
1000
2000
x 10^4
Peak intensity
10
5
0
Total current
1000
500
0

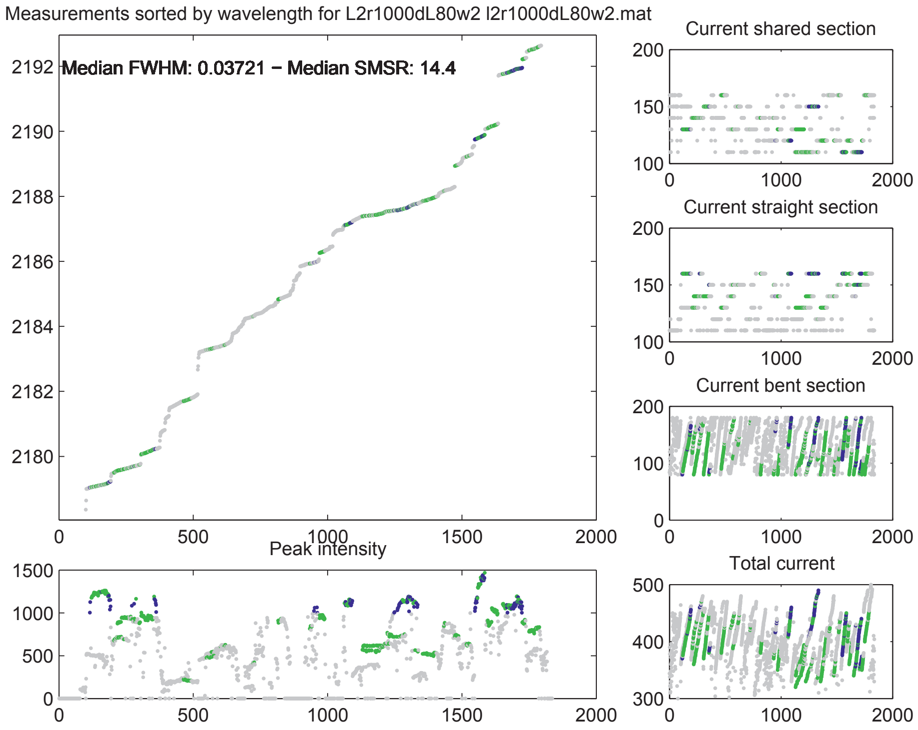
Measurements sorted by wavelength for L2r1000dL80w2 l2r1000dL80w2.mat
Median FWHM: 0.03721 – Median SMSR: 14.4
2192
2190
2188
2186
2184
2182
2180
0
500
1000
1500
2000
Peak intensity
1500
1000
500
0
0
500
1000
1500
2000
Current shared section
200
150
100
0
1000
2000
Current straight section
200
150
100
0
1000
2000
Current bent section
200
100
0
0
1000
2000
Total current
500
400
300
0
1000
2000

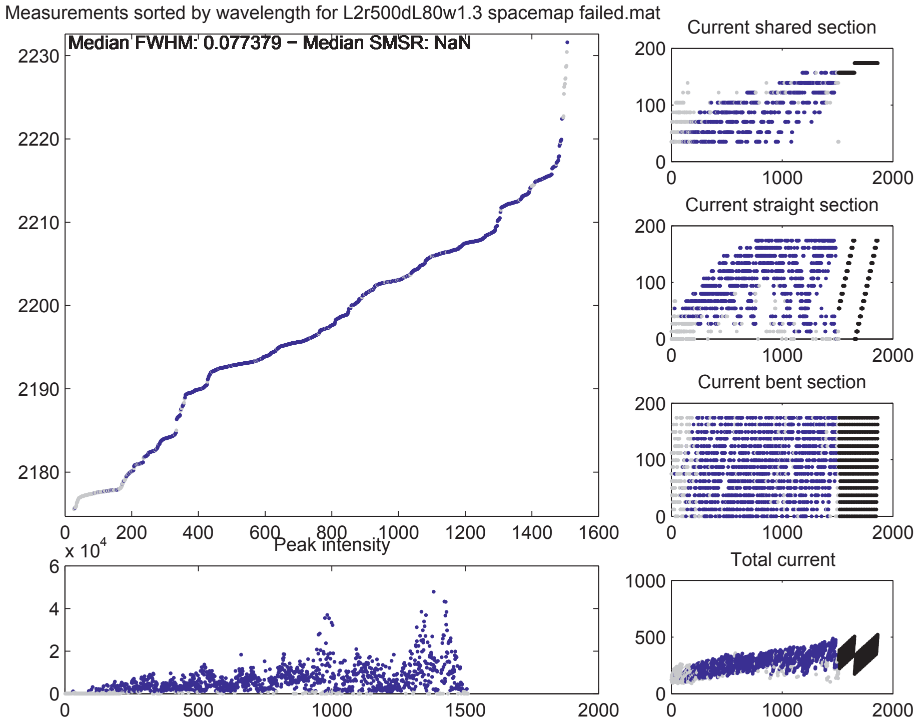
Measurements sorted by wavelength for L2r500dL80w1.3 spacemap failed.mat
Median FWHM: 0.077379 – Median SMSR: NaN
2230
2220
2210
2200
2190
2180
0
200
400
600
800
1000
1200
1400
1600
Peak intensity
x 10^4
6
4
2
0
0
500
1000
1500
2000
Current shared section
200
100
0
0
1000
2000
Current straight section
200
100
0
0
1000
2000
Current bent section
200
100
0
0
1000
2000
Total current
1000
500
0
0
1000
2000

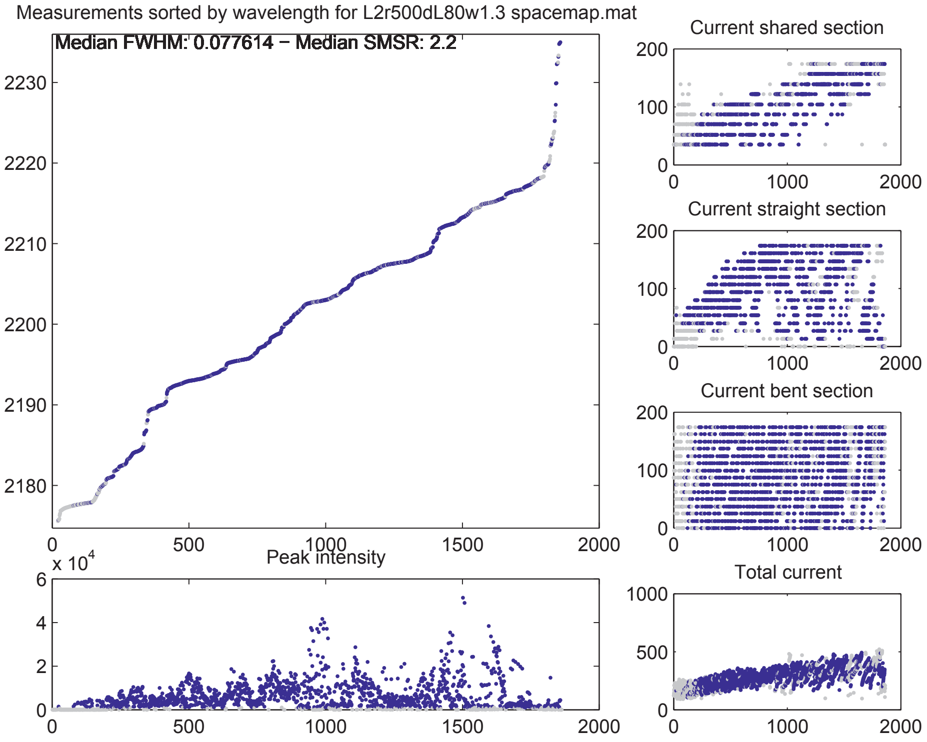
Measurements sorted by wavelength for L2r500dL80w1.3 spacemap.mat
Median FWHM: 0.077614 – Median SMSR: 2.2
2180
2190
2200
2210
2220
2230
0
500
1000
1500
2000
Peak intensity
x 10^4
0
2
4
6
Current shared section
Current straight section
Current bent section
0
100
200
0
1000
2000
Total current
0
500
1000

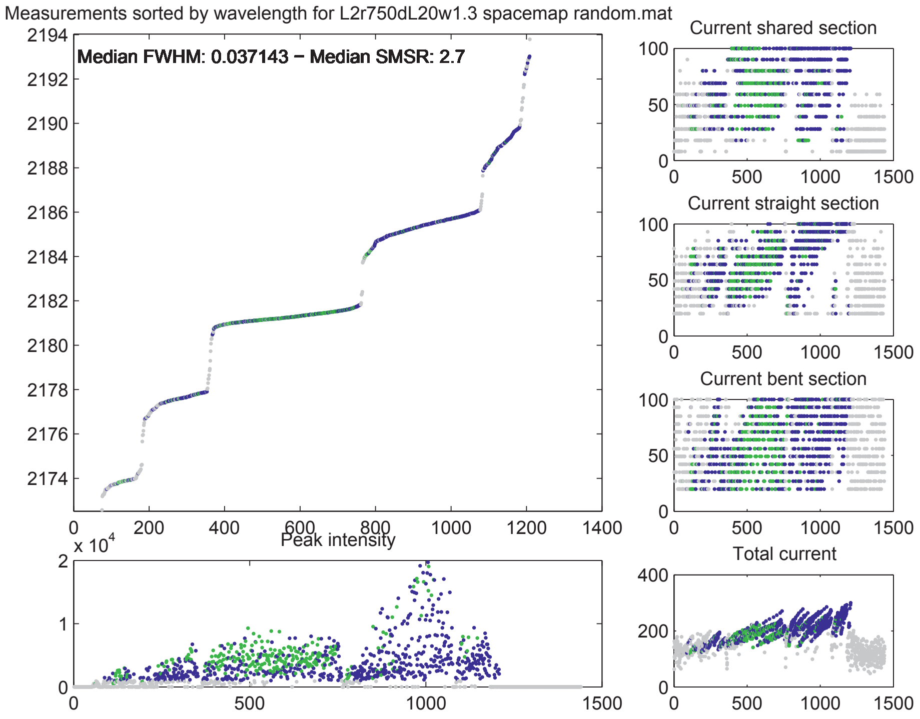
Measurements sorted by wavelength for L2r750dL20w1.3 spacemap random.mat
Median FWHM: 0.037143 – Median SMSR: 2.7
2174
2176
2178
2180
2182
2184
2186
2188
2190
2192
2194
0
200
400
600
800
1000
1200
1400
Peak intensity
x 10^4
0
1
2
0
500
1000
1500
Current shared section
Current straight section
Current bent section
0
50
100
Total current
0
200
400

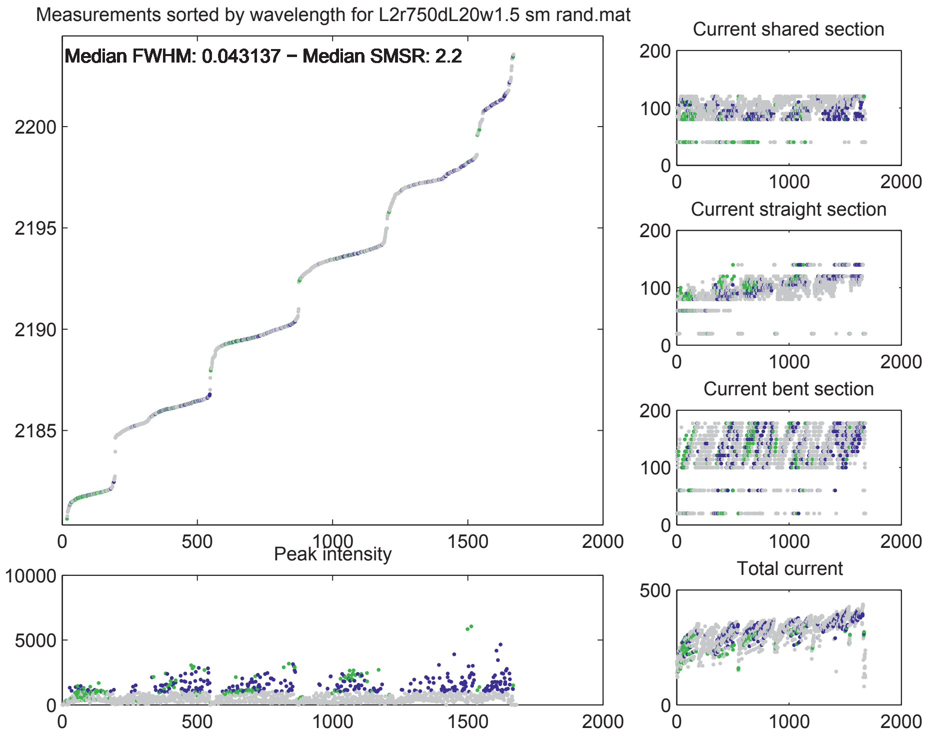
Measurements sorted by wavelength for L2r750dL20w1.5 sm rand.mat
Median FWHM: 0.043137 – Median SMSR: 2.2
2200
2195
2190
2185
0
500
1000
1500
2000
Peak intensity
10000
5000
0
0
500
1000
1500
2000
Current shared section
200
100
0
0
1000
2000
Current straight section
200
100
0
0
1000
2000
Current bent section
200
100
0
0
1000
2000
Total current
500
0
0
1000
2000

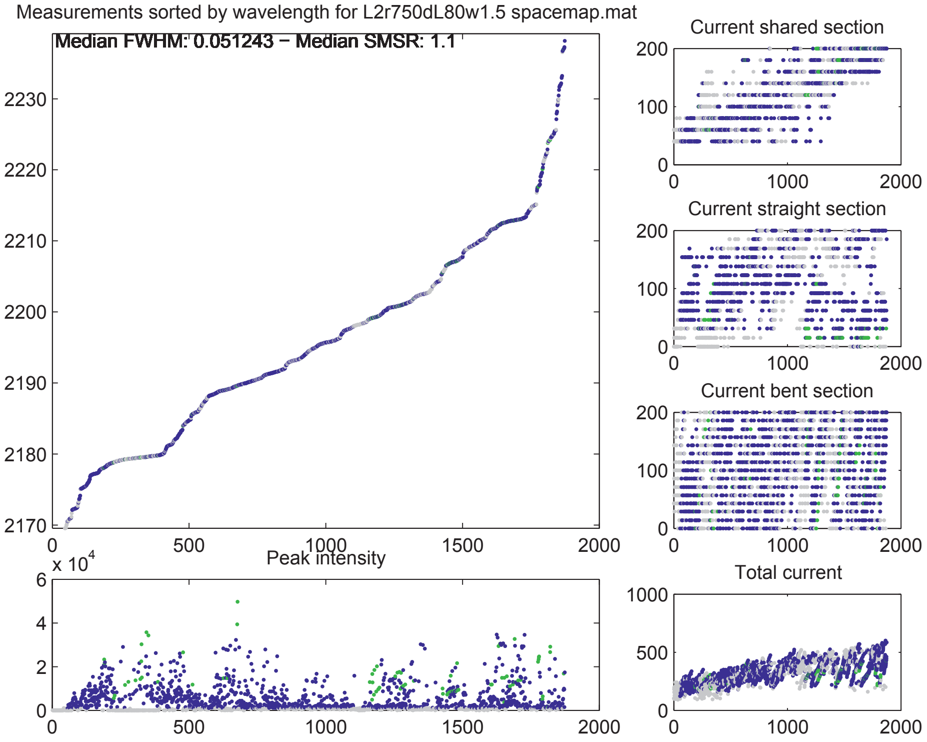
Measurements sorted by wavelength for L2r750dL80w1.5 spacemap.mat
Median FWHM: 0.051243 – Median SMSR: 1.1
2230
2220
2210
2200
2190
2180
2170
0
500
1000
1500
2000
Peak intensity
x 10^4
6
4
2
0
0
500
1000
1500
2000
Current shared section
200
100
0
0
1000
2000
Current straight section
200
100
0
0
1000
2000
Current bent section
200
100
0
0
1000
2000
Total current
1000
500
0
0
1000
2000

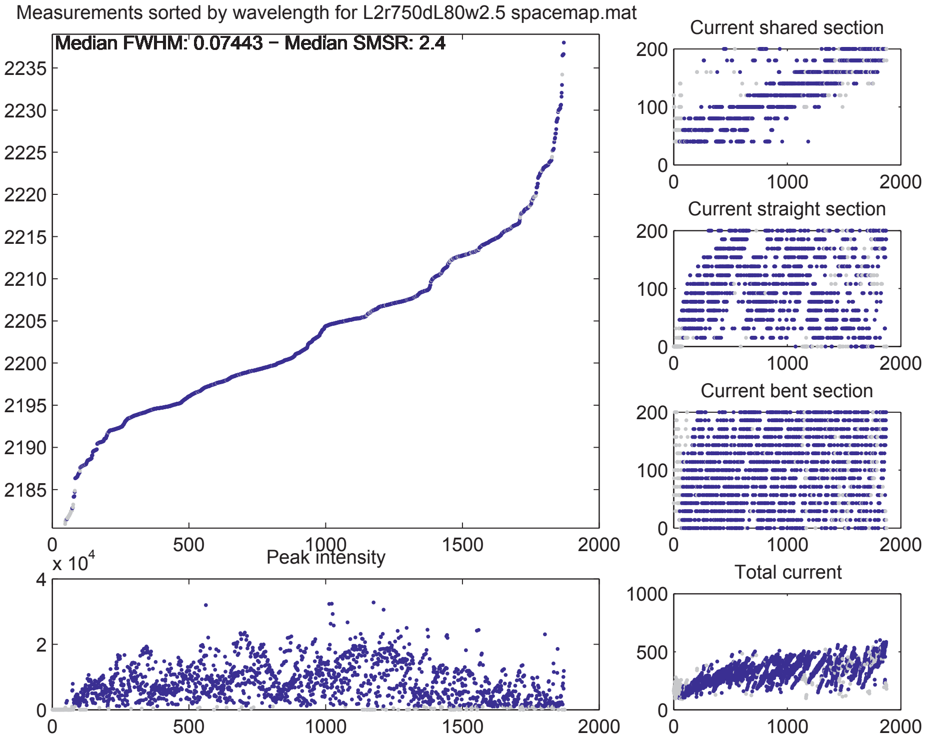
Measurements sorted by wavelength for L2r750dL80w2.5 spacemap.mat
Median FWHM: 0.07443 – Median SMSR: 2.4
2235
2230
2225
2220
2215
2210
2205
2200
2195
2190
2185
0
500
1000
1500
2000
Peak intensity
x 10^4
4
2
0
0
500
1000
1500
2000
Current shared section
200
100
0
0
1000
2000
Current straight section
200
100
0
0
1000
2000
Current bent section
200
100
0
0
1000
2000
Total current
1000
500
0
0
1000
2000

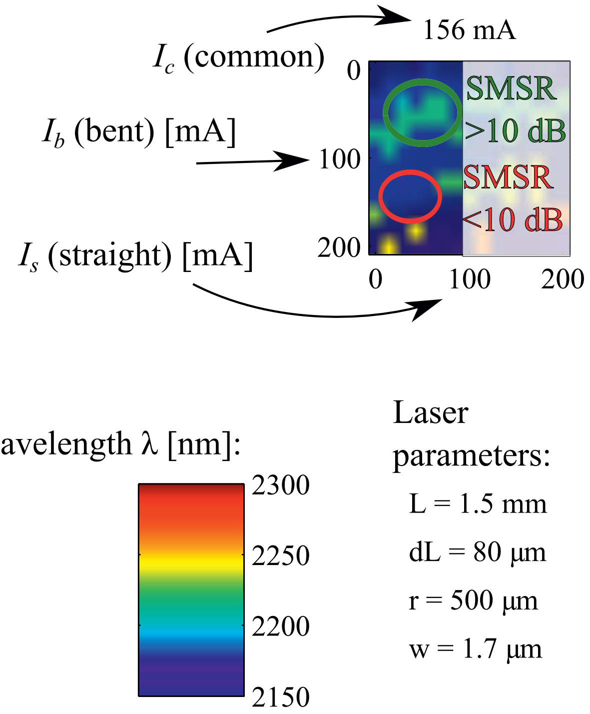

Figure E.3: Description of the plots of the laser wavelength maps. For each plot the common current, I_c, is kept constant. The x-axis shows the straight section current, I_s, and the y-axis shows the bent section current, I_b. The laser measurements with an SMSR of at least 10 dB are highlighted by their brightness in the plots, as shown in the top right plot. Note that dL is used for ΔL in these plots.

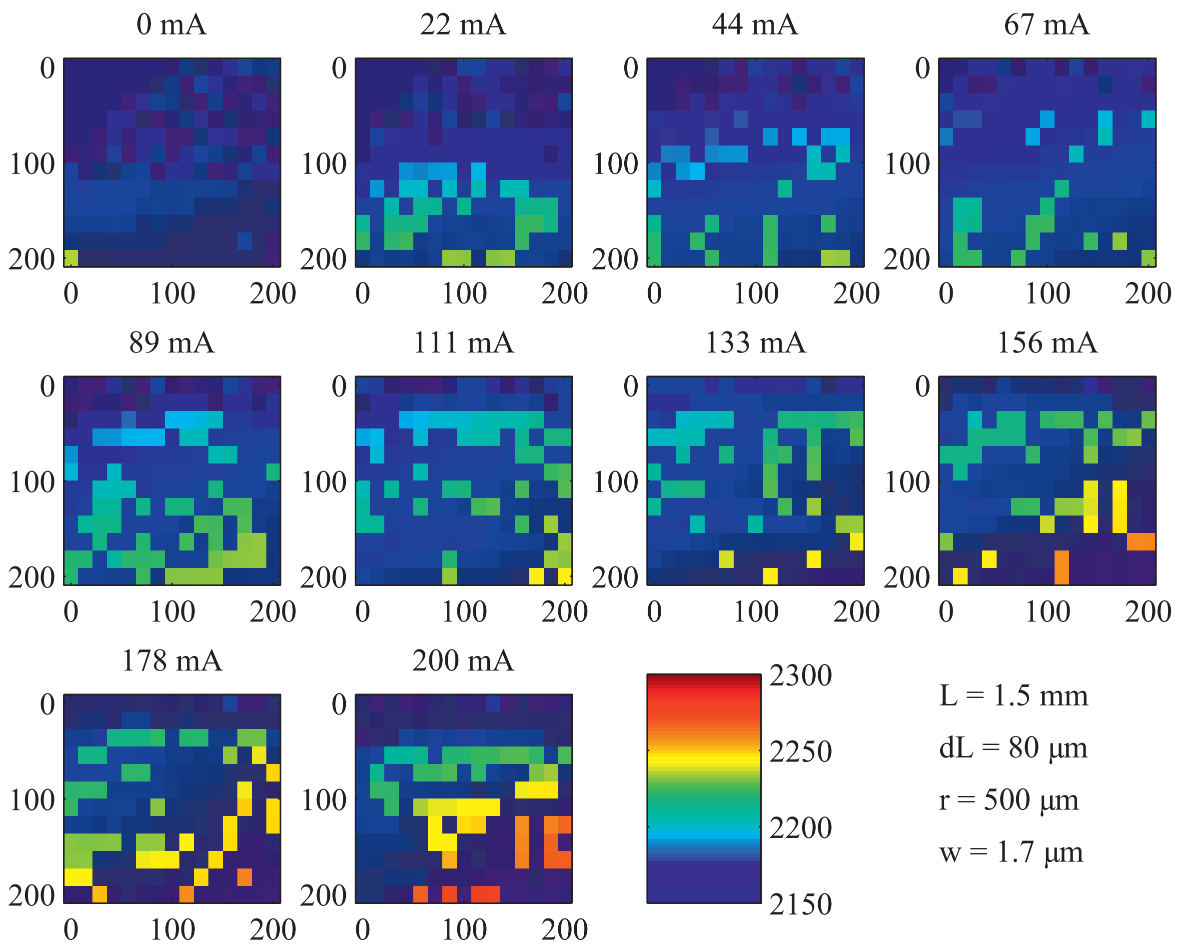
0 mA
22 mA
44 mA
67 mA
89 mA
111 mA
133 mA
156 mA
178 mA
200 mA
0
100
200
2300
2250
2200
2150
L = 1.5 mm
dL = 80 µm
r = 500 µm
w = 1.7 µm

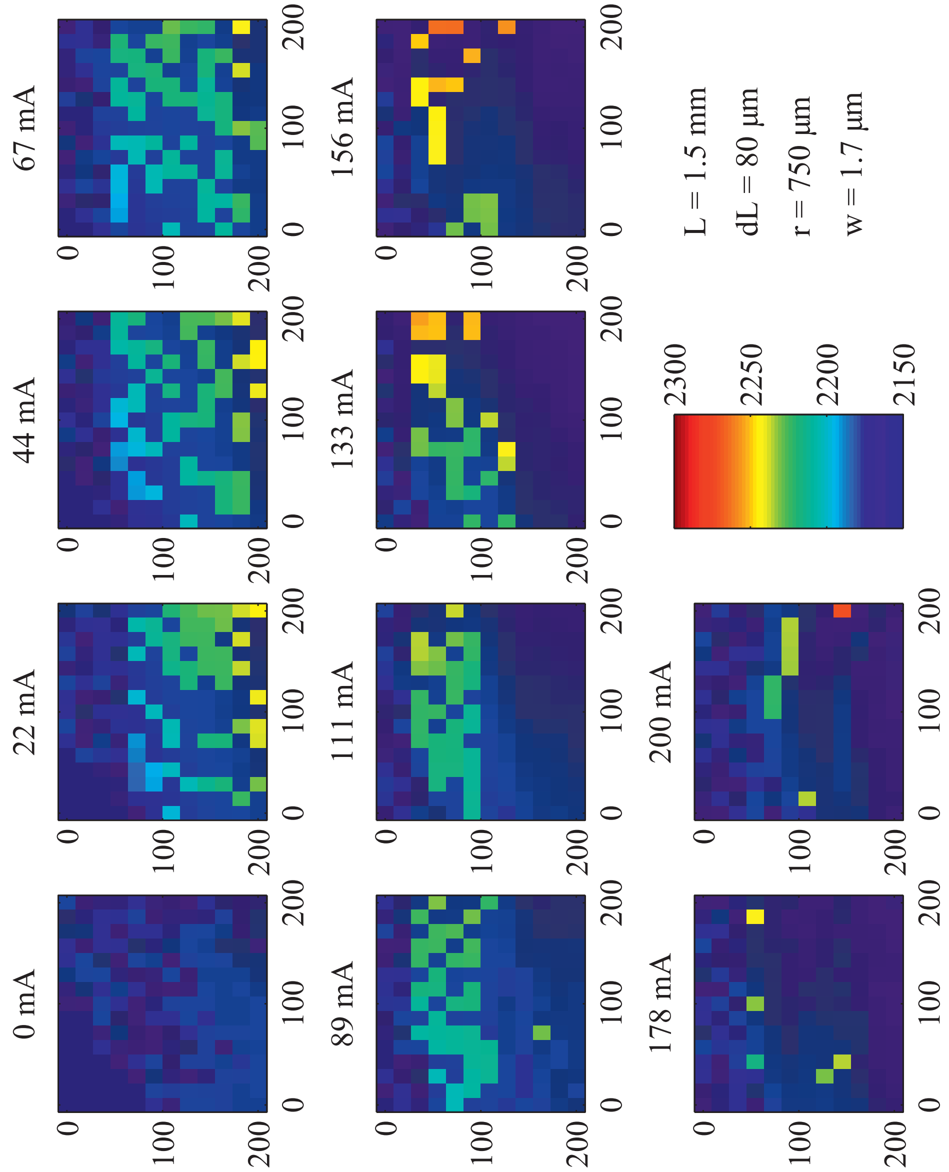
0 mA
22 mA
44 mA
67 mA
89 mA
111 mA
133 mA
156 mA
178 mA
200 mA
0
100
200
2300
2250
2200
2150
L = 1.5 mm
dL = 80 µm
r = 750 µm
w = 1.7 µm

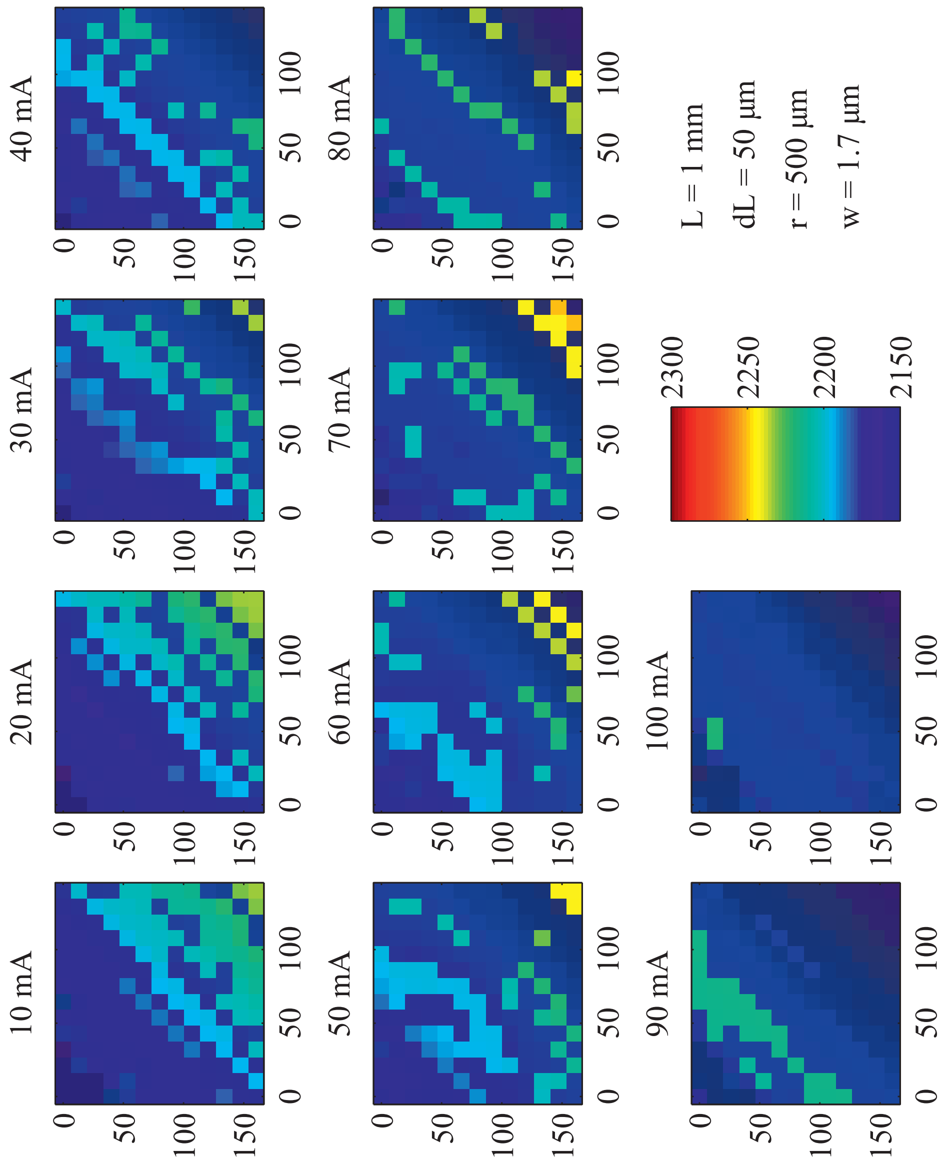
10 mA
20 mA
30 mA
40 mA
50 mA
60 mA
70 mA
80 mA
90 mA
100 mA
0
50
100
150
0
50
100
2300
2250
2200
2150
L = 1 mm
dL = 50 µm
r = 500 µm
w = 1.7 µm

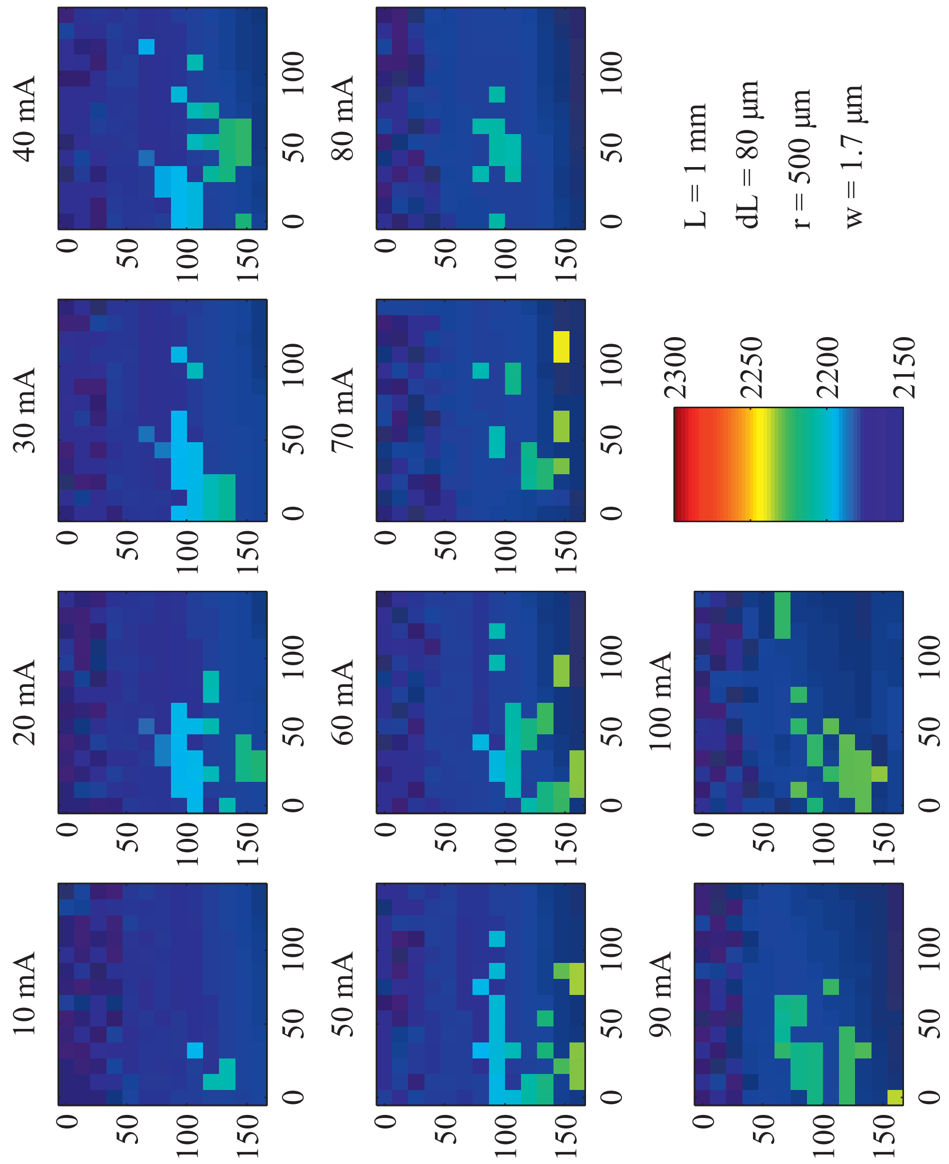
10 mA
20 mA
30 mA
40 mA
50 mA
60 mA
70 mA
80 mA
90 mA
100 mA
0
50
100
150
2300
2250
2200
2150
L = 1 mm
dL = 80 µm
r = 500 µm
w = 1.7 µm

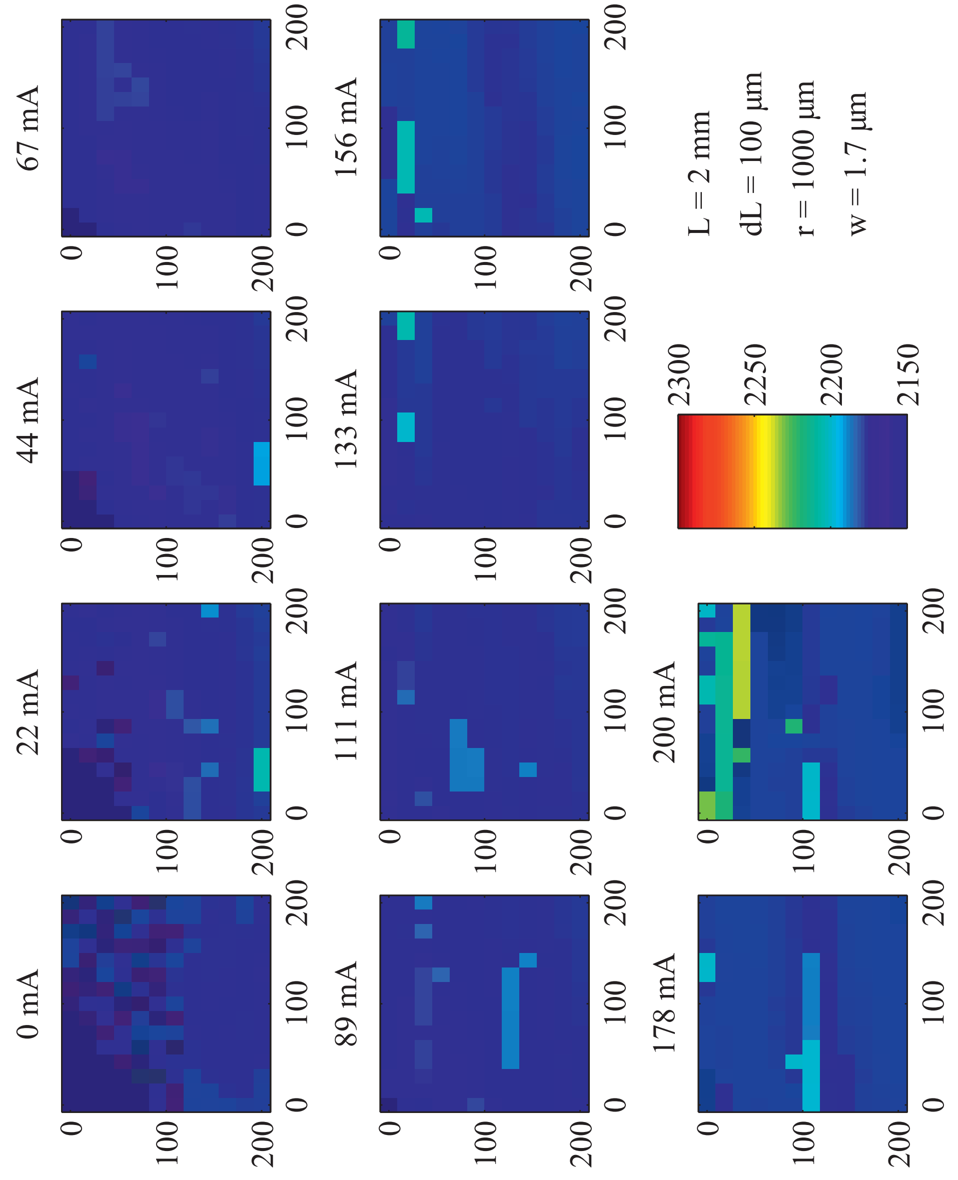
0 mA
22 mA
44 mA
67 mA
89 mA
111 mA
133 mA
156 mA
178 mA
200 mA
0
100
200
2300
2250
2200
2150
L = 2 mm
dL = 100 µm
r = 1000 µm
w = 1.7 µm

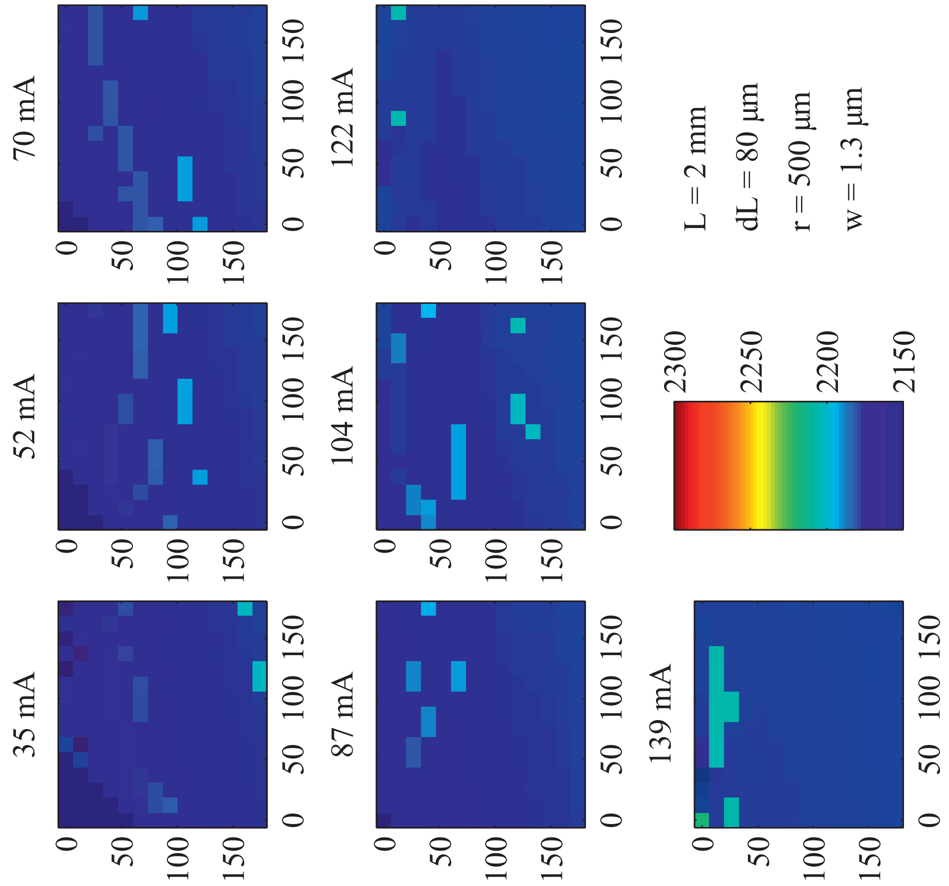
35 mA
52 mA
70 mA
87 mA
104 mA
122 mA
139 mA
0
50
100
150
2300
2250
2200
2150
L = 2 mm
dL = 80 µm
r = 500 µm
w = 1.3 µm

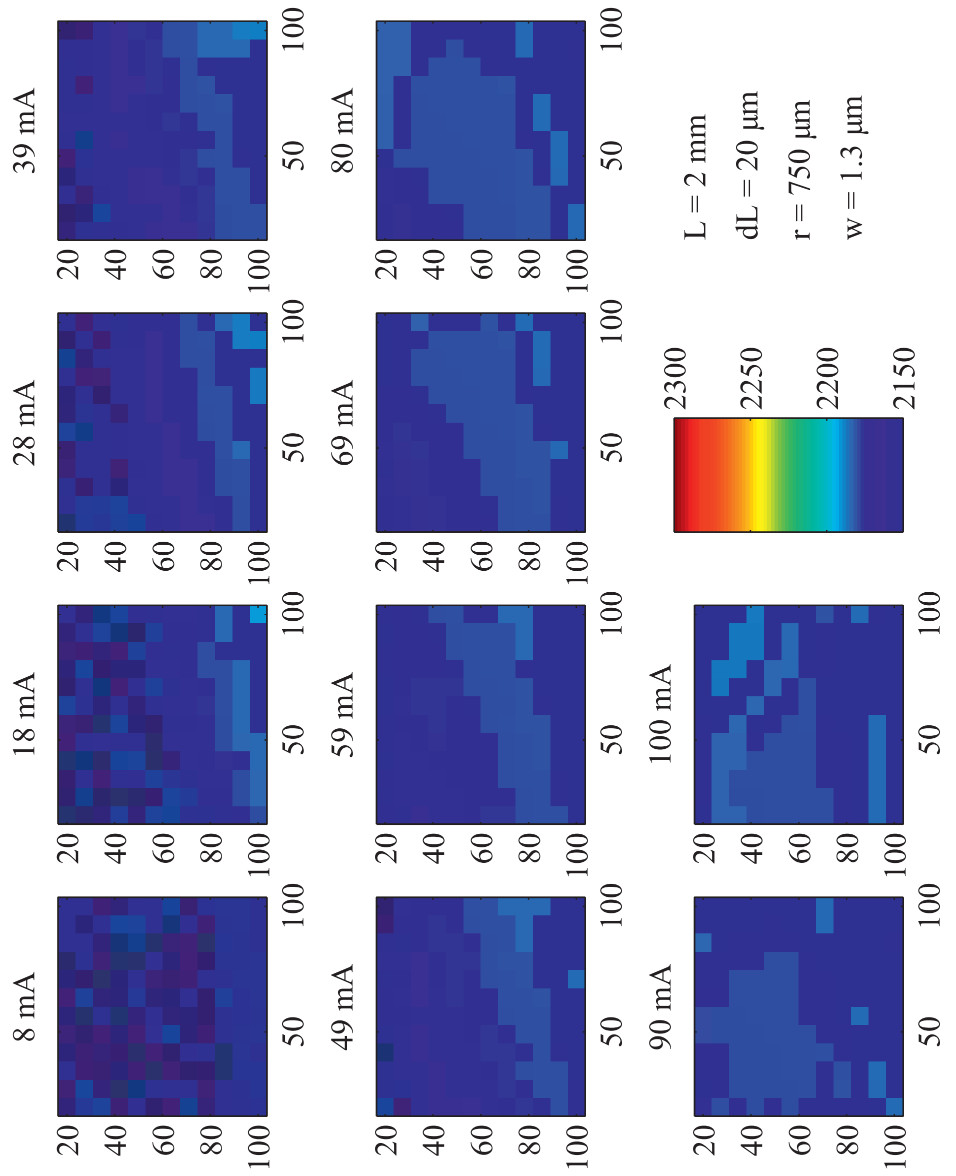
8 mA
18 mA
28 mA
39 mA
49 mA
59 mA
69 mA
80 mA
90 mA
100 mA
20
40
60
80
100
50
100
2300
2250
2200
2150
L = 2 mm
dL = 20 µm
r = 750 µm
w = 1.3 µm

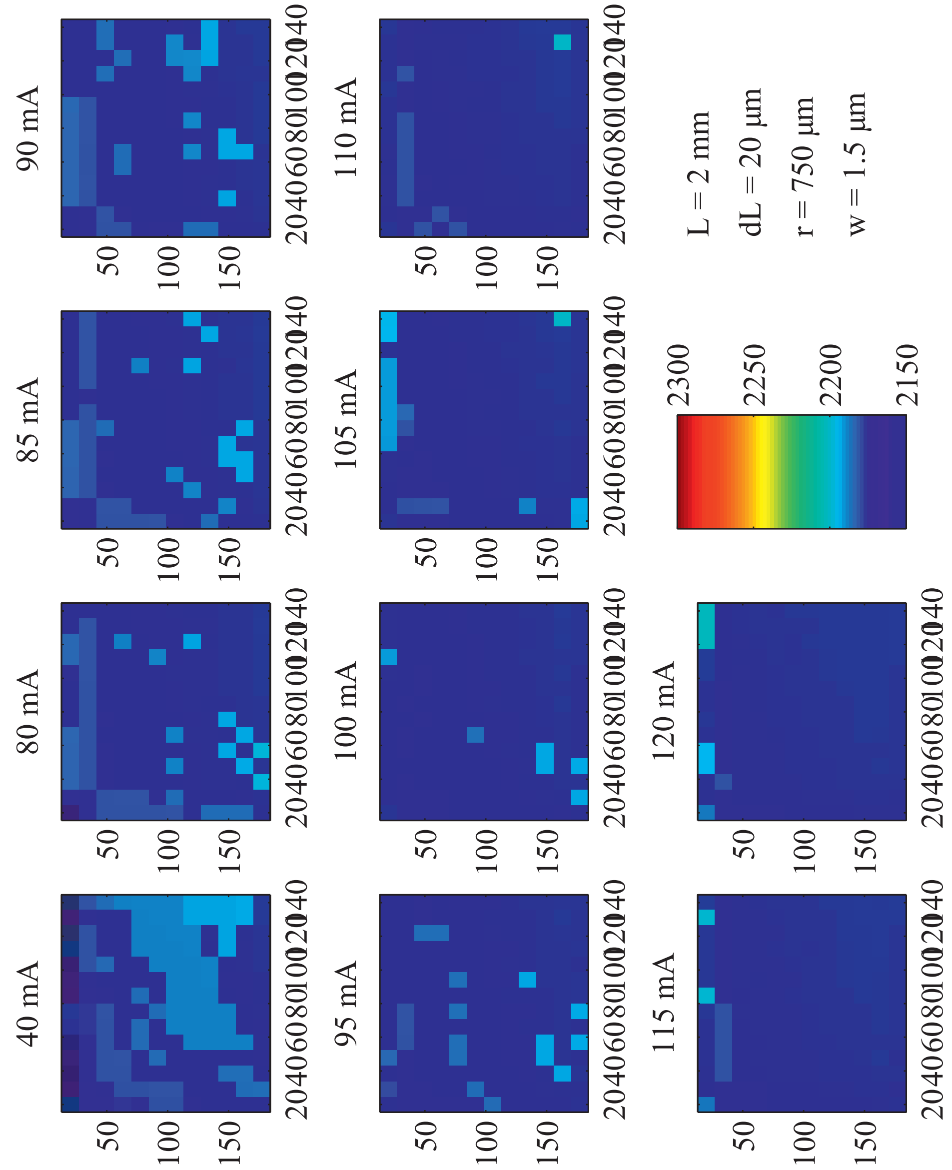
40 mA
80 mA
85 mA
90 mA
95 mA
100 mA
105 mA
110 mA
115 mA
120 mA
50
100
150
20
40
60
80
100
120
140
2300
2250
2200
2150
L = 2 mm
dL = 20 µm
r = 750 µm
w = 1.5 µm

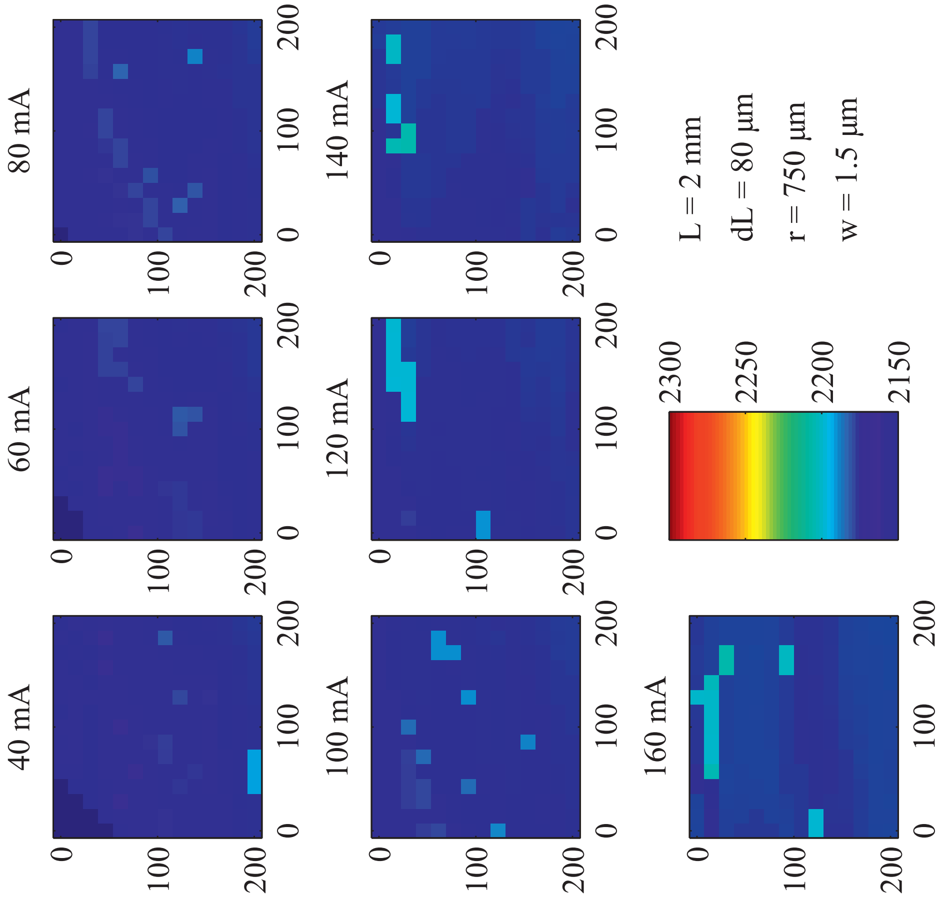
40 mA
60 mA
80 mA
100 mA
120 mA
140 mA
160 mA
0
100
200
2300
2250
2200
2150
L = 2 mm
dL = 80 µm
r = 750 µm
w = 1.5 µm

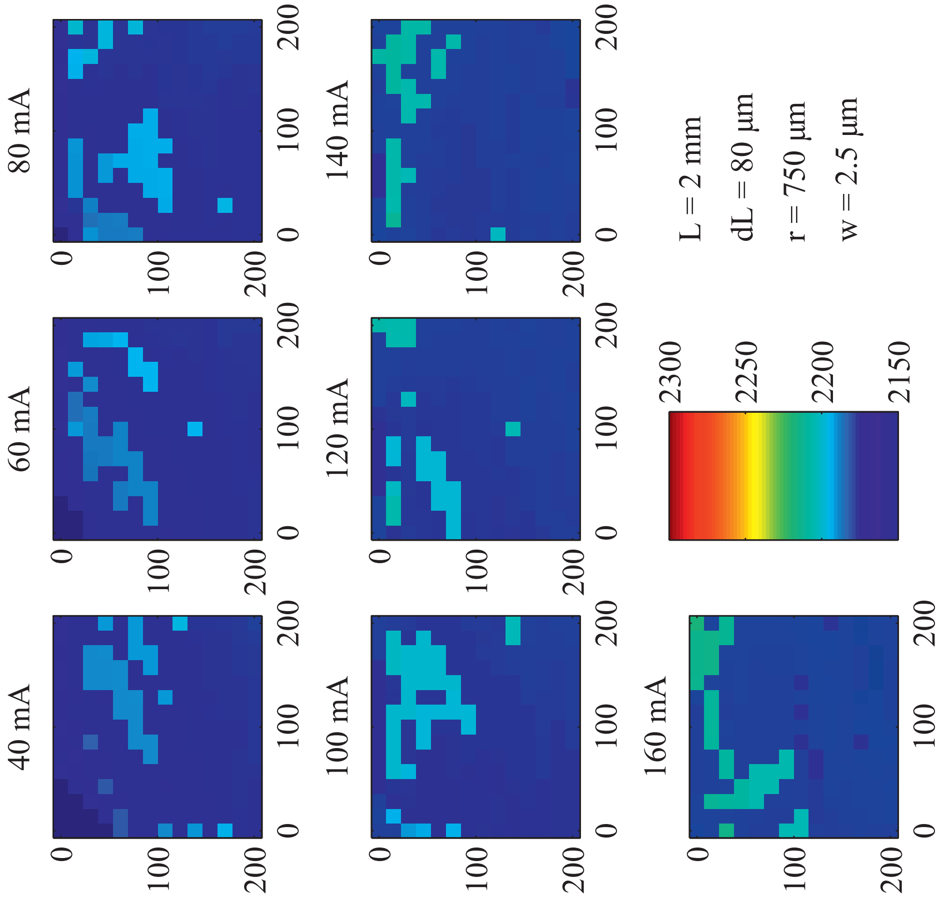
40 mA
60 mA
80 mA
100 mA
120 mA
140 mA
160 mA
0
100
200
2300
2250
2200
2150
L = 2 mm
dL = 80 µm
r = 750 µm
w = 2.5 µm

Appendix F

Near and far field simulations

Solutions to the mode profiles for different etch depths were simulated using the Lights software by Sarangan [73]. These simulations were performed to relate near and far field measurements to the processed laser structure, and to see if it was possible to determine the refractive index profile from far field measurements.

Here, the refractive index profile presented in fig. 4.4 was used, including a value of 3.408 for the AlGaAsSb cladding layers. To account for the etched ridge profile, most of the top cladding material was replaced by a medium with a refractive index of 1.5, which represents the insulation layer (see section 5.8.2). The results are shown in figs. F.1 and F.2.

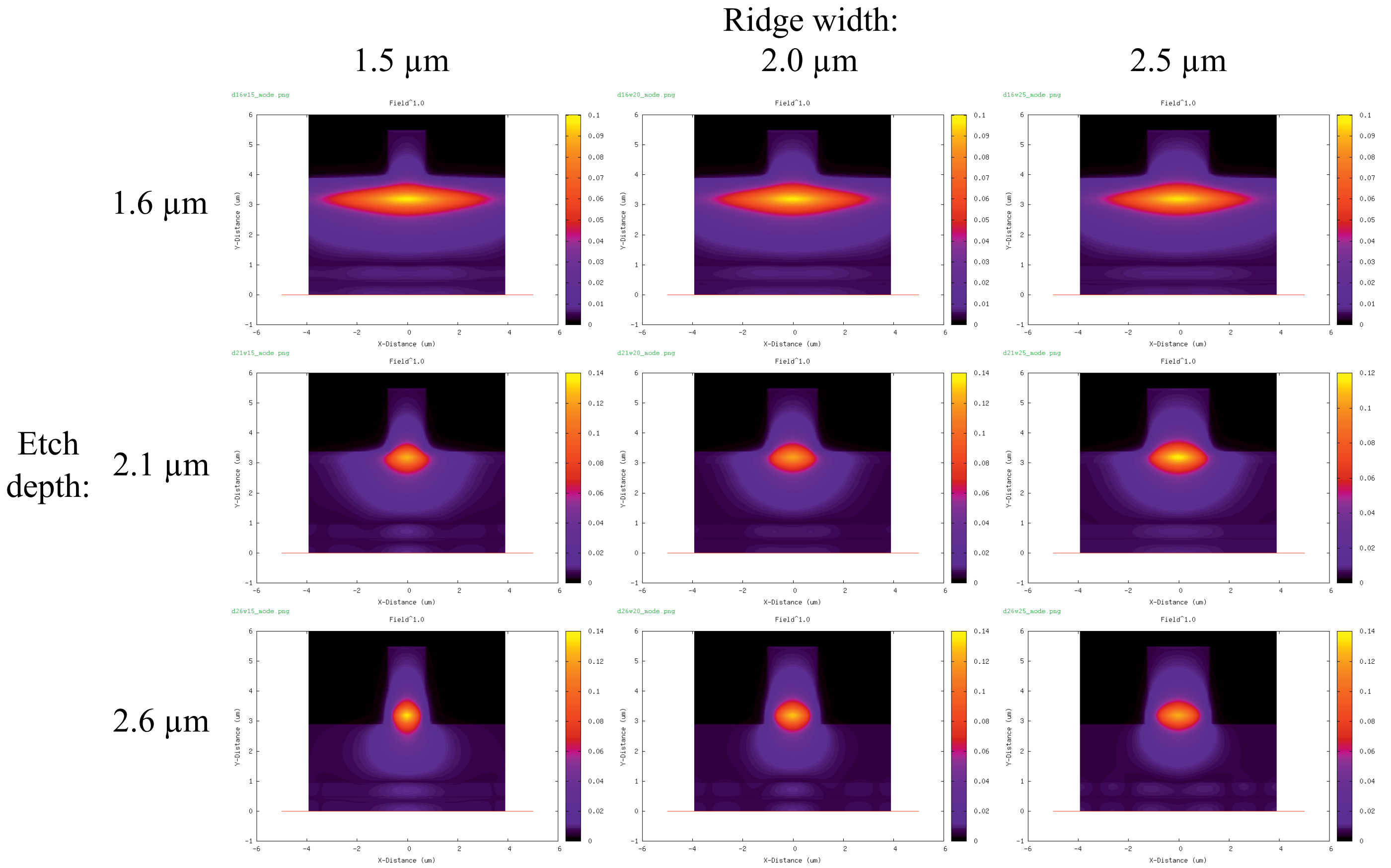

Figure F.1: 2D mode solutions for the waveguide modes in laser structures Sb 142 and Sb 145. Simulated using Lights [73]. From left to right: Ridge width 1.5, 2.0 and 2.5 µm. From top to bottom: Etch depth 1.6, 2.1 and 2.6 µm. The laser structure above the waveguide core is nominally 2.092 µm.

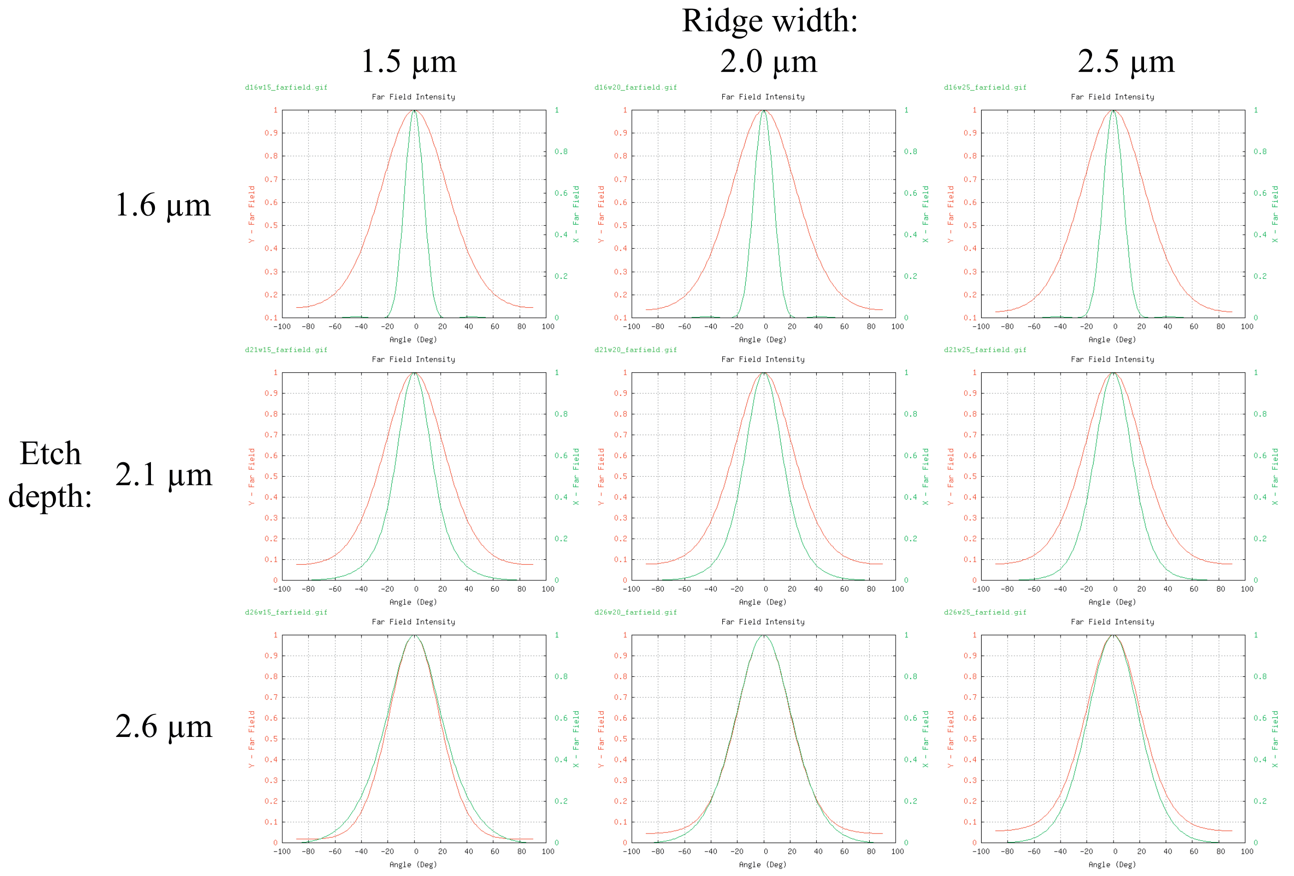

Figure F.2: 2D mode solutions for the far field of laser structures Sb 142 and Sb 145. Simulated using Lights [73]. From left to right: Ridge width 1.5, 2.0 and 2.5 µm. From top to bottom: Etch depth 1.6, 2.1 and 2.6 µm. The thickness of the laser structure above the waveguide core is nominally 2.092 µm. The green line is the in-plane (x), and the red line is the out-of-plane (y) far field, respectively.

List of symbols

Notation	**Description**
a_0	The bulk lattice constant of a cubic crystal.
a_{sub}	The bulk lattice constant of the substrate.
a_x	The in-plane lattice constant of a crystal.
a_z	The out-of-plane lattice constant of a crystal.
β	wavenumber for propagating light wave, see page 13.
ΔE	Energy difference between well and barrier energy levels in a quantum well, given by the VBO and CBO in the valence band and conduction band, respectively. See appendix A.
E_c	conduction band edge energy. See appendix A.
E_g	bandgap energy, $E_g = E_c - E_v$. See appendix A.
E_v	valence band edge energy. See appendix A.
m_b^*	Electron or hole effective mass in a quantum well barrier.
m_w^*	Electron or hole effective mass in a quantum well.
$\mathbf{N}$	Carrier concentration, electrons.
n	Refractive index. See appendix A.
n_{eff}	effective refractive index for propagating wave.
$n_{g,\text{eff}}$	effective group refractive index.

Notation	**Description**
ω	The Bragg angle relative to the sample surface, see fig. 3.6.
P	Carrier concentration, holes.
τ	The angle between the crystal plane and the sample surface, see fig. 3.6.
θ	The Bragg angle; the angle of constructive interference of the diffracted X-ray.
θ_c	Critical angle for total internal reflection.

List of acronyms

Notation	Description
BPM	beam propagation method.
CBO	conduction band offset.
CW	continuous wave.
DBR	distributed bragg reflector.
DFB	distributed feedback.
EBL	electron beam lithography.
EBR	edge bead removal.
FCPE	free-carrier plasma effect.
FFT	fast Fourier transform.
FPL	Fabry-Perot laser.
FTIR	Fourier transform infrared.
FWHM	full-width at half maximum.
HEMT	high-electron mobility transistors.
HF	hydrofluoric acid.
HH	heavy hole valence band.
HITRAN	high-resolution transmission molecular absorption database.
ICL	interband cascade lasers.
ICP-RIE	inductively coupled plasma reactive ion etching.
IR	infrared.

Notation	Description
LH	light hole valence band.
LPE	liquid phase epitaxy.
MBE	molecular beam epitaxy.
ML	mono-layer.
MQW	multiple quantum wells.
NA	numerical aperture.
NIL	nanoimprint lithography.
PL	photoluminescence.
PR	photoresist.
QCL	quantum cascade lasers.
QCSE	the quantum confined stark effect.
QW	quantum well.
RIE	reactive ion etching.
SCH	separate confinement heterostructure.
SEM	scanning electron microscope.
SMSR	side-mode suppression ratio.
SNR	signal-to-noise ratio.
TDLS	tunable diode laser (absorption) spectroscopy.
TE	transverse electric.
TEC	thermoelectric cooler.
TIR	total internal reflection.
TM	transverse magnetic.
UHV	ultra-high vacuum.
VBO	valence band offset.
VCSEL	vertical cavity surface-emitting laser.
VECSEL	vertical external cavity surface-emitting laser.

Notation	Description
XRD	X-ray diffraction.
ZB	zinc blende.

Bibliography

[1] V. T. Bublik, J. Wilke, and A. T. Pereversev. “Die Natur der festen Lösungen der überschüssigen Komponenten in unlegiertem Galliumantimonid”. *Phys. Status Solidi A* **73** (1982), K271–K273. DOI: `10.1002/pssa.2210730270`.

[2] A. Vicet, D. A. Yarekha, A. Perona, Y. Rouillard, S. Gaillard, and A. N. Baranov. “Trace gas detection with antimonide-based quantum-well diode lasers”. *Spectrochim. Acta, Part A* **58** (2002), pp. 2405–2412.

[3] K. Vizbaras and M.-C. Amann. “Room-temperature 3.73 µm GaSb-based type-I quantum-well lasers with quinternary barriers”. *Semicond. Sci. Technol.* **27** (2012), p. 032001.

[4] L. S. Rothman, D. Jacquemart, A. Barbe, D. C. Benner, M. Birk, L. R. Brown, M. R. Carleer, C. C. Jr., K. Chance, L. H. Coudert, V. Dana, V. M. Devi, J.-M. Flaud, R. R. Gamache, A. Goldman, J.-M. Hartmann, K. W. Jucks, A. G. Maki, J.-Y. Mandin, S. T. Massie, J. Orphal, A. Perrin, C. P. Rinsland, M. A. H. Smith, J. Tennyson, R. N. Tolchenov, R. A. Toth, J. V. Auwera, P. Varanasi, and G. Wagner. “The HITRAN 2004 molecular spectroscopic database”. *J. Quant. Spectrosc. Radiat. Transfer* **96** (2005), pp. 139–204. DOI: `10.1016/j.jqsrt.2004.10.008`.

[5] NASA. *File:Diode laser.jpg*. Apr. 2013. URL: `http://commons.wikimedia.org/wiki/File:Diode_laser.jpg`.

[6] N. Kobayashi, Y. Horikoshi, and C. Uemura. “Room Temperature Operation of the InGaAsSb/AlGaAsSb DH Laser at 1.8 pm Wavelength”. *Jpn. J. Appl. Phys.* **19** (1980), p. L30.

[7] H. K. Choi and S. J. Eglash. “High-efficiency high-power GaInAsSb-AlGaAsSb double-heterostructure lasers emitting at 2.3 µm”. *IEEE J. Quantum Electron.* **27** (1991), pp. 1555–1559.

[8] W. T. Tsang, T. H. Chiu, D. W. Kisker, and J. A. Ditzenberger. “Molecular beam epitaxial growth of $In_{1-x}Ga_xAs_{1-y}Sb_y$ lattice matched to GaSb”. *Appl. Phys. Lett.* **46** (1985), pp. 283–285.

[9] J. Coleman, A. Bryce, and C. Jagadish. *Semiconductors and Semimetals*. Advances in Semiconductor Lasers v. 86. Elsevier/Academic Press, 2012. ISBN: 9780123910660.

[10] A. Joullié and P. Christol. “GaSb-based mid-infrared 2–5 μm laser diodes”. *C.R. Phys.* **4** (2003), pp. 621–637.

[11] I. Vurgaftman, C. L. Canedy, C. S. Kim, M. Kim, W. W. . Bewley, J. R. Lindle, J. Abell, and J. R. Meyer. “Mid-infrared interband cascade lasers operating at ambient temperatures”. *New J. Phys.* **11** (2009), p. 125015.

[12] H. K. Choi, G. W. Turner, and S. J. Eglash. “High-power GaInAsSb-AlGaAsSb multiple-quantum-well diode lasers emitting at 1.9 μm”. *IEEE Photonics Technol. Lett.* **6** (1994), pp. 7–9.

[13] G. W. Turner, H. K. Choi, and M. J. Manfra. “Ultralow-threshold (50 A/cm 2) strained single-quantum-well GaInAsSb/AlGaAsSb lasers emitting at 2.05 μm”. *Appl. Phys. Lett.* **72** (1998), pp. 876–878.

[14] H. K. Choi, J. N. Walpole, G. W. Turner, M. K. Conners, L. J. Missaggia, and M. J. Manfra. “GaInAsSb-AlGaAsSb tapered lasers emitting at 2.05 μm with 0.6-W diffraction-limited power”. *IEEE Photonics Technol. Lett.* **10** (1998), pp. 938–940.

[15] H. Lee, P. K. York, R. J. Menna, R. U. Martinelli, D. Z. Garbuzov, S. Y. Narayan, and J. C. Connolly. “Room-temperature 2.78 μm AlGaAsSb/InGaAsSb quantum-well lasers”. *Appl. Phys. Lett.* **66** (1995), pp. 1942–1944.

[16] S. J. Eglash and H. K. Choi. “Efficient GaInAsSb/AlGaAsSb diode lasers emitting at 2.29 μm”. *Appl. Phys. Lett.* **57** (1990), pp. 1292–1294.

[17] H. K. Choi and S. J. Eglash. “Room-temperature cw operation at 2.2 μm of GaInAsSb/AlGaAsSb diode lasers grown by molecular beam epitaxy”. *Appl. Phys. Lett.* **59** (1991), pp. 1165–1166.

[18] H. K. Choi, S. J. Eglash, and G. W. Turner. “Double-heterostructure diode lasers emitting at 3 μm with a metastable GaInAsSb active layer and AlGaAsSb cladding layers”. *Appl. Phys. Lett.* **64** (1994), pp. 2474–2476.

[19] H. K. Choi and G. W. Turner. “Antimonide-based strained quantum-well diode lasers”. *Phys. Scr.* **1997** (1997), p. 17.

[20] A. Bachmann, K. Kashani-Shirazi, S. Arafin, and M.-C. Amann. “GaSb-Based VCSEL With Buried Tunnel Junction for Emission Around 2.3 μm”. *IEEE J. Sel. Top. Quantum Electron.* **15** (2009), pp. 933–940.

[21] A. Bachmann, T. Lim, K. Kashani-Shirazi, O. Dier, C. Lauer, and M.-C. Amann. “Continuous-wave operation of electrically pumped GaSb-based vertical cavity surface emitting laser at 2.3 µm”. *Electron. Lett* **44** (2008), pp. 202–203.

[22] K. Vizbaras and M.-C. Amann. “3.6 µm GaSb-based type-I lasers with quinternary barriers, operating at room temperature”. *Electron. Lett* **47** (2011), pp. 980–981.

[23] M. Grau, C. Lin, O. Dier, C. Lauer, and M.-C. Amann. “Room-temperature operation of 3.26 μm GaSb-based type-I lasers with quinternary AlGaInAsSb barriers”. *Appl. Phys. Lett.* **87** (2005), p. 241104.

[24] L. Shterengas, G. Kipshidze, T. Hosoda, D. Donetsky, and G. Belenky. “Room Temperature Operated 3.1-µm Type-I GaSb-based Diode Lasers with 80mW Continuous Wave Output Power”. In: *Conference on Lasers and Electro-Optics*. Optical Society of America. 2008. URL: `http://www.opticsinfobase.org/abstract.cfm?URI=CLEO-2008-CTuZ1`.

[25] G. L. Belenky, J. G. Kim, L. Shterengas, A. Gourevitch, and R. U. Martinelli. “High-power 2.3 µm laser arrays emitting 10 W CW at room temperature”. *Electron. Lett* **40** (2004), pp. 737–738.

[26] L. Shterengas, G. Belenky, T. Hosoda, G. Kipshidze, and S. Suchalkin. “Continuous wave operation of diode lasers at 3.36 µm at 12°C”. *Appl. Phys. Lett.* **93** (2008), pp. 011103–011103.

[27] T. Hosoda, G. Kipshidze, L. Shterengas, and G. Belenky. “Diode lasers emitting near 3.44 µm in continuous-wave regime at 300K”. *Electron. Lett* **46** (2010), pp. 1455–1457.

[28] M. Kim, W. W. Bewley, J. R. Lindle, C. S. Kim, I. Vurgaftman, J. R. Meyer, J. G. Kim, and R. U. Martinelli. “Midinfrared ”W” diode lasers with improved electrical characteristics”. *Appl. Phys. Lett.* **83** (2003), pp. 5374–5376.

[29] L. J. Olafsen, E. H. Aifer, I. Vurgaftman, W. W. Bewley, C. L. Felix, J. R. Meyer, D. Zhang, C.-H. Lin, and S. S. Pei. “Near-room-temperature mid-infrared interband cascade laser”. *Appl. Phys. Lett.* **72** (1998), pp. 2370–2372.

[30] I. Vurgaftman, W. W. Bewley, C. L. Canedy, C. S. Kim, M. Kim, C. D. Merritt, J. Abell, J. R. Lindle, and J. R. Meyer. “Rebalancing of internally generated carriers for mid-infrared interband cascade lasers with very low power consumption”. *Nat. Commun.* **2** (2011), p. 585.

[31] C. S. Kim, M. Kim, J. Abell, W. W. Bewley, C. D. Merritt, C. L. Canedy, I. Vurgaftman, and J. R. Meyer. “Mid-IR distributed-feedback interband cascade lasers”. In: *SPIE OPTO*. International Society for Optics and Photonics. 2013, 86311O. DOI: `10.1117/12.2004163`.

[32] W. W. Bewley, C. L. Felix, I. Vurgaftman, R. E. Bartolo, J. R. Lindle, J. R. Meyer, H. Lee, and R. U. Martinelli. “Mid-infrared photonic-crystal distributed-feedback laser with enhanced spectral purity and beam quality”. *Appl. Phys. Lett.* **79** (2001), pp. 3221–3223.

[33] C. S. Kim, W. W. Bewley, C. L. Canedy, I. Vurgaftman, M. Kim, and J. R. Meyer. “Broad-stripe near-diffraction-limited mid-infrared laser with a second-order photonic-crystal distributed feedback grating”. *IEEE Photonics Technol. Lett.* **16** (2004), pp. 1250–1252.

[34] J. A. Gupta, P. J. Barrios, J. Lapointe, G. C. Aers, and C. Storey. “Single-mode 2.4 µm InGaAsSb/AlGaAsSb distributed feedback lasers for gas sensing”. *Appl. Phys. Lett.* **95**, 041104 (2009), p. 041104. DOI: `10.1063/1.3189814`.

[35] J. A. Gupta, A. Bezinger, P. J. Barrios, J. Lapointe, D. Poitras, and P. Waldron. “High-resolution methane spectroscopy using InGaAsSb/AlInGaAsSb laterally-coupled index-grating distributed feedback laser diode at 3.23 μm”. *Electron. Lett* **48** (2012), pp. 396–397.

[36] J. A. Gupta, P. J. Barrios, G. C. Aers, P. Waldron, and C. Storey. “Room-temperature continuous-wave operation of type-I GaSb-based lasers at 3.1 µm”. *Electron. Lett* **45** (2009), pp. 835–837.

[37] A. Salhi, D. Barat, D. Romanini, Y. Rouillard, A. Ouvrard, R. Werner, J. Seufert, J. Koeth, A. Vicet, and A. Garnache. “Single-frequency Sb-based distributed-feedback lasers emitting at 2.3 µm above room temperature for application in tunable diode laser absorption spectroscopy”. *Appl. Opt.* **45** (2006), pp. 4957–4965.

[38] J.-C. Nicolas, A. N. Baranov, Y. Cuminal, Y. Rouillard, and C. Alibert. “Tunable diode laser absorption spectroscopy of carbon monoxide around 2.35 μm”. *Appl. Opt.* **37** (1998), pp. 7906–7911.

[39] L. Cerutti, A. Garnache, A. Ouvrard, and F. Genty. “High temperature continuous wave operation of Sb-based vertical external cavity surface emitting laser near 2.3 μm”. *J. Cryst. Growth* **268** (2004), pp. 128–134.

[40] A. Ouvrard, A. Garnache, L. Cerutti, F. Genty, and D. Romanini. “Single-frequency tunable Sb-based VCSELs emitting at 2.3 µm”. *IEEE Photonics Technol. Lett.* **17** (2005), pp. 2020–2022.

[41] D. Sanchez, L. Cerutti, and E. Tournié. “Mid-IR GaSb-Based Bipolar Cascade VCSELs”. *IEEE Photonics Technol. Lett.* **25** (2013), pp. 882–884. DOI: `10.1109/LPT.2013.2254707`.

[42] A. Wilk, M. El Gazouli, M. El Skouri, P. Christol, P. Grech, A. N. Baranov, and A. Joullie. “Type-II InAsSb/InAs strained quantum-well laser diodes emitting at 3.5 μm”. *Appl. Phys. Lett.* **77** (2000), pp. 2298–2300.

[43] A. N. Baranov, N. Bertru, Y. Cuminal, G. Boissier, C. Alibert, and A. Joullie. “Observation of room-temperature laser emission from type III InAs/GaSb multiple quantum well structures”. *Appl. Phys. Lett.* **71** (1997), pp. 735–737.

[44] H. K. Choi. “Mid-infrared lasers fabricated from III–V compound semiconductors”. *Curr. Opin. Solid State Mater. Sci.* **1** (1996), pp. 212–217.

[45] F. Poletti, N. V. Wheeler, M. N. Petrovich, N. Baddela, E. N. Fokoua, J. R. Hayes, D. R. Gray, Z. Li, R. Slavík, and D. J. Richardson. “Towards high-capacity fibre-optic communications at the speed of light in vacuum”. *Nat. Photonics* (2013).

[46] J. Buus, M. C. Amann, and D. J. Blumenthal. *Tunable laser diodes and related optical sources*. SPIE PM. Wiley-Interscience, 2005. ISBN: 9780471208167.

[47] P. Adamiec, A. Salhi, R. Bohdan, A. Bercha, F. Dybala, W. Trzeciakowski, Y. Rouillard, and A. Joullié. “Pressure-tuned InGaAsSb/AlGaAsSb diode laser with 700 nm tuning range”. *Appl. Phys. Lett.* **85** (2004), pp. 4292–4294. DOI: `10.1063/1.1815069`.

[48] T. Kruczek, K. A. Fedorova, G. S. Sokolovskii, R. Teissier, A. N. Baranov, and E. U. Rafailov. “InAs/AlSb widely tunable external cavity quantum cascade laser around 3.2 µm”. *App. Phys. Lett.* **102** (2013), p. 011124. DOI: `10.1063/1.4774088`.

[49] N. Koslowski, A. Heger, K. Roessner, M. Legge, J. Koeth, and L. Hildebrandt. “Monolithic wide tunable laser diodes for gas sensing at 2100 nm”. In: *Proceedings of SPIE*. Vol. 8640. 2013, p. 864008. DOI: `10.1117/12.2004020`.

[50] G. Belenky, D. Wang, Y. Lin, D. Donetsky, G. Kipshidze, L. Shterengas, D. Westerfeld, W. L. Sarney, and S. P. Svensson. “Metamorphic InAsSb/AlInAsSb heterostructures for optoelectronic applications”. *Appl. Phys. Lett.* **102** (2013), pp. 111108–111108.

[51] T. Hosoda, D. Wang, G. Kipshidze, W. L. Sarney, L. Shterengas, and G. Belenky. “3 µm diode lasers grown on (Al)GaInSb compositionally graded metamorphic buffer layers”. *Semicond. Sci. Technol.* **27** (2012), p. 055011.

[52] L. Cerutti, J.-B. Rodriguez, and E. Tournié. “GaSb-Based Laser, Monolithically Grown on Silicon Substrate, Emitting at 1.55 µm at Room Temperature”. *IEEE Photonics Technol. Lett.* **22** (2010), pp. 553–555.

[53] H. Kataria, C. Junesand, Z. Wang, W. Metaferia, Y. T. Sun, S. Lourdudoss, G. Patriarche, A. Bazin, F. Raineri, P. . Mages, N. Julian, and J. E. Bowers. “Towards a monolithically integrated III-V laser on silicon: optimization of multi-quantum well growth on InP on Si”. *Semicond. Sci. Technol.* **28** (2013), p. 094008.

[54] A. Garnache, A. Ouvrard, L. Cerutti, D. Barat, A. Vicet, F. Genty, Y. Rouillard, D. Romanini, and E. A. Cerda-Mendez. “2–2.7 µm single frequency tunable Sb-based lasers operating in CW at RT: Microcavity and External–cavity VCSELs, DFB”. In: *Proc. SPIE*. Vol. 6184. 2006, 61840N. DOI: `10.1117/12.663448`.

[55] P. Werle. “A review of recent advances in semiconductor laser based gas monitors”. *Spectrochim. Acta, Part A* **54** (1998), pp. 197–236. DOI: `10.1016/S1386-1425(97)00227-8`.

[56] P. W. Werle, P. Mazzinghi, F. D. Amato, M. D. Rosa, K. Maurer, and F. Slemr. “Signal processing and calibration procedures for in situ diode-laser absorption spectroscopy”. *Spectrochim. Acta, Part A* **60** (2004), pp. 1685–1705. DOI: `10.1016/j.saa.2003.10.013`.

[57] M. Reason, B. R. Bennett, R. Magno, and J. B. Boos. “Molecular Beam Epitaxial Regrowth of Antimonide-Based Semiconductors”. *J. Electron. Mater.* **40** (2010), pp. 6–10. DOI: `10.1007/s11664-010-1399-6`.

[58] K. Haring, J. Viheriälä, M.-R. Viljanen, J. Paajaste, R. Koskinen, S. Suomalainen, A. Laakso, K. Leinonen, T. Niemi, and M. Guina. “Laterally-coupled distributed feedback InGaSb/GaSb diode lasers fabricated by nanoimprint lithography”. *Electron. Lett* **46** (2010), pp. 1146–1147.

[59] B.-O. Fimland, R. Bugge, G. Myrvågnes, and E. Selvig. “Critical thickness of MBE-grown $Al_{0.9}Ga_{0.1}As_ySb_{1-y}$ on GaSb”. In preparation.

[60] M. Breivik, T. A. Nilsen, G. Myrvågnes, E. Selvig, and B.-O. Fimland. “Temperature dependent lattice constant of $Al_{0.90}Ga_{0.10}As_ySb_{1-y}$”. *J. Vac. Sci. Technol., B* **28** (2010), p. C3I1.

[61] T. A. Nilsen, M. Breivik, G. Myrvågnes, and B.-O. Fimland. “Thermal expansion of GaSb measured by temperature dependent x-ray diffraction”. *J. Vac. Sci. Technol., B* **28** (2010), pp. C3I17–C3I20. DOI: `10.1116/1.3336341`.

[62] T. A. Nilsen, S. K. Patra, M. Breivik, and B.-O. Fimland. “Thermal dependence of the lattice constant and the Poisson ratio of AlSb above room temperature”. *J. Cryst. Growth* **336** (2011), pp. 29–31. DOI: `10.1016/j.jcrysgro.2011.09.034`.

[63] N. N. Sirota and Y. I. Pashintsev. “Dynamic displacements of atoms as related to linear expansion coefficients in aluminum, gallium and indium arsenides”. *Doklady Akad. Nauk SSSR* **127** (1959), pp. 609–611.

[64] J. C. Brice. *Properties of Gallium Arsenide*. 2nd. London: INSPEC, 1990.

[65] M. Breivik, T. A. Nilsen, and B.-O. Fimland. “Temperature dependent lattice constant of InSb above room temperature”. *J. Cryst. Growth* **381** (2013), pp. 165–168. DOI: `10.1016/j.jcrysgro.2013.06.034`.

[66] J. Grünenpütt. *Pseudomorphic and metamorphic HEMT-technologies for industrial W-band low-noise and power applications*. PhD thesis. Universität Ulm, 2009.

[67] S. R. Kurtz, R. M. Biefeld, A. A. Allerman, A. J. Howard, M. H. Crawford, and M. W. Pelczynski. “Pseudomorphic InAsSb multiple quantum well injection laser emitting at 3.5 μm”. *Appl. Phys. Lett.* **68** (1996), pp. 1332–1334.

[68] R. Loesch, R. Aidam, L. Kirste, and A. Leuther. “Molecular beam epitaxial growth of metamorphic AlInSb/GaInSb high-electron-mobility-transistor structures on GaAs substrates for low power and high frequency applications”. *J. Appl. Phys.* **109** (2011), pp. 033706–033706.

[69] R. Liang, J. Chen, G. Kipshidze, D. Westerfeld, L. Shterengas, and G. Belenky. “High-Power 2.2-µm diode lasers with heavily strained active region”. *IEEE Photonics Technol. Lett.* **23** (2011), pp. 603–605.

[70] P. C. Hemmer. *Kvantemekanikk*. Tapir akademisk forlag, 2005.

[71] D. J. BenDaniel and C. B. Duke. “Space-charge effects on electron tunneling”. *Phys. Rev.* **152** (1966), p. 683.

[72] B. E. A. Saleh and M. C. Teich. *Fundamentals of photonics*. Wiley series in pure and applied optics. Wiley, 1991. ISBN: 9780471839651.

[73] A. Sarangan. *LIGHTS Online Optical Simulation Software*. May 2012. URL: `http://www.nano-fab.com/lights/`.

[74] E. V. Arzhanov, A. P. Bogatov, V. P. Konyaev, O. M. Nikitina, and V. I. Shveikin. “Waveguiding properties of heterolasers based on InGaAs/GaAs strained quantum-well structures and characteristics of their gain spectra”. *Quantum Electron.* **24** (1994), p. 581.

[75] A. P. Bogatov, A. E. Drakin, and V. I. Shveikin. “Efficiency and intensity distribution in a semiconductor laser operating in the ’leaky’ regime”. *Quantum Electron.* **29** (1999), p. 28.

[76] F. A. Jenkins and H. E. White. *Fundamentals of Optics*. 4th. International student edition. McGraw-Hill, 1976. ISBN: 9780070323308.

[77] N. Hodgson and H. Weber. *Optical Resonators: Fundamentals, Advanced Concepts, Applications*. Vol. 108. Springer Verlag, 2005. ISBN: 9780387400785.

[78] B. W. Hakki and T. L. Paoli. “Gain spectra in GaAs double-heterostructure injection lasers”. *J. Appl. Phys.* **46** (1975), pp. 1299–1306.

[79] D. Z. Garbuzov, R. J. Menna, M. A. Maiorov, H. Lee, V. Khalfin, L. A. DiMarco, D. R. Capewell, R. U. Martinelli, G. L. Belenky, and J. C. Connolly. “2.3- to 2.7-μm room-temperature cw operation of InGaAsSb/AlGaAsSb broad-contact and single-mode ridge-waveguide SCH-QW diode lasers”. *Proc. SPIE, In-Plane Semiconductor Lasers III* **3628** (1999), pp. 124–129. DOI: `10.1117/12.344538`.

[80] R. J. Kumar, J. M. Borrego, P. S. Dutta, R. J. Gutmann, C. A. Wang, and G. Nichols. “Auger and radiative recombination coefficients in 0.55-eV InGaAsSb”. *J. Appl. Phys.* **97** (2005), pp. 023530–023530.

[81] H. Iwamura, T. Saku, H. Kobayashi, and Y. Horikoshi. “Spectrum studies on a GaAs-AlGaAs multi-quantum-well laser diode grown by molecular beam epitaxy”. *J. Appl. Phys.* **54** (1983), pp. 2692–2695.

[82] H. Kobayashi, H. Iwamura, T. Saku, and K. Otsuka. “Polarisation-dependent gain-current relationship in GaAs-AlGaAs MQW laser diodes”. *Electron. Lett* **19** (1983), pp. 166–168.

[83] A. Mathur and P. D. Dapkus. “Polarization insensitive strained quantum well gain medium for lasers and optical amplifiers”. *Appl. Phys. Lett.* **61** (1992), pp. 2845–2847.

[84] J. A. Gonzalez-Cuevas, T. F. Refaat, M. N. Abedin, and H. E. Elsayed-Ali. “Calculations of the temperature and alloy composition effects on the optical properties of $Al_xGa_{1-x}As_ySb_{1-y}$ and $Ga_xIn_{1-x}As_ySb_{1-y}$ in the spectral range 0.5–6 eV”. *J. Appl. Phys.* **102** (2007), p. 014504. DOI: `DOI : 10.1063/1.2751406`.

[85] A. Kosterev, G. Wysocki, Y. Bakhirkin, S. So, R. Lewicki, M. Fraser, F. Tittel, and R. F. Curl. “Application of quantum cascade lasers to trace gas analysis”. *Appl. Phys. B* **90** (2008), pp. 165–176.

[86] I. Vurgaftman, J. R. Meyer, and L. R. Ram-Mohan. “Band parameters for III–V compound semiconductors and their alloys”. *J. Appl. Phys.* **89** (2001), pp. 5815–5875. DOI: `10.1063/1.1368156`.

[87] Y. W. Jung, T. H. Ghong, J. S. Byun, Y. D. Kim, H. J. Kim, Y. C. Chang, S. H. Shin, and J. D. Song. “Dielectric response of AlSb from 0.7 to 5.0 eV determined by in situ ellipsometry”. *Appl. Phys. Lett.* **94** (2009), pp. 231913–231913.

[88] R. Ferrini, M. Patrini, and S. Franchi. “Optical functions from 0.02 to 6 eV of $Al_xGa_{1-x}Sb$/GaSb epitaxial layers”. *J. Appl. Phys.* **84** (1998), pp. 4517–4524.

[89] S. Adachi. “Optical dispersion relations for GaP, GaAs, GaSb, InP, InAs, InSb, AlGaAs, and InGaAsP”. *J. Appl. Phys.* **66** (1989), p. 6030.

[90] O. Madelung. *Semiconductors–basic Data*. 2nd. Springer Berlin, 1996, pp. 80–86. ISBN: 9783540608837.

[91] R. Pino, Y. Ko, and P. S. Dutta. “Adhesion-free growth of AlSb bulk crystals in silica crucibles”. *J. Cryst. Growth* **290** (2006), pp. 29–34. DOI: `10.1016/j.jcrysgro.2005.05.084`.

[92] T. Shibata, J. Nakata, Y. Nanishi, and M. Fujimoto. “A Rutherford backscattering spectroscopic study of the aluminum antimonide oxidation process in air”. *Jpn. J. Appl. Phys.* **33** (1994), pp. 1767–1772.

[93] *Wafer Technologies*. May 2012. URL: `http://www.wafertech.co.uk/`.

[94] *Galaxy Compound Semiconductors, Inc.* June 2012. URL: `http://www.galaxywafer.com`.

[95] *MTI Corporation*. June 2012. URL: `http://www.mtixtl.com`.

[96] *Semiconductor Wafer Inc.* June 2012. URL: `http://www.semiwafer.com`.

[97] *NewWay Semiconductor Inc.* June 2012. URL: `http://www.newwaysemiconductor.com/`.

[98] A. Z. Li, J. X. Wang, Y. L. Zheng, G. P. Ru, W. G. Bi, Z. X. Chen, and N. C. Zhu. “The behavior of dopant incorporation and internal strain in $Al_xGa_{1-x}As_{0.03}Sb_{0.97}$ grown by molecular beam epitaxy”. *J. Cryst. Growth* **127** (1993), pp. 566–569. DOI: `DOI:10.1016/0022-0248(93)90684-O`.

[99] A. Y. Polyakov, S. J. Eglash, A. G. Milnes, M. Ye, S. J. Pearton, and R. G. Wilson. “Electrical properties of MBE grown layers of AlGaAsSb and the effects of proton implantation and hydrogen plasma treatment”. *J. Cryst. Growth* **127** (1993), pp. 728–731.

[100] S. Miya, S. Muramatsu, N. Kuze, K. Nagase, T. Iwabuchi, A. Ichii, M. Ozaki, and I. Shibasaki. “AlGaAsSb Buffer/Barrier on GaAs substrate for InAs channel devices with high electron mobility and practical reliability”. *J. Electron. Mater.* **25** (1996), pp. 415–420.

[101] H. Kroemer. “The 6.1 A family (InAs, GaSb, AlSb) and its heterostructures: a selective review”. *Physica E* **20** (2004), pp. 196–203.

[102] M. Fatemi and R. E. Stahlbush. “X-ray rocking curve measurement of composition and strain in Si-Ge buffer layers grown on Si substrates”. *Appl. Phys. Lett.* **58** (1991), pp. 825–827. DOI: `10.1063/1.104501`.

[103] *D8 X-ray Diffractometer User Manual Vol. III*. Bruker AXS GmbH. 2006.

[104] *DHS 900 Domed Hot Stage Instruction Handbook*. Anton Paar GmbH. 2001.

[105] R. Resel, E. Tamas, B. Sonderegger, P. Hofbauer, and J. Keckes. “A heating stage up to 1173K for X-ray diffraction studies in the whole orientation space”. *J. Appl. Crystallogr.* **36** (Feb. 2003), pp. 80–85. DOI: `10.1107/S0021889802019568`.

[106] C. R. Wie. “Rocking curve peak shift in thin semiconductor layers”. *J. Appl. Phys.* **66** (1989), pp. 985–988.

[107] W. L. Bond. “Precision lattice constant determination”. *Acta Crystallogr.* **13** (Oct. 1960), pp. 814–818. DOI: `10.1107/S0365110X60001941`.

[108] M. Fatemi. “An X-ray rocking curve technique for the absolute characterization of epitaxial layers and single-crystal solids”. *Appl. Phys. Lett.* **80** (2002), pp. 935–937. DOI: `10.1063/1.1447012`.

[109] E. N. Maslen. *Internation tables for crystallography volume c*. Kluwer Academic Publishers Dordrect/Boston/London, 1995, pp. 520–529.

[110] M. Fatemi. “Absolute measurement of lattice parameter in single crystals and epitaxic layers on a double-crystal X-ray diffractometer”. *Acta Crystallogr., Sect. A: Found. Crystallogr.* **61** (2005), pp. 301–313. DOI: `10.1107/S0108767305004496`.

[111] B. G. Streetman and S. K. Banerjee. *Solid state electronic devices*. 6th. Springer Berlin, 2006. ISBN: 9780132454797.

[112] M. A. Herman and H. Sitter. *Molecular beam epitaxy: fundamentals and current status*. Springer Series in Materials Science Series. Springer-Verlag, 1996. ISBN: 9783540605942.

[113] T. A. Nilsen, M. Breivik, E. Selvig, and B. O. Fimland. “Critical thickness of MBE-grown $Ga_{1-x}In_xSb(x < 0.2)$ on GaSb”. *J. Cryst. Growth* **311** (2009), pp. 1688–1691.

[114] L. M. Murray, A. Yildirim, S. R. Provence, D. T. Norton, T. F. Boggess, and J. P. Prineas. “Causes and elimination of pyramidal defects in GaSb-based epitaxial layers”. *J. Vac. Sci. Technol., B* **31** (2013), pp. 03C108–03C108.

[115] R. G. Bedford, G. Triplett, D. H. Tomich, S. W. Koch, J. Moloney, and J. Hader. “Reduced auger recombination in mid-infrared semiconductor lasers”. *J. Appl. Phys.* **110** (2011), pp. 073108–073108.

[116] O. Dier, S. Dachs, M. Grau, C. Lin, C. Lauer, and M.-C. Amann. “Effects of thermal annealing on the band gap of GaInAsSb”. *Appl. Phys. Lett.* **86** (2005), pp. 151120–151120.

[117] V. R. Manfrinato, L. Zhang, D. Su, H. Duan, R. Hobbs, E. A. Stach, and K. Berggren. “Resolution limits of electron-beam lithography towards the atomic scale”. *Nano Lett.* (2012).

[118] H. Schift. “Nanoimprint lithography: An old story in modern times? A review”. *J. Vac. Sci. Technol., B* **26** (2008), pp. 458–480.

[119] M. Quirk and J. Serda. *Semiconductor manufacturing for technology*. Prentice Hall PTR, 2001. ISBN: 9780130815200.

[120] L. Zhang, L. F. Lester, R. J. Shul, C. G. Willison, and R. P. Leavitt. “Inductively coupled plasma etching of III–V antimonides in BCl_3/Ar and Cl_2/Ar”. *J. Vac. Sci. Technol., B* **17** (1999), pp. 965–969.

[121] K. Swaminathan, P. E. Janardhanan, and O. V. Sulima. “Inductively coupled plasma etching of III–V antimonides in BCl_3/$SiCl_4$ etch chemistry”. *Thin Solid Films* **516** (2008), pp. 8712–8716.

[122] R. Germann. “Characterization Of Dry Etch Induced In Ill/V Micro-structures”. In: *Epitaxial Materials and In-Situ Processing for Optoelectronic Devices, 1991/Microfabrication for Photonics and Optoelectronics, 1991. LEOS 1991 Summer Topical Meetings on*. IEEE. 1991, pp. 33–34. DOI: `10.1109/LEOSST.1991.639005`.

[123] K. Ikossi, M. Goldenberg, and J. Mittereder. “Metallization options and annealing temperatures for low contact resistance ohmic contacts to n-type GaSb”. *Solid-State Electron.* **46** (2002), pp. 1627–1631.

[124] H. K. Choi, J. N. Walpole, G. W. Turner, S. J. Eglash, L. J. Missaggia, and M. K. Conners. “GaInAsSb-AlGaAsSb tapered lasers emitting at 2 µm”. *IEEE Photonics Technol. Lett.* **5** (1993), pp. 1117–1119.

[125] J. A. Robinson and S. E. Mohney. “An improved In-based ohmic contact to n-GaSb”. *Solid-State Electron.* **48** (2004), pp. 1667–1672.

[126] A. Vogt, A. Simon, J. Weber, H. L. Hartnagel, J. Schikora, V. Buschmann, and H. Fuess. "Non-annealed ohmic contacts to p-GaSb grown by molecular beam epitaxy". *Mater. Sci. Eng., B* **66** (1999), pp. 199–202. DOI: `10.1016/S0921-5107(99)00098-7`.

[127] J. A. Robinson. *Study of palladium/gallium antimonide reactions and ohmic contacts to n-type gallium antimonide*. PhD thesis. University Park, Pennsylvania, USA: The Pennsylvania State University, 2005.

[128] A. Piotrowska, E. Kaminska, T. Piotrowski, S. Kasjaniuk, M. Guziewicz, S. Gierlotka, X. W. Lin, Z. Lilientalweber, J. . Washburn, and S. Kwiatkowski. "Interaction of Au with GaSb and its impact on the formation of ohmic contacts". *Acta Phys. Pol. A* **87** (1995), pp. 419–422.

[129] G. M. Smith, D. V. Forbes, R. M. Lammert, and J. J. Coleman. "Metallization to asymmetric cladding separate confinement heterostructure lasers". *Appl. Phys. Lett.* **67** (1995), pp. 3847–3849. DOI: `10.1063/1.115293`.

[130] A. Piotrowska and E. Kaminska. "Ohmic contacts to III–V compound semiconductors". *Thin Solid Films* **193** (1990), pp. 511–527.

[131] A. Vogt, A. Simon, H. L. Hartnagel, J. Schikora, V. Buschmann, M. Rodewald, H. Fuess, S. Fascko, C. Koerdt, and H. Kurz. "Ohmic contact formation mechanism of the PdGeAu system on n-type GaSb grown by molecular beam epitaxy". *J. Appl. Phys.* **83** (1998), pp. 7715–7719.

[132] J. A. Robinson and S. E. Mohney. "Solid-state phase formation between Pd thin films and GaSb". *J. Electron. Mater.* **35** (2006), pp. 48–55.

[133] T. W. Bonder. *Copper bonding. Copper Wire bonding with TPT Wire Bonder*. TPT, 2011. URL: `http://www.youtube.com/watch?v=cCHXIYnYMTc` (visited on 05/21/2013).

[134] F. Hickmann. *Wire Bonding Technology*. Version 3.03. TPT. 2006. URL: `www.tpt.de`.

[135] Nanolab. *Profilometer*. 2013. URL: `http://www.norfab.no/technologies/characterization/ntnu-nanolab/profilometer-2/`.

[136] M. A. Hartney, D. W. Hess, and D. S. Soane. "Oxygen plasma etching for resist stripping and multilayer lithography". *J. Vac. Sci. Technol., B* **7** (1989), pp. 1–13.

[137] E. Poppe. Private communications. 2009.

[138] *Collection of etch recipes for the Plasmalab System100 ICP 180*. Oxford Instruments Plasma Technology. 2009. Collection of etch recipes given to NTNU Nanolab as a part of the purchase of the "Plasmalab System100 ICP 180" ICP-RIE etch system.

[139] T.-N. Tran. Private communications. June 2013.

[140] T.-N. Tran. Private communications. Sept. 2013.

[141] K. Dutting, O. Hildebrand, D. Baums, W. Idler, M. Schilling, and K. Wunstel. "Analysis and simple tuning scheme of asymmetric Y-lasers". *IEEE J. Quantum Electron.* **30** (1994), pp. 654–659.

[142] M. Kinzer, Q. K. Yang, S. Hugger, M. Brunner, F. Fuchs, and J. Wagner. "Diffraction-Limited Infrared-Imaging of the Near-Field Intensity Emitted by Quantum-Cascade Lasers". *IEEE J. Quantum Electron.* **48** (2012), pp. 696–702.

[143] S. Adachi. "Band gaps and refractive indices of AlGaAsSb, GaInAsSb, and InPAsSb: Key properties for a variety of the 2–4-μm optoelectronic device applications". *J. Appl. Phys.* **61** (1987), pp. 4869–4876.

[144] C. Alibert, M. Skouri, A. Joullie, M. Benouna, and S. Sadiq. "Refractive indices of AlSb and GaSb-lattice-matched $Al_xGa_{1-x}As_ySb_{1-y}$ in the transparent wavelength region". *J. Appl. Phys.* **69** (1991), pp. 3208–3211.

[145] Z. Q. Li and Z. M. Simon Li. "Comprehensive anaylsis of GaSb-based mid-infrared vertical-cavity surface-emitting lasers". In: *SPIE OPTO*. International Society for Optics and Photonics. 2013, p. 863907. DOI: `10.1117/12.1000108`.

[146] L. Cerutti, A. Ducanchez, G. Narcy, P. Grech, G. Boissier, A. Garnache, E. Tournié, and F. Genty. "GaSb-based VCSELs emitting in the mid-infrared wavelength range (2–3μm) grown by MBE". *J. Cryst. Growth* **311** (2009), pp. 1912–1916.

[147] H. Loui. *Fourier Beam Propagation*. Report. Course #: ECEN-6006, Special topics - Numerical Methods in Photonics. University of Colorado, 2004. URL: `http://ecee.colorado.edu/~mcleod/teaching/ugol/references/project5%20by%20Loui.pdf` (visited on 29/11/2012).

[148] E. G. Codina. *Finite Difference Beam Propagation Method*. 2007. URL: `http://www.mathworks.com/matlabcentral/fileexchange/14887-finite-difference-beam-propagation-method` (visited on 2012).

[149] J. M. López-Doña, J. G. Wangüemert-Pérez, and I. Molina-Fernández. "Fast-Fourier-based three-dimensional full-vectorial beam propagation method". *IEEE Photonics Technol. Lett.* **17** (2005), pp. 2319–2321.

[150] J. Wangüemert-Pérez, I. Molina-Fernández, and M. A. Luque-Nieto. "A novel Fourier based 3D full-vectorial beam propagation method". *Opt. Quantum Electron.* **36** (2004), pp. 285–301.

[151] O. Yasumasa and T. Yozo. “Precise determination of lattice parameter and thermal expansion coefficient of silicon between 300 and 1500 K”. *J. Appl. Phys.* **56** (1984), pp. 314–320. DOI: `10.1063/1.333965`.

[152] T. Brudevoll. Private communications. Apr. 2013.

[153] N. Devi, S. Sharma, and U. P. Verma. “Ab-initio study of $Al_{1-x}Ga_xSb$ compound”. *Z. Kristallogr.* **226** (2011), pp. 83–88.

[154] G. P. Donati, R. Kaspi, and K. J. Malloy. “Interpolating semiconductor alloy parameters: Application to quaternary III–V band gaps”. *J. Appl. Phys.* **94** (2003), pp. 5814–5819. DOI: `10.1063/1.1613371`.

[155] P. M. Mooney. “Donor-related levels in GaAs and $Al_xGa_{1-x}As$”. *Semicond. Sci. Technol.* **6** (1991), B1.

[156] J.-J. He and D. Liu. “Wavelength switchable semiconductor laser using half-wave V-coupled cavities”. *Opt. Express* **16** (Mar. 2008), pp. 3896–3911. DOI: `10.1364/OE.16.003896`.

[157] J. Jin, L. Wang, T. Yu, Y. Wang, and J.-J. He. “Widely wavelength switchable V-coupled-cavity semiconductor laser with $\sim$40 dB side-mode suppression ratio”. *Opt. Lett.* **36** (Nov. 2011), pp. 4230–4232. DOI: `10.1364/OL.36.004230`.

[158] J.-O. Wesström, G. Sarlet, S. Hammerfeldt, L. Lundqvist, P. Szabo, and P.-J. Rigole. “State-of-the-art performance of widely tunable modulated grating Y-branch lasers”. In: *Optical Fiber Communication Conference*. Optical Society of America. 2004.

[159] D. Z. Garbuzov, R. U. Martinelli, H. Lee, P. K. York, R. J. Menna, J. C. Connolly, and S. Y. Narayan. “Ultralow-loss broadened-waveguide high-power 2 μm AlGaAsSb/InGaAsSb/GaSb separate-confinement quantum-well lasers”. *Appl. Phys. Lett.* **69** (1996), pp. 2006–2008.

[160] D. A. Yarekha, A. Vicet, A. Perona, G. Glastre, B. Fraisse, Y. Rouillard, E. M. Skouri, G. Boissier, P. Grech, A. Joullié, C. Alibert, and A. N. Baranov. “High efficiency GaInSbAs/GaSb type-II quantum well continuous wave lasers”. *Semicond. Sci. Technol.* **15** (2000), p. 390.

[161] *Optical End Point Detectors*. Oxford Instruments Plasma Technology. 2013. URL: `http://www.oxford-instruments.com/support/plasma-technology-support/upgrades/end-point-detection-upgrades` (visited on 01/10/2013).

[162] F. Capasso and G. F. Williams. “A Proposed Hydrogenation/Nitridization Passivation Mechanism for GaAs and Other III–V Semiconductor Devices, Including InGaAs Long Wavelength Photodetectors”. *J. Electrochem. Soc.* **129** (1982), pp. 821–824.

[163] M.-C. Wu and C.-C. Chen. “Photoluminescence of high-quality GaSb grown from Ga-and Sb-rich solutions by liquid-phase epitaxy”. *J. Appl. Phys.* **72** (1992), pp. 4275–4280.